

# Metastable Zone Determination and Nucleation kinetics during Melt Crystallization of Poly-unsaturated Fatty Acids

Von der Fakultät für Umwelt und Naturwissenschaften  
der Brandenburgischen Technischen Universität Cottbus-Senftenberg  
zur Erlangung des akademischen Grades eines Doktor-Ingenieurs

genehmigte Dissertation

vorgelegt von

Master of Science

Sunanda Dasgupta

aus Kolkata, India

Gutachter: Prof. Dr.-Ing. habil. Peter Ay

Gutachter: Prof. Dr.-Ing. Christian Stollberg

Tag der mündlichen Prüfung: 26.09.2017

*'Don't limit a child to your own learning, for he was born in another time.'*

*Rabindranath Tagore*

*for my grandparents*

## Acknowledgement

It is a humbling experience to thank those who have made this thesis possible. My deepest gratitude goes to my supervisor Prof. Dr.-Ing. habil. Peter Ay, who has guided and supported me throughout my thesis whilst allowing me to work in my own way. I appreciate and treasure the counsel and continuous cooperation extended by him throughout my professional experience, here. I must add a special note of appreciation to Mrs. Margitta Ay for being so endearing and encouraging every time I had the opportunity to meet her.

I am greatly indebted to Prof. Dr.-Ing. Christian Stollberg, my second supervisor, for his open minded and understanding approach. It is not always easy to find a supervisor who is ever so ready to listen and place himself in our shoes. He supported me in my research pursuits and interfered only to criticize constructively. I value and appreciate the support and advice.

I would like to express my deepest gratitude to all of my dissertation committee members, led by Prof. Dr.-Ing Ulrich Riebel for finding the time to sit and discuss my work.

I have immensely enjoyed the company of previous and current academic members of the Chair of Mineral processing group, Brandenburg University of Technology, Cottbus-Senftenberg. I would like to specially thank Nadine Dreijack, Florian Rettig, Karl-Andreas Eckert, Constantin Jurischka and Benjamin Selge for their valuable reviews and comments. I appreciate the friendship, discussions and the stimulating working environment.

I would like to specially thank Stephanie Schulz, who apart from being a great friend has assisted me with the sample analyses at the laboratory. Siegfried Müller-Fehn and Uwe Kränzel, the men with the golden hands, as our Professor rightly says, consistently came up with suggestions and prototypes as and when I required any. I would also like to thank Grit Gericke for meticulously taking care of all the administrative details without hesitation.

Some of my experimental work would not have been complete without the help of Dr. Rudolph Riesen at the Materials Characterization Market Support Lab of Mettler Toledo Analytical in Schwerzenbach, Switzerland. To him, I am indebted.

It was my pleasure to have interacted and collaborated with fellow researchers at conferences and webinars. I owe a lot to the research community at large, the forums, lecturers providing free online tutorials, open source software contributors for tools, etc. I am grateful to the reviewers of my journal publications for their encouragement and invaluable suggestions, which have significantly improved my work.

To all the readers, whether you find this thesis stimulating or soporific, either way my husband, Mayutan, is to blame. I could not have finished this manuscript without his unflinching support, encouragement and patience. Naina, you might not understand now, but you were the one who kept me going whenever I felt that I had reached my limits. You came into our lives when I was in the midst of my PhD and since then you have shown us that no matter what, we can bring that priceless smile on your face. My parents, Jayanti and Rajat Dasgupta, has given me the gift of this life and the knowledge, wisdom and integrity to deal with it. I



would not embarrass my sister, Sukanya, by thanking her but I have to mention that in spite of tolerating me her entire life, she has helped me a great deal during the preparation and editing phase of this manuscript. My new family through marriage have been always been a source of encouragement in my career ambitions. A special mention of my great-aunts, Abhaya and Ajaya Dasgupta and Vijaya Mukhopadhyay; aunts, Chandra Kar, Supriya Chaudhuri, Aditi Dasgupta and Jolly Sengupta; cousins, Sourjya, Sonia, Siddhartha, Vinayak, Avishek, Rituparna, Aparna, Anoushka and Aakriti for their enthusiasm and positive rallying. Being an aunt to Arna, Dhara and Akhilan gives me so much joy for which I cannot thank my family enough. Special thanks goes to my best friend, Padma, for whom friendship goes as far as proofreading my work although memories of spending time on the terrace of our apartment are definitely the most special ones.

I dedicate this thesis to my grandparents, Amalendu and Sushmita Dasgupta and Amiya and Anila Dasgupta, who have loved and supported me unconditionally. I admire them for their humility in spite of being so accomplished and for standing tall and independent yet accepting aging so gracefully.

Finally, I thank Germany for providing me with such a wide variety of culture, which kept me sane, of course, not forgetting the excellent quality of life and research opportunity.



# Table of Contents

Table of Contents.....	i
Notation.....	iv
Acryonyms.....	v
Contributions to Publications .....	vi
Contributions to Conferences.....	vii
Declaration.....	viii
1. Introduction and motivation .....	1
1.1. Dissertation overview.....	6
2. Vegetable oils and Fatty acids – Fundamentals and State of the Art.....	7
2.1. Global production of vegetable oils .....	10
2.1.1. Trend.....	10
2.1.2. Location.....	10
2.1.3. Climate.....	12
2.2. Application.....	15
2.2.1. Edible oil.....	15
2.2.2. Biodiesel.....	18
2.2.3. Biopolymers .....	19
3. Melt crystallization of fatty acids .....	22
3.1. Nucleation kinetics and modeling .....	24
3.2. Crystal growth kinetics .....	30
3.3. Metastable zone width determination for SLE phase diagrams .....	31
4. Material, method and experimental setup .....	33
4.1. Chemical, equipment and software list.....	33
4.2. Sample characterization .....	36
4.2.1. Differential Scanning Calorimeter - Thermal analysis.....	36
4.2.2. Differential Scanning Calorimeter – Visual analysis (Microscopy).....	37
4.2.3. Flash Differential Scanning Calorimeter – Thermal Analysis .....	39
4.2.4. Gas Chromatography - Flame Ionization Detector - Chemical analysis.....	40
4.2.5. Raman microscopic Analysis- Positional composition analysis.....	42
4.2.6. Contact angle measurement.....	44
4.3. Multistage melt crystallization – phase diagrams and metastable zone determination .....	46
4.3.1. EasyMax™ reactor – tempered centrifuge setup .....	46

4.4.	Melt crystallization - nucleation kinetics.....	49
4.4.1.	Polarized light microscopy with high definition camera ( $\mu\text{l}$ scale) .....	50
4.4.2.	Capillaries for crystal growth rates ( $\mu\text{l}$ scale).....	53
4.4.3.	Focused beam reflectance technology (ml scale).....	54
4.4.4.	V-form Reactor – FBRM™ setup (ml scale) .....	55
4.4.5.	EasyMax™ Reactor – FBRM™ setup (ml scale) .....	57
4.5.	State of the art.....	60
4.5.1.	Fractionation and modification of oil.....	60
4.5.2.	Separation of saturated and unsaturated fractions from PUFA mixtures.....	60
4.5.3.	FBRM™ and its contemporaries – critical analysis.....	62
4.5.4.	Metastable zone width determination .....	66
5.	Result and discussion .....	68
5.1.	Melt crystallization of linseed oil based PUFA .....	68
5.2.	Phase diagrams of plant oil based PUFA – Metastable zone determination .....	72
5.2.1.	Interpretation of a thermogram from Differential Scanning calorimeter .....	72
5.2.2.	Differential Scanning Calorimeter – Thermal analysis .....	75
5.2.3.	Differential Scanning Calorimeter – Visual analysis (Microscopy).....	77
5.2.4.	Flash Differential Scanning Calorimeter .....	80
5.2.5.	Chemical analysis of the samples.....	84
5.2.6.	Phase diagrams at low saturated content including metastable ranges.....	86
5.2.7.	Modelling of the liquidus and solidus curves for all PUFA mixtures at low saturated concentrations.....	90
5.2.8.	Dependency of liquidus and solidus curves on mono-unsaturated acid fraction in mixture.....	92
5.3.	Nucleation kinetics .....	94
5.3.1.	Effects of supercooling and cooling rate on nucleation kinetics ( $\mu\text{scale}$ ).....	94
5.3.2.	Crystal growth kinetics ( $\mu\text{l}$ scale) .....	107
5.3.3.	Confocal Raman Spectroscopy ( $\mu\text{l}$ scale) .....	112
5.3.4.	Contact angle measurement as a function of surface type and composition of PUFA.....	115
5.3.5.	Effects of supercooling and cooling rate on induction time (ml scale).....	117
5.3.6.	Minimum size class detected under the FBRM- Easymax setup .....	126
5.3.7.	Gibbs free energy for nucleation using the Fisher Turnbull and Gibbs Thompson model (ml scale).....	128
5.3.8.	Outlook: FBRM™ on crystal growth kinetics in a Vibromix reactor (L scale) .....	131

*Table of Contents*

---

6. Summary.....	135
References .....	138
List of Figures .....	148
List of Tables .....	153
Appendix .....	156

## Notation

$\Delta\mu$	difference in chemical potential	J.mol <sup>-1</sup>
$f$	activity	-
$p$	pressure	Pa; kgm <sup>-1</sup> s <sup>-2</sup>
$R$	gas constant	J.mol <sup>-1</sup> .K <sup>-1</sup>
$T$	temperature	K; °C
$c$	mole fraction	-
$e$ (subscript)	at equilibrium	-
$k_B$	Boltzmann constant	J.K <sup>-1</sup>
$\hbar$	Planck's constant	Js
$J$	Rate of formation of a nucleus	m <sup>-3</sup> .s <sup>-1</sup>
$\tau$	Induction time	s
$S$	relative supersaturation	-
$\Delta S$	Reduction in entropy	J.K <sup>-1</sup> .mol <sup>-1</sup>
$N_A$	Avogadro's number	mol <sup>-1</sup>
$\Delta H_m$	Melt enthalpy	J.mol <sup>-1</sup>
$\Delta H$	Heat of fusion	J
$\Delta G$	Gibb's free enthalpy	J.mol <sup>-1</sup>
$\Delta G_{\text{interface}/A}$	Gibb's free enthalpy at the interface	J.mol <sup>-1</sup>
$\Delta G_{\text{bulk}/V}$	Gibb's free enthalpy at the bulk of melt	J.mol <sup>-1</sup>
$\Delta G_v$	Gibb's free energy per unit volume	J.m <sup>-3</sup>
$\Delta G_C$	Gibb's free energy of formation/nucleation	J
$\Delta G_D$	Gibb's free energy of molecular diffusion	J
$\Delta G_C'$	Specific Gibb's free energy of nucleation	J.mol <sup>-1</sup>
$T_M^\circ$	equilibrium melting temperature	K
$\Delta T$	supercooling	K
$r$	size	m
$r_c$	critical size	m
$\gamma$	interfacial free energy	J.m <sup>-2</sup>
$\sigma$	surface free energy at crystal/melt interface	J.m <sup>-2</sup>
$v_S$	volume of molecule in the solid phase	m <sup>3</sup>
$\rho$	population distribution	s <sup>-1</sup>
$A$	Rate of addition of monomers to critical nuclei	s <sup>-1</sup>
$N$	number of molecules per unit volume	m <sup>-3</sup>
$a$	shape factor	-
$\alpha$	conformation of molecules	-
$B$	Constant of growth	-
$\vartheta$	Contact angle	°
$T_r$	reactor temperature	°C
$T_j$	jacket temperature	°C
$T_{R1}$	Temperature sensor near wall of reactor	°C
$T_{R2}$	Temperature sensor at center of reactor	°C

## Acryonyms

<i>DAF</i>	Days after flowering
<i>PBE</i>	Population balance model
<i>KRE</i>	Kinetic rate equation
<i>PUFA</i>	Poly-Unsaturated Fatty Acid
<i>MUFA</i>	Mono-Unsaturated Fatty Acid
<i>PUFA1</i>	High linoleic sunflower oil based fatty acid mixture
<i>PUFA2</i>	High oleic sunflower oil based fatty acid mixture
<i>DSC</i>	Differential Scanning Calorimetry
<i>FBRM™</i>	Focused Beam Reflectance Technology
<i>SLE</i>	Solid Liquid Equilibrium
<i>FAME</i>	Fatty Acid Methyl Ester
<i>ATR-FTIR</i>	Attenuated total reflection Fourier Transform Infra-Red
<i>PsyA</i>	Particle System Analysis

## Contributions to Publications

### as First Author

- |   |      |
|---|------|
| <p><u>Nucleation kinetics during melt crystallization of plant based high oleic and linoleic polyunsaturated fatty acid mixtures</u><br/><b>S Dasgupta</b>, F Rettig, P Ay<br/>Crystal Growth &amp; Design, Volume 16 (2), Pages 861-866, American Chemical Society</p>     | 2016 |
| <p><u>Melt crystallization kinetics for enrichment of highly unsaturated fatty acid fractions based on Linseed oil</u><br/><b>S Dasgupta</b>, N Dreiack, P Ay<br/>Journal of Environmental Research And Development, Volume 11(1), Pages 1-6, Jerad Publications, GSEED</p> | 2016 |
| <p><u>Determination and Comparison of Equilibrium Data of Various Plant-Based Fatty Acid Mixtures</u><br/><b>S Dasgupta</b>, P Ay, S Schulz<br/>Chemical Engineering &amp; Technology , Volume 37 (6), Pages 1002-1008, WILEY-VCH Verlag</p>                                | 2014 |
| <p><u>Kinetics of Melt Crystallization of a Sunflower Oil-Based Polyunsaturated Fatty Acid Mixture</u><br/><b>S Dasgupta</b>, P Ay, R Kommolk, S Xu<br/>Chemical Engineering &amp; Technology, Volume 36 (7), Pages 1225-1230, WILEY-VCH Verlag</p>                         | 2013 |

### as Corresponding Author\*

- |  |      |
|--|------|
| <p><u>Novel model for the prediction of SSLE temperatures and crystallization paths of any mixture containing palmitic, stearic, oleic, linoleic and linolenic acid</u><br/>KA Eckert, <b>S Dasgupta*</b>, B Selge, P Ay<br/>Thermochimica Acta, Volume 652, 10 June 2017, Pages 126–140</p>   | 2017 |
| <p><u>Solvent-Free crystallization of a vegetable oil based fatty acid fraction in a Vibromix Reactor</u><br/>J. Poessnecker, KA Eckert, <b>S. Dasgupta*</b>, P Ay<br/>Journal of Environmental Research And Development, Volume 11(3), Pages 1-9, Jerad Publications, GSEED</p>   | 2017 |
| <p><u>Solid liquid phase diagrams of binary fatty acid mixtures – palmitic/stearic with oleic/linoleic/linolenic acid mixture</u><br/>KA Eckert, <b>S Dasgupta*</b>, B Selge, P Ay<br/>Thermochimica Acta, Volume 630, Pages 50–63, Elsevier</p>   | 2016 |
| <p><u>Construction and comparison of solid liquid phase diagrams of binary sat-sat and unsat-unsat fatty acid mixtures comprising two of palmitic/stearic/oleic/linoleic/linolenic acid</u><br/>KA Eckert, <b>S Dasgupta*</b>, B Selge, P Ay<br/>Journal of Environmental Research And Development, Volume 10(4), Pages 1-9, Jerad Publications, GSEED</p> | 2016 |



## Contributions to Conferences

as First Author

- |   |      |
|---|------|
| <p><u>SLE diagram for a high oleic palm oil based fatty acid mixture at low saturated content</u><br/><b>S Dasgupta</b>, C Glaser, P Ay<br/>9th Workshop on Fats and Oils as Renewable Feedstock for the Chemical Industry, abiosus e.V. Conferences, Karlsruhe, Germany (Poster)</p>                                   | 2017 |
| <p><u>Melt crystallization kinetics for enrichment of highly unsaturated fatty acid fractions based on Linseed oil</u><br/><b>S Dasgupta</b>, N Dreiack, P Ay<br/>8th International Congress of Environmental Research, Lübeck, Germany (Poster)</p>  | 2016 |
| <p><u>In-situ monitoring and induction time measurements during melt crystallization of plant based fatty acid mixtures in V-form reactor</u><br/><b>S Dasgupta</b>, P Ay<br/>6th Workshop on Fats and Oils as Renewable Feedstock for the Chemical Industry, abiosus e.V. Conferences, Karlsruhe, Germany (Poster)</p> | 2013 |
| <p><u>Enrichment of unsaturated fractions in a Linseed oil based fatty acid mixture by melt crystallization</u><br/><b>S Dasgupta</b>, N Dreiack, P Ay<br/>5th Workshop on Fats and Oils as Renewable Feedstock for the Chemical Industry, abiosus e.V. Conferences, Karlsruhe, Germany (Poster)</p>                    | 2012 |

as Corresponding Author\*

- |   |      |
|---|------|
| <p><u>Construction and comparison of solid liquid phase diagrams of synthetic binary fatty acid mixtures – palmitic/stearic and oleic/linoleic/linolenic acid mixtures</u><br/>KA Eckert, <b>S Dasgupta*</b>, B Selge, P Ay<br/>8th International Congress of Environmental Research, Lübeck, Germany (Poster)</p>            | 2016 |
| <p><u>Liquid solid phase behavior of ternary fatty acid systems of palmitic, stearic, oleic and linoleic acid,</u><br/>KA Eckert, <b>S Dasgupta*</b>, B Selge<br/>P Ay, 8th Workshop on Fats and Oils as Renewable Feedstock for the Chemical Industry, abiosus e.V. Conferences, Karlsruhe, Germany (Poster)</p>             | 2015 |
| <p><u>Novel techniques to optically characterize melt crystallization kinetics of high oleic sunflower oil based fatty acid mixture</u><br/>KA Eckert, <b>S Dasgupta*</b>, P Ay<br/>7th Workshop on Fats and Oils as Renewable Feedstock for the Chemical Industry, abiosus e.V. Conferences, Karlsruhe, Germany (Poster)</p> | 2014 |
| <p><u>Pelletization of Rye-and Wheat straw with additives</u><br/>S Narra, S Dasgupta, P Ay, T Zeng, N Weller, 19th European Biomass Conference and Exhibition, proceedings, ICC Berlin International Congress Center Berlin, Germany (Paper)</p>   | 2011 |

## Declaration

I hereby declare that I have written this thesis independently without any help from others and without the use of documents or aids other than those stated. I have mentioned all used sources and cited them correctly according to established academic citation rules.

I ensure that I have not submitted this dissertation to any other PhD board and that it has not been rejected by any other doctoral committee.

Cottbus, 28.07.2017.



## 1. Introduction and motivation

Vegetable oils and fatty acids play an important role in the process of replacing mineral oil based products with renewable ones. The field of application for fatty acids is as wide as the different types of fatty acids themselves, ranging from large scale applications such as biodiesel or lubricants over customer products like cosmetics, medicines or nutritional additives to smaller scale specialty chemicals like epoxy resins, insect repellents and many more.<sup>1,2</sup> In spite of the demand, the production of fatty acids is continuously decreasing over the last few decades<sup>3</sup>, and few changes have been applied to the techniques for the processing and purification of these valuable compounds.

The crystallization temperatures of the unsaturated fatty acids are significantly lower than those of the saturated ones.<sup>4</sup> This is an essential and desirable property for raw materials in biodiesel production.<sup>4-7</sup> Moreover, multiple double bonds in the unsaturated fatty acid chains furnish more cross linking opportunities. This property is utilized for the production of a variety of epoxy resins.<sup>4,8,9</sup> Mono (MUFA) and Poly-unsaturated fatty acid mixtures (PUFA) along with saturated fatty acids are abundantly present in plant oils albeit in the form of triglycerides. The later can be easily hydrolyzed to form free fatty acids and glycerol. Research to address the challenges of finding a technically and economically affordable method to separate the unsaturated and saturated fatty acid mixtures is being aggressively pursued. One such effective method is melt crystallization.<sup>10</sup> Separation and purification of these fatty acids depending on their applications is mainly performed by two thermal fractionation processes, namely, distillation and crystallization.<sup>11</sup> Separation of fatty acids with different chain lengths is performed among other methods with vacuum distillation although purification of fatty acids with similar chain lengths but differing degrees of unsaturation is difficult by the same.<sup>12</sup> This is due to the fact that the boiling temperatures of these saturated, mono-unsaturated and poly-unsaturated fatty acids lie relatively close to one another.<sup>13,14</sup> Wanasundara et. al suggested an enrichment of unsaturated fatty acids to facilitate the manufacturing of biodiesel by saponification of the blend, thereon complexing the free fatty acids with urea and further separating them chemically.<sup>15</sup> On the other hand, the potential behind purification of these multi-component organic fatty acid mixtures with the help of crystallization has been recognized since long.<sup>16,17</sup> Therefore, investigations on crystallization

techniques which can be applied either on the melt directly or by the addition of a solvent are on the rise. Melt crystallization especially has proved to be cost effective owing to the obvious reduction of solvent removal and regeneration steps.<sup>11,16</sup> Another important factor attributed to the success of melt crystallization as a separation process is that of the relatively large differences in the melting points of the individual fatty acids.<sup>13,14</sup> A detailed overview of the boiling and melting points of the main components in vegetable oils have been presented in Table 4-4.

The experimental part of the dissertation can be divided into three main sections. Firstly, the effectiveness of melt crystallization and therein the influence of the temperature profile to purify the mother liquor of its saturated content was investigated. Therefore, a multi-step crystallization was performed to reach product compositions including a saturated content of C16:0 (palmitic acid) of around 2% and C18:0 (stearic acid) of below 1%. As per theory, melt crystallization can be applied as an efficient method to enrich PUFA mixtures as long as an appropriate temperature profile is found. Different temperature profiles and crystallization temperatures lead to differences in quality of the final product. Measures must be taken to not cool the system too far or fast as the saturated fatty acids would then start to crystallize unfavorably thereby reducing the yield. So, the difficulties lie in the choice of temperature regime within the metastable ranges, which has to be optimized for different systems. Therefore, information gathered from the equilibrium data of the samples, determined upon analyzing the multi-step crystallization fractions were used to determine the temperature profiles for the subsequent crystallization steps. Different end crystallization temperatures (13°C; 8°C; 3°C; -2°C) were employed to create varying degrees of super-saturation. The results were analyzed and compared and it was found that the process successfully almost depleted a linseed oil based fatty acid mixture of its saturated content. The final product contained around 2% palmitic and 0.8% stearic acid. Therefore, the success of melt crystallisation on the enrichment of unsaturated fractions was established although not optimised with respect to time and yield.<sup>11,18</sup>

Crystallization of the desired product from the melt, as established in theory, can generally be achieved by following a predetermined temperature profile.<sup>4,19</sup> Hence, it is of utmost importance to thermally and chemically characterize the samples and determine the metastable ranges within which the product would crystallize post required induction

times.<sup>17,20,21</sup> In other words, information about the metastable range of crystallization is indispensable as it is required to control and set the parameters of the crystallization process to achieve desired product quantity and quality.<sup>22</sup>

That leads to the second part which aims to determine the technically significant areas of the solid liquid equilibrium phase diagrams including metastable ranges of these mixtures. Therefore, PUFA mixtures with high unsaturated content obtained from a variety of plant oil resources were subjected to multistage melt crystallization processes with the objective of separating the saturated fatty acid content from the rest. Probes from every stage, both crystal and mother liquor fractions, were characterized thermally and chemically to determine the metastable range of crystallization and solidification. Due to the limited literature available, it was clear that sufficient fundamental research still needed to be done to create an overview of the melt crystallization behaviors of various naturally occurring fatty acid mixtures in order to study the prospects and effectiveness of this separation process. Hence, to generate the phase diagrams of these real systems, crystallization processes on the samples have been chosen in a manner such that the resulting curves concentrate on their behaviors at lower saturated fatty acids' concentrations, which is naturally of special relevance in technical applications. Apart from the Solid Liquid Equilibrium (SLE) phase diagrams, it was important to find their metastable zone widths so as to realize at which temperatures, nucleation or growth as mechanisms of crystallization limit one another as the primary process. Plant oil sources with high oleic, high linoleic and high linolenic acid were all chosen so as to provide a comparison as a function of the degree of unsaturation. The high linoleic sunflower oil PUFA mixture was also sent for an in-melt analysis of the crystal by means of a confocal Raman Microscope. This was done to determine the composition of the crystal pre-separation, such that a positional composition analysis of the crystal could be made. The chemical analyses of the samples and fractions post separation by centrifugation were performed by a Gas Chromatography – Flame Ionization Detector (GC-FID) setup. Experiments to measure the contact angles of the PUFA sample droplets on a variety of material surfaces were also performed. This was done to check which substrate showed similar and better properties than glass on which the nucleation kinetic investigations were later executed.

Differential scanning calorimetry (DSC) was used to investigate the thermal phase transitions of the samples. Interpretation of the thermogram is a significant part of data generation. A detailed illustration followed by further clarification of the reading of peak onsets, endsets and maximums; and translation of these points into physically significant phase transitions or boundaries were realized. In addition to this, an exemplary sample was tested under the in-situ DSC-Microscope setup so as to justify the interpretations of these peaks exhibited in the thermograms. Flash DSC was also used in order to check the effects of rapid cooling rates and specimen volume on the metastable ranges of crystallization.

Crystallization can be broadly classified into two steps: nucleation and growth.<sup>10,23</sup> Nucleation is possible only once the mixture or solution is supersaturated. This is realized by either changing the temperature, eliminating the solvent by evaporation or sublimation or by adding reactants.<sup>10,23</sup> In the case of melt crystallization, the desired product can be crystallized from the feed simply by following a pre-determined temperature regime. The temperature profile is decided upon the direct influence of two important factors namely, supercooling and cooling rates. On the other hand, parameters like induction time, nucleation rate, and crystal growth rate influence the efficiency of the separation of the desired product with respect to time, quality, and quantity.<sup>10,24</sup> Therefore, an attempt to experimentally quantify the induction times of nucleation during melt crystallization and thereby correlate the Gibbs free energy involved depending on supercooling and cooling rates have been made in the **last part of** this work. Samples were investigated both in micro and macro scale. A Polarized light microscopy - Gradient chamber setup was applied for experiments in micro scale. On the other hand, an Easymax™/V-form reactor- Focused Reflectance Beam Measurement (FBRM™) sensor setup was used for the macro (milliliter) experiments. Determination of a single 2D regression fitting the trends of the induction times as a function of supercooling at different cooling rates was performed. The same regression fit was then implemented on the macro scale experiments with good coefficients of determination,  $R^2$ . Fisher Turnbull plot and the Gibbs Thompsons model were adjusted and applied to correlate the Gibbs free energy,  $\Delta G'_c$  involved with the rate of nucleation captured by the FBRM™ technology. The dependency of this activation energy of nucleation on supercooling and cooling rates were then further discussed and interpreted. According to the plot,  $\Delta G'_c$  decreases exponentially with increasing supercooling. It could be concluded that

while the plot justifies the effect of supercooling on  $\Delta G'_c$ , it does not incorporate the effects of molecular diffusion or viscosity and hence the cooling rate.

A higher level of supercooling leads to a faster nucleation. Apart from this, the cooling rate is also an influencing factor on the induction time. The viscosity in the pertinent temperature range is the key influencing factor as higher cooling rate enables faster reaching of lower temperatures which in turn leads to higher viscosities. Therefore, it reduces the probability of nucleation due to molecular diffusion resistance. The opposing effects of supercooling and cooling rate decides the magnitude of induction time.<sup>25,26</sup> The combined effect of these opposing factors were successfully interpreted upon visualization of the hull obtained by 3D modeling of the parameter - induction time, as a function of supercooling and cooling rate. This was performed with the help of a data fitting library of pyeq2, a collection of python equations and a plotting program called gnuplot Version 5.0.<sup>27</sup>

The application of FBRM™ technology on the detection of crystal size during melt crystallization of a linseed oil based PUFA fraction was also tested in a relatively larger reactor called the Vibromix. The name comes from a vibrating disc or mixer fixed at the axis of the reactor which moves vertically along the length of the reactor depending on the parameters set. The disc also is of the same size as the inner diameter of the reactor thereby scraping any content adhering to the wall. Samples were taken from the reactor and tested under the microscope. The results were compared with those detected by the FBRM™ sensor so as to test the scope of FBRM™ to monitor larger scale and more concentrated samples.<sup>28</sup>



## 1.1. Dissertation overview

The dissertation starts with an in-depth review and analysis of the production of various plant oils on the basis of their fatty acid composition and type in the following section, **Chapter 2**. Information gathered is used to investigate the connection between the type of oils produced and the areas and art of cultivation. Composition of sunflower oil as a function of time of harvesting and place of cultivation was also studied. The two main types of sunflower oils produced: high linoleic and the high oleic, have been reviewed on the basis of their effectiveness as a raw material towards their applications.

Crystallization kinetic modeling with a road map starting from the very basic equation for the driving force or the difference in chemical potentials to the models used in this work to characterize the nucleation kinetics and to evaluate enthalpy parameters involved have been provided in **Chapter 3**. Fisher-Turnbull model and the Gibbs-Thomson equation have been applied here to study the induction time of crystal formation and its relation with the Gibbs free enthalpy of nucleation.

**The fourth Chapter** deals with the materials, methods and experimental setups used in this work. The basic mechanisms and concepts behind each method and setup involved in this study have been discussed along with a brief overview of the state of the art. A critical analysis of the FBRM™ laser method and equipment used to detect nucleation, with respect to its contemporaries has been also added.

The results obtained from the experiments and modeling, have been illustrated and discussed in **Chapter 5** followed by a summary in **Chapter 6**.

An **Appendix** has been added at the end of the thesis to add any missing data or extra diagrams which have been excluded in the main text of the dissertation to enable an easy read.

## 2. Vegetable oils and Fatty acids – Fundamentals and State of the Art

A variety of oils are naturally present in plants worldwide. These plant oils are primarily triacylglycerol or simply triglycerides containing a sequence of three fatty acids combined with a glycerol molecule.<sup>29</sup> A summary of reactions pertaining to vegetable oils and fats have been enlisted in Table 2-1. The saturated ones which are often found are namely, palmitic and stearic whereas oleic, linoleic and linolenic acids are the common unsaturated ones.

Reaction	Reactants	Products
<i>Hydrolysis of Triacylglycerol</i>	Triacylglycerol + Water (in the presence of enzyme or H <sup>+</sup> , double-metal cyanide [DMC])	3 Fatty acids + Glycerol
<i>Esterification of Fatty acids</i>	Fatty acid + Alcohol (in the presence of heat and H <sup>+</sup> )	Ester + Water
<i>Hydrogenation</i>	Unsaturated fat + Hydrogen (in the presence of Pt)	Saturated Fat
<i>Saponification (Ester)</i>	Fatty acid ester + strong base (e.g. NaOH)	Sodium salt of carboxylic acid + alcohol
<i>Saponification (Oil/Fat)</i>	Triacylglycerol + 3 base (e.g. 3NaOH)	3 Sodium salts of carboxylic acid + glycerol

TABLE 2-1: BRIEF SUMMARY OF REACTIONS OF OILS AND FATTY ACIDS<sup>30</sup>

According to previous investigations<sup>4,24</sup>, the more the unsaturation, the lower the crystallization temperature thereby making them more applicable as a resource for biodiesel production. In other words, the melting points for unsaturated fatty acids are much lower than those of saturated ones, as lower energy is required to melt samples with rising number of double bonds.<sup>31</sup>

Additionally, more unsaturation leads to more degrees of freedom and hence more variety when it comes to crosslinking themselves to form a polymer such as epoxy resins. In the absence of double bonds as in the case of saturated fatty acids, all carbon atoms are surrounded by hydrogen atoms in a tetrahedral angle. Hence, the saturated ones are almost linearly shaped, stack easily and develop strong intermolecular interactions. The molecular structures of the five main fatty acids have been illustrated in Figure 2-1.

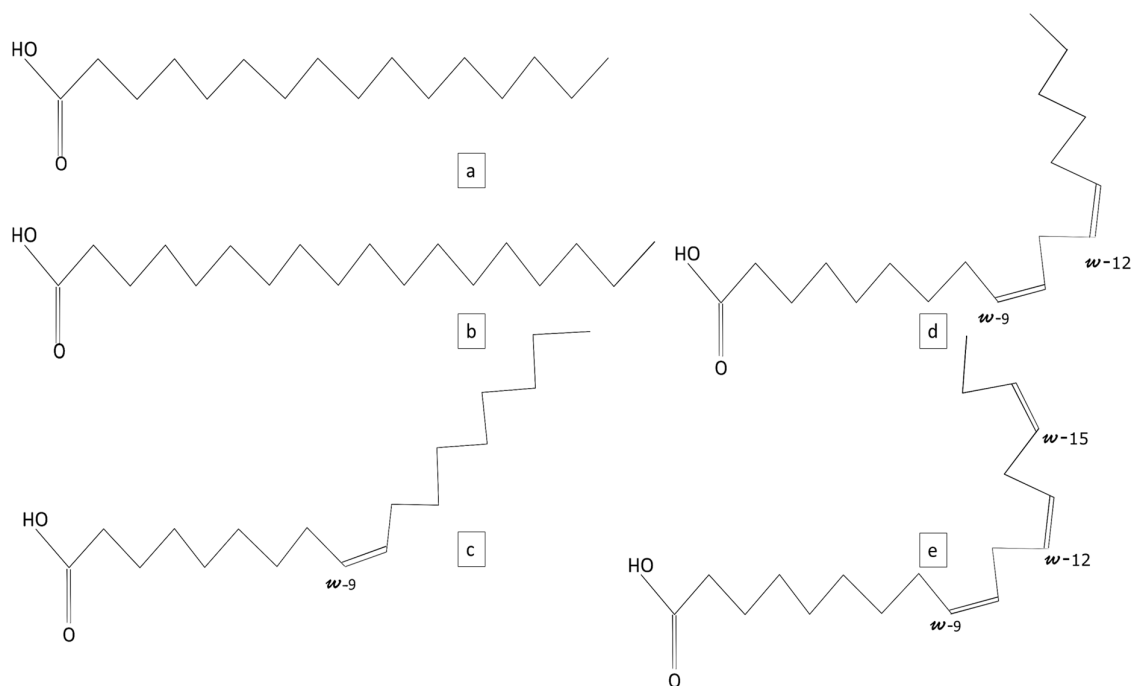


FIGURE 2-1: MOLECULAR STRUCTURES OF THE MAIN FATTY ACIDS: A.-PALMITIC ACID, B.-STEARIC ACID, C.-OLEIC ACID, D.-LINOLEIC ACID AND E.-LINOLENIC ACID\*

Introduction of a double bond, either in *cis* or in *trans* configuration, results in a kink in the shape. This in turn inhibits proper stacking of the molecules. Consequently, weaker molecular interaction in the unsaturated fatty acids results in lower melting points.<sup>37,38</sup> Due to the same reasons, the saturated fatty acids also exhibit higher thermal stability. Detailed investigations and trials on the high oleic acid sunflower oil also reveal that they crystallize much too quickly, once in their metastable zone of crystallization, leading to many small crystals. This amounts to smaller crystals which translate into lesser crystal growths<sup>4,10,24</sup> making separation of the crystal fraction from the mother liquor more difficult. The more the number of crystals, the more the chances of mother liquor being entrapped between them. This is of course when the form or shape of the crystal is not taken into account which also plays a big role.

There has been an increasing demand in the production of free unsaturated fatty acids owing to the reasons mentioned above. Free fatty acid mixtures and glycerol are obtained from fats and oils upon hydrolysis. These fatty acids can again be converted into fatty alcohols, surfactants, esters, amides, amines or soaps by reacting and transforming the carboxyl group attached at the end of the fatty acid chain.<sup>1,39,40</sup> Methyl esterification of these fatty acids is

\* Own representations based on chemical drawings in the Open Chemistry database, PubChem project by the U.S. Department of Health & Human Services<sup>32-36</sup>

for example applied for the production of biodiesel.<sup>1,41</sup> The by-product glycerol, now being produced in bulk in the biodiesel industry is being used for the manufacturing of fuel oxygenates (glycerol tertiary butyl ether), propylene glycols and epoxides like epichlorohydrin.<sup>1,42-44</sup>

## 2.1. Global production of vegetable oils

### 2.1.1. Trend

The annual production of plant oils has been illustrated in Figure 2-2<sup>45,46</sup> to obtain a better understanding of the production and demand of each of these oils in the global market over the years. The global production data clearly depicts that while the production of palm and soya oil has increased by around 10% and 20% respectively over 5 years, coconut and olive oil production among others has remained more or less constant.

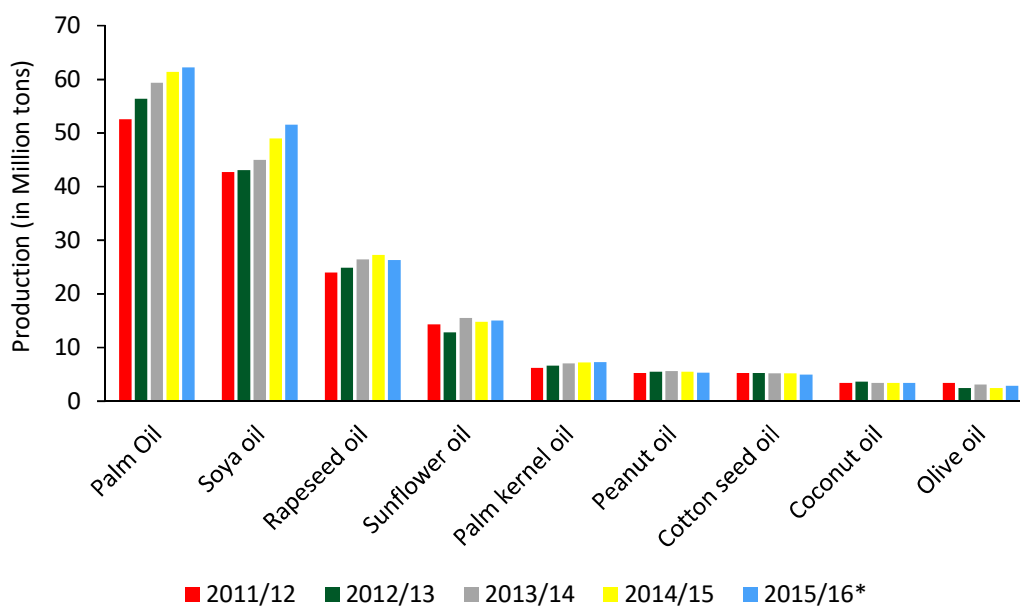


FIGURE 2-2: GLOBAL ANNUAL PLANT OIL PRODUCTION<sup>45,46</sup>

It can be also noted that in spite of the ‘health food hype’, the annual production of olive oil is still in the range of 2- 4 Mt whereas the production of sunflower oil ranges in between 14 and 15 Mt. Palm oil production is the highest which has increased from 52 to 63 Mt over the years. The negative ecological impact of such increased production is although not be underestimated.

### 2.1.2. Location

There is a variety of vegetable oils being produced worldwide. An attempt to investigate the connection between geographical distribution of the plants and the compositions of their respective oils has been made here. A composition distribution of the main fatty acids,

present in the vegetable oils have been illustrated in Table 2-2. The table classifies the oils as between lauric acid, C12 to linoleic acid. There are a few oil types listed here which do not add up to 100% due to traces of acids present other than classified here.

Type of oil	C12:0	C14:0	C16:0	C18:0	C18:1	C22:1	C18:2	C18:3
High linoleic sunflower	0	0.1	6	5.9	16	0	71.4	0.6
High oleic sunflower	0	0	3.5	3	85.4	0	6.7	0.1
Linseed	0	0	4.92	2.41	19.7	0	18.03	54.94
Soybean	0	0.1	10.3	4.7	22.5	0	54.1	8.3
Canola	0	0.1	3.9	3.1	60.2	0.5	21.1	11.1
Olive	0	0	11	3.6	75.3	0	9.5	0.6
Palm	0.9	1.3	43.9	4.9	39	0	9.5	0.3
Cottonseed	0	0.8	22.9	3.1	18.5	0	54.2	0.5
High oleic safflower	0	0.34	5.46	1.75	79.36	0	12.86	0
Safflower	0	0.1	6.6	3.3	14.4	0	75.5	0.1
Peanut	0	0	10.4	8.9	47.1	0.2	32.9	0.5
Cottonseed	0	0.8	22.9	3.1	18.5	0	54.2	0.5

TABLE 2-2: FATTY ACID DISTRIBUTION OF DIFFERENT VEGETABLE OILS FROM LITERATURE<sup>47-49</sup> AND GC-FID ANALYSES†

Annual global production of individual vegetable oils in different countries have been illustrated in Figure 2-3 for the agricultural year 2015/2016.<sup>45</sup> It can be noted that warmer countries like India, Indonesia, Malaysia, parts of the United States and China produce a lot of highly saturated oils like either palm or cotton seed oil whereas the European Union (represented in violet) concentrates more upon the production of olive, rapeseed, sunflower and soya bean oil. The latter are rich in unsaturated fatty acid content leading to the discussion in Section 2.1.3 of whether a connection exists.

† Analyses at the department laboratory of Mineral processing, BTU – Cottbus-Senftenberg

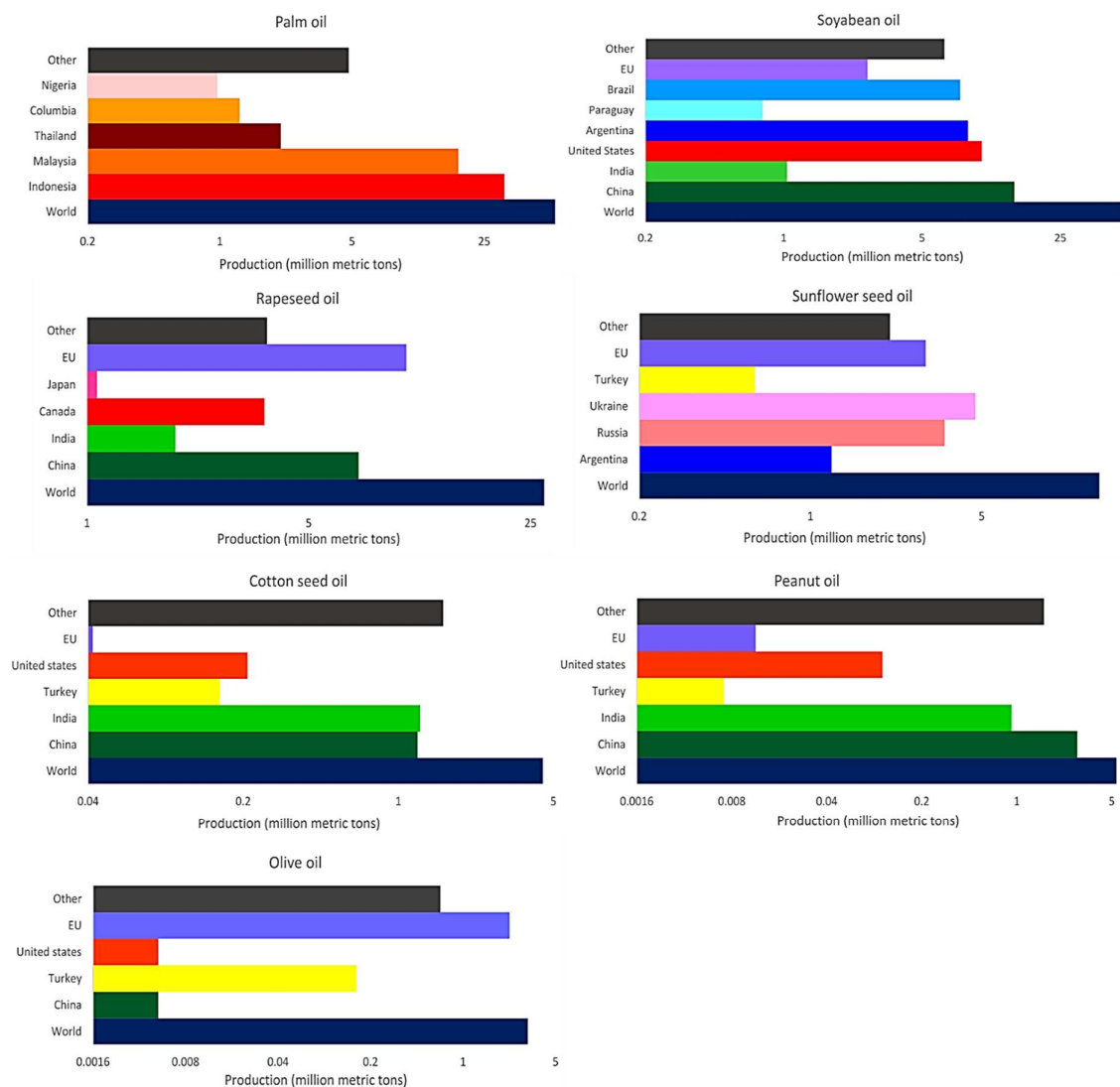


FIGURE 2-3: ANNUAL PRODUCTION OF VEGETABLE OILS IN DIFFERENT COUNTRIES IN THE YEAR 2015/2016<sup>45,46,50</sup>

### 2.1.3. Climate

#### *Effects of temperature and water*

To understand precisely the connection between the composition of oils and their origin, a study of the function of days after flowering and temperature on the fatty acid composition of sunflower oil was undertaken by Robertson et. al.<sup>51</sup> The physiological maturity, which is the time at which the yield and oil content of the seed is maximum<sup>52</sup>, was reached in this case at about 35 Days after Flowering (DAF). This has been depicted in Figure 2-4 along with the change in fatty acid compositions over time.

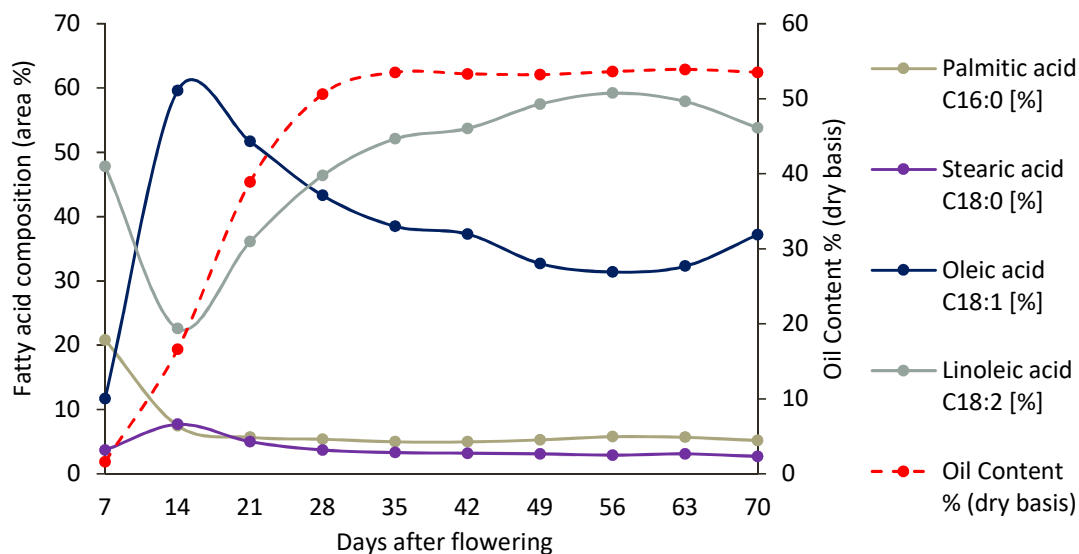


FIGURE 2-4: EFFECT OF MATURITY (DAYS AFTER FLOWERING) OF SEED ON FATTY ACID DISTRIBUTION IN THE SUNFLOWER OIL SEED – DATA COLLECTED FROM AND REPLOTED FROM ROBERTSON ET. AL. <sup>51</sup>‡

On the effects of surrounding temperature, it was noted in literature<sup>51</sup> that a decrease in every K amounted to a decrease of 0.87% oleic acid content. On the other hand, linoleic acid content increased with every K by 0.32%.<sup>51</sup> Proper tests to statistically prove the accuracy of these results were not done but a trend that oleic acid content decreased wherein linoleic acid increased with a decrease in temperature was duly noted. While every oil has a different dependency and other deciding factors, in the case of sunflower seeds, the compositions of oleic and linoleic acid depend largely on environmental temperature. Previous investigations have clearly indicated that the linoleic acid content decreased with the increase of temperature during the maturation of seeds.<sup>53–55</sup> Sunflowers from cooler regions like South Carolina, Alabama and central Georgia in the United states have higher linoleic acid content than those in warmer states like Texas and Louisiana.<sup>53,55</sup> Hence it could be deduced that the lower the surrounding temperature, the more the unsaturation in the oil. This is influenced by the concomitant increase of oxygen with colder air, wherein the former is the key reagent for the desaturation of saturated stearic to oleic to linoleic acid.<sup>51,56</sup> There are two enzymes, namely  $\Delta$ -9 desaturase and  $\Delta$ -12 desaturase which cause desaturation. The former causes the formation of oleic from stearic acid while the latter linoleic from oleic acid.<sup>57</sup> The  $\Delta$ -12 desaturase activity starts getting impaired with increasing temperature especially above 20°C

‡Own representations based on literature<sup>53,51</sup>



reaching almost zero at 35°C.<sup>58</sup> This also acts as an important factor to the formation of either high oleic or the standard version of high linoleic sunflower oil. Hence, both temperature and oxygen play an inter-related effect on the composition of sunflower oils as well. Water also has an effect on the composition of sunflower oils. According to Baldini et. al.<sup>57</sup>, water stress increases the amount of oleic acid in the oil as it reduces the duration of enzyme activity by accelerating seed growth and lipid accumulation. Both kinds of sunflower oil have been included in this work for investigations with respect to metastable ranges of melt crystallization and therein the nucleation kinetics.

## 2.2. Application

### 2.2.1. Edible oil

The global consumption of the main vegetable oils for the last year has been depicted in Figure 2-5. Palm oil is the highest with 62.53 million tons per year followed by soya and rapeseed or canola oil. Sunflower oil amounts to a total production of around 14 million tons per year.<sup>45,46</sup>

#### ***Palm oil***

A major 70 percent of palm oil is used in the food industry including cooking oil, margarine and salads leaving only around 24% which is used in the manufacturing of cosmetics, soaps and candles as per data from 2010. A mere 5% is put into the generation of energy as fuel for heating, electricity, etc.<sup>45,46</sup> The two main reasons behind palm oil's success as a food oil is that it is cheap and readily available. This is due to the fact that palm oil has the highest yield per hectare of harvest compared to other oil crops.<sup>59,60</sup>

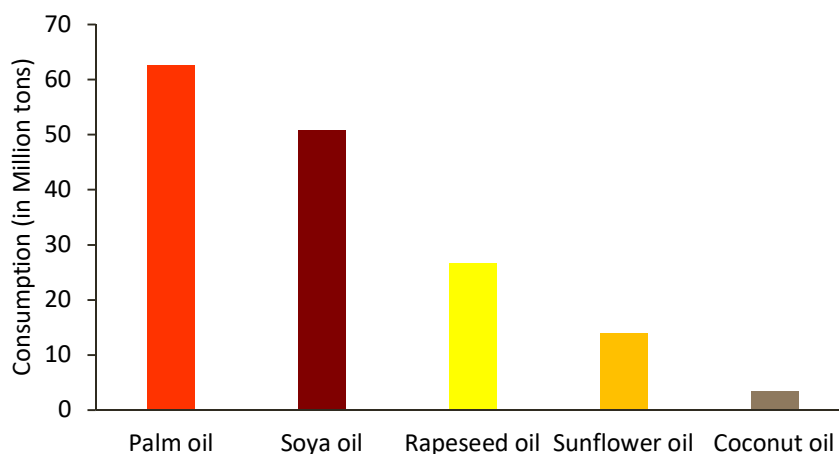


FIGURE 2-5: GLOBAL CONSUMPTION OF VEGETABLE OILS IN THE YEAR 2015/2016<sup>45,46</sup>

Palm oil yield is around 3.3 tons per hectare crops in comparison to 0.7 tons per hectare of sunflower, coconut or rapeseed oil.<sup>60</sup> Palm oil being semi solid at room temperature owing to a 50% content of saturated fat acts as an excellent spray fat for confectioneries.<sup>59</sup> Combining the advantages of the saturated content in palm oil being more resistant to oxidation and that palm oil has excellent non sticky and antifoaming properties, the latter proves to be suitable for cooking. In spite of these advantages, the high amount of longer saturated fatty acids does

have a negative effect on health, especially leading to cardiovascular diseases.<sup>57,59,61</sup> Another advantage of palm oil is that the crop or the palm tree in itself is fully usable. Other parts are applied as palm kernel oil, trunks as furniture, construction materials and in paper, bio-methane and bio-hydrogen (palm oil mill effluent) production etc.<sup>59</sup>

Taking Germany as an example, 41% of palm oil yield is applied in the biodiesel industry whereas 34% in the food industry.<sup>60</sup> Around 17% of palm oil yield is used for pharmaceutical and cosmetic industries and the rest as animal fodder.<sup>60</sup>

### ***Sunflower oil***

The composition of fatty acid in the sunflower oil produced is largely a function of the climate and location rather than the type of seed sown. This has been discussed in detail in the previous section. Of course, there is a possibility of genetic manipulation of the seed which would not only change the fatty acid composition but also have a significant effect on the seed oil content.<sup>62</sup> It has also been seen that while on one hand the palmitic acid content in the sunflower oil remains more or less constant, on the other the total of stearic, oleic and linoleic remains constant as well.<sup>62</sup> This is in accordance to the theories and literature mentioned above wherein stearic converts to oleic and then oleic to linoleic in favorable conditions. According to literature, the temperature after flowering till ripening is the limiting factor deciding the composition of sunflower oils.

### ***High linoleic sunflower oil***

It is common knowledge that unsaturated fatty acids are healthier and reduces the risks of cardiovascular diseases than saturated ones.<sup>57,61</sup> Hence, traditionally high linoleic acid oils such as sunflower, safflower and rapeseed/canola are commonly used in cooking. Linoleic acid is one of the common  $\omega$ -6 fatty acid and is also one of two essential fatty acids. The health benefits of  $\omega$ -3,  $\omega$ -6 and  $\omega$ -9 fatty acids are being studied extensively. However, high linoleic sunflower oil is known to be the lesser healthy of all the sunflower oils. This gives rise to the demand in the production of high oleic sunflower oil.<sup>63</sup> There is also a mid-oleic sunflower oil with around 65% oleic acid and approximately 25% PUFAs.<sup>63</sup>

### ***High oleic sunflower oil***

A diet rich in monounsaturated fatty acids helps to control the harmful low density lipoproteins or cholesterol.<sup>57,64</sup> In addition to these, studies have concluded that an increase in the quantity of oleic acid in cell tissues increases their survival chances when subjected to high oxygen stress (95%) in comparison to linoleic and arachidonic acid.<sup>57,65</sup> This could be due to the fact that oleic acid possess antioxidant properties<sup>66</sup> and hence higher quantities of oleic acid in the cell could improve cellular protection during high oxygen stress situations.<sup>57</sup> These including many other positive health effects of the high monounsaturated fatty acid mixtures have led to an extensive study on the production of high oleic sunflower oil. As mentioned before, monounsaturated fatty acids having only one double bond also exhibit better thermal stability and oxidation resistance when compared to PUFAs, thereby making them more suitable for cooking purposes.<sup>37,38,63</sup>

### ***Rapeseed or Canola oil***

Rapeseed or Canola oil is of the similar composition as of the high oleic sunflower oil. Due to the presence of a high amount of oleic acid it also serves as a great cooking oil which on one hand is healthy while on the other exhibit higher thermal stability compared to poly-unsaturated oils. Hence, as common knowledge, this oil is often used for frying food.

### ***Olive oil***

Olive oil which boasts of at least 65% monounsaturated fatty acid content is primarily produced in the EU and other Mediterranean countries like Turkey, Morocco, Syria, Tunisia, etc.<sup>67</sup> The consumption of this oil proportionally is also high in the EU followed by USA and Turkey.<sup>68–70</sup> Taking Germany as an example, olive oil yields the maximum revenue ranging around 108 million Euros in the year 2013/2014, followed by sunflower at approximately 69 million and rapeseed oil at 61 million Euros.<sup>71</sup>

### ***Coconut oil***

Among other oils, coconut oil is widely used in confectionaries and also in medical and infant food formulations. Coconut oil is a major source for medium chain fatty acids (C-6 – C-12).<sup>72,73</sup> Investigations on Japanese quails suggested these acids have been proven to be less atherogenic when compared to longer saturated acids like palmitic acid.<sup>73,74</sup> Due to the

presence of large amounts of saturated fat, it remains solid at temperatures above 25°C. This helps in its application as a confectionary fat such as in chocolates and cookies to prevent them from melting easily.<sup>73</sup>

### 2.2.2. Biodiesel

The obvious advantages of vegetable oils as biodiesel resources are that they are cheap, readily available and renewable. Other factors enhancing their use include that they are naturally liquid and have a relatively higher heat content (80% of diesel fuel).<sup>41,75</sup> Vegetable oils are not directly used as an automotive fuel but a transesterification process is performed mainly to reduce the viscosity of these oils.<sup>41</sup> Vegetable oils could be classified into three main parts: edible, non-edible and recycled.<sup>76</sup> Among these and animal fats, edible plant oil is the main feedstock for the production of biodiesel. According to literature edible vegetable oil accounts for more than 95% of biodiesel production.<sup>76</sup>

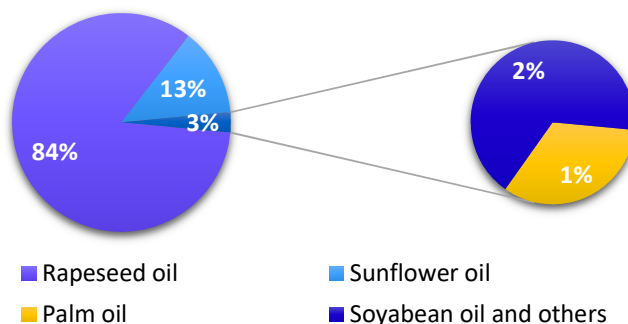


FIGURE 2-6: EDIBLE VEGETABLE OILS AS BIODIESEL FEEDSTOCK<sup>76</sup>

Figure 2-6 illustrates the various vegetable oils that are presently used as biodiesel feedstock, wherein it can be noted that rapeseed and sunflower oil account for the most part.<sup>76</sup> This in turn could be seen as a cause for the rising demand of the production of rapeseed and sunflower oil among others. In spite of these advantages, there are major problems associated with their applicability as a diesel fuel. As previously mentioned, unsaturated fatty acids are very susceptible to polymerization through oxidation leading to the formation of gum.<sup>41</sup> Apart from this, the ‘food vs. fuel’ crisis debate is unavoidable whenever we deal with edible resources. Hence one needs to focus more into the non-edible oils. Some of the non-edible vegetable oil resources for biodiesel are jatropha seed/kernel, karanja seed/kernel,

rubber seed and jojoba seed.<sup>76</sup> Further research of these oils is required for a definite understanding of their potential. An investigation was performed as a part of this dissertation to reduce the saturated concentration of linseed oil based PUFA to less than 3% so as to enable it to remain completely liquid even at temperatures as low as -2°C.<sup>77</sup> This will be further discussed later in Section 5.1.

### 2.2.3. Biopolymers

The ratio of production of biodegradable to non-biodegradable polymers is readily decreasing over the years.<sup>78</sup> The capacity for last year that is 2016, has been suggested to be almost 1.3 million tons of non-biodegradable whereas the biodegradable polymer amounts to a little over 0.75 million tons (Figure 2-7).<sup>78,79</sup>

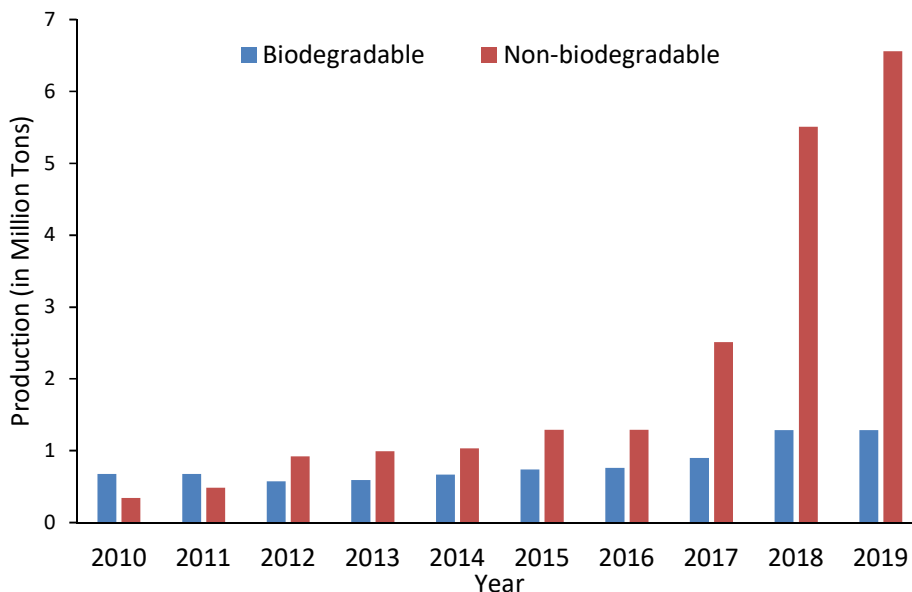


FIGURE 2-7: PRODUCTION OF BIODEGRADABLE AND NON-BIODEGRADABLE POLYMERS OVER THE YEARS<sup>79</sup>

The term, 'Bioplastics' represents both bio-based and biodegradable polymers. The former saves fossil fuels whereas the latter benefits the environments by converting themselves into natural substances.<sup>80</sup> Biodegradable need not be bio-based or vice versa. An interesting way to interpret the concept is by classification of the products or applications as enlisted in Table 2-3.<sup>80</sup> Bio-based plastics such as bio-polyethylene (PE) is being manufactured by Braskem, Brazil for large scale applications (200,000 tons per annum). According to information by the European bioplastics organization located in Berlin, Germany, bio-polypropylene and bio-polyvinylchloride are next in line.<sup>80</sup> Another commonly used partial bio-polyester is in the

‘Plant bottle’ by The Coca Cola company.<sup>80</sup> Research on fatty acids and derivatives and other bio-based monomers are being aggressively pursued in an attempt to produce long life, bio-based and biodegradable polymers.<sup>80</sup>

	Bio - based <sup>80</sup>	Fossil based <sup>80</sup>
Biodegradable	Bioplastics e.g. <ul style="list-style-type: none"> <li>• Polylactic acid</li> <li>• Polyhydroxyalkanoate</li> <li>• Modified starch</li> </ul>	Bioplastics, e.g. <ul style="list-style-type: none"> <li>• Polybutyrate</li> <li>• Polycaprolactone</li> </ul>
Non-biodegradable	Bioplastics e.g. bio-based <ul style="list-style-type: none"> <li>• Polyethylene</li> <li>• Polyvinylchloride</li> <li>• Polyamides</li> <li>• Polyesters</li> <li>• Polyurethanes</li> </ul>	Plastics e.g. <ul style="list-style-type: none"> <li>• Polyethylene</li> <li>• Polypropylene</li> <li>• Polyethylene terephthalate (PET)</li> </ul>

TABLE 2-3: CLASSIFICATION OF BIO-BASED AND FOSSIL BASED PLASTICS<sup>80</sup>

The European standard EN 13432:2000, a directive for bioplastics for packaging states among others, that 90% of the material needs to be decomposed biologically within 6 months of disposal and that 90% of the compound needs to pass through a 2 X 2 mm mesh within 12 weeks of disposal. EN 14995:2006 encompasses the bioplastics which are used for purposes other than packaging, broadening the leeway.<sup>80</sup> Coming to the definition or rather measure of partial bioplastics, the EU standard CEN/TS 16137 and US standard ASTM 6866 are used to determine the bio-based carbon content.<sup>80</sup>

Linseed oil is the most popular of the epoxidized vegetable oils which can be applied as plasticizers or additives in the polymer industry.<sup>8</sup> These can be further converted into thermosetting resins, diverse materials due to the long alkyl chains of the linoleic acid triglycerides.<sup>8,9</sup> The success of linseed oil as a raw material for epoxy resins also owes to the triple unsaturations present in each of the linolenic acid chain, which constitute about 50 – 60% of the oil.<sup>4</sup> Investigations on epoxy systems based on crosslinking vegetable oil based resins and amine based hardeners are on the rise.<sup>8</sup> This in turn has increased the demand for separating the linolenic acid or rather the unsaturated content of linseed oil from its saturated content. Linseed oil and its derivatives as explained before have a much higher tendency to get polymerized forming a 3D cross-linked solid phase or in other words dry even under atmospheric oxygen in comparison to less unsaturated oils like of sunflower, soya or relatively

saturated oils like of palm.<sup>81,82</sup> These highly poly-unsaturated oils such are hence called drying oils and find application as binders in adhesives, paints, varnishes and other coatings.<sup>82</sup>

Average double bonds per triacylglyceride	Rapeseed oil	Olive oil	Soya oil	Linseed oil	Cottonseed oil
	3.9	2.8	4.5	6.6	3.9

**TABLE 2-4: NUMBER OF DOUBLE BONDS PER TRIACYLGLYCERIDE IN VARIOUS VEGETABLE OILS<sup>81</sup>**

Hydro-peroxidation of a methylene group between two double bonds in a PUFA chain occurs through a reduction of hydrogen atom. Recombination of radicals, cross-linking and eventual thermal decomposition converts them into alkoxy groups such as ethers.<sup>83-85</sup> Naturally, hydro-peroxidation is possible also on oleic and linoleic chains, the mechanisms have been detailed by E.N. Frankel in previous literature.<sup>86</sup> Other means of polymerizing these highly unsaturated oils via oxidation have been discussed by Malléjol et. al.<sup>82</sup> The number of double bonds per triacylglyceride molecule in an oil have been enlisted in the following Table 2-4.



### 3. Melt crystallization of fatty acids

Crystallization process can be broadly defined as a process where a solute is transferred from a fluid to solid phase.<sup>87</sup> The thermodynamic driving force for crystallization is the free enthalpy  $G$  of the system. In case the mixture is disturbed from its equilibrium state due to supersaturation caused by for example - cooling, the system acquires a free enthalpy higher than the minimum enthalpy which it has during equilibrium state. Hence, the system tries to reduce  $G$  as long as there is a deviation from thermodynamic equilibrium by reducing the supersaturation through crystallization.

The kinetic driving force can also be described according to thermodynamics by the difference between the chemical potentials of the crystallizing component and the equilibrium state,  $\Delta\mu$  (Equation 3-1).<sup>16,17,87</sup>

$$\Delta\mu = k_B T \ln\left[\frac{f(p, T, c)}{f_e(p, T, c_e)}\right]$$

**EQUATION 3-1**

The thermodynamic driving force for crystallization,  $\Delta\mu_T$  can also be expressed as the product of entropy,  $\Delta S$  and the supercooling,  $(T_M^\circ - T)$  as in Equation 3-2.<sup>88</sup>

$$\Delta\mu_T = \Delta S(T_M^\circ - T)$$

**EQUATION 3-2**

In Equation 3-1,  $f$  denotes activity and  $p$ ,  $T$  and  $c$  represent pressure, temperature and concentration wherein the subscript  $e$  refers to equilibrium state. In the case of an ideal mixture, where the concentration difference from the equilibrium state is low, Equation 3-1 can be rewritten as

$$S = \Delta\mu/k_B T \cong \frac{c - c_e}{c_e}$$

**EQUATION 3-3**

In Equation 3-3,  $S$  is the relative supersaturation, which is equated to the first term of the expanded logarithmic part of a Taylor series.  $R$  is the universal gas constant. On differentiation as a function of supercooling  $\Delta T$  and application of the Van't Hoff equation,

supersaturation can be expressed as in Equation 3-4.<sup>16</sup>  $\Delta H_m$  denotes the melt enthalpy in Equation 3-4.<sup>17</sup>

$$S = (-\Delta H_m/k_B T^2)\Delta T$$

**EQUATION 3-4**

As already discussed in Chapter 1, the two underlying mechanisms of crystallization are nucleation and growth.<sup>23,89</sup> There are others effects such as breakage and agglomeration which are also associated to crystallization.<sup>87</sup> In an unseeded solution or melt, crystallization begins with a dominant nucleation process followed by crystal growth.<sup>87</sup> This is controlled especially in the case of melt crystallization by a temperature profile based on previous fundamental analyses. Parameters like induction time, nucleation rate, and crystal growth rate influence the efficiency of the separation of the desired product with respect to time, quality, and quantity.<sup>24</sup> Breakage and agglomeration of crystals occur thereafter depending on crystal or particle interactions within themselves and with the reactor, thereby affecting the size and structure of each crystal in the fraction.<sup>87</sup> As all these mechanisms proceed, supersaturation decreases thereby reducing the minimum critical size of a stable crystal nucleus. This leads to another mechanism called Ostwald's ripening, influencing the crystallization process wherein larger crystals are formed at the expense of smaller ones.<sup>90-93</sup> This can be directly attributed to the fact that smaller particles, in this case crystals have higher surface to volume ratio than larger ones, and hence higher solubility.<sup>93,94</sup> This is coined as the Gibbs Thomson effect which would lead to Ostwald's ripening. Theoretically, Ostwald's ripening should finally result in a large, single crystal formation but of course this is a slow process and realistically unachievable.<sup>93</sup> There are also other factors like agitation, attrition, reactor geometry, etc. which oppose the ripening of crystals.<sup>90,91,93</sup> There are comprehensive models describing nucleation, growth and Ostwald's ripening in literature.<sup>87</sup> The two established ones are the Population balance model – PBE<sup>87,95-97</sup> and the Kinetic rate equation – KRE.<sup>87,98</sup>

### 3.1. Nucleation kinetics and modeling

A nucleus is a crystalline aggregate of molecules of a certain critical size, which is stable at the prevalent conditions and capable of further growth leading to a decrease of its Gibbs free energy.<sup>99</sup> In other words, nucleation is the process of addition of monomers to form an aggregate such that its radius is limiting to a critical size.<sup>25</sup> The critical size is reached when further addition of monomers, that is, crystal growth leads to a decrease in its Gibbs free energy, thereby making the aggregate stable at those physical conditions.<sup>25,99</sup> Hence, nucleation is completely irreversible once it happens for those conditions as an amount of energy separates the product from the reactants. It is possible only once the mixture or solution is supersaturated which is achieved by either altering the temperature, eliminating the solvent by evaporation or sublimation, or by adding reactants.<sup>23</sup> Nucleation as a mechanism is the first order of liquid to solid phase transition and can be classified into *homogeneous* and *heterogeneous* nucleation, which depend on the availability of foreign or other existing particles.<sup>10,16,17,100</sup> Table 3-1 enlists the classification of nucleation along with causes. Homogeneous nucleation occurs in a mixture free of pre-existing crystals or other impurities whereas heterogeneous nucleation occurs in the presence of foreign particles or seeds.<sup>16,101</sup>

Nucleation	Primary	Homogenous Heterogeneous
	Secondary	Contact with foreign surface (stirrer, reactor, air, etc.) Seeding Shear force Breakage Attrition, etc.

TABLE 3-1: CLASSIFICATION OF NUCLEATION

Classical nucleation theory describes nucleation rates of systems involving both heterogeneous and homogenous nucleation mechanisms.<sup>87,98</sup> It is based on the difference between the driving force favoring stability of the melt or solution and energy paid into the formation of the interfacial surface between the crystal and liquid phase over nucleation.<sup>16,17,94,102</sup>

$$\Delta G = \Delta G_{interface/A} + \Delta G_{bulk/V}$$

EQUATION 3-5

$$\Delta G = \sigma 4\pi r^2 - \Delta G_v \frac{4}{3} \pi r^3$$

EQUATION 3-6

such that,

$$\Delta G_v = \Delta \mu v_s^{-1}$$

EQUATION 3-7

Equation 3-5 has been expanded in the Equation 3-6, such that  $\sigma$  is the interfacial tension,  $r$  is the radius of the nucleating phase.  $\Delta G_v$  has been defined in Equation 3-7 where  $v_s$  stands for the volume per molecule of crystal phase. Hence, while the first term in Equation 3-6 shows the interfacial energy, the second represents the free energy of the bulk per unit volume. This can be simplified as the following in Equation 3-8,

$$\Delta G = \sigma a n^{2/3} - n \Delta \mu$$

EQUATION 3-8

$a$  is a form factor to represent the shape of the crystal and  $n$  is the number of atoms/molecules in the nucleus.<sup>§,102-104</sup> According to theory, as the crystallization temperature  $T$  tends towards the equilibrium temperature,  $T_M^\circ$ ,  $\Delta G_v$  favoring crystallization tends to zero and the critical size of the nuclei tend to infinity making nucleation impossible. According to this theory at low driving force or supersaturation, nuclei have to be infinitely large to sustain and therefore, the waiting time also has to be infinitely long.

Figure 3-1 illustrates the same philosophy wherein free enthalpy is depicted as a function of the size of the nucleus. The critical size,  $r_c$ , is the radius at which the opposing interfacial energy term equals the bulk energy term. After this, the nucleus is stable as the driving force towards bulk stability or nucleation increases and dominates the process.<sup>94,102</sup>

---

<sup>§</sup> Possible values of  $a$  depending on crystal shape has been provided in the Appendix in Section 3.1.2

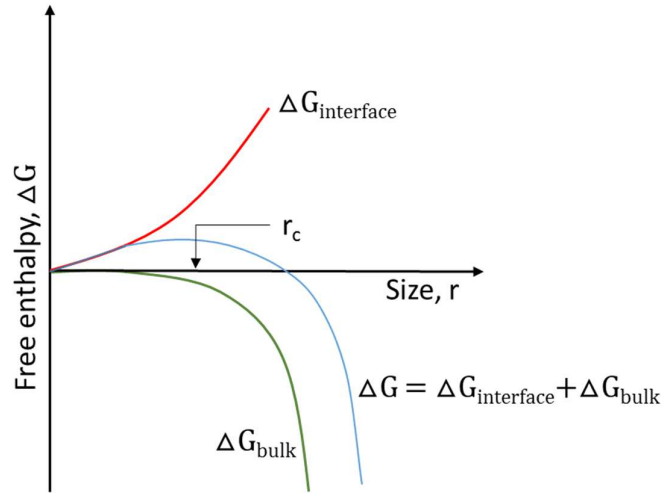


FIGURE 3-1: FREE ENTHALPY  $\Delta G$  AS A FUNCTION OF RADIUS OF THE NUCLEUS\*\*

On differentiating the Equation 3-6 with the size of the nucleus and equating  $\frac{d\Delta G}{dr}$  to zero at the critical nucleus size,  $r_c$ , one arrives at Equation 3-9,

$$r_c = \frac{2\sigma}{\Delta G_v}$$

EQUATION 3-9

On substitution of the value of  $r = r_c$ , Equation 3-10 gives,

$$\Delta G = 16 \frac{\pi\gamma^3}{3\Delta G_v^2}$$

EQUATION 3-10

Classical nucleation theory also assumes that the free energy,  $\Delta G$ , is directly related to the population distribution,  $\rho_e$ , of the nuclei of size  $N$  and size 1 (monomers) at equilibrium (Equation 3-11).<sup>102,105</sup>

$$\Delta G = -k_B T \ln \left[ \frac{\rho_e(N)}{\rho_e(1)} \right]$$

EQUATION 3-11

\*\* Sketch is own representation based on Crystallization technology handbook by Mersmann, A., published by Marcel Dekker, New York, 1995<sup>17</sup>

Hence as derived from Arrhenius equation, critical nuclei population,  $\rho_e(r)$  can be expressed in Equation 3-12 as

$$\rho_e(r) \propto e^{-\Delta G_c/k_B T}$$

**EQUATION 3-12**

and the rate of addition of monomers to critical nuclei, A, to make it grow spontaneously, as in Equation 3-13.<sup>106</sup> The activation energy required has been denoted as  $\Delta G_d$  as it is a diffusion controlled process.

$$A \propto e^{-\Delta G_d/k_B T}$$

**EQUATION 3-13**

Hence, the rate of nucleation, J can be formulated as the sum of these two effects as in Equation 3-14.<sup>106</sup>

$$J \propto e^{-(\Delta G_c + \Delta G_d)/k_B T}$$

**EQUATION 3-14**

The Fisher Turnbull equation (Equation 3-15) is a kinetic model that shows that the rate of formation of a nucleus, J, is related to the Gibbs free energy of formation,  $G_c$ , Gibbs free energy of molecular diffusion,  $G_d$ , and the crystallization temperature.<sup>10,25,107–109</sup>

$$J = \frac{N k_B T}{\hbar} e^{(-\Delta G_c/k_B T)} e^{(-\Delta G_d/k_B T)}$$

**EQUATION 3-15**

The rate of formation of a nucleus, J is assumed to be the inverse of the induction time of crystallization,  $\tau_i$  as in Equation 3-16.<sup>10,25,107–109</sup>

$$J \cong 1/\tau$$

**EQUATION 3-16**

In Equation 3-15, N is the number of crystallizing molecules per unit volume,  $k_B$  is the Boltzmann constant, T is absolute temperature, and  $\hbar$  is Planck's constant.<sup>25,109</sup> The time required for the first crystal nucleus to appear in the sample once the crystallization or the observed temperature is reached, is defined as the induction time.<sup>24</sup> Factors like the degree

of supercooling and the rate of cooling greatly influence the speed and behavior of the nucleation. In our work, the sample's induction time has been calculated as the difference between the time at which the probe reaches the crystallization temperature and when the first sign of the presence of nuclei is noted by the FBRM™ sensor.<sup>24,110,111</sup> Furthermore, the Gibbs free energy of crystallization can be correlated to the crystallization temperature  $T$ , with the Gibbs-Thompson equation (Equation 3-17).<sup>10,25,108,109,112</sup>

$$-\Delta G_c = \frac{16}{3} \frac{\pi \sigma^3 (T_M^\circ)^2}{(\Delta H)^2 (\Delta T)^2}$$

**EQUATION 3-17**

where (16/3) results from the spherical shape assumed to be that of the nucleus and  $\Delta H$  is the heat of fusion<sup>25,113</sup>. The supercooling factor in the denominator,  $\Delta T$ , effectively amounts to  $|T_M^\circ - T|$ , which is the difference between the equilibrium melting temperature,  $T_M^\circ$ , and the crystallization temperature,  $T$ .<sup>10,25,109</sup>

On substituting Equation 3-16 and Equation 3-17 in Equation 3-15<sup>114</sup>, one arrives at Equation 3-18

$$\tau^{-1} = J = \frac{Nk_B T}{\hbar} e^{(-\frac{16}{3} \frac{\pi \sigma^3 (T_{M0})^2}{(\Delta H)^2 k_B T (\Delta T)^2})} e^{(-\alpha \frac{\Delta S}{k_B})}$$

**EQUATION 3-18**

where  $\alpha$  is the fraction of molecules in the right conformation for incorporation into the aggregate to form a nucleus,  $\Delta S$  is the reduction of entropy on crystallization of 1 mole of fatty acid.<sup>10,99</sup>

$$\Delta S = \frac{\Delta H}{T}$$

**EQUATION 3-19**

On application of natural logarithm and the formula of a straight line with an intercept

$$y = sx + c$$

**EQUATION 3-20**

where  $s$  is the slope,  $\Delta y / \Delta x$ , and  $c$  is the intercept of the line on the  $y$  axis. It can be deduced from Equation 3-18 that,

$$\log \tau T \propto \frac{1}{T(\Delta T)^2}$$

EQUATION 3-21

such that the energy of formation (J), that is, in this case, nucleation can be determined<sup>10,109,114</sup>, as in Equation 3-22,

$$\Delta G_c = \frac{sk_B}{(\Delta T)^2}$$

EQUATION 3-22

To specify  $\Delta G_c$ (J) further, it is normalized with the Avogadro number,  $N_A$ .  $\Delta G'_c$  (Jmol<sup>-1</sup>) is the activation barrier of nucleation or formation as shown in Equation 3-23.

$$\Delta G'_c = \Delta G_c \cdot N_A$$

EQUATION 3-23

It can be concluded as per theory that as supercooling increases, nucleation also increases till the factor of diffusivity drops and nucleation stops. The Fisher Turnbull approach has been previously used in various studies for the analysis of nucleation data of fatty acid mixtures including by those of Ng et. al.<sup>115</sup> wherein the interactions of tripalmitin and triolein mixtures were investigated. Chalepa<sup>114</sup> has investigated the nucleation kinetics upon application of additives to coconut oil using the Fisher Turnbull equation in a similar manner as in this work.

### **Validation of theory**

To validate the arrived conclusion at Equation 3-6 when temperature,  $T$  approaches  $T_M^\circ$ , that is the desired crystallization temperature closes on the SLE temperature, supercooling is infinitely small then chemical potential also limits to zero, then  $\Delta G_v$  tends to 0. Therefore, according to the definition of  $r_c$  as in Equation 3-9,  $r_c \rightarrow \infty$  and  $\Delta G$  at  $r_c \rightarrow \infty$ .

In the case of Equation 3-11, if there is only one molecule  $n = 1$ , then  $\ln 1 = 0$ , thereby making  $\Delta G = 0$



### 3.2. Crystal growth kinetics

There are comprehensive models describing nucleation, growth and Ostwald's ripening in literature.<sup>87</sup> The term relating to spontaneous growth of nucleus by addition of monomers to the post critical size nuclei is again as in Equation 3-24 proportional to the exponent of  $\Delta G_d$ .

The rate of growth,  $\frac{dr}{dt}$ , can be then expressed in terms of the Gibb's energy of unfavorable positioning in the lattice ( $\Delta G_d$ ) and moving over to a more stable or favorable position in the crystal lattice unit ( $v\Delta G_v$ ). B is the constant of growth to equate the proportionality to the attachment and detachment terms of molecules to the lattice.<sup>87</sup>

$$\frac{dr}{dt} = B e^{-\Delta G_d/k_B T} (1 - e^{-v\Delta G_v/k_B T})$$

**EQUATION 3-24**

It can be concluded from this equation that at temperatures tending towards  $T_M^\circ$ , growth is slow. Likewise, at very high supercooling, growth is also slow as diffusion is inhibited and the maxima of the rate of growth, similar to nucleation, is at an intermediate temperature gradient. This can be easily predicted from Equation 3-2 and Equation 3-24 wherein

$\Delta G_v \xrightarrow{\text{Equilibrium}} 0$ , thereby no driving potential, and hence the second term tends to zero as exponent of 0 is 1 such that rate of growth is zero.

### 3.3. Metastable zone width determination for SLE phase diagrams

To generate a controlled and desired quantity and quality of crystal fraction, it is very important to know which of the two mechanisms is the limiting one at which temperature and cooling rate. The most effective way of understanding the system kinetics, is to construct the metastable ranges of SLE phase diagrams.<sup>89,116–120</sup> One main objective of this dissertation is to determine the range of supercooling under which a desired nucleation rate can be realized.

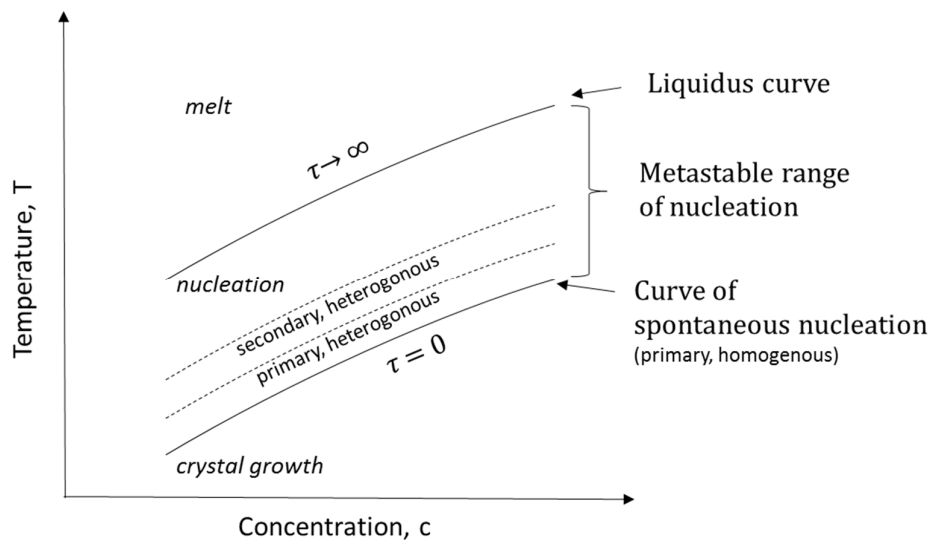


FIGURE 3-2: TYPES OF NUCLEATION IN THE METASTABLE RANGE OF AN SLE PHASE DIAGRAM<sup>††</sup>

Figure 3-2 shows that as the melt of the sample is cooled, the sample starts becoming supersaturated at the liquidus point although the induction time of nucleation still limits to  $\infty$ . Upon further cooling, the sample reaches the point of spontaneous nucleation which is a bulk phenomenon and hence homogenous. At this point, induction time is zero. Primary heterogenous and homogenous nucleation is possible in between these two temperatures. These two temperatures also form the boundary of the metastable range of nucleation.<sup>17</sup>

A basic explanation of methods used is necessary before the clarification of determination of metastable ranges. The interpretation and determination of SLE metastable ranges for the

<sup>††</sup> Sketch is own representation based on *Crystallization technology handbook* by Mersmann, A., published by Marcel Dekker, New York, 1995<sup>17</sup>

systems from the analytical methods chosen post crystallization has been detailed upon in Section 5.2.1 – Section 5.2.6.

## 4. Material, method and experimental setup

### 4.1. Chemical, equipment and software list

A list of the chemicals, equipment and the various software used for modeling and data analyses have been enlisted in Table 4-1, Table 4-2 and Table 4-3.

Chemicals	Supplier
≥98% Palmitic acid	Sigma–Aldrich Inc.
≥98.5% Stearic acid	Sigma–Aldrich Inc.
≥99% Oleic acid	Sigma–Aldrich Inc.
≥97% Linoleic acid	Sigma–Aldrich Inc.
≥96% Linolenic acid	Sigma–Aldrich Inc.
High linoleic sunflower oil PUFA	IOI Oleo GmbH, Wittenberge, Germany
High oleic sunflower oil PUFA	IOI Oleo GmbH, Wittenberge, Germany
Linseed oil PUFA	IOI Oleo GmbH, Wittenberge, Germany
Soya oil PUFA	IOI Oleo GmbH, Wittenberge, Germany
Nitrogen (DSC dry atmosphere: Purity 5.0)	Linde AG, Munich, Germany
Helium (GC)	Linde AG, Munich, Germany
>99.5% Diethyl ether Rotipuran®	Carl Roth GmbH + Co. KG
96% Sulphuric acid Rotipuran®	Carl Roth GmbH + Co. KG
≥99,98 %, Methanol (GC grade)	Carl Roth GmbH + Co. KG
≥99,9 %, Sodium chloride (NaCl) Cellpure®	Carl Roth GmbH + Co. KG

TABLE 4-1: LIST OF CHEMICALS USED

Instrument	Supplier
Differential Scanning Calorimeter – DSC	Mettler Toledo GmbH
Weighing machine - XS105 Dual Range	Mettler Toledo GmbH
Soxtherm extraction apparatus, S306 AK/ S 306A	Gerhardt Analytical Systems, Fabrik und Lager chemischer Apparate GmbH & Co. KG, Königswinter, Germany
Gas chromatograph - Flame Ionization detector setup, Chrompack CP 9001	Chrompack, Middelburg, The Netherlands
FFAP column	INNOPEG
Tempered laboratory centrifuge	Multifuge 3S-R, Heraeus Centrifuges, DJB Labcare Ltd, Buckinghamshire, England
Polarized Light Leica DM-RME Microscope	Leica Microsystems, Wetzlar, Germany
Leica Camera DPC 320 and DFC 500	Leica Microsystems, Wetzlar, Germany
Gradient chamber LTS 120	Resultec Analytic Equipment, Illerkirchberg, Germany (German distributor for Linkam Scientific Instruments Limited)
Standard borosilicate frames	-
Peltier elements with electronic controls PE 94	-
EasyMax™	Mettler Toledo GmbH
FBRM™	Mettler Toledo GmbH
Almemo Data logger 2890-9 with LCD graphic display	Ahlborn Mess- und Regelungstechnik GmbH
Thermal sensor Pt 100/Pt 1000	Ahlborn Mess- und Regelungstechnik GmbH
Thermal foil sensor Pt100 4-wire (ZA 9030 FS1)	Ahlborn Mess- und Regelungstechnik GmbH
ALMEMO USB Data cable and converter	Ahlborn Mess- und Regelungstechnik GmbH
Thermostat Model No.: CC 515	Peter Huber Kältemaschinenbau GmbH

TABLE 4-2: LIST OF INSTRUMENTS USED

Software	Supplier
Temperature control Software WinControl V6 Light for 20 measurement cells (COM- oder TCP/IP- connection)	Ahlborn Mess- und Regelungstechnik GmbH
Software - Linksys 32 Version 1.6.0	Resultec Analytic Equipment Illerkirchberg, Germany (German distributor for Linkam Scientific Instruments Limited)
Sigma Plot (Curve Fitting) 11.0	Systat Software Inc.
MATLAB R2016b (Curve Fitting)	MathWorks, Natick, MA, United states of America
Python 2 (curve fitting and surface fitting equations)	Open source zunzun/pyeq2, Github
Gnuplot version 5.0 (January 2015)	Open source, Copyright 1986 - 1993, 1998, 2004 Thomas Williams, Colin Kelley
Microsoft office tools 2016	Microsoft Corporation

**TABLE 4-3: LIST OF SOFTWARE USED**

## 4.2. Sample characterization

Samples collected at every stage during the investigations were analyzed thermally in the Differential Scanning Calorimeter (DSC) and chemically in the Gas Chromatograph (GC). The GC was coupled with a Flame Ionization Detector (FID), which determined the composition of the sample. Every sample was weighed in a precision scale (XS105 Dual Range, Mettler Toledo Ltd.) with a tolerance of  $\pm 0.1$  mg.

### 4.2.1. Differential Scanning Calorimeter - Thermal analysis

The DSC is a thermal analysis instrument used to detect or measure phase transitions occurring in a sample when subjected to a pre-determined temperature profile. Thermal effects are determined here by subjecting two probes, the sample and a reference, namely water or air (as in this case) to the same temperature profile. The differences in the enthalpy supplied or received between the two in order to maintain the same temperature profile is plotted as a function of temperature and time. The sudden changes in the differences in enthalpy, resulting in peaks either endothermic or exothermic point towards phase transition effects. An example thermal process which represent an exothermic peak is crystallization whereas an endothermic reaction could be the opposite thermal effect of melting. The effects as mentioned in the examples, particularly, have been exploited to investigate the SLE metastable ranges.

#### **Method**

The PUFA mixtures and the respective fractions obtained upon crystallization were subjected to a specific temperature regime depending on the composition in the DSC. The enthalpy behaviors of the samples determined from the thermograms obtained were then analyzed as a function of time and temperature.<sup>121-123</sup> The DSC employed was fitted with an auto sampler to enable a more efficient use of time. The auto sampler used allows 34 samples to be placed at a time.

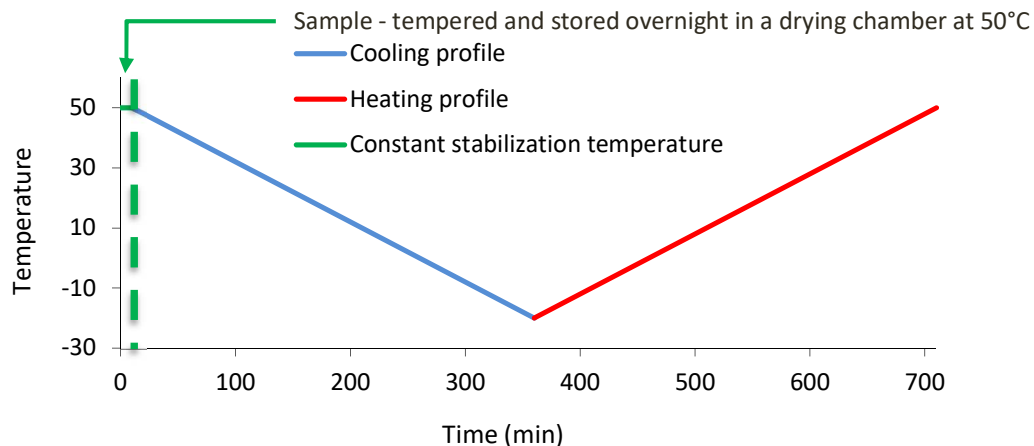


FIGURE 4-1: EXAMPLE STANDARD DSC TEMPERATURE PROFILE (50 °C ► -20 °C ► 50 °C AT 0.2 K/MIN)

Figure 4-1 illustrates an example of a commonly used temperature profile to analyze the sample over a large temperature range. First, the PUFA mixtures were pre-tempered in a heated chamber at 50°C overnight. The sample was heated and held at 50°C for about 10 minutes in the DSC. This was done to ensure a homogenous mixture void of any crystallization history as well as to stabilize the system at 50°C. Then the sample was cooled to a low temperature in the range of -20°C to -40°C depending on the samples at a slow cooling rate of 0.2 Kmin<sup>-1</sup> so as to ensure every phase transition is realized and discrete in the thermogram. The negative effects of faster cooling rates have been shown in Section 5.2.4.

#### 4.2.2. Differential Scanning Calorimeter – Visual analysis (Microscopy)

At the ‘Materials Characterization Market Support Lab’ of METTLER TOLEDO Analytical in Schwerzenbach, Switzerland, a microscope was fitted into the DSC in order to be able to simultaneously visualize and thermally characterize a specific enriched crystal fraction of a high oleic sunflower oil PUFA mixture (Figure 4-2). These experiments were conducted to ensure that the DSC detected phase transformation effects thermally before any visual effects were seen through the microscope.

##### **Method**

The standard oven cover is replaced by quartz windows to enable optical access for the microscope. Similar to the standard DSC method, the sample and reference probe were subjected to the same temperature profile. An external light source through a glass fiber bundle is used to light up the sample.<sup>124</sup>



In addition, as previously mentioned, a microscope was fitted to note the phase transition changes over the temperature profile. Images of the sample are taken at pre-adjusted time intervals. At first, the usual aluminum crucibles were used for the experiments. However, crystals formed in the PUFA mixtures upon cooling are milky white in color, thereby hindering easy visualization against the silver background of the crucible. The silver background also tends to reflect the light from the fiber optics. Hence, copper crucibles were taken not only to increase the contrast but also to overcome the problems of reflection due to the light generated by the microscope. Thus, these copper crucibles were then oxidized in order to obtain a black surface color, thereby increasing the contrast between the sample and background and also reducing reflection. Illustrations demonstrating the differences in the thermograms and pictures of identical samples in both of the crucible types have been shown in Table 5-4 in the following chapter and in detail in Section 1.1 in the Appendix.

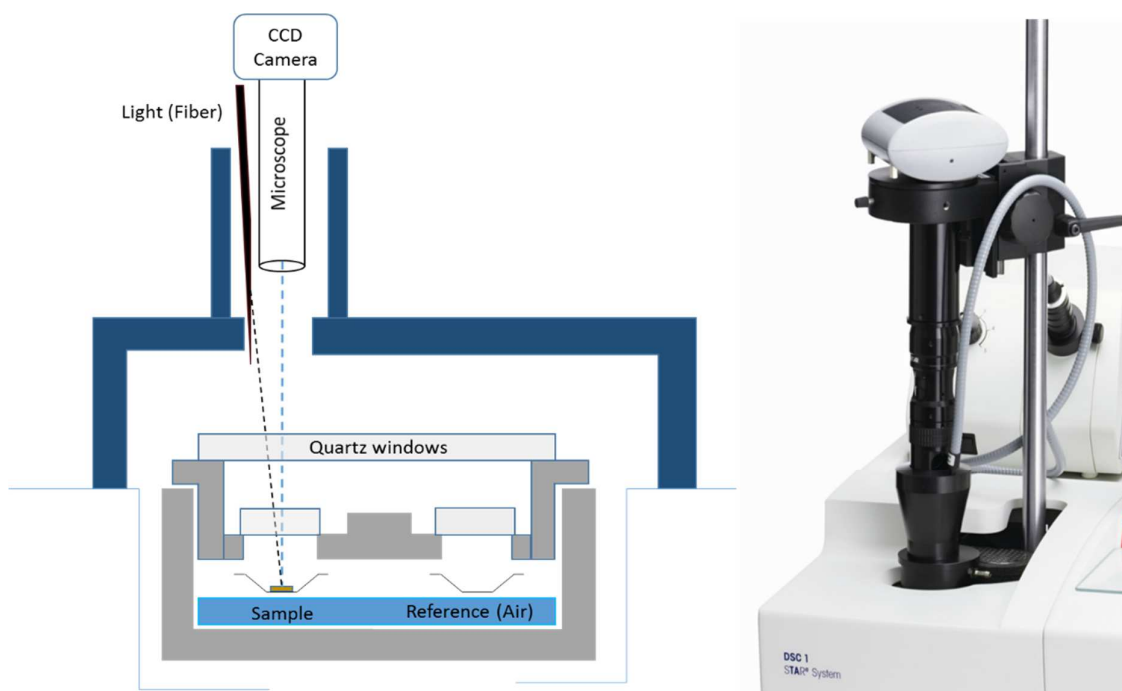


FIGURE 4-2: DSC - MICROSCOPY SYSTEM<sup>\*\*</sup>

The main reason behind choosing an enriched saturated crystal fraction for this investigation was to ensure that all of the solid liquid phenomena associated with the mixture were then shifted towards the higher scale of temperature. This is also because visualization through a

<sup>\*\*</sup> Sketch is own representation based on- and picture directly taken from a METTLER TOLEDO webinar named DSC Microscopy, Chemiluminescence and Photocalorimetry, June 2010 by Dr. M. Schubnell<sup>124</sup>

microscope gets difficult owing to the chance that condense water from the moisture in the oven may develop on the objective lens at cooler temperatures. In this manner, a further look into the behavior of the mixture at lower temperatures could also be realized. The mixture was cooled with  $10 \text{ Kmin}^{-1}$  from  $50^\circ\text{C}$  to  $-60^\circ\text{C}$ , with a hold temperature of 10 minutes at  $-60^\circ\text{C}$ . The DSC was run in nitrogen atmosphere so as to avoid any ice formation between the cryostat and the DSC. The sample was then reheated to  $50^\circ\text{C}$  with  $10 \text{ Kmin}^{-1}$ . A photo series to illustrate the progress along with the DSC thermogram has been given in Figure 5-7. A comparison of the sample run in an aluminum crucible and oxidized copper crucible was done to ensure that the results are not wrong and misinterpreted. An influence of the microscope light on the nucleation process was not investigated because the microscope was not used during the collection of data for the determination of the metastable ranges.

#### **4.2.3. Flash Differential Scanning Calorimeter – Thermal Analysis**

A similarly enriched saturated crystal fraction of the high oleic sunflower oil PUFA mixture was subjected to intense and rapid cooling in a Flash DSC to detect its effect on the solid liquid equilibrium point and the metastable zone of crystallization. These experiments were conducted at the Materials Characterization Market Support Lab of Mettler Toledo Analytical in Schwerzenbach, Switzerland as well.

A flash DSC has a MultiSTAR UFS™ 1 sensor containing 16 thermocouples, 8 on either probe, wherein the sample is directly placed. This Microelectromechanical systems (MEMS) enabled sensor on a ceramic plate generates a fast response to any changes in the sample. A detailed illustration of the DSC sensors is available in the Appendix as Figure 1-9. The impact of different cooling and heating rates on the samples was also investigated and compared. Investigations on sample sizes between 10 ng to 1  $\mu\text{g}$  is possible in this kind of DSC whereas operating temperature ranges between  $-95^\circ\text{C}$  to  $420^\circ\text{C}$  is applicable.<sup>125</sup> Owing to the small size of the sample, the entire sampling happens under a microscope.<sup>125</sup>

#### ***Method***

A flat thin film sample as well as a relatively larger sample were used to see the influence of the volume of sample during the cooling stage. Samples were subjected to cooling rates from  $-2$  to  $-500 \text{ Kmin}^{-1}$ . Experiments were repeated to validate the reproducibility of the procedure.

#### **4.2.4. Gas Chromatography - Flame Ionization Detector - Chemical analysis**

##### ***Method***

The gas chromatographic method coupled with a Flame Ionization Detector, FID (Chrompack CP 9001, Chrompack, Middelburg, The Netherlands with an INNOPEG-FFAP column) was chosen to determine compositions of samples and products. The German standard method of the analysis of fat, fat products, surfactants and related products (DGF) C-Fat C-VI 10a: Analysis of fatty acids and fatty acid composition by gas chromatography<sup>126</sup> was employed for the determination of the composition of the products. Prior to analysis by the GC method, each fatty acid mixture was esterified to its methyl ester form (FAME).<sup>126</sup> The recorded chromatograms were processed and analyzed with a Varian Maitre 2.5 software package.

##### ***Fatty acid to FAME***

The esterification process used was according to the German standard methods of the analysis of fat, fat products, surfactants and related products (DGF) C-Fat C-VI 11b: Fatty acid methyl ester and fatty acid propyl ester – Esterification or Transesterification.<sup>127</sup> Each sample, weighing 2g, was mixed with 30 mL methanol (Merck; standard purification grade used for liquid chromatography) and 1 mL of concentrated sulphuric acid (Merck; 95%-97% for analysis) and boiled for one hour under reflux. The esterification was carried out in a Soxtherm extraction apparatus, S306 AK/ S 306A supplied by Gerhardt Analytical Systems. The advantage of this apparatus is that there are 6 simultaneous extractors each amounting to a volume of maximum 150 ml. The mixture post esterification, was added to diethyl ether in a separating funnel. Distilled water is added to the Ether/FAME mixture such that the latter is neutralized. Once the organic layer phased out, the desired separation was achieved. The latter was then evaporated to obtain the fatty acid methyl ester. Sodium chloride was at times added to the water phase to enable easier phase separation.

##### ***Gas Chromatography***

Gas chromatography is applied to samples used to separate the components based on their adsorption properties in the gas phase. It is to be noted that the specific analytical method has been developed and employed in this work only in order to reaffirm their molecular identity and to obtain the relative proportions of the components present in the samples as

well as their subsequent crystal and mother liquor fractions.<sup>128</sup> Figure 4-3 illustrates the GC-FID setup used. The GC instrument is equipped with an FS INNOPEG-FFAP 50m column having an inner diameter of 0.25mm and film thickness of 0.25  $\mu\text{m}$ . Each experiment was conducted isothermally at 190°C and at a constant pressure of 150 KPa with an injection volume of 0.2  $\mu\text{L}$ .

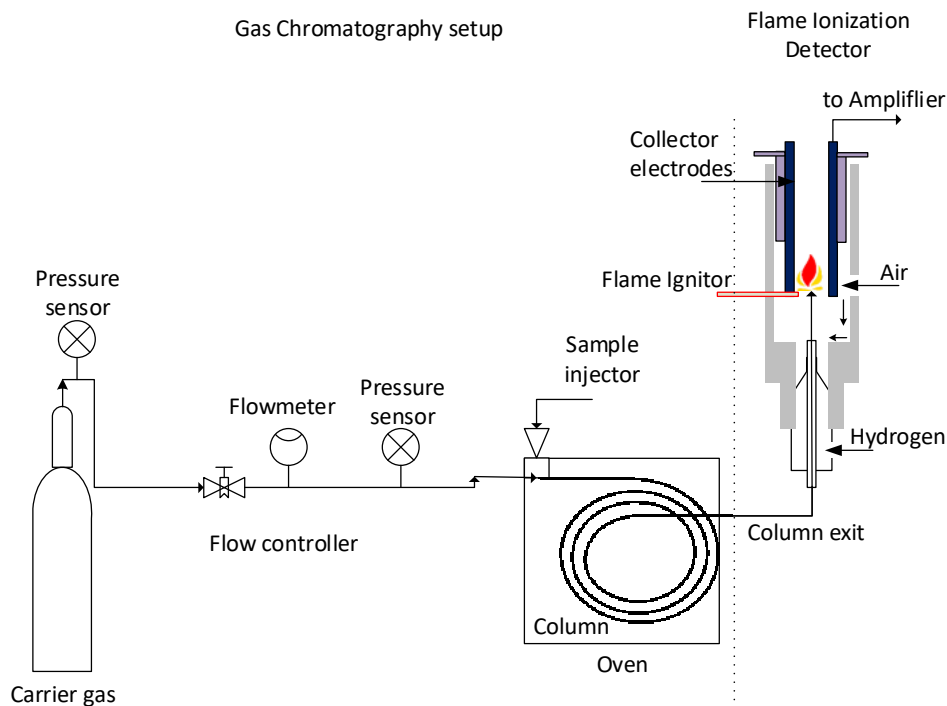


FIGURE 4-3: GAS CHROMATOGRAPHY FLAME IONIZATION DETECTOR - GCFID SETUP <sup>§5</sup>

### **Detector - FID**

The FID was chosen of all the other detectors because of its special properties like ‘*unit carbon response*’, fast feedback and broad operating range.<sup>130</sup> A schematic representation of the FID has been done as a part of Figure 4-3. The chromatography column exit enters the FID and passes through a hydrogen/air flame thereby ionizing the separated components. These positively charged ions (by removal of an electron) are then collected by negative collector electrodes, resulting in current flow. The signal, proportional to the ions generated is then amplified and electronically seen by means of an appropriate chromatogram software.<sup>130</sup> As a result of the detection procedure, the sample gets completely destroyed post analysis in

<sup>§5</sup>Own representation based on gas chromatography sketches found in <sup>128–130</sup> and laboratory setup at the Department of Mineral Processing, Brandenburg University of Technology, Cottbus-Senftenberg

the FID. The most important advantage of the FID is that the detector response is directly proportional to the mass of carbon per unit of time, that is, the mass of carbon irrespective of the compound passing through the detector flame is linearly related to the detector results.<sup>130</sup> Therefore, the mass of individual components in the sample passing through the detector can be directly correlated to their corresponding peak area in the chromatogram. The latter as a result, closely depicts the relative ratio of the components in a sample.<sup>130</sup> This property of the FID was especially useful as during the component analyses of the various vegetable oil PUFAs, it is important to check on one hand the relative or fractional ratio of one component to another and secondly the change in the amount of the same component in the sample over various crystallization processes. In most cases, the FID response can closely measure the composition of samples within 2% error of their actual concentrations, especially as in the case of this work which deals with the same functional group, methyl acetate of the individual components.<sup>130</sup> Moreover, the deviation from the unit carbon response reduces with increasing carbon atoms in the chain.

#### **4.2.5. Raman microscopic Analysis- Positional composition analysis**

The high linoleic sunflower oil PUFA mixture was also sent to Bruker Optik GmbH for a compositional analysis under the Raman microscope to check the compositional difference between the crystal fraction and melt fraction upon crystallization.<sup>\*\*\*</sup> The confocal Raman microscope, Senterra® comes with the technology of FlexFocus®. The included software SureCal® ensures a stable wavelength scale conversion of high throughput to confocal mode such that a further calibration is not required. The confocal mode also physically allows a deeper profiling of the sample. The maximum local resolution of this microscope is approximately about 5 µm. This is quite good, as the spectral range of the Infra-Red and Raman spectroscopy is between 1µm and 1 cm.<sup>†††</sup>

---

<sup>\*\*\*</sup> Acknowledgements to Mr. Eric Klein and Mr. Matthias Boese from Bruker Optik GmbH for the test measurements for the compositional analysis of high oleic PUFA. Acknowledgements also to the organization of Bruker Optik GmbH in Ettlingen, Germany to make the confocal Raman microscope available for measurements.

<sup>†††</sup> Data obtained from the report submitted by Mr. Eric Klein and Mr. Matthias Boese from Bruker Optik GmbH for the test measurements for the compositional analysis of high oleic PUFA. Acknowledgements also to the organization of Bruker Optik GmbH in Ettlingen, Germany to make the confocal Raman microscope available for measurements.

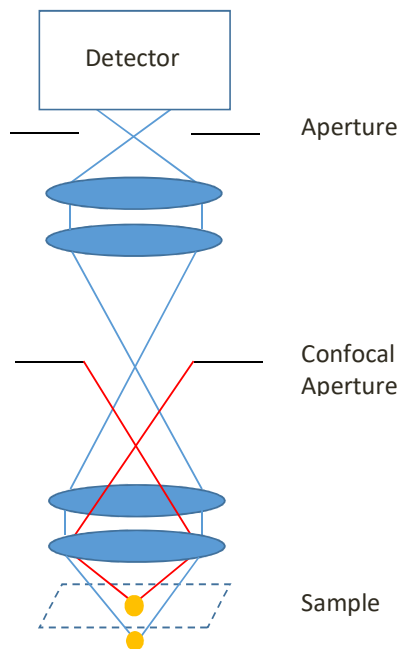


FIGURE 4-4: CONFOCAL RAMAN MICROSCOPY PRINCIPLE IN SENTERRA® \*\*\*

### **Method**

The high linoleic sunflower oil based PUFA mixture was heated to 30°C for some time so as to remove any crystallization history. A drop of the sample was placed on the glass slide with a pipette and covered with another. The sample was cooled to 17°C at around 0.5Kmin<sup>-1</sup>. Crystals both star and lancet shaped were formed. These crystals were then further analyzed under the confocal Raman microscope. The differences in the spectrums generated by the melt and crystal fraction were analyzed. The composition of the crystal was also checked.

---

\*\*\* Own representation of picture obtained from report submitted by Mr. Eric Klein and Mr. Matthias Boese from Bruker Optik GmbH for the test measurements for the compositional analysis of high oleic PUFA.

#### 4.2.6. Contact angle measurement

The contact angle between a sample and its reactor was also investigated to check whether the composition of the PUFA samples had an effect on the wettability of the glass surface used in this work. Three samples, one high oleic, linoleic and linolenic acid PUFA were chosen such that the effect of the degree of unsaturation could be tested here as well. A variety of surfaces were also chosen so as to compare the contact angle of the PUFAs with different surfaces. Figure 4-5 illustrates the setup used to measure the contact angle between a drop of the PUFA sample and the glass object slide. A Keyence VHX 2000D® microscope was used to view the drop on the cooling chamber at right angle such that a projection of the interface is shown as in the monitor of Figure 4-5. The interpretation of the picture has been further clarified in the next Figure 4-6.

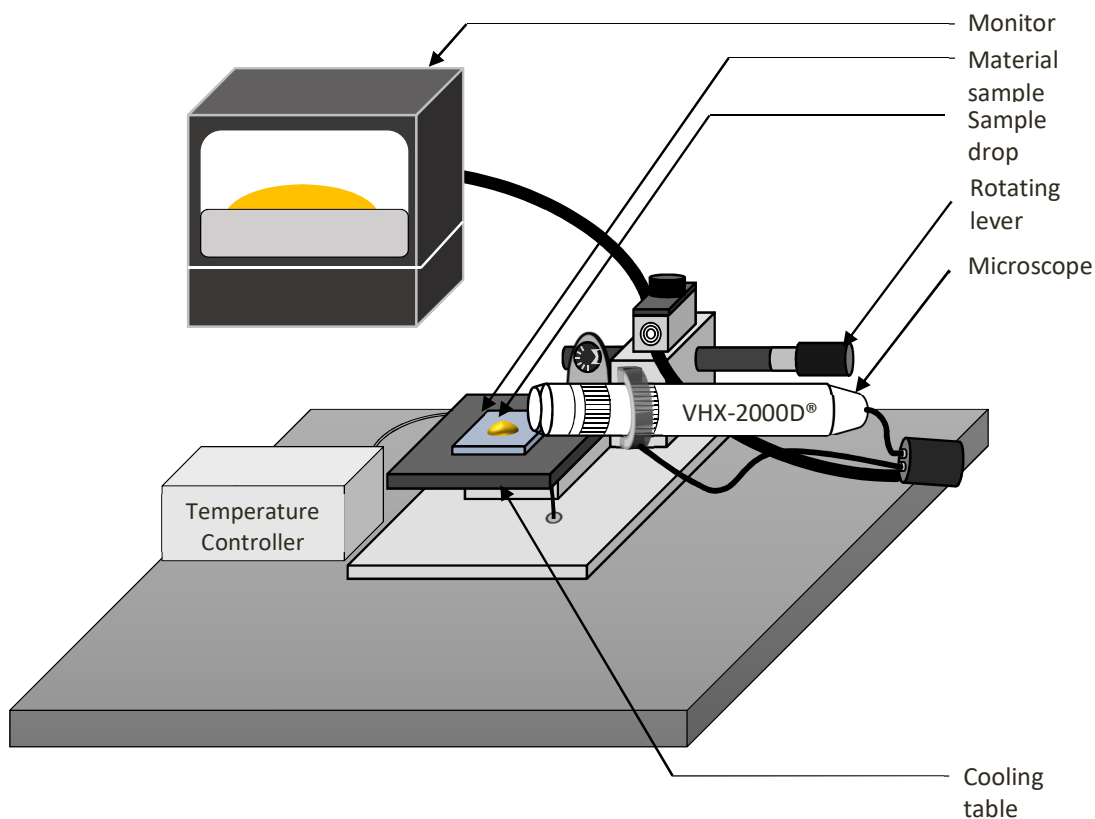


FIGURE 4-5: CONTACT ANGLE MEASUREMENT SETUP WITH A KEYENCE VHX 2000D® MICROSCOPE FITTED AT 90° TO THE SAMPLE

#### **Method**

The procedure for the contact angle measurement of different fatty acid mixtures on different material surfaces refers to DIN 55660. Therefore, three different fatty acid mixtures, one high

oleic (18.1), one high linoleic (18.2) and one high linolenic (18.3) together with seven different materials (PVC, PETG, PC, Aluminum (AlCu4PbMgMn), structural steel (St37), stainless steel (V2A) and glass) were investigated. Furthermore, the measurements were performed at different temperatures, starting with 50 °C and followed by 40, 30, 25, 20, 15, 10 and 5 °C. The different temperatures were set and controlled with a cooling table. The microscope was rotated at 90° so that the drop on the material surface could be seen from the side.

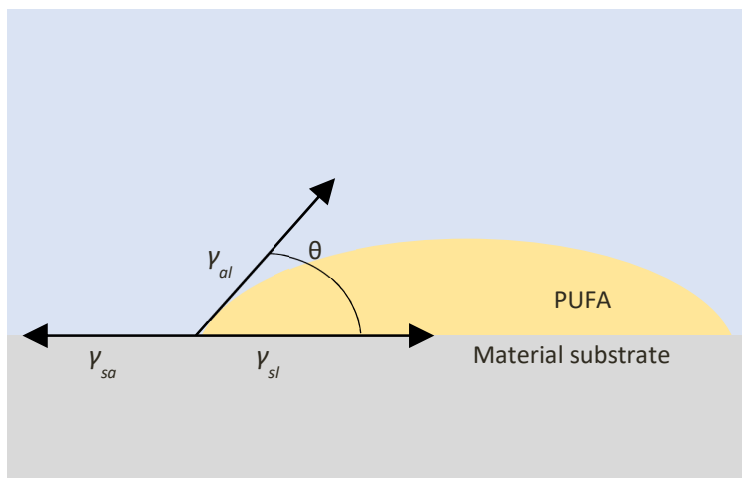


FIGURE 4-6: DETERMINATION OF CONTACT ANGLE ON DIFFERENT SUBSTRATES

Three drops of the respective fatty acid mixture each with a volume of 10  $\mu$ l were placed on the surface of each material sample placed on the cooling table. A Peltier element and a temperature sensor were integrated which were operated via a HAT Soft Pro Controller by Belektronig for an exact temperature control. The fatty acid mixtures were stored in a compartment dryer at 50 °C throughout the investigations. The corresponding material sample was also preheated on the cooling table up to 50 °C before the respective fatty acid mixture was put on it. An image of each drop was taken by means of the microscope and the next temperature was set. The evaluation of the pictures was performed using ImageJ. At first a baseline through the two triple points of each drop was made. After that the shape of an ellipse was put above the outline of the drop. With the help of these geometrical shapes the angle could be measured in the two intersections of the ellipse and the baseline. The comparison of the results was performed by determination of the arithmetic average of all drops at each temperature for every fatty acid mixture and material.



### 4.3. Multistage melt crystallization – phase diagrams and metastable zone determination

Each fatty acid mixture was put through a multistage crystallization process based on the results obtained by subjecting them through a broad spectrum of temperature profile in the DSC. Every phase transition in this temperature range was identified and characterized. During the melt crystallization process, probes P, as shown in Figure 4-7, were analyzed again both in the DSC and GC. The combined results of the thermograms and the chromatograms derived from the DSC and GC-FID were used to construct a technically relevant section of the SLE diagram including the metastable range.

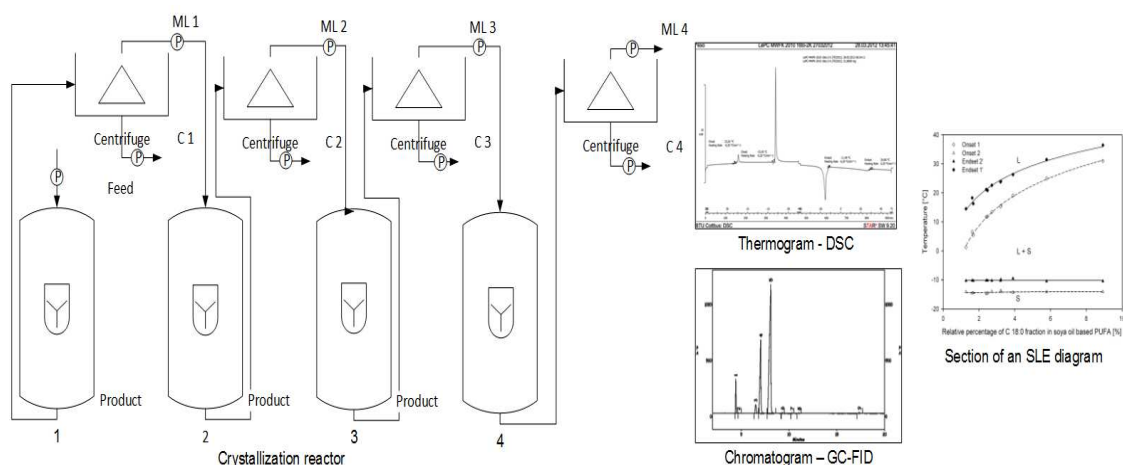


FIGURE 4-7: THERMAL AND CHEMICAL SAMPLE CHARACTERIZATION FROM MULTI-STEP MELT CRYSTALLIZATION

The interpretation of the thermograms and eventual characterization of peaks in the DSC has been discussed in the Sections 5.2.1 - 5.2.3. The method developed and chosen for the chemical analyses of the PUFA mixtures has been detailed in Section 5.2.5.

#### 4.3.1. EasyMax™ reactor – tempered centrifuge setup

The aforementioned fatty acid mixtures were crystallized in an automated laboratory reactor called the EasyMax™ (Mettler Toledo Ltd., Greifensee, Switzerland) in multiple steps in order to obtain various crystallization fractions, which were then further analyzed. As previously mentioned, each fatty acid mixture was subjected to a particular crystallization temperature depending on its thermal behavior post investigations in the DSC. Figure 4-8 illustrates the basic automated EasyMax™ reactor setup without the stirrers and reactors inserted. The full

reactor setup with stirrers, thermal sensors and inline probe have been shown in the following section in Figure 4-17.

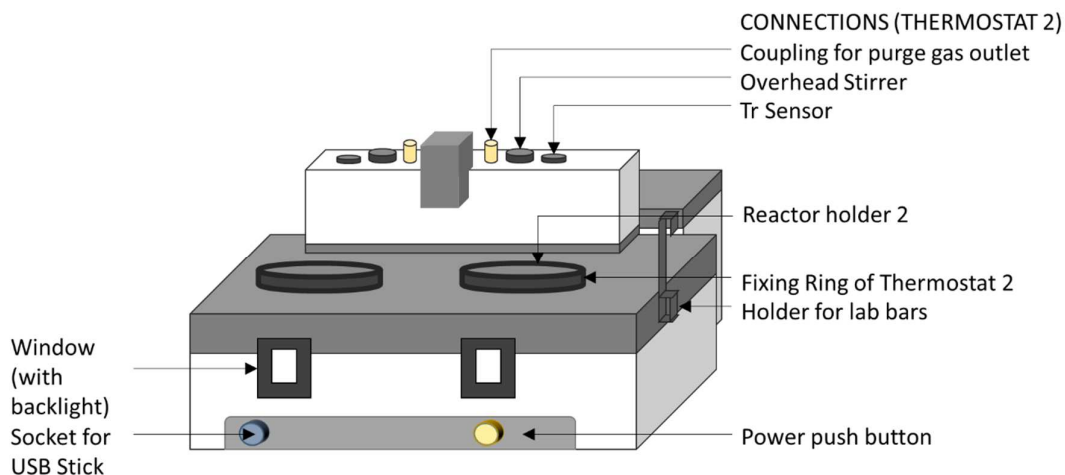


FIGURE 4-8: EASYMAX™ - AUTOMATED REACTOR SETUP WITH TWO INDEPENDENT REACTOR SYSTEMS<sup>§§§</sup>

The EasyMax™ hosts two reactor vessels functioning completely independent of one another. They are each equipped with stirrers and temperature controllers, which regulate the reactor ( $T_r$ ) as well as the reactor jacket ( $T_j$ ) temperature.

### Method

Each fatty acid mixture was subjected to a particular crystallization temperature depending on its thermal behavior after investigations in the DSC (DSC 822e/400 Mettler Toledo Ltd., Greifensee, Switzerland). Upon crystallization, the suspension was centrifuged in a laboratory thermal centrifuge (Multifuge 3 S-R, Heraeus Centrifuges, DJB Labcare Ltd, Buckinghamshire, England) at a relative centrifugal force of 4000g and exactly at the same crystallization temperature for around 20 minutes. The mother liquor was then separated from the crystal suspension by decantation. The mother liquor as well as the crystal suspension was used as feed for further crystallization at lower and higher crystallization temperatures respectively. Thus, a multistage crystallization process was realized.

<sup>§§§</sup> Own representation based on EasyMax™ 102 automated reactor sketch found in the operations manual provided by Mettler Toledo AC, Mettler Toledo GmbH, edited by Ms. Sukanya Dasgupta

### ***Why EasyMax™?***

The advantage of the EasyMax™ reactor is that the temperature gradient between the jacket and the sample in the reactor can be maintained and controlled up to a  $\Delta T$  of 0.1K, thereby controlling wall nucleation due to increased cooling of the jacket. This is of course also dependent on the cooling rate applied. Another big advantage is that the jacket is dark in color thereby providing a great contrast for light based analysis of the crystallization process wherein the crystals are whitish in color. There are also viewing windows enabled with backlight available for an in-situ visual analysis. Automated magnetic and anchor stirrers were also available for homogenous mixing. The anchor stirrers which were matched with the reactor geometry were chosen for the multistage melt crystallization process such that any wall nuclei and crystal sediment at the reactor bottom are scraped off and pushed back into the bulk for better crystal growth and yield.

#### 4.4. Melt crystallization - nucleation kinetics

The SLE data obtained from the phase diagrams of the various PUFA mixtures have been applied to develop temperature profiles for crystallizing the samples in different setups so as to generate fundamental data of the nucleation kinetics during crystallization. A polarized light microscope setup coupled with a high definition camera was used for  $\mu$ -scale investigations in a gradient chamber. On the other hand, crystal formation in a larger sample volume (ml –scale) was explored in the automated EasyMax™ and FBRM™ laser sensor system. The determined nucleation and induction time data were then characterized as a function of supercooling and cooling rates. The crystal growth rates of the standard pure components in PUFA were also compared with the crystal growth rate of PUFA.

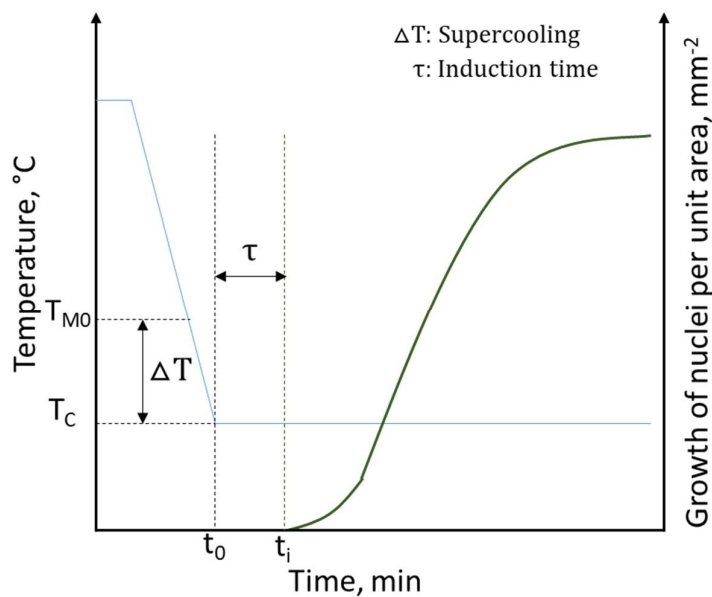


FIGURE 4-9: MATHEMATICAL DEFINITIONS OF INDUCTION TIME,  $\tau$  AND SUPERCOOLING,  $\Delta T$  USED IN THIS WORK

Some important parameters as applied in this work have been pre-defined here to avoid any confusion. Firstly, supercooling, has been taken as the difference between the desired temperature at which the sample is crystallized and the temperature at which the sample reaches its SLE temperature/ liquidus point. The SLE temperature here is defined as the highest temperature limit up to which the traces of the sample could exist in solid phase during the reheating step. The sample can only exist in its molten or liquid form from this temperature upwards. This was determined for each sample by means of the DSC.

Crystallization is eminent once the sample is cooled below its equilibrium temperature. The time required for the first crystal nucleus to appear in the sample is defined as the induction time. Factors like, the degree of supercooling and the rate of cooling decide the speed and behavior of the nucleation that occurs. The mathematical definition of induction time and supercooling used in this work has been illustrated in Figure 4-9. Induction time has been defined as the difference in the time at the sample reaches the desired crystallization temperature and the time at which the first crystal is noted by the detector. Supercooling on the other hand has been defined as the difference between the solid liquid equilibrium temperature (liquidus point) and the crystallization temperature.<sup>111,131,132</sup>

#### **4.4.1. Polarized light microscopy with high definition camera ( $\mu\text{l}$ scale)**

The experiments under the microscope were performed in a tempered gradient stage (LTS 120, Linkam Scientific Instruments Ltd., Surrey, UK; Standard Glass-slide frames / Peltier element with electronic controls PE 94 in connection with controls software Linksys 32 Version 1.6.0) where PUFA was subjected to a specific temperature regime depending on the experiment (Figure 4-10).<sup>24</sup>

##### ***Method***

Single droplet crystallization process on the object slide was chosen under the high resolution polarized light microscope so as to avoid any other effects that could arise from disturbing the sample after placing it. A glass slide was placed inside the gradient chamber before the sample injection and maintained at a temperature much above the liquidus point of sample. A standard temperature of 50°C was chosen as in the case of the DSC experiments. The fatty acid droplet was placed on top of a glass slide with the help of a micro-syringe and then covered with another as illustrated in Figure 4-11. The gradient chamber cover was then sealed and subjected to the pre-determined temperature profile. The crystallization process including the induction time and nucleation rate was then observed through the microscope-camera setup. Supercooling ranges to be investigated were chosen based upon the thermal metastable ranges of the samples used as determined by the DSC. Each of these experiments was repeated with a variety of cooling rates. The sample volume was kept constant at 32 $\mu\text{l}$  after consideration via trial and error of various optimizing factors like capillary action, enough sample mass, etc. Every experiment was repeated at least 3 times and performed

with a fresh sample each time. The high linoleic sunflower oil based PUFA was subjected to various degrees of supercooling in the tempered Linkam gradient stage ranging from 4.9 to 6.9 K in steps of 0.5 K. Each of these experiments was then carried out with different cooling rates namely, 5, 10, 20 and 30 Kmin<sup>-1</sup>.<sup>24</sup> Samples investigated were the high linoleic and high oleic sunflower oil and the high linoleic soya oil PUFA mixtures. The microscope used is a Leica DM-RME from Leica Microsystems, Wetzlar, Germany. Adaptable mounted cameras - Leica DPC 320/DFC 500, Leica Microsystems, Wetzlar, Germany were used for the in-situ observations (Figure 4-10).

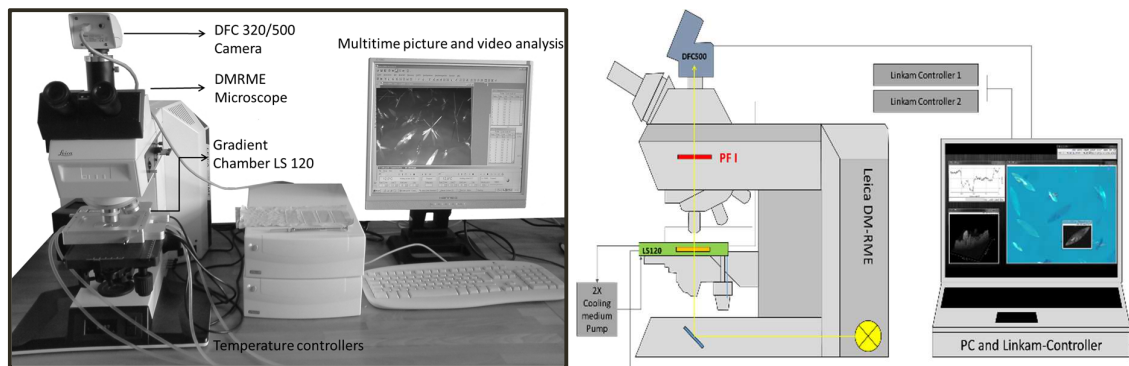
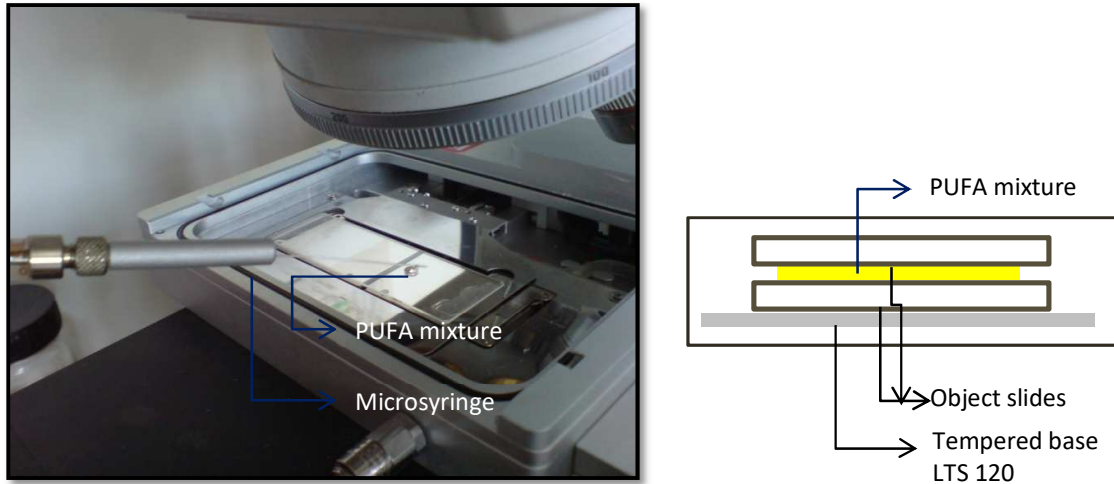


FIGURE 4-10: POLARIZED LIGHT MICROSCOPE, LEICA DM-RME WITH HIGH DEFINITION LEICA DFC 500/320 CAMERA<sup>133</sup>

Standard samples of the five main constituents of PUFA, namely, palmitic, stearic, oleic, linoleic and linolenic acids were also investigated under the microscope for the determination of their individual crystal growth rates. These experiments were performed in 0.68 mm capillaries made of borosilicate glass placed inside the Linkam gradient chamber. The linear crystal growth rates of each of the pure fatty acid standards and sunflower oil PUFA were determined and compared. The crystal growth rates of the high linoleic sunflower oil based PUFA mixture were also investigated in capillaries of various sizes (0.68 mm, 68  $\mu\text{m}$ , 25  $\mu\text{m}$ ) as a function of degrees of supercooling and cooling rates. For calibration purposes, a total scale length of 50 mm with a minimum measurable distance of 100  $\mu\text{m}$  was used (provided by Leica Microsystems). The equilibrium temperatures for these experiments were also derived in a similar manner as mentioned before by means of the DSC. To measure the linear growth rate, a crystal was randomly selected in the capillary and its growth in one dimension (length) was observed and measured. These crystal growth rates were then compared with one another.<sup>24</sup>



**FIGURE 4-11: PICTORAL AND SCHEMATIC REPRESENTATION OF SAMPLE PREPARATION ON THE OBJECT SLIDE IN THE GRADIENT CHAMBER (LTS 120, LINKAM SCIENTIFIC INSTRUMENTS LTD.) UNDER THE MICROSCOPE (LEICA DM-RME, LEICA MICROSYSTEMS)**

### Calibration

Firstly, it was important to calibrate the gradient stage thermally on which the experiments were to be conducted. The calibration experiments were done exactly as in the case of an experiment. Similar sample volume of 32 $\mu$ l was added on an object slide and a special flat and flexible Pt100 4-wire foil sensor (Almemo ZA 9030-FS1 Norm E4) was applied for the purpose such that another object slide could be used to cover the same as shown in Figure 4-12. The resolution of the thermal sensor chosen was  $\pm 0.1^{\circ}\text{C}$  whereas the operating range is between  $-200^{\circ}\text{C}$  and  $850^{\circ}\text{C}$ . Then the chamber was closed and the experiments were run at each cooling rate. A data logging module (Almemo 2890-9) was used to log the temperature profiles. Experiments were conducted on either side of the gradient stage.

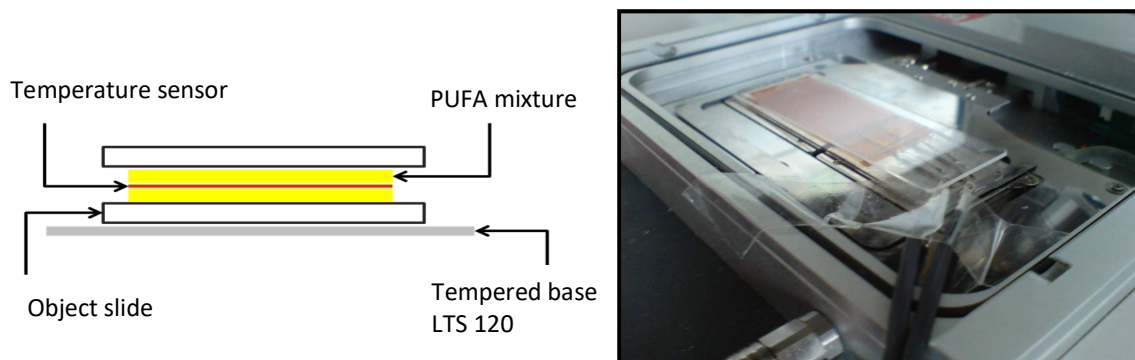


**FIGURE 4-12: PICTORAL AND SCHEMATIC REPRESENTATION OF TEMPERATURE CALIBRATION WITH THE HIGH OLEIC SUNFLOWER OIL BASED PUFA MIXTURE IN THE GRADIENT CHAMBER (LTS 120, LINKAM SCIENTIFIC INSTRUMENTS LTD.) WITH A ALMEMO RTD FOIL SENSOR**

#### 4.4.2. Capillaries for crystal growth rates ( $\mu\text{l}$ scale)

Crystal growth rates also play a vital role in the separation process. Therefore, the linear crystal growth rates of standards of each of the main components present in the poly-unsaturated fatty acid mixture have been studied. These have been then compared with the actual crystal growth rate of PUFA.<sup>24</sup>

##### **Method**

The saturated fatty acids that are, namely, palmitic and stearic acid crystallize at very moderate temperatures which can be achieved with less energy expenditure. For this, capillaries (inner diameter,  $d_i = 0.68$  mm) were placed in the tempered gradient stage and the linear crystal growth rates were determined. To measure the linear growth rate, a crystal was randomly selected in the capillary and its growth in one dimension was observed and measured.<sup>24</sup>

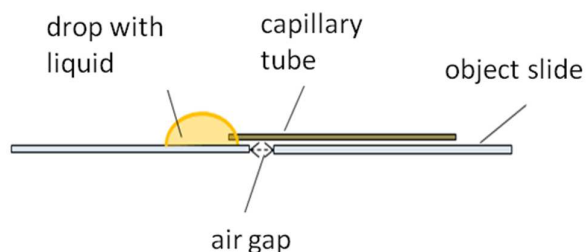


FIGURE 4-13: INTRODUCTION OF THE FATTY ACID MIXTURE SAMPLES INTO CAPILLARIES FOR CRYSTAL GROWTH TESTS

A comparison of the linear crystal growth rates of the pure saturated and unsaturated fatty acid standards in the aforementioned capillaries depending on the supercooling are depicted in Section 5.3.2.<sup>24</sup>

Further investigations on the crystal growth rate of sunflower oil PUFA were carried out in 25  $\mu\text{m}$  capillaries. Special care had to be taken during sample filling as the capillaries tend to have had some sample on the outer wall preventing proper analysis through the microscope. Only the tip of the capillary was made to be in touch with the probe as illustrated in Figure 4-13. An air gap between the sample droplet and the rest of the capillary was realized so as to prevent the sample to stick to the exterior of the capillary. The sample was subjected to a particular temperature profile as per the DSC thermograms with the help of the pre-calibrated Linkam gradient chamber. Capillaries with internal diameter of 68  $\mu\text{m}$  were also taken into consideration for comparison purposes.



#### 4.4.3. Focused beam reflectance technology (ml scale)

This Lasentec D600L sensor is a probe based measurement system which can be directly inserted into the reactor such that a real time characterization of the process which is melt crystallization in this case can be performed. As can be seen in Figure 4-14, a laser beam is sent through an optical setup and made to focus on a point on the sapphire window. The optical module rotates at a fixed speed of  $2 \text{ ms}^{-1}$  such that the spot on the window becomes a full circle. The laser as a result when inserted into sample or reactor scans the reactor content. Once the laser comes in contact with a particle, it would scatter back into the detector. These discrete pulses are noted, characterized in real time such that a measure of the time at which the first nuclei are formed in the PUFA mixtures can be very well established. Count classified as a function of chord length can also be measured by this sensor.

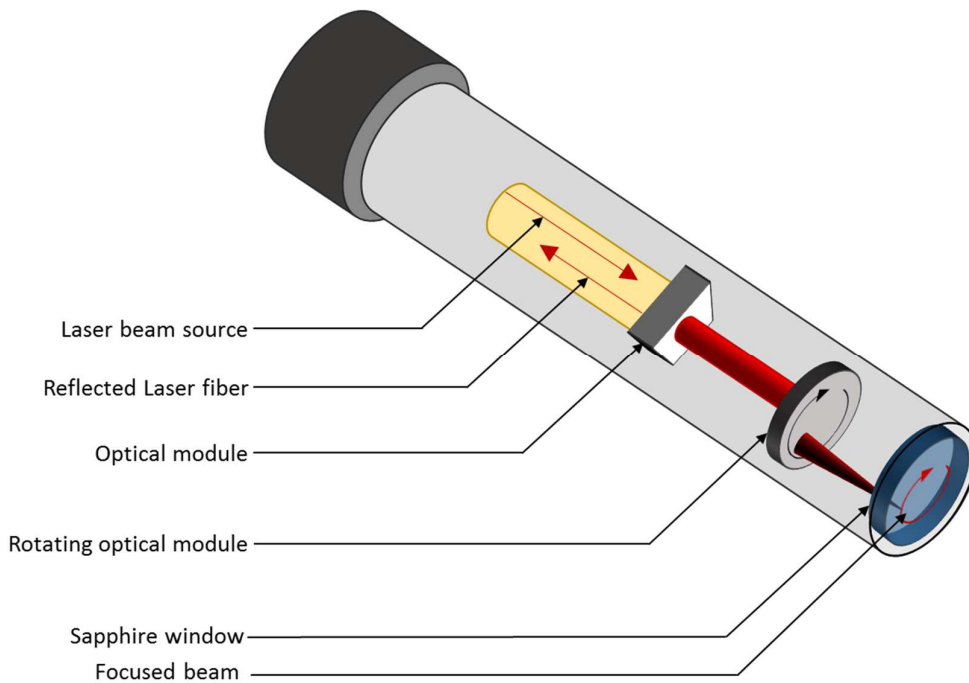


FIGURE 4-14: SCHEMATIC ILLUSTRATION OF IN-SITU PARTICLE SENSOR BASED ON FOCUSED BEAM REFLECTANCE TECHNOLOGY, METTLER TOLEDO AC, METTLER TOLEDO GMBH \*\*\*\*

Naturally, the FBRM™ technology is also limited to its own resolution which is between  $0.5 \mu\text{m}$  to  $3 \text{ mm}$ . Another limitation of this method is that overlapping crystals are counted as one large crystal because of lack of depth analysis capability. On the other hand, it is quite

\*\*\*\* Own representation based on FBRM technology sketch found in FBRM Method of Measurement – Introduction Webinar provided by Mettler Toledo GmbH<sup>134</sup>, edited by Ms. Sukanya Dasgupta

well suited for nucleation as overlapping is hardly envisioned at the early stages of the formation of the solid phase. Nucleation kinetics of the high linoleic and high oleic polyunsaturated fatty acid (PUFA) mixtures were investigated and compared during melt crystallization by means of this FBRM™ sensor.

#### 4.4.4. V-form Reactor – FBRM™ setup (ml scale)

Among the hurdles to be dealt with, the most important were firstly of maximal heat transfer, crystallization being an exothermic reaction and secondly the continuous stirring of the bulk solution so as to enable the FBRM™ to get a representative sample lattice to analyze.

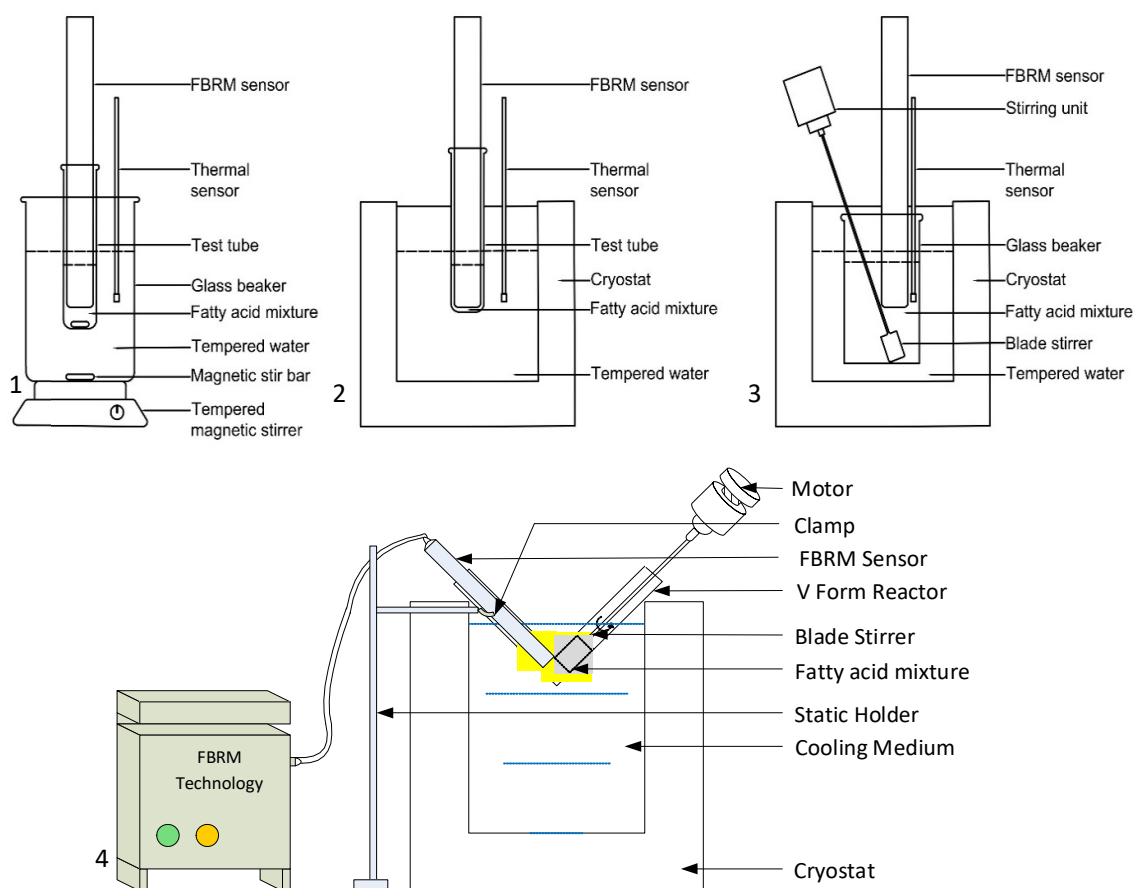


**FIGURE 4-15: EVOLUTION OF V REACTOR FOR ONLINE DETECTION BY FBRM™ IN A STIRRED REACTOR DETECTION BY FBRM™ IN A STIRRED REACTOR<sup>135,††††</sup>**

It was of critical importance that the stirrer was capable of putting all the crystals into motion as otherwise they would sink at the bottom of the reactor making the FBRM™ analysis pointless. This is especially because the FBRM™ just analyses a very small area of the bulk

†††† Own representation and edited by Ms. Sukanya Dasgupta and Mr. Benjamin Selge

solution and is static. The reactor which finally fulfilled the requirements for easy and better real time analysis of crystal formation and growth was a customized V form reactor. Enhanced heat transfer, specially to deal with the heat given out during crystallization, was enabled through minimal volume of sample, optimized mixing and the special shape of the reactor. A schematic representation that led to the development of this reactor form has been presented in steps 1 to 4 in Figure 4-15.

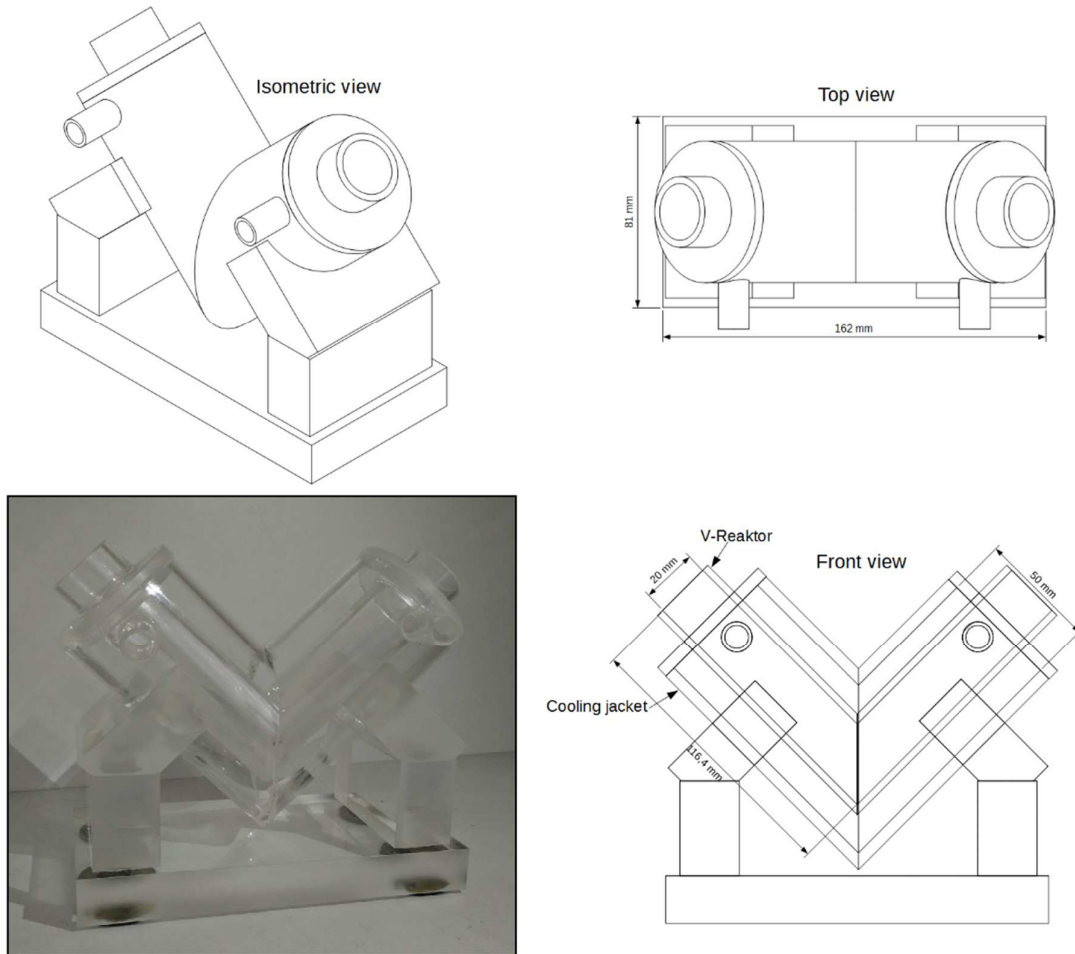


FIGURE 4-16: SCHEMATIC REPRESENTATION OF JACKETED V REACTOR\*\*\*\*

As can be seen in the illustration in Figure 4-15, setups tried started from a basic beaker, tempered plate and a temperature sensor, followed by the inclusion of a cryostat and blade stirrer. The stainless steel blade stirrer created an interruption in the data collection by the FBRM™ leading to a manipulation of the data. On the other hand, there was a problem in maintaining the temperature profile. If the sample temperature was chosen as the controlling

\*\*\*\* Own representation and edited by Mr. Benjamin Selge

temperature, the cooling medium went far below the expected profile so as to enable actual expected temperature in the sample. This led to extreme wall nucleation. Hence a different reactor geometry was conceptualized so as to tackle both problems. The novel V form reactor is shown in Figure 4-16.

The FBRM™ was inserted through one arm of the V form reactor whereas a blade stirrer was manufactured exactly to fit the other arm. This form enabled ideal mixing of the sample right in front of the laser analyzer. The V form reactor has an inner diameter of 2.5 cm and each arm is 12.5 cm long. The inner diameter was made just a little bigger than the outer diameter of the FBRM™ (1.9 cm). The two arms are joined at an angle of 90°. It was also ensured by the right angle of the reactor geometry in between that the blade stirrer was not in the line of sight of the FBRM™ laser such that any visual influence of the stirrer was negated. Sample volume of 40 ml was used for each experiment with a blade stirrer speed of 15 rpm. Important parameters like induction time, mixing speed, etc. have been determined and compared as functions of degree of supercooling and composition of PUFA mixtures. Although many obstacles were overcome by the construction of this V form reactor, an important one pertaining to the application of temperature profile still posed a problem. The problem was not so much with the reactor itself but the cryostat maintaining the cooling medium temperature profile and the difference between the temperature in the cooling medium and the inside of the wall of the V-reactor. In order to get through these problems, an automated reactor system called EasyMax™, was ordered and tested which is explained in the next section.<sup>10</sup>

#### **4.4.5. EasyMax™ Reactor – FBRM™ setup (ml scale)**

##### ***Method***

Figure 4-17 shows the EasyMax™- FBRM™ setup wherein the two sunflower oil fatty acid mixtures were crystallized and monitored.<sup>4,136</sup> The EasyMax™ apparatus as mentioned before includes two reactor vessels functioning completely independent of one another. The magnetic stirrers were chosen as they would not interrupt the in-situ FBRM™ laser detectors. On trial with the anchor stirrers, it was noted that the steel reflected light into the sensor thereby manipulating the data collected. A detailed temperature sensor system comprising of four discrete PT 100 sensors connected to an Almemo Multi-sensor (2890-9) device was

set up in order to obtain a detailed profile as the latter influences the crystallization behavior significantly. The pre-installed EasyMax™ temperature sensors were one for the cooling agent,  $T_{Cr}$  and one for the jacket of the reactor,  $T_J$ . The third temperature sensor ( $T_{R1}$ ) was placed exactly next (1 mm) to the reactor wall keeping in mind that it is immersed well into the PUFA mixture in the reactor. The fourth one was placed at the center of the crystallization reactor ( $T_{R2}$ ).  $T_{R1}$  was used as the controlling temperature by subjecting its corresponding sensor to the suggested temperature profiles. In case of ideal mixing and instantaneous heat transfer  $T_{R1}$  should be exactly equal to  $T_{R2}$ . Owing to real conditions,  $T_{R1}$  being right next to the wall is subjected to the cooling earlier than at the center  $T_{R2}$ . As the parameter, induction time is being determined through these experiments, it is only justified to take the lower temperature,  $T_{R1}$  into account as it is more likely to crystallize at the wall than anywhere else in the reactor.<sup>10</sup>

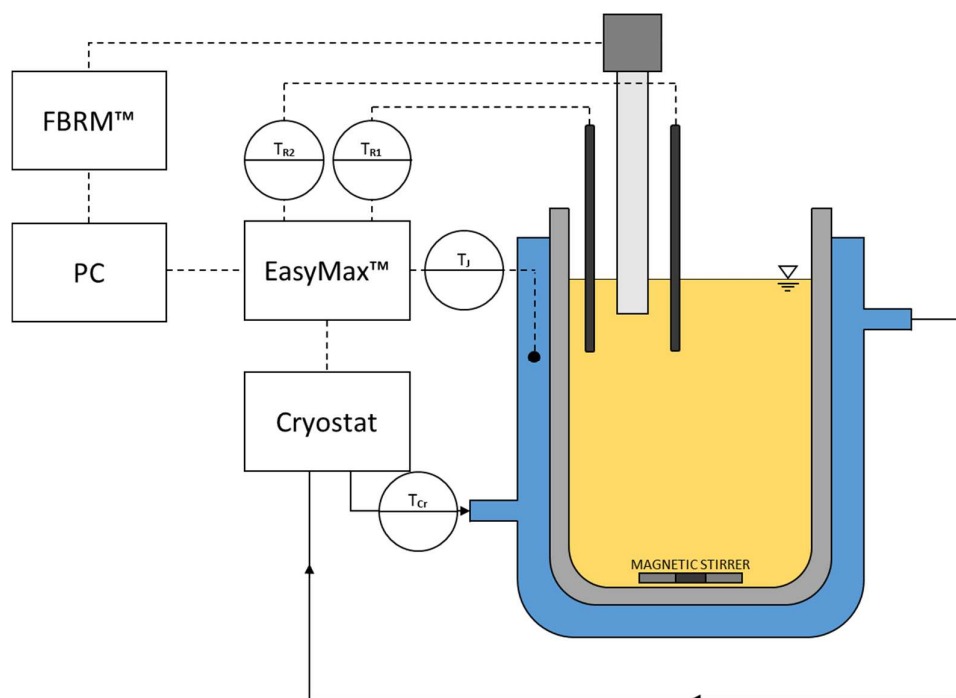


FIGURE 4-17: EASYMAX™ - FBRM™ SETUP<sup>§§§§, 137</sup>

The FBRM™ probe was used to provide an in-process particle system characterization in real time.<sup>136</sup> The FBRM™ sensor (outer diameter 1.9 cm) was installed 4 cm away from the reactor wall, strictly parallel to the axis of the cylindrical reactor. A magnetic PTFE stirrer with a

§§§§ Own representation, edited by Ms. Sukanya Dasgupta

frequency of 50 rpm was used for the experiments. The sample temperature ( $T_{R1}$ ) was held at 50°C for 5 minutes for stabilization, followed by a specific linear temperature gradient until it reached the final crystallization temperature within the specific metastable zone of crystallization of the sample.<sup>4,21</sup> The in-situ FBRM™ sensor was applied in this work especially to detect the onset of crystallization. The curves of the detected crystals were smoothed with the help of a moving average so as to compensate the fluctuation noises caused by impurities. An air cooled thermostat (Peter Huber Kältemaschinenbau GmbH, Model No.: CC 515) with an operating temperature range of -55°C to 100°C and cooling power of 3.3 KW at 0°C was attached to the EasyMax™ to circulate the cooling medium through the automated tempered jacket.<sup>10</sup>

## 4.5. State of the art

### 4.5.1. Fractionation and modification of oil

It has been established and previously discussed in Section 2.1 -2.3, that fatty acids, both saturated and unsaturated, constitute an important resource in the food as well as chemical industry. The five main fatty acids present in almost every vegetable oil based PUFA mixtures are of more value in the chemical industry separated into saturated and unsaturated fractions than in their mixed form. In spite of the increasing demand, an efficient large industrial scale method to separate the two type of acids is yet to be applied. Although, firstly it is required to obtain the free fatty acid mixtures from its triglyceride form as present in the oil. Current methods to obtain the original PUFA mixtures from the oils include hydrolytic splitting, rectification and distillation, enzymatic splitting and short path distillation.<sup>14,138</sup> The latter methods are employed such that the oils are not subjected to prolonged high temperatures. DMCs such as the Fe-Zn DMC have been used successfully as catalysts for the hydrolysis of soybean, coconut, palm oil etc.<sup>30,139</sup> Other modification techniques so as to meet the demands based on their applications are as previously mentioned in Table 2-1, esterification, hydrogenation and saponification.<sup>140</sup>

### 4.5.2. Separation of saturated and unsaturated fractions from PUFA mixtures

An example of the combination in which the five main fatty acids are present in the high oleic sunflower oil based PUFA mixture is shown in the following Figure 4-18. This relative composition of the PUFA mixtures has been analyzed using a GC-FID setup. While some of the previous processes mentioned are chemical modifications of the original oil, separation of the desired unsaturated fraction from the obtained PUFA mixture can be made possible due to the differences in the physical properties of the individual components. Hence any thermodynamic process based on the fundamentals of crystallization, distillation, extraction or physico-thermal process such as filtration, adsorption, membrane separation, etc. could be applied provided their individual fundamental properties such as solubility, crystallization temperature, volatility, size, differ.<sup>140,141</sup>

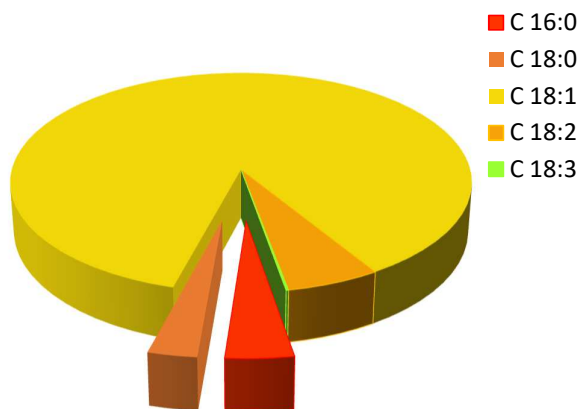


**FIGURE 4-18: FATTY ACIDS PRESENT IN THE HIGH OLEIC SUNFLOWER OIL BASED PUFA MIXTURE (SEE TABLE 5-3 FOR PRECISE COMPOSITION)**

Distillation is a thermal separation process which works by means of exploiting the differences in boiling points of individual molecules in a mixture. The method of short path distillation column owes its name to the short path the distillate has to travel from the evaporator to the cooler condenser chamber placed internally. Distillative evaporation temperatures can range from 80°C to 210°C even on an industrial scale with pressures reaching as low as 0.001 mbar.<sup>14</sup> Studies showed that in spite of attempted short path distillation, there were very little changes in the composition of the concerned fractions obtained.<sup>14</sup> This is in good agreement with literature as the double bonds in the unsaturated fractions have very little effect on their vapor pressures and hence volatility. In the case of PUFA mixtures from vegetable oils, each of the main constituents are made of more or less the same amount of C atom, ranging from 16 to 18 to be precise. The unsaturated fatty acids in the mixtures only differ in the number of hydrogen atoms and shape from one another wherein the number of carbon atoms present is the same. The presence of a double bond instead of a single bond which translates into subtraction of two hydrogen atoms is of little consequence on the molecular weights of the fatty acids concerned. The boiling points and molecular weights of the main fatty acids present in vegetable oils have been enlisted in Table 5-3.

The main obstacle faced by separation processes such as distillation is that, it is impossible to deplete the mother liquor of a saturated content below a satisfactorily applicable concentration. Although maybe lesser, depending upon chain length, this saturated content present still remains a cause for concern as it leads to clouding of the mixture at low temperatures and hence difficult to use as a fuel resource in the automotive industry. They do not optimally satisfy the minimum requirements for application as a raw material for the



manufacture of epoxy resins as well due to reduced possibility of crosslinking. There are, of course, other mechanisms such as adsorption as applied in chromatography which could be used to result in pure samples but one has to factor in the economical and throughput factor which are not yet ideal for larger scale operations.

Melt crystallization, on the other hand, enables one to separate this pseudo-binary system of saturated and unsaturated fatty acids because there is a relatively large difference between the melting points of both systems. The melting point for unsaturated fatty acids is much lower to those of saturated ones, as lower energy is required to melt samples with rising number of double bonds.<sup>31</sup> This is due to the molecular geometry of these acid structures. As there are no double bonds in the saturated fatty acids, all carbon atoms are surrounded by hydrogen atoms in a tetrahedral angle. That results in almost linear shapes of the molecules and in turn enables them to stack together and develop strong intermolecular interactions. It is quite the opposite case for the unsaturated fatty acids. Introduction of a double bond, either in *cis* or in *trans* configuration, results in a kink in their shape thereby rendering poor stacking properties. Consequently, weaker molecular interactions in the unsaturated fatty acids result in lower melting points.<sup>37,142</sup> Hence, the first part of this dissertation concentrated to check whether it was possible to fractionate the PUFA mixture into favorable unsaturated fractions. This has been elaborated in Section 5.1.

### **4.5.3. FBRM™ and its contemporaries – critical analysis**

The FBRM™ sensor has become a prominent technology with increasing popularity in the field of nucleation and polymorphism research. This sensor basically projects a spinning laser which gets backscattered once it is incident on some particle. A fitted detector detects the changed intensity of this laser till the spinning laser reaches the end of the particle and hence a chord length data is generated. This data is classified into chord length classes which can be monitored during the crystallization process simultaneously. In spite of the increasing popularity, it has certain drawbacks. One important problem is that this technology does not allow the user to look into the depth of the particles that are being monitored. Due to this, any overlapping of multiple crystals might result into the sensor reading it as one larger crystal leading to a reduction in the crystal count. However, these limitations are more prevalent during measurement of crystal growth rather than the onset of nucleation wherein the number of crystals are limited.<sup>143</sup> On the other hand it provides an in-situ monitoring which

is of prime importance for the determination of induction time. It is also very important to mention that the success of such a technology is even more so, at the onset of nucleation as it attributes to a more restricted crystal size class in a less dense melt or solution. It has been also noted in previous literature that the intensity of back scattering laser might vary depending on the roughness of the surface of the crystal, the refractive indices<sup>143</sup> or the contrast in the colors of the crystal and background. If the intensity is reduced, it might be lesser than the threshold of the counter in the FBRM™, leading to a reduction in crystal count or chord length. This also gives way for another problem, which is while the chances that the FBRM™ might detect the crystal is high, the fact that it might give the exact length or boundaries is rather low.<sup>144</sup> In a study conducted by Ruf et. al.,<sup>144</sup> a ceramic spherical particle was made to pass the spinning laser of the FBRM™. The data collected showed that the results significantly depended on the distance of the particle from the focal point of the laser beam.<sup>144</sup> Theoretically, it is impossible for the entire particle to be within the focal point as it grows. The parts of the particle that intersected with the widened and hence weakened laser resulted in less accurate edge detection.<sup>144</sup> This study also highlighted the overestimation of the particle size owing to the conical shape of the laser beam as shown in Figure 4-14. On one hand, previous literature reported the failure to correlate particle size distribution to the chord length based data from the FBRM™ whereas on the other they do not undermine the usefulness of this sensor as an in-line detector for crystallization or more generally particle detection. The main problem arises as Yu, Chow et. al.<sup>143,145</sup> put it, from the quantification of the particle size. They also pointed out based on their studies and experiments, that FBRM™ is a valuable solution for the assessment of the onset of primary nucleation.<sup>143</sup> Some of the previous literature which reported similar assessment of this technology have been enlisted in the reference.<sup>143-146</sup> Concentrated crystallization kinetics include various analytical methods such as FTIR, Raman and UV-Vis Spectroscopy. The first two methods, correctly so require extensive calibration for the exact quantification of the characteristic particle size parameter or mass. The advantage of FBRM™ with respect to them is that it can easily determine the begin and the end of the crystallization process.<sup>145</sup> Sieve and image analysis, laser diffraction are other particle size analysis methods available in the market, to name a few. However, they are offline methods.<sup>146</sup> Image analysis is possible on-line as well if a tempered customized chamber could be brought under the microscope as has been performed in the work presented here in addition.

The FBRM™ could not detect particles less than 1µm in literature and a standard of 10µm is suggested as a reliable size for detection.<sup>143</sup> These results were based on experiments done on polystyrene particles. Size detection might vary depending on the color and surface properties of the sample.

**FBRM™ and Laser Diffractometer**

Experiments with a FBRM™ and magnetic stirrer as in this study were also successfully conducted by Hu, Cunningham et. al. to follow the nucleation kinetics of micro crystalline cellulose granules on a fluidized bed.<sup>146</sup>

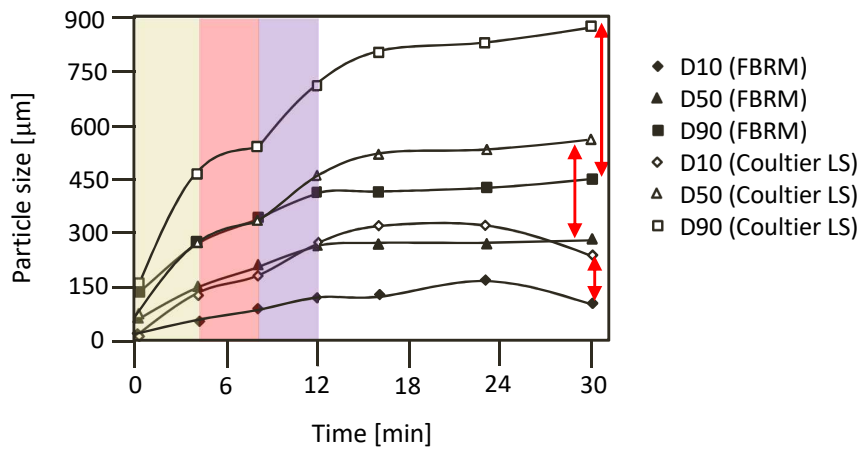


FIGURE 4-19: COMPARISON OF ABSOLUTE PARTICLE SIZE ANALYSIS OF MCC GRANULES BY FBRM™ AND COULTER LS DIFFRACTOMETER\*\*\*\*\*

This study also showed that FBRM™ was equipped to show the qualitative trends of growth as compared to results obtained by means of a laser diffractometer (Coulter LS instrument - Model 13-320, Beckman Coulter Inc., Fullerton, CA).

Comparisons showed that time stamps on the onset and end of the nucleation and growth process were almost identical although the quantification of the absolute size varied, increasing with larger granules class sizing up to 90 µm.

Figure 4-19 illustrates this diagnosis. The smallest class used here was 10µm as well.<sup>146</sup>

\*\*\*\*\* Self-edited re-representation of Figure 4 by Hu, Cunningham et. al. in <sup>146,146</sup>

### ***FBRM™ and ATR-FTIR***

Another instrument which is used to monitor the varying effects of supersaturation and cooling rates on crystallization kinetics is the in-situ total reflectance Fourier Transform Infra-Red, ATR-FTIR spectroscope. Liotta and Sabesan<sup>89</sup> applied a Mettler Toledo ReactIR™ 1000 with a DiComp immersion probe along with a Lasentec FBRM™ D600L for the in-situ monitoring of crystallization of an active pharmaceutical agent. The probes were also immersed in sample filled in an automated reactor and cryostat setup similar to this study. The ReactIR™ gives out an infrared spectra signal based on the IR absorbance of the dissolved component or solute in the mixture. These were collected at regular intervals. This is converted into a digital signal which in turn is transformed into an analogue output giving the concentration data based on a detailed calibration done between mixture concentration and IR absorbance data.<sup>89</sup> As can be predicted from this literature, FTIR is more suited to determine supersaturation or concentration data rather than the exact time of nucleation. The FTIR reports a sudden drop in the solution or melt concentration when primary nucleation occurs and hence is an indirect manner of detection of nucleation. To study the nucleation kinetics one needs to investigate a gamut of parameters influencing the induction times, including very low supercooling and high cooling rates. This in accordance to theory would generate very high induction times and less crystal count. Such mild changes in solution or melt concentration might be missed by IR spectroscope resulting in a delayed response.

### ***FBRM™ and PSyA***

Another very similar application of laser backscattering is the fiber optical device by Meßtechnik Schwartz GmbH, Germany called the Particle System Analysis (PSyA). It also uses an infra-red laser beam to detect particles between 2 µm and 1000 µm. Unlike the FBRM™, the PSyA moves the focal point horizontally and radially, making it capable of detection in higher concentrations of solutions.<sup>14,147,148</sup> The measuring technique suggest that at a later stage of crystallization, crystal growth measurements might be more suitable with the PSyA device. This although would also mean that the minimum size of detectable particle will be more than that of the FBRM™, making it less suitable for nucleation detection.

### ***FBRM™ and LiquiSonic 30***

Nucleation of fatty acid mixtures based on vegetable oils were also monitored using laboratory scale ultrasonic sensors such as LiquiSonic 30 supplied by SensoTech GmbH, Germany.<sup>14</sup> This sensor as in the case of FBRM™ is an in-line sensor directly placed inside the crystallizer. At less and moderate to high agitation rate (0-200 rpm) and even at relatively low cooling rates of  $10\text{K h}^{-1}$  ( $0.17\text{K min}^{-1}$ ), nucleation of the saturated content could not be detected by this method.<sup>14</sup> The details given according to the data generated was that the ultrasonic velocity increased with decreasing temperature and the delay in detecting nucleation was as high as 19 minutes.<sup>14</sup>

### ***Other methods***

While inline particle analysis in the reactor is increasingly gaining popularity, due to the reasons stated previously an in-situ optical analysis under the microscope is indispensable.<sup>149</sup> Section 4.4.1 discusses the polarized light microscopy setup used for detection of nucleation in this work. Previous studies show investigations on induction times of crystallization of hydrogenated sunflower seed oil by means of an optical setup.<sup>131</sup> In the aforementioned case, a calcium sulphide photo diode was used to detect the occurrence of crystallization in a glass cell where polarized helium laser was used as the source of light.<sup>131</sup>

#### **4.5.4. Metastable zone width determination**

FBRM™ and ATR-FTIR together is a powerful automated tool to generate metastable ranges of crystallization in-situ,<sup>89,116,117</sup> although temperature control in reactor volumes to fit both the immersion probes might not be ideal. The FBRM™ can return the count data above a pre-determined threshold depending on noise and fluctuations, whereas the FTIR can calculate the concentration data simultaneously.

### ***Why DSC and GC-FID?***

Accurate determination of a metastable zone width is one of the most meticulous and arduous tasks of crystallization kinetics research. Apart from including a tedious multistage crystallization process, every sample needs to be thermally and chemically characterized. Metastable zone width is highly influenced by cooling rates. The most accurate metastable zone data can be achieved only by application of slow heating and cooling rates on samples

wherein heat transfer to and out of sample or in other words temperature control is relatively accurate.<sup>89,116,117,119</sup> Hence DSC with its highly sensitive heat control system, less sample volume and cooling or heating rates as less as  $0.2\text{Kmin}^{-1}$  were found to be apt to justify such requirements. Another advantage is that the DSC also provides a partial automation possibility of the entire process when compared to FBRM™-FTIR setup, with an auto sampler which is very useful with experiments running around 700 – 900 minutes. The reasons behind choosing the GC-FID setup for the chemical analysis has been discussed in detail in Section 4.2.4.

## 5. Result and discussion

This chapter has been divided into three sections. Firstly, it was important to verify and establish that purification, that is the removal of saturated content from these PUFA mixtures is possible by means of melt crystallization. It was also important to test whether it was possible to deplete the PUFA mixtures of their saturated content to a favorable concentration that would allow the product to be used as a raw material for industries such as the production of epoxy resins. A linseed oil based fatty acid mixture was used to investigate the effectiveness of this thermal separation process. The second section describes the determination of SLE phase diagrams and their metastable zone widths whereas the third section discusses the results of nucleation kinetic investigations both in micro- and milliscale. These subjects would be detailed upon in each sub-section in this chapter.

### 5.1. Melt crystallization of linseed oil based PUFA

Melt crystallization was chosen to separate this pseudo binary system of saturated and unsaturated fatty acid mixtures exploiting the relatively large differences in their melting points as enlisted in Table 5-3. Melt crystallization would prove to be an efficient method to enrich these fatty acid mixtures with unsaturated fractions only as long as an appropriate temperature profile is found.<sup>11,18</sup>

Different temperature profiles and crystallization temperatures lead to significant differences in the quality of the final product. Hence, measures were taken not to cool the system too far or too fast as that would create very many small crystals simultaneously thereby reducing the final crystal size. So, the difficulties lay in the choice of temperature regime for optimal nucleation, crystal growth and further separation. This had to be also optimized for different systems. Therefore, SLE data for each of the samples, determined upon analyzing the fractions thermally and chemically were determined which has been discussed in detail in Section 5.2.<sup>11,18</sup>

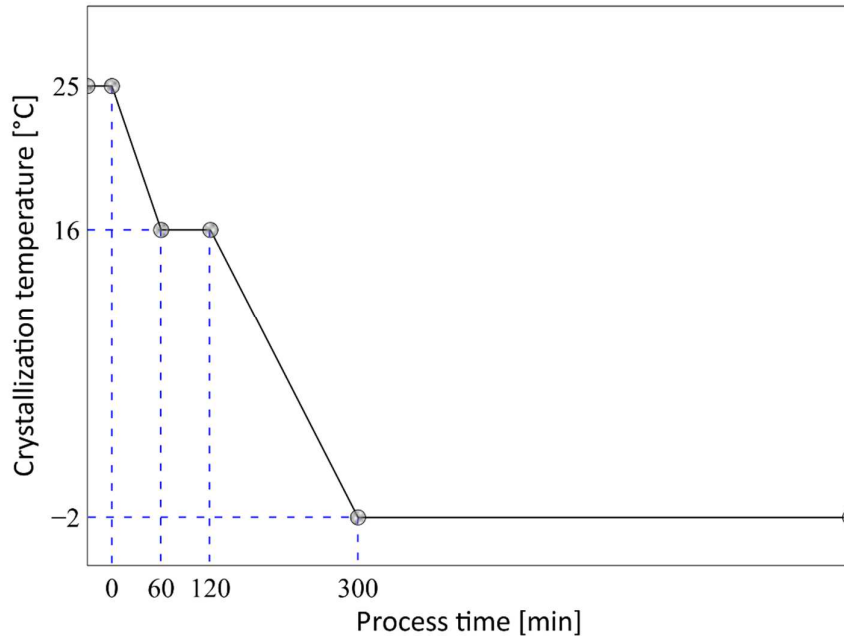


FIGURE 5-1: TEMPERATURE PROFILE FOR THE MELT CRYSTALLIZATION OF LINSEED OIL BASED FATTY ACID MIXTURE AT END TEMPERATURE OF  $-2^{\circ}\text{C}$ <sup>11,18</sup>

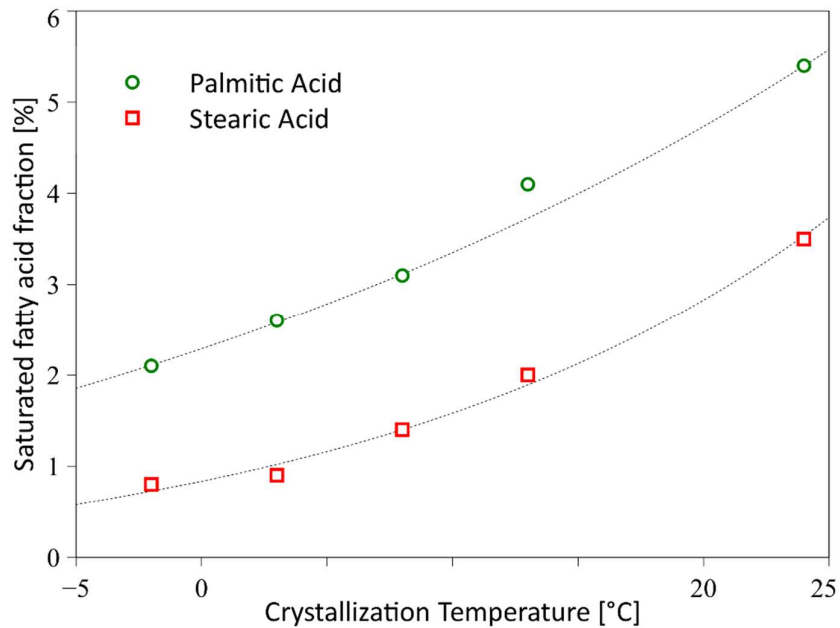


FIGURE 5-2: DEPLETION OF PALMITIC ACID (C 16:0) AND STEARIC ACID (C 18:0) AT DIFFERENT CRYSTALLIZATION TEMPERATURES ( $25^{\circ}\text{C}$ ;  $16^{\circ}\text{C}$ ;  $8^{\circ}\text{C}$ ;  $3^{\circ}\text{C}$  AND  $-2^{\circ}\text{C}$ ) ANALYZED BY GC, ISOTHERMAL AT  $190^{\circ}\text{C}$ ,  $0.2\ \mu\text{L}$  INJECTION VOLUME AND  $150\ \text{KPA}$ <sup>11,18</sup>

The temperature profiles for the subsequent crystallization steps for this system were also chosen from the SLE data of the same. The system was then subjected to various temperature profiles with different crystallization temperatures ( $13^{\circ}\text{C}$ ;  $8^{\circ}\text{C}$ ;  $3^{\circ}\text{C}$ ;  $-2^{\circ}\text{C}$ ), thereby creating varying degrees of supersaturation followed by nucleation. Figure 5-1 illustrates one such



temperature profile wherein the end temperature is  $-2^{\circ}\text{C}$ . It was important that the experiments were started at a temperature above the liquidus point of the sample so as to ensure complete homogenous mixtures. All the samples were cooled from  $25^{\circ}\text{C}$  to  $16^{\circ}\text{C}$  in one hour. Then they were left at that temperature for another hour to ensure that the system reaches equilibrium. Subsequently the mixtures were further cooled to the different crystallization temperatures over a period of maximum three hours. This end temperature was held constant for some time, so as to allow the crystals to grow. The objective of this work was to find the temperature profile in which crystallization temperature for the samples were such that nucleation started as late as plausible. Hence the system was supercooled as far and as slowly as possible to obtain big crystals and hence enrich the mother liquor with unsaturated fatty acids in a single stage crystallization process.<sup>11,18</sup>

Crystallization Temperature[ $^{\circ}\text{C}$ ]	Palmitic acid C16:0 [%]	Stearic acid C18:0 [%]	Oleic acid C18:1 [%]	Linoleic acid C18:2 [%]	Linolenic acid C18:3 [%]	Yield [%] (Mother liquor/Total)*100
24	5.4	3.5	21.3	15.6	53.3	
13	4.1	2.0	22.0	16.2	55.1	77.1
8	3.1	1.4	22.3	16.5	56.3	75.1
3	2.6	0.9	22.5	16.7	56.8	72.5
-2	2.1	0.8	20.1	17.3	57.2	70.6
GC-FID retention time [min]	4.7	7.1	7.8	8.8	10.8	

**Table 5-1: COMPOSITION AND RETENTION TIMES OF THE FATTY ACIDS IN THE MOTHER LIQUOR FRACTION AFTER MELT CRYSTALLIZATION AND SEPARATION WITH THE CENTRIFUGE ANALYZED BY GAS CHROMATOGRAPHY (ISOTHERMAL AT  $190^{\circ}\text{C}$ ,  $0.2\ \mu\text{L}$  INJECTION VOLUME AND  $150\ \text{kPa}$ )<sup>11,18</sup>**

In the case of our sample, a final crystallization temperature of  $-2^{\circ}\text{C}$  in addition to the previously mentioned temperature profile of Figure 5-1 was successful and effective for the separation of the saturated fatty acids. As a result, the mother liquor comprised of only 2.1 % palmitic acid and 0.8 % stearic acid. Table 5-1 provides the exact composition and yield of the mother liquor along with each of the different final crystallization temperatures. Satisfying yields, ranging between 70% and a little above 77%, were achieved. Naturally, the yields reduced with decreasing final crystallization temperatures.

	Saturated fatty acid	Regression equation	Coefficient			
			$y_0$	a	b	$R^2$
Depletion of saturated fatty acid fractions (Figure 5-2)	Palmitic acid (C 16:0)	$y = a \cdot e^{(bx)} - y_0$	1.23	3.52	0.03	1
	Stearic acid (C 18:0)	$y = a \cdot e^{(bx)} - y_0$	0.29	1.12	0.05	1

Table 5-2:REGRESSION COEFFICIENTS AND EQUATIONS WITH RESPECT TO OPERATING PARAMETERS FOR FIGURE 4-2<sup>11</sup>

The unsaturated high linoleic acid fraction produced in this work met with the standard provided by a parallel investigation going on the application of linseed oil based PUFA fractions on the manufacturing of flame resistant cured reactive resins.<sup>81</sup> The depletion of saturated content with respect to crystallization temperatures have been illustrated in Figure 5-2. Table 5-2 provides the regression coefficients for the functions behind the depletion of these saturated acids. The mother liquor obtained from the crystallization experiment, wherein the final crystallization temperature is -2°C, can, not only remain liquid for industrial applications at temperatures at least as low as -2°C but also possesses less than 3% saturated content. The latter makes it an attractive resource for the manufacture of epoxy resins. Thermal analysis by DSC in combination with GC were effectively used to characterize the products.<sup>4,150</sup>

**Outlook**

These experiments to produce an enriched unsaturated linseed oil based PUFA fraction were preliminary examples to validate the potential of a single stage melt crystallization process on vegetable oil based PUFA mixtures. The process needs to be further tested on other PUFA mixtures of differing compositions. Further, the process needs to be optimized with respect to time. Yield, although not unsatisfactory might be an issue upon upscaling as an appropriate separation procedure needs to be also investigated for larger scale operations. An extensive research on crystallization reactors and separation processes was outside the scope of this work.

## 5.2. Phase diagrams of plant oil based PUFA – Metastable zone determination

This section aims to provide an overview of the liquid solid equilibrium behaviors during melt crystallization of diverse plant based natural fatty acid mixtures. Phase behaviors at low saturated fatty acid concentrations have been investigated as it is of immense technical relevance with respect to efficient depletion of saturated content in PUFA mixtures.<sup>4</sup> Determination and identification of the metastable zone is the first step to understand the crystallization kinetics as it provides the operating range in which the crystallization experiments are to be carried out. It also gives an accurate understanding of whether or when spontaneous nucleation would occur and if crystal growth would be favored over nucleation.<sup>4,89</sup>

### 5.2.1. Interpretation of a thermogram from Differential Scanning calorimeter

The enthalpy behavior of an enriched saturated linseed oil based PUFA fraction is shown in Figure 5-3a. These results were obtained by subjecting the samples to the previously mentioned (Section 4.2.1) temperature regime in the DSC [for example: 50°C ► -20°C ◻ 50°C at 0.2 K/min]. Upon cooling, the sample exhibits two exothermic peaks (1 and 2) whereas during the heating run, it goes through the expected two endothermic transitions (1' and 2'). The onset of the first peak, 1 refers to the start of the spontaneous nucleation and crystallization of the enriched saturated fraction whereas the second exothermic transition, peak 2 denotes the beginning of the spontaneous solidification.<sup>4,121</sup> Peaks 2' and 1' represent the melting of the solid phases formed in peaks 2 and 1, respectively. A pictorial explanation (enthalpy and temperature not to scale) for better understanding of how the DSC thermograms have been interpreted in this work is illustrated in Figure 5-3b. The onset and endset points of significant phase transition peaks of a generalized DSC thermogram have been projected on a small section of a basic liquid solid phase diagram in Figure 5-3b so as to clarify the physical significance of these points. One can note that it is possible to also determine the metastable ranges of super saturation for nucleation and solidification by means of this method.<sup>4</sup> Figure 5-4 is a pictorial representation of what actually happens to the PUFA melt in the crucible as the temperature profile progresses.<sup>4</sup>

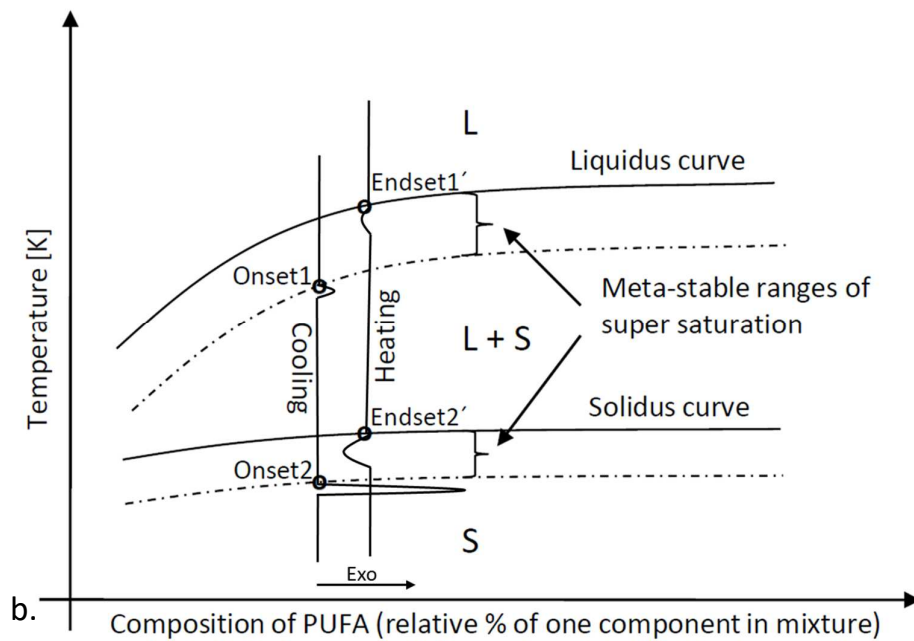
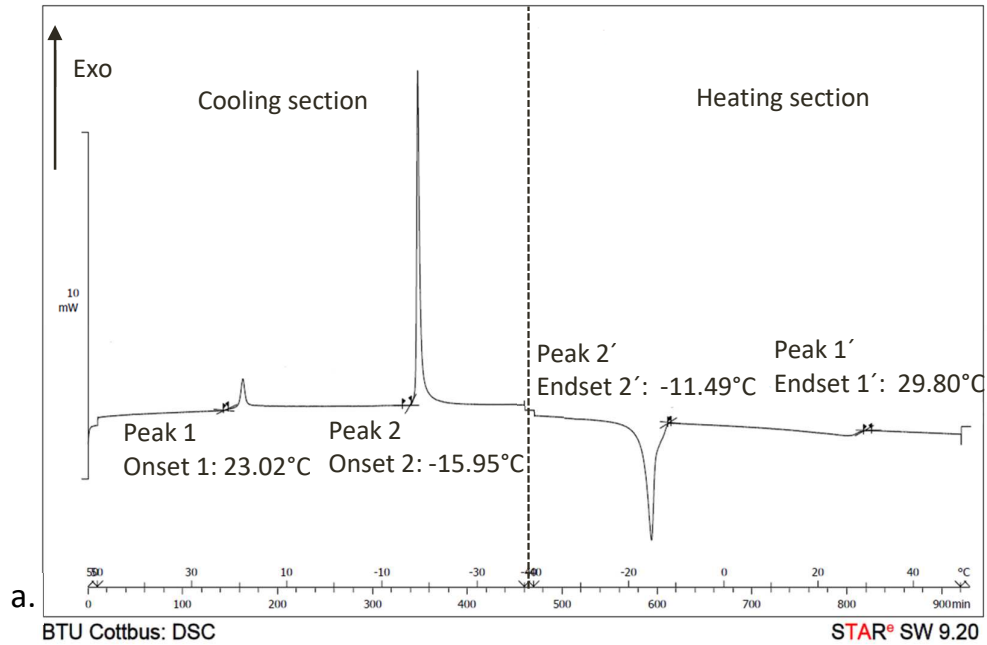


**FIGURE 5-3: A) ENTHALPY VS. TEMPERATURE OF A LINSEED OIL BASED PUFA FRACTION IN THE DSC [50 °C TO -40 °C TO 50 °C AT 0.2 KMIN-1] B) PLACEMENT OF DSC ONSETS AND ENDSETS OF SIGNIFICANT PEAKS IN A SMALL SECTION OF A GENERALIZED LIQUID SOLID EQUILIBRIUM DIAGRAM <sup>4</sup>**

Onset1: Onset of spontaneous crystallization; Endset1': End of super saturation – liquid solid equilibrium point; Onset2: Start of spontaneous solidification; Endset2': End of complete solidification (L: only liquid phase; L+S: Liquid and solid phase; S: Solid phase)

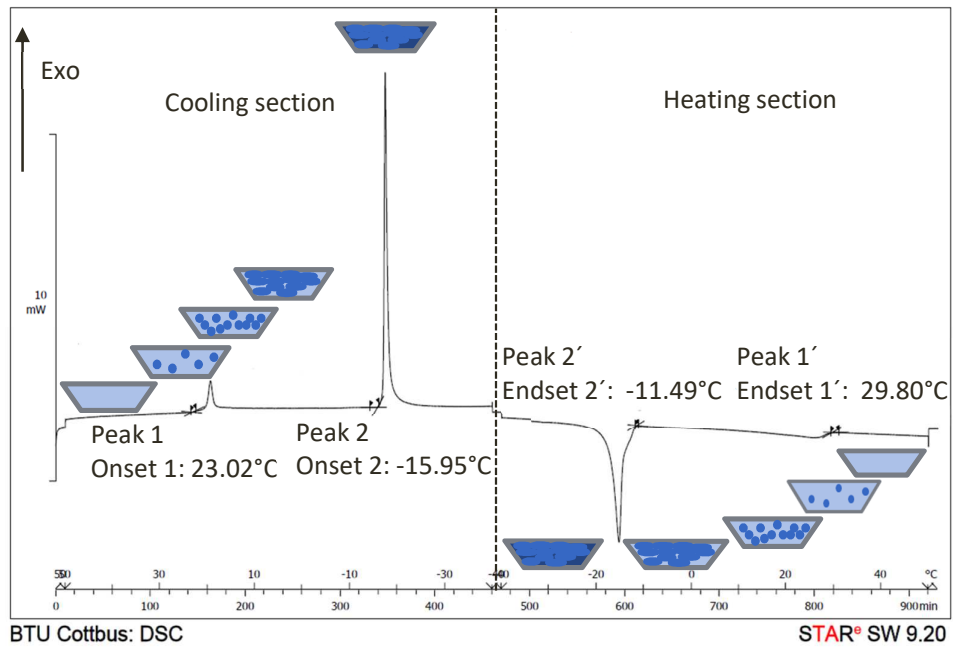


**FIGURE 5-4: ENTHALPY VS. TEMPERATURE OF PUFA IN THE DSC [50°C TO -20°C TO 50°C AT 0.2 K/MIN] WITH INTERPRETATION OF WHAT HAPPENS IN A CRUCIBLE**

It is to be noted and underlined that the liquidus point, here, represents the end of the melting process temperature above which absolutely no traces of crystal phase can be found.

### 5.2.2. Differential Scanning Calorimeter – Thermal analysis

Figure 5-5 shows examples of a saturated (a. Stearic, C18:0) and an unsaturated fatty acid (b. Linoleic, C18:2). The results of the thermal analyses of the five main fatty acids in their pure forms have been presented in Table 5-3 and the rest of the thermograms in the Appendix in Section 1.1.

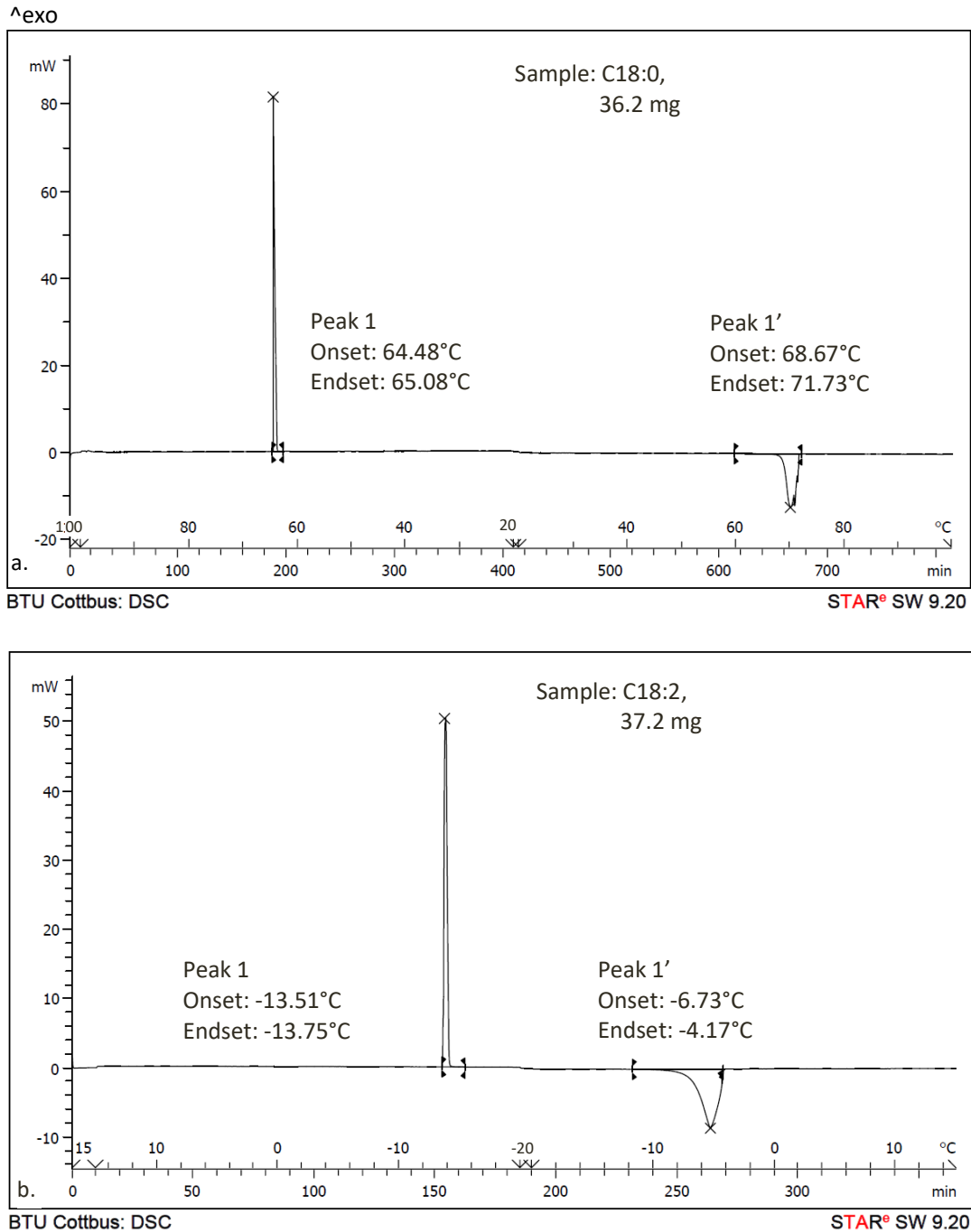


FIGURE 5-5: THERMOGRAMS OF PURE A. STEARIC AND B. LINOLEIC ACID ANALYZED BY THE DSC AND STAR<sup>E</sup> SOFTWARE

Poly-unsaturated Fatty Acid Mixture (PUFA)	Molecular weight <sup>36,151</sup>	Boiling point [°C] <sup>35,36,151-153</sup> at 10 mm Hg	Liquidus point [°C]	Crystallization point [°C]
Palmitic acid C16:0	256.42	212	62.58	60.04
Stearic acid C18:0	284.47	227	71.73	64.48
Oleic acid C18:1	282.45	223	14.16	4.79
Linoleic acid C18:2	280.44	224	-4.17	-13.51
Linolenic acid C18:3	278.4	225	-10.44	-15.96

**TABLE 5-3: BOILING AND LIQUIDUS POINTS OF THE FIVE MAIN FATTY ACIDS IN VEGETABLE OILS<sup>4</sup>**

The endset of the melting peak in Figure 5-5, which is the last sign of any endothermic reaction representing the SLE/liquidus point of the sample. Completely pure samples ideally should have identical SLE and melting points.<sup>4</sup>

### 5.2.3. Differential Scanning Calorimeter – Visual analysis (Microscopy)

Significant positions in the thermogram have been numbered and the corresponding pictures have been illustrated in Figure 5-6. Position 0 is when the sample is tempered well above the SLE temperature (50°C in most cases) such that it is completely liquid before the start of DSC experiment. Position 1 clearly depicts start of nucleation, whereas peak 2 represents solidification.<sup>4</sup>

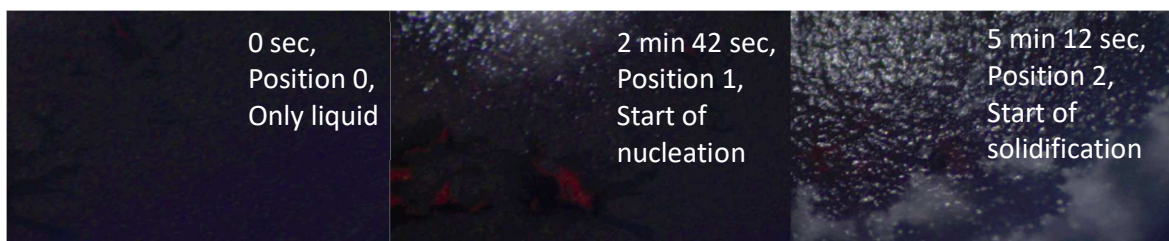
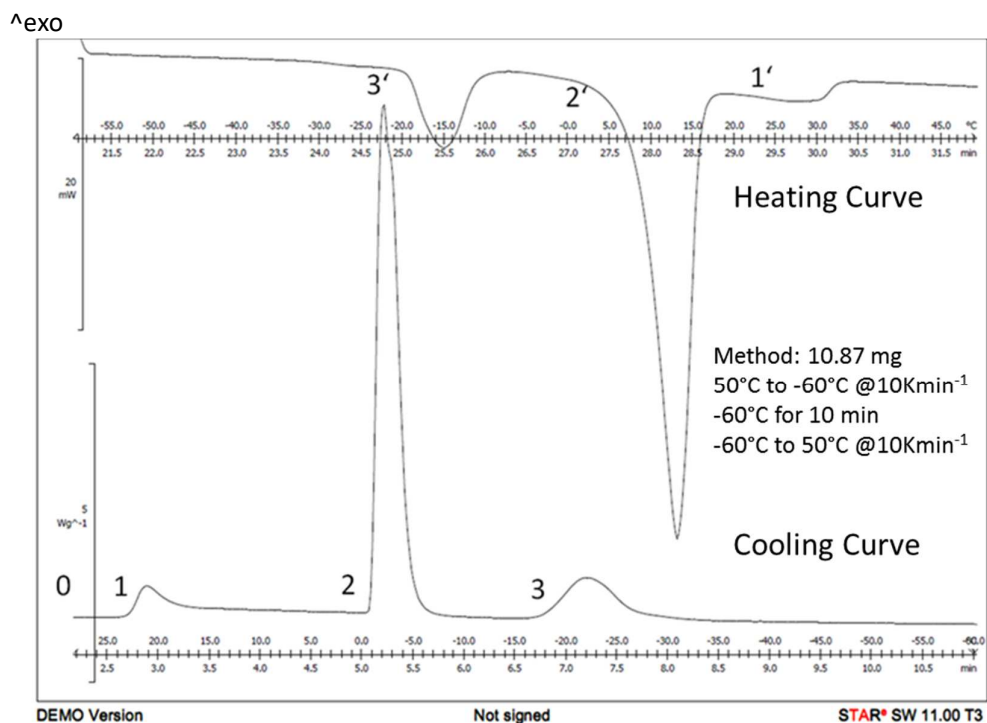


FIGURE 5-6: ENTHALPY VS. TEMPERATURE OF A CRYSTAL FRACTION OF AN HIGH OLEIC SUNFLOWER OIL BASED PUFA MIXTURE IN THE DSC [50 °C TO -60 °C TO 50 °C AT 10 K/MIN] WITH PICTORIAL REPRESENTATION OF CHARACTERISTIC STAGES IN THE COOLING CURVE<sup>4</sup>

The significance of position 3 was not investigated in detail as it is of little interest for industrial fractionation processes for separation of saturated and unsaturated mixtures. Although, as known from literature, oleic acid exhibits polymorphism.<sup>154</sup> Oleic acid transforms reversibly from  $\alpha$ - to  $\gamma$ - form on cooling and vice versa on heating. This characteristic is



observed for the high oleic PUFA fraction as shown in Figure 5-6 as a third peak (point 3). Kobayashi et. al. investigates with the help of Raman spectroscopy that the  $\alpha$ - form melts at 13.3°C when present in pure form.<sup>154</sup>

	Black oxidized copper crucible	Silver aluminum crucible
	2 min 36 sec Spontaneous nucleation	2 min 36 sec No change
	2 min 48 sec Increase in number of crystals	2 min 48 sec Spontaneous nucleation with lot of crystals
	5 min 12 sec Solidification of mother liquor	5 min 12 sec Solidification of mother liquor
	6 min 54 sec Solid transition	7 min 0 sec Solid transition
	10 min 0 sec No further change	10 min 0 sec No further change

TABLE 5-4: COMPARISON OF BLACK OXIDIZED COPPER AND SILVER ALUMINUM CRUCIBLES (WHITE LIGHT ON TOP LEFT CORNER OF EACH PICTURE IS THE REFLECTION OF THE INCIDENT LIGHT FROM MICROSCOPE)

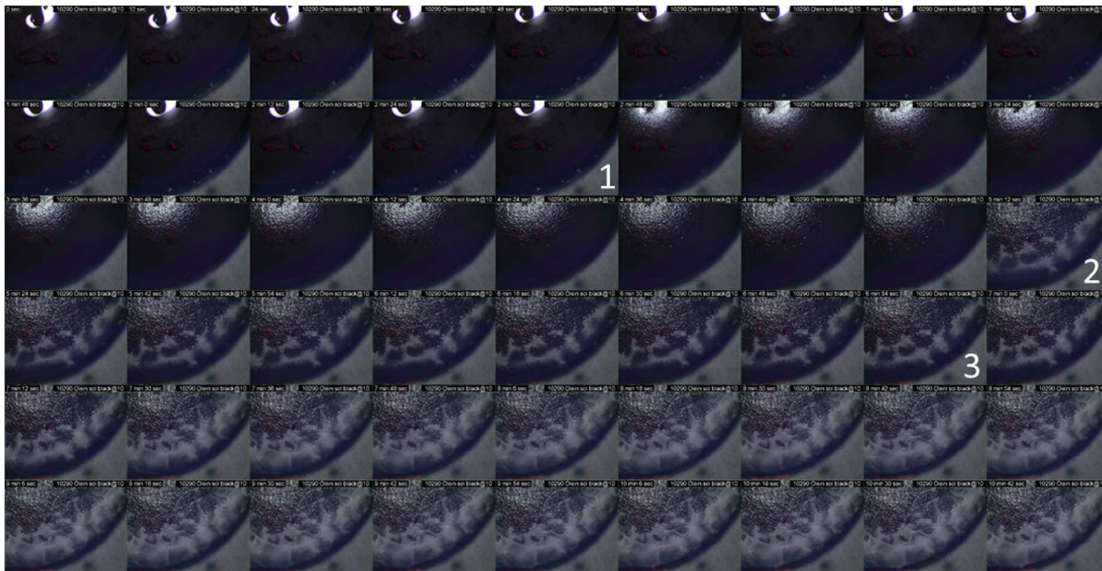


FIGURE 5-7: PHASE BEHAVIOR OF ENRICHED CRYSTAL FRACTION OF HIGH OLEIC SUNFLOWER OIL @ 10KMIN-1 COOLING RATE FROM 50°C TO - 60°C; 1. ONSET OF SPONTANEOUS NUCLEATION - 1 IN FIGURE 5-6, ONSET OF SOLIDIFICATION - 2 IN FIGURE 5-6, ONSET OF THIRD EXOTHERMIC PEAK - 3 IN FIGURE 5-6 (WHITE LIGHT IN TOP LEFT CORNER OF EACH PICTURE IS THE REFLECTION OF THE INCIDENT LIGHT FROM MICROSCOPE)

In accordance to theory, there is a time lag between the DSC peaks and their corresponding pictures of about few seconds. This is also a direct proof that the DSC realizes the change in enthalpy earlier, thereby detecting the transition prior to the light microscope. A photo series illustrating the phase behavior of the sample every 12 seconds is given in Figure 5-7. A more detailed view of the sample is given in the Appendix in Figure 1-2 and Figure 1-3. A comparison between the aluminum crucible and the oxidized copper crucible was also done to prevent misinterpretation due to any unforeseen discrepancy or reaction. A pictorial comparison of the contrast levels between the crystals and the backgrounds of the aluminum crucible and the black oxidized copper crucible was also done to establish the motivation behind the oxidization process. This has been tabulated in Table 5-4. An influence of the microscope fiber light on the crystal formation was not tested as nucleation or induction times were not measured by means of the DSC.

### 5.2.4. Flash Differential Scanning Calorimeter

Figure 5-8 gives a comprehensive illustration of the characteristics of an enriched crystal fraction of high oleic sunflower oil PUFA when subjected to flash cooling. These investigations were primarily done to check whether very high cooling rates had an effect on the spontaneous nucleation temperatures of the PUFA mixture. Cooling rates between  $-10$  to  $-200 \text{ K s}^{-1}$  were applied to the sample in the Flash DSC.

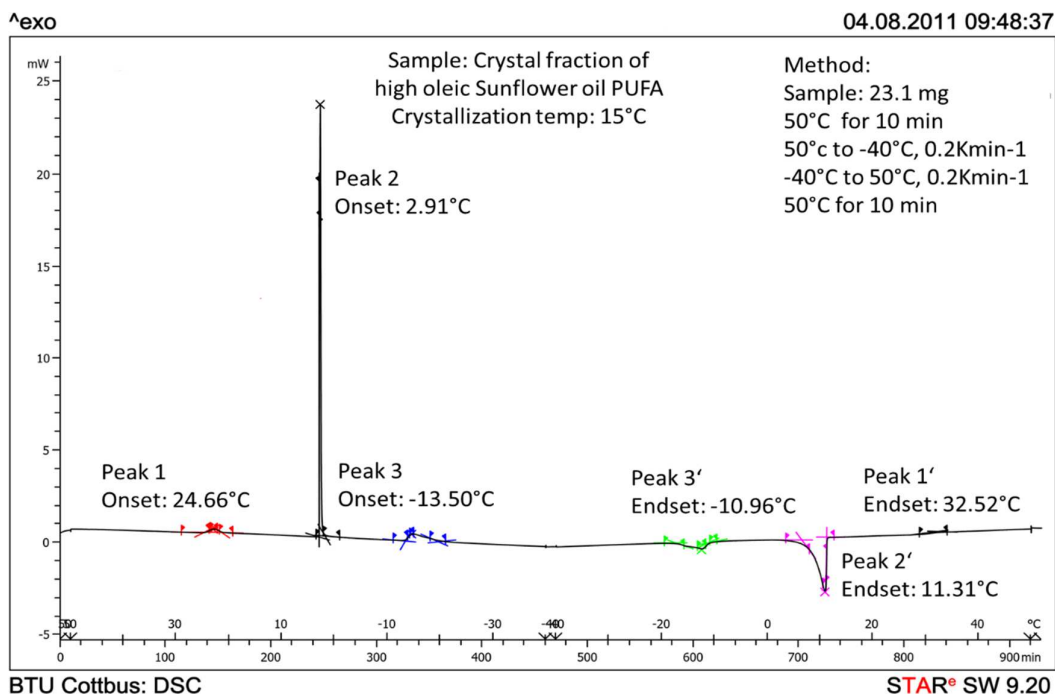
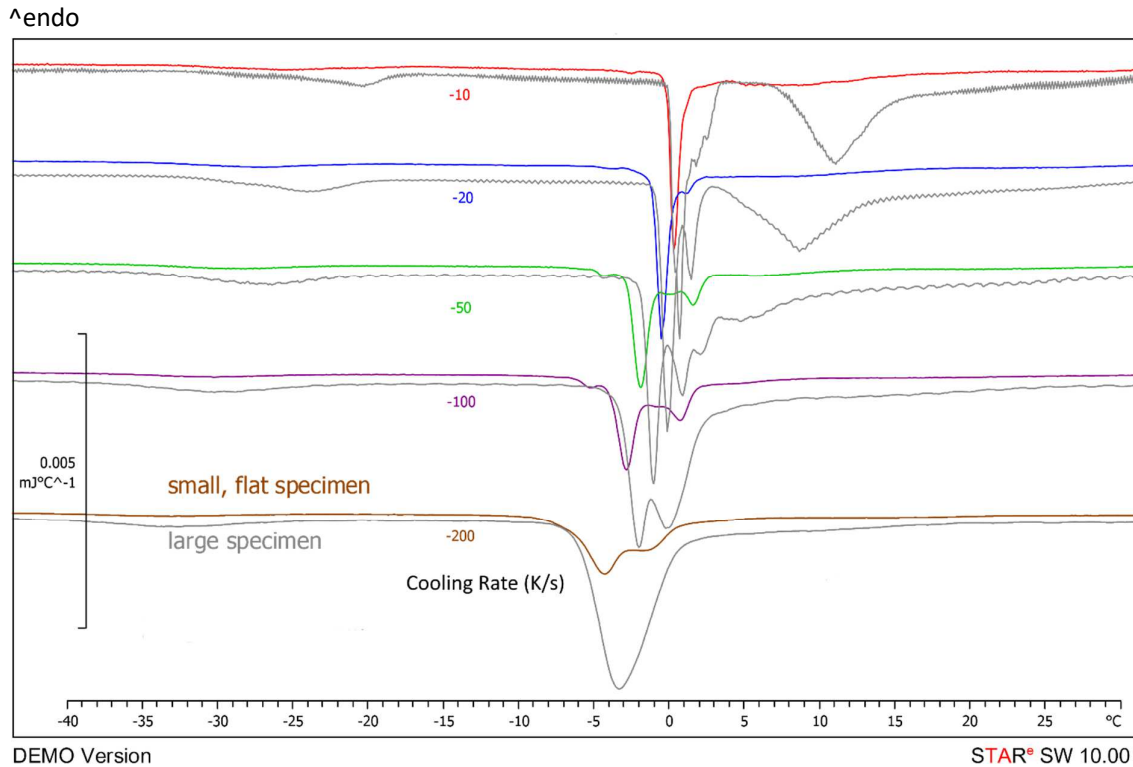


FIGURE 5-8: DSC THERMOGRAM OF A CRYSTAL FRACTION OF A HIGH OLEIC SUNFLOWER OIL BASED PUFA MIXTURE (FRACTIONATION TEMPERATURE 15°C)

Higher cooling rates, give lesser time for the molecules to find one another, thereby increasing the induction time which in turn pushes the metastable zone further down the temperature scale.<sup>10</sup> The technical aspect to furthering the metastable zone to lower crystallization temperatures would mean purer unsaturated fractions but such is only possible in microscale reactors and would also endure technical and economical obstacles.

Figure 5-9 depicts the cooling of two specimens, large and small, cooled at rates ranging from  $10 \text{ K s}^{-1}$  to  $200 \text{ K s}^{-1}$  so as illustrate the number and quality of phenomena detected in a fixed temperature range of  $-40^\circ\text{C}$  to  $30^\circ\text{C}$ . As can be noted, the larger specimen at lower cooling rates could detect three peaks instead of an overlapping double peak in the lesser volume specimen with high cooling rates (for example:  $200 \text{ K s}^{-1}$ ).



**FIGURE 5-9: COOLING OF AN ENRICHED CRYSTAL FRACTION OF A LARGE AND SMALL SPECIMEN OF HIGH OLEIC SUNFLOWER OIL BASED PUFA MIXTURE IN THE FLASH DSC (FRACTIONATION TEMPERATURE 15°C)<sup>++++</sup>**

The latter shows that while smaller flat film specimen might deliver more accurate results owing to better heat transfer rates, the specimen with the larger volume clearly depicts all the phenomena. It clearly shows each of the three peaks that is inherent to this high oleic PUFA fraction as shown in Figure 5-8 with a much slower cooling rate and also large volume. Hence, in spite of differences in actual temperatures, maybe it is in the interest of the investigator to use larger samples to clarify and understand the trends and phenomena better. Therefore, adhering to the inference drawn here, larger specimens with lower cooling rates were taken to investigate the effects and construct the SLE diagrams at lower saturated concentrations, later in this work. It clearly also suggested that higher flash cooling rates pushed the temperature of spontaneous nucleation towards lower temperatures which is in accordance to theory.<sup>10</sup>

<sup>++++</sup> Acknowledgement to Dr. Rudolph Riesen at the Materials Characterization Market Support Lab of Mettler Toledo Analytical in Schwerzenbach, Switzerland for his help with the experiments.

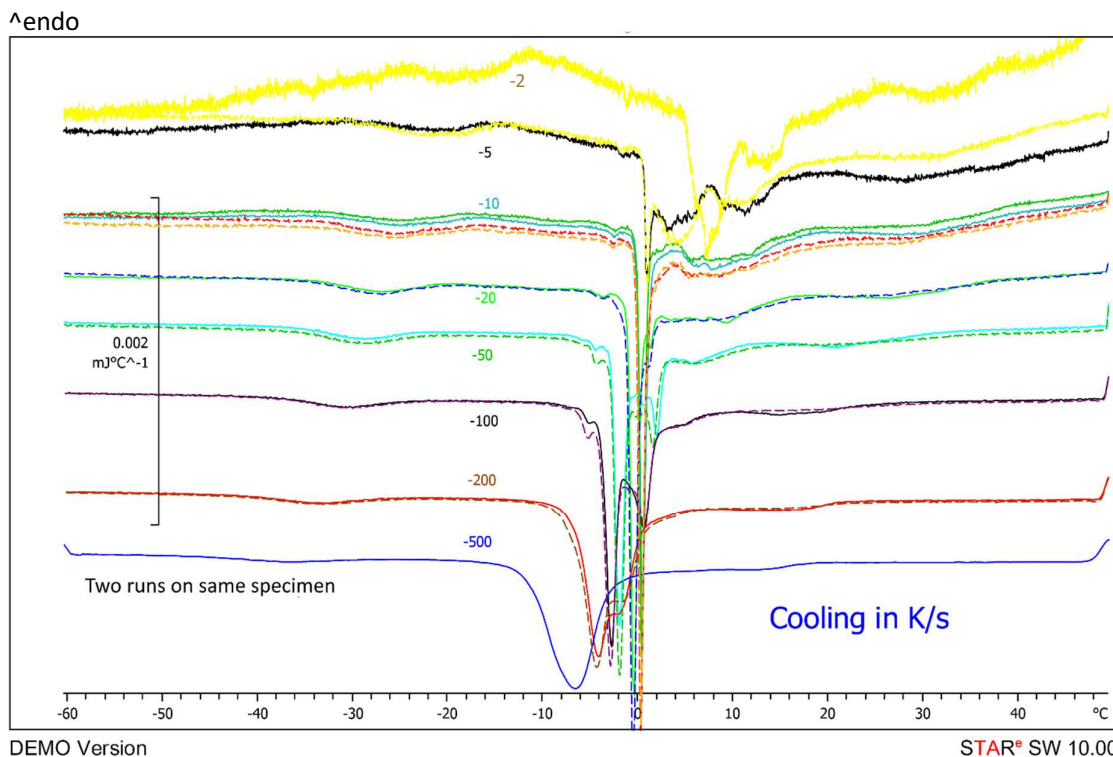


**FIGURE 5-10: VALIDATION OF REPRODUCIBILITY DURING COOLING OF AN ENRICHED CRYSTAL FRACTION OF HIGH OLEIC SUNFLOWER OIL BASED PUFA MIXTURE IN THE FLASH DSC (FRACTIONATION TEMPERATURE 15°C)\*\*\*\*\***

Figure 5-10 validates the reproducibility of the flash DSC even at cooling rates of 200 Ks<sup>-1</sup>. All cooling rates with the same specimen were repeated twice. The dashed lines represent the repeated experiments. Figure 5-11 illustrates the heating curves at 100 Ks<sup>-1</sup> of the small specimen post being subjected to various cooling rates as in Figure 5-10. The latter shows that the SLE point remains around 32°C with a slight shift towards higher temperatures with rapidly increasing cooling rates again in accordance to literature. It can be also noted from Figure 5-11 that melting peak of the saturated crystal phase becomes flatter and less detectible as the cooling rate increases, making it more and more difficult to analyze the SLE point. All these experiments from Figure 5-9 to Figure 5-11 were conducted at the Materials Characterization Market Support Lab of Mettler Toledo Analytical in Schwerzenbach, Switzerland.

\*\*\*\*\* Acknowledgement to Dr. Rudolph Riesen at the Materials Characterization Market Support Lab of Mettler Toledo Analytical in Schwerzenbach, Switzerland for his help with the experiments.

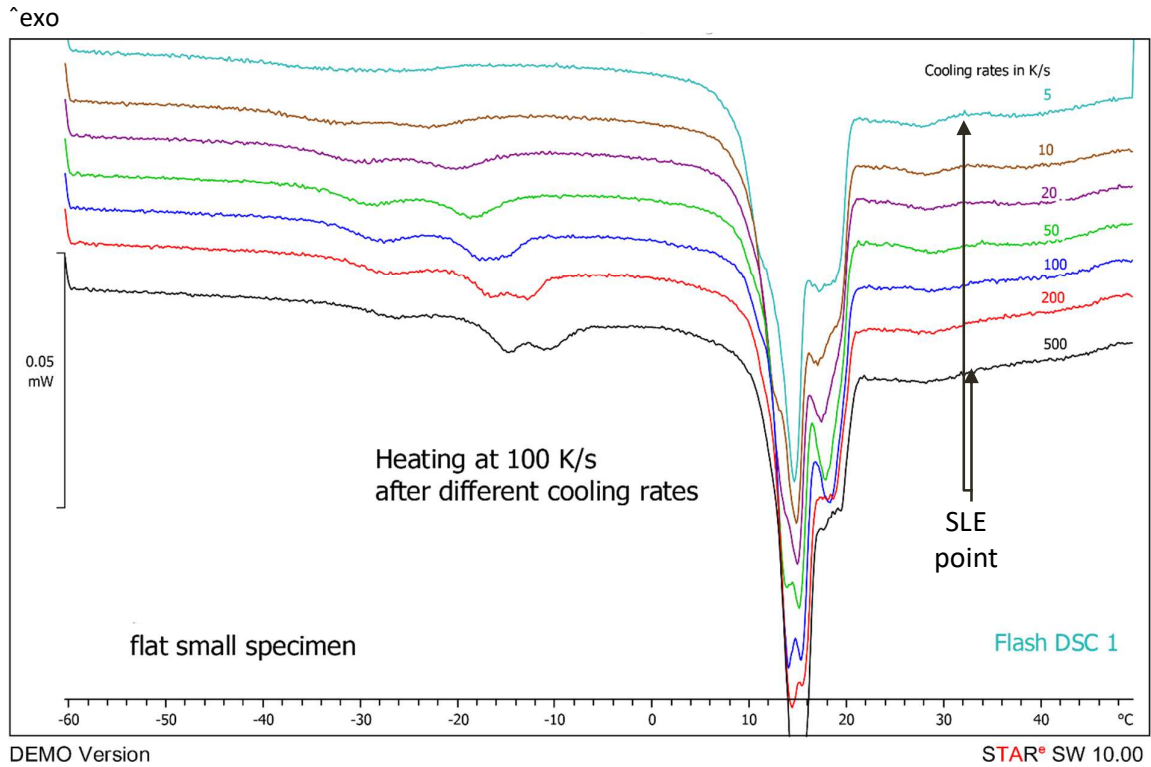


FIGURE 5-11: HEATING OF AN ENRICHED CRYSTAL FRACTION OF HIGH OLEIC SUNFLOWER OIL BASED PUFA MIXTURE IN THE FLASH DSC (FRACTIONATION TEMPERATURE 15°C)§§§§§

§§§§§ Acknowledgement to Dr. Rudolph Riesen at the Materials Characterization Market Support Lab of Mettler Toledo Analytical in Schwerzenbach, Switzerland for his help with the experiments.

### 5.2.5. Chemical analysis of the samples

To characterize the products, they were analyzed by means of the GC-FID method which shows five main peaks. The chemical names and formula of the five main components of the vegetable oil based PUFA mixtures investigated are tabulated in Table 5-5.

Poly-unsaturated Fatty Acid Mixture (PUFA)	Chemical formula	Chemical name	Short form
Palmitic acid	$H_3C-(CH_2)_{14}-COOH$	Hexadecanoic acid	C16:0
Stearic acid	$H_3C-(CH_2)_{16}-COOH$	Octadecanoic acid	C18:0
Oleic acid	$H_3C-(CH_2)_7-(CH)_2-(CH_2)_7-COOH$	cis-9-Octadecenoic acid	C18:1
Linoleic acid	$H_3C-(CH_2)_4-(CH)_2-CH_2-(CH)_2-(CH_2)_7-COOH$	9,12 Octadecadienoic Acid	C18:2
Linolenic acid	$H_3C-CH_2-(CH)_2-CH_2-(CH)_2-CH_2-(CH)_2-(CH_2)_7-COOH$	9,12,15 Octadecatrienoic acid	C18:3

TABLE 5-5: CHEMICAL NAMES AND ABBREVIATIONS OF THE FIVE MAIN COMPONENTS OF THE PUFA MIXTURES INVESTIGATED \*\*\*\*\*

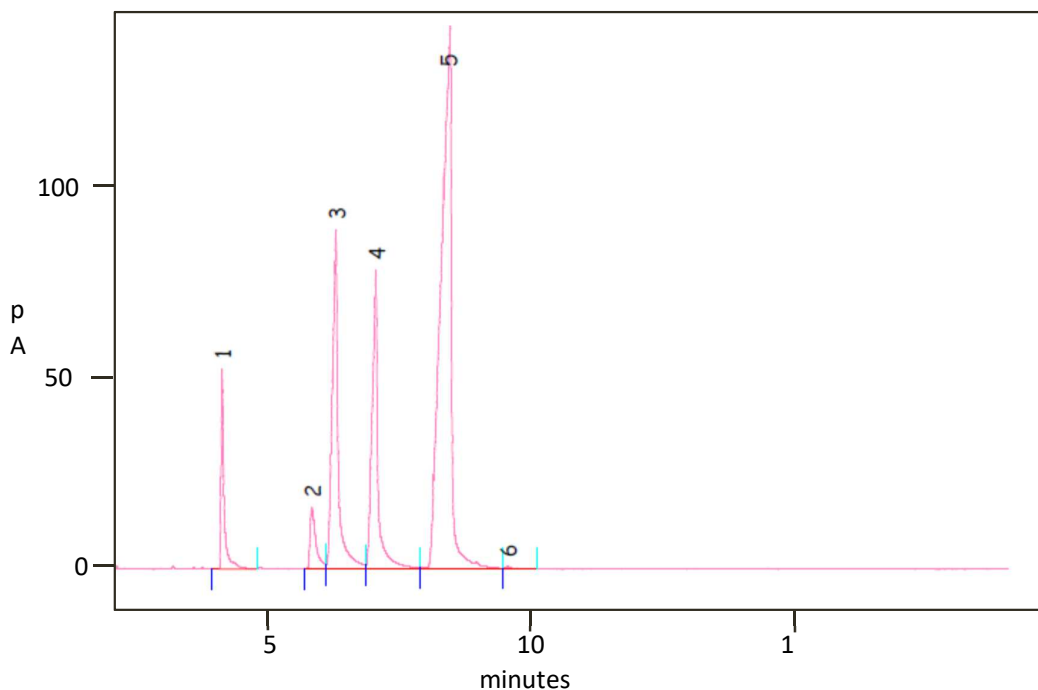


FIGURE 5-12: GAS CHROMATOGRAM OF THE LINSEED OIL BASED FATTY ACID MIXTURE MEASURED WITH GC PARAMETER CONDITIONS OF 190°C (ISOTHERMAL), 0.2 µL INJECTION VOLUME AND 150 KPA

\*\*\*\*\* All data has been taken from the official website of PubChem, National Institute of Health, U.S. Department of Health & Human Services<sup>32-36</sup>



	Palmitic acid	Stearic acid	Oleic acid	Linoleic acid	Linolenic acid
	C16:0 (Peak 1)	C18:0 (Peak 2)	C18:1 (Peak 3)	C18:2 (Peak 4)	C18:3 (Peak 5)
Content	5.4%	3.8%	19.2%	16.3%	54.6%
Liquidus point	63.5°C	69.66°C	12.7°C	-6.71°C	-16.7°C

**TABLE 5-6: GAS CHROMATOGRAPHIC ANALYSIS AND THE SLE POINTS<sup>24</sup> OF INDIVIDUAL FATTY ACIDS OF THE USED LINSEED OIL BASED FATTY ACID MIXTURE IN FIGURE 5-10**

Figure 5-12 is a chromatogram which illustrates the five main components of the high linolenic linseed PUFA mixture. Each of them belongs to one of the fatty acid methyl esters which represent the main fatty acids in the mixture. The results of the chromatogram is tabulated in Table 5-6. Standard samples were used and run every time before an analysis to determine the elution order of the fatty acids. The liquidus points (taken from DSC) of the pure fatty acids are a bit higher than the usual melting points as they represent the end of the melting peak when reheated, which is the true liquidus point. The five main components present in the PUFA mixtures investigated have been listed in Table 5-7 again so as to highlight the variety in the unsaturated compositions.

Poly-unsaturated Fatty Acid Mixture (PUFA)	Palmitic acid C16:0 [%]	Stearic acid C18:0 [%]	Oleic acid C18:1 [%]	Linoleic acid C18:2 [%]	Linolenic acid C18:3 [%]
High linoleic Sunflower oil based PUFA	7.4	4.2	28.3	59.7	0.09
High linoleic Soya oil based PUFA	10.6	3.9	25.0	52.1	6.4
High oleic Sunflower oil based PUFA	3.5	3.0	85.4	6.7	0.1
High oleic Palm oil based PUFA	3.2	8.5	76.8	9.7	0.6
High linolenic Linseed Oil based PUFA	5.4	3.5	21.3	15.6	53.3

**TABLE 5-7: COMPOSITIONS OF THE DIFFERENT PUFA MIXTURES OBTAINED FROM NATURALLY OCCURRING PLANT OILS<sup>4</sup>**



### 5.2.6. Phase diagrams at low saturated content including metastable ranges

Liquid solid equilibrium curves, at low saturated fatty acid concentration ranges, of fatty acid mixtures obtained from **high linoleic and high oleic sunflower, high linoleic soya and high linolenic linseed oil** have been depicted in the following figures. The liquid solid phase diagram of the high linoleic sunflower oil based PUFA mixture has been illustrated in Figure 5-13. The equilibrium behavior at lower concentrations of saturated content with respect to that of stearic acid has been investigated here as it is of highest technical relevance for separation by crystallization.

In Figure 5-13, it can be observed that the metastable range of the liquidus curve intersects with the solidus curve at a stearic acid concentration of less than 1%. An exact observation clarifies that it is possible to separate at least until 0.63% stearic acid without entering the metastable range of the solidus curve.<sup>4</sup>

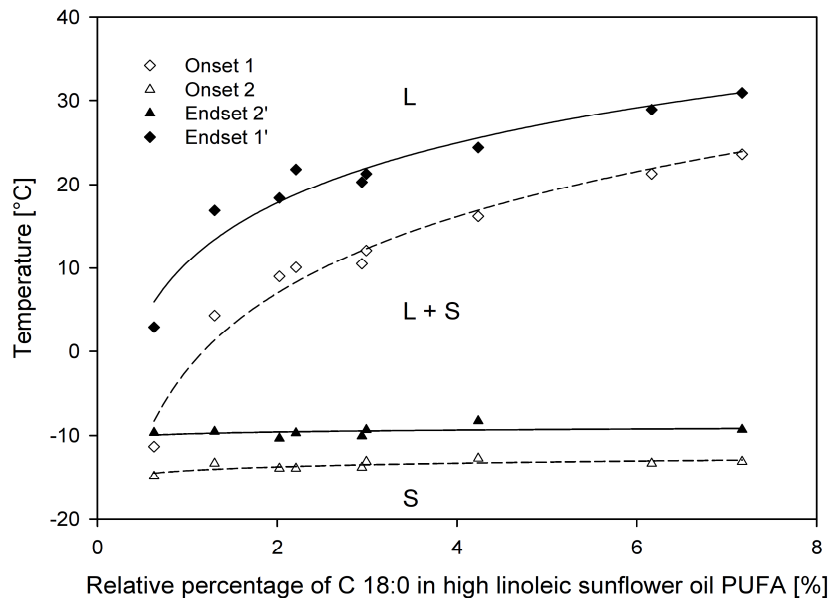


FIGURE 5-13: LIQUID SOLID EQUILIBRIUM DATA OF STEARIC ACID IN HIGH LINOLEIC SUNFLOWER OIL BASED PUFA MIXTURE<sup>4</sup>

Similar separation of the metastable ranges of the liquidus and solidus curves is noted for the PUFA mixture from soya oil in Figure 5-14. The supersaturated metastable ranges are separated by at least 11K even at a low stearic composition of 1.2% (enriched unsaturated mixture) whereas in Figure 5-13 by 13.8K at a stearic acid composition of 1.3%. This

observation clarifies that the crystallization behavior of these natural plant oil based PUFAs largely depend on their original composition. Soya oil and the high linoleic sunflower oil based PUFAs are similar in composition, both having between 50-60% linoleic acid. Similar investigations on PUFAs with other compositions resulted in quite different crystallization behaviors.<sup>4</sup>

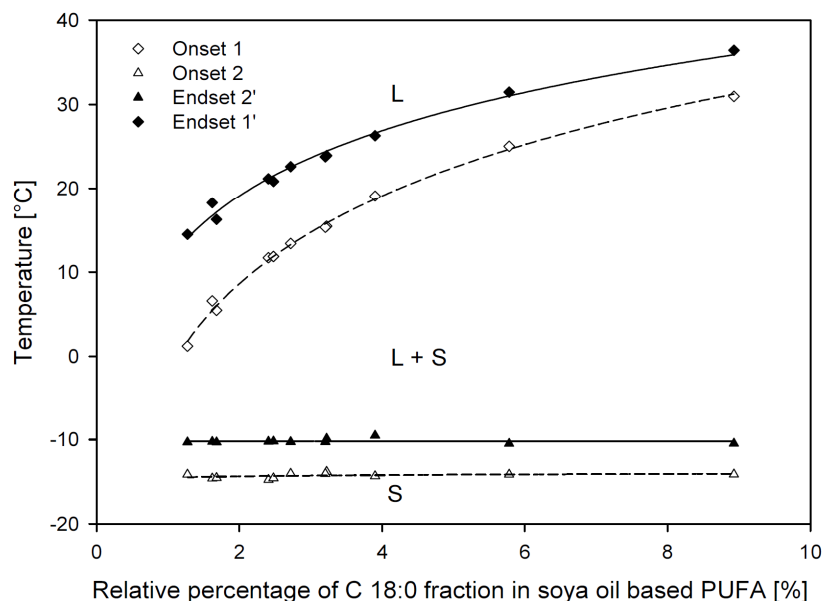


FIGURE 5-14: LIQUID SOLID EQUILIBRIUM DATA OF STEARIC ACID IN HIGH LINOLEIC SOYA OIL BASED PUFA MIXTURE<sup>4</sup>

The high oleic PUFA mixture is a challenging mixture and is more difficult to deal with. Figure 5-15 represents the thermal behavior of the high oleic PUFA mixture. A larger sample volume was taken to explicitly detect each of the phenomena associated with this mixture. It can be clearly seen that this mixture when characterized thermally depicts three endothermic and exothermic peaks each. Hence there are three exothermic peak onsets and endothermic peak endsets in this case. This PUFA mixture is particularly different from the other three mixtures mainly by its high content of oleic acid, C18:1. During experiments it was also noted that the crystals formed were very fine compared to the ones in other mixtures. Peak 1 represents the spontaneous nucleation and crystallization of saturated fraction, whereas peak 2 represents crystallization of the rest enriched unsaturated fractions (**Eutectic mixture**).<sup>155</sup> Peak 3 represents the solid phase transformation of the enriched oleic acid fraction from  $\alpha$ - to  $\gamma$ -form.<sup>154,156</sup> On the other hand, peak 1' represents the melting of saturated fraction, whereas 2' and 3' the melting and transformations of the enriched unsaturated fractions.<sup>4</sup>

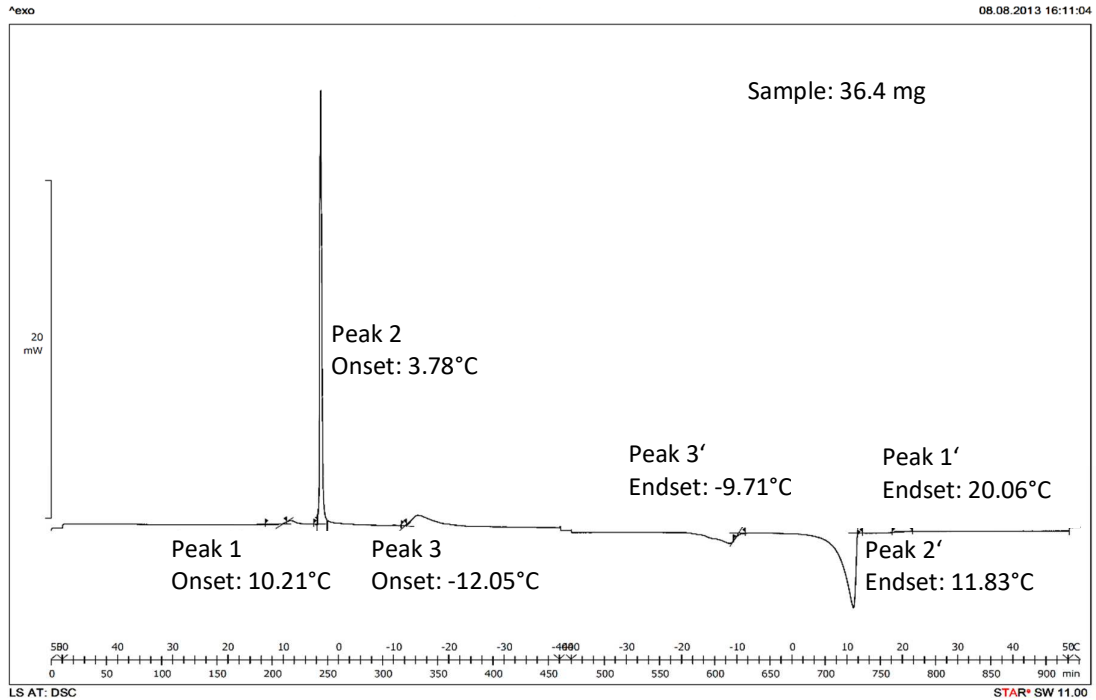


FIGURE 5-15: ENTHALPY VS. TEMPERATURE OF HIGH OLEIC SUNFLOWER OIL PUFA MIXTURE IN THE DSC [50 °C TO -40 °C TO 50 °C AT 0.2 K/MIN]<sup>4</sup>

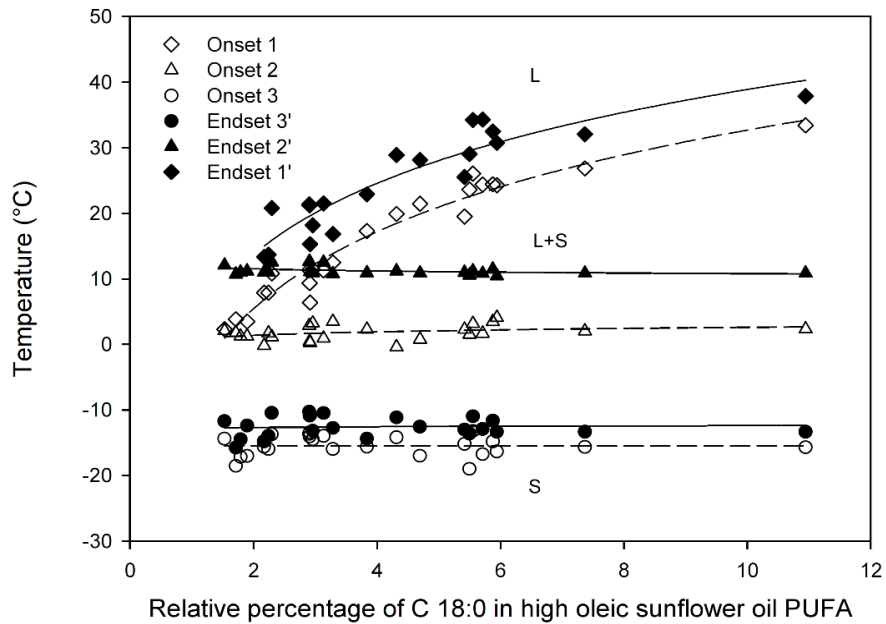


FIGURE 5-16: LIQUID SOLID EQUILIBRIUM DATA OF STEARIC ACID IN HIGH OLEIC SUNFLOWER OIL BASED PUFA MIXTURE<sup>4</sup>

The liquid solid equilibrium curve for the high oleic mixture at low saturated fatty acid concentration range is depicted in Figure 5-16. In case of this mixture, the metastable range of the liquidus intersects with the solidus curve already at a stearic acid composition of 3%.

That basically means that the degree of supercooling required for the onset of spontaneous nucleation, thereby crystallization is already within the solidification range. This clearly shows that it is much more difficult to separate the saturated fraction from the high oleic PUFA in comparison to the other mixtures. It was possible to crystallize further and get fractions with a stearic acid content of 1.53 % but the endothermic peak representing the start of the liquidus range disappeared from the thermogram. It is supposed that this endothermic peak overlaps with the second one and hence is not visible.<sup>4</sup>

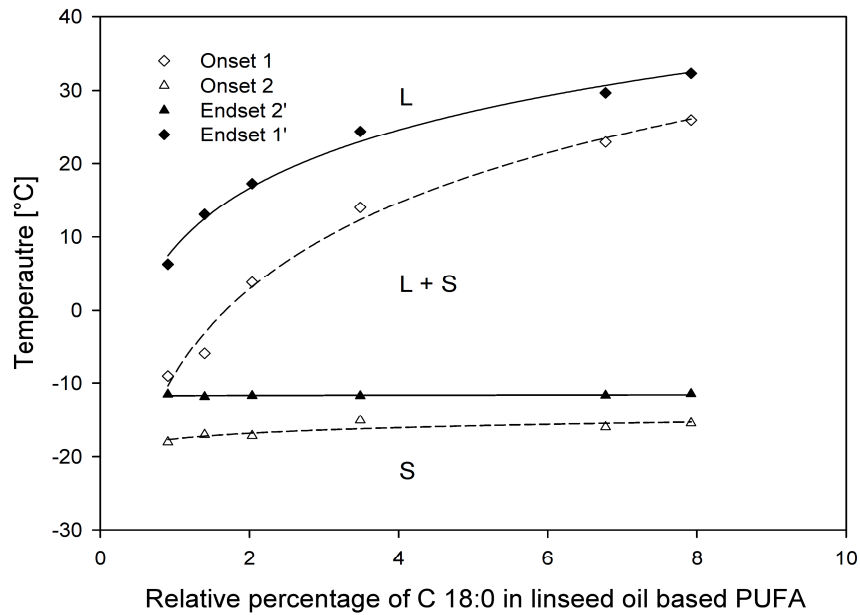


FIGURE 5-17: LIQUID SOLID EQUILIBRIUM DATA OF STEARIC ACID IN HIGH LINOLENIC LINSEED OIL BASED PUFA MIXTURE<sup>4</sup>

To obtain a better perspective, the phase behavior of a high linolenic fatty acid mixture based on linseed oil was also investigated (Figure 5-17). The latter also exhibited results similar to that of the high linoleic sunflower oil, showing no intersection of metastable ranges till 0.9% stearic acid. Crystal fraction yields and compositions of separated mother liquor in the case of linseed oil based PUFA have been further discussed in Section 5.1.<sup>11,18</sup> A high oleic palm kernel oil sample was also investigated in a similar manner. Details are available in the Appendix.<sup>4,157</sup>

### 5.2.7. Modelling of the liquidus and solidus curves for all PUFA mixtures at low saturated concentrations

A single simple logarithmic function (Equation 5-1) was found to fit both all the liquidus curves for each of the concerned vegetable oil based PUFA mixtures with very good regression factors. In other words, the SLE temperature is a function of the composition of the PUFA mixture but of a unique origin (specific vegetable oil based PUFA mixture) and is satisfied by

$$SLE \text{ temperature, } y = y_0 + \ln(ax)$$

EQUATION 5-1

wherein, x is the amount of C 18:0 present in the PUFA.

Equilibrium curves	Regression equation	PUFA origin	Coefficient		No of iterations required for convergence (total 200)	R <sup>2</sup>
			y <sub>0</sub>	a		
Liquidus line	$y = y_0 + \ln(ax)$	High oleic Sunflower oil	2.91	15.63	9	0.85
		High linoleic Sunflower oil	10.7	10.28	8	0.93
		High linolenic Linseed oil	8.61	11.54	1	1.0
		High linoleic Soya oil	11.33	11.21	9	0.99
		High oleic Palm kernel oil	4.76	14.76	9	0.97
Solidus line, Eutectic temperature	$y = y_0$	High oleic Sunflower oil	11.84			
		High linoleic Sunflower oil	-9.78			
		High linolenic Linseed oil	-11.71			
		High linoleic Soya oil	-10.17			
		High oleic Palm kernel oil	10.21			

TABLE 5-8: LIQUIDUS AND SOLIDUS CURVES AT LOW SATURATED CONCENTRATIONS FOR PUFA MIXTURES

A  $R^2 \rightarrow 1$  for the liquidus temperature curves indicated that the fitted model is in good agreement with the actual values. On the other hand, owing to the linearity of the curves in

the case of the solidus temperature, the intercept,  $y_0$ , which basically represents the solidus point of the mixture, is very much dependent on the composition of the PUFAs which can be seen in the graph in Figure 5-19. The solidus line is a result of the eutectic behavior of all the PUFA systems.<sup>155</sup>

### 5.2.8. Dependency of liquidus and solidus curves on mono-unsaturated acid fraction in mixture

It can be seen that there is a definite dependency on the composition of the PUFAs when it comes to the temperatures range in which the crystallization occurs. These have been illustrated in Figure 5-18 and Figure 5-19.

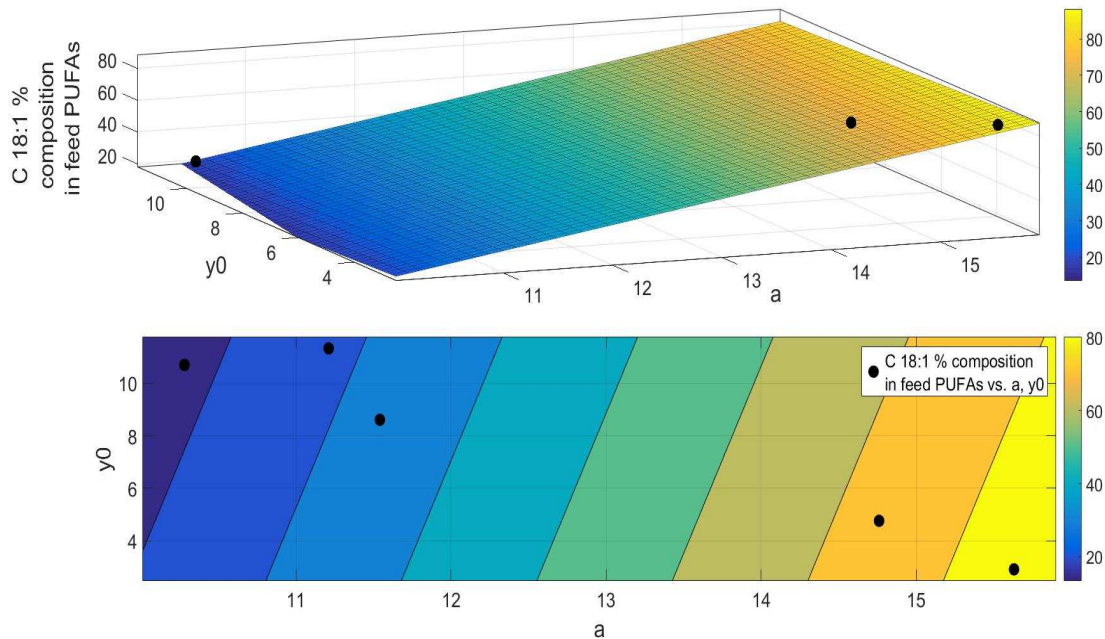


**FIGURE 5-18: DEPENDENCY OF PARAMETERS Y0 AND A OF LIQUIDUS CURVE FIT ON THE C18:1 FRACTION PRESENT IN VEGETABLE OIL BASED PUFA MIXTURES ALONG WITH THE CONTOUR MAP**

Figure 5-18 is a 3D plot depicting the effects of the C18:1 fraction in the original composition of the oil PUFA mixtures on parameters ‘a’ and ‘y<sub>0</sub>’ of the liquidus line fit. It is noted that the dependency is almost linear for the high oleic and high linoleic PUFA mixtures. The effect of a high linolenic fraction in the acid is a bit different although the fraction of oleic acid is still the limiting factor. A simple linear surface fit was used to fit the data as in Equation 5-2, validating the linearity of the dependence of the coefficients on the oleic acid content of the PUFA mixtures irrespective of other content.

$$f(x, y) = p_{00} + p_{10} * x + p_{01} * y$$

**EQUATION 5-2**

As we know from the models, a 2D graph showing the dependency of the intercept , y<sub>0</sub> which is the eutectic temperature of the PUFA, on the composition is shown in Figure 5-19. The results as in Figure 5-19 and Table 5-8, show that the linoleic and linolenic acid further the

solidus point down the temperature scale, thereby lowering the point of intersection between the liquidus and solidus curves.

Coefficients	Value	95% confidence bounds	R <sup>2</sup>
p <sub>00</sub>	-91.65	(-880.3, 696.9)	0.926
p <sub>10</sub>	11.44	(-33.68,56.56)	
p <sub>01</sub>	-0.80	(-29.61,28)	

Table 5-9: COEFFICIENTS FOR THE LINEAR SURFACE FIT USED IN EQUATION FOR THE DEPENDENCY OF THE LIQUIDUS LINE FIT ON FRACTION OF MONO-UNSATURATED ACID

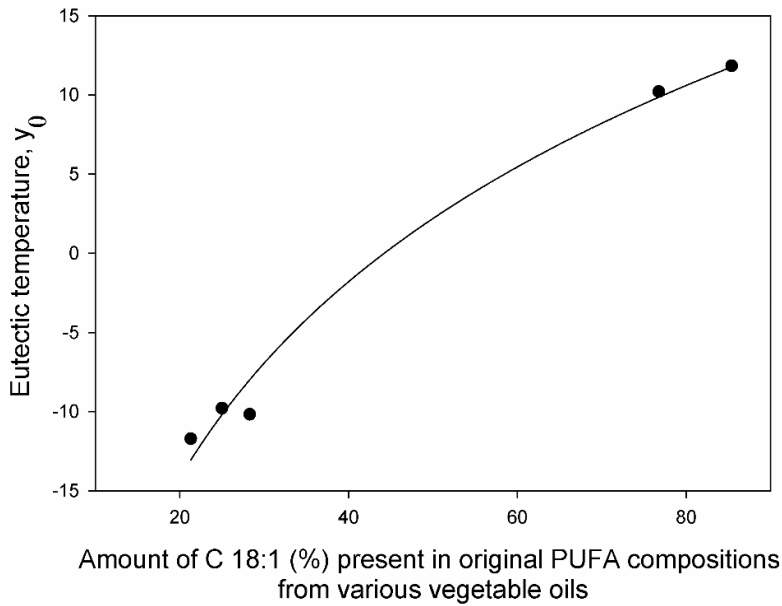


FIGURE 5-19: DEPENDENCY OF PARAMETER  $y_0$  OF SOLIDUS LINE FIT ON THE C18:1 FRACTION PRESENT IN VEGETABLE OIL BASED PUFA MIXTURES

Hence, naturally the high oleic PUFA mixtures having higher temperature intersection points between the liquidus and solidus curves limits the crystallization process thermodynamically at a higher temperature than the high linoleic and linolenic fractions. As lower temperatures are reached by the high linoleic and linolenic PUFA fractions with the unsaturated fractions still in molten state, naturally larger saturated crystals are also formed during the crystallization process.



### 5.3. Nucleation kinetics

#### 5.3.1. Effects of supercooling and cooling rate on nucleation kinetics ( $\mu$ scale)

##### 5.3.1.1. Calibration

The results of the experiments performed to calibrate the gradient tempered stage is shown in Figure 5-20. As it can be noted there is a parallel shift with increasing cooling rates. At  $2\text{Kmin}^{-1}$  the maximum deviation from the Pt 100 sensor temperature placed inside the probe is  $-0.9\text{K}$ . This is expected due to the presence of the glass object slide in between the sample and the Peltier elements of the gradient stage. To negate the effects all calibrated temperatures were used for the characterization of the data.

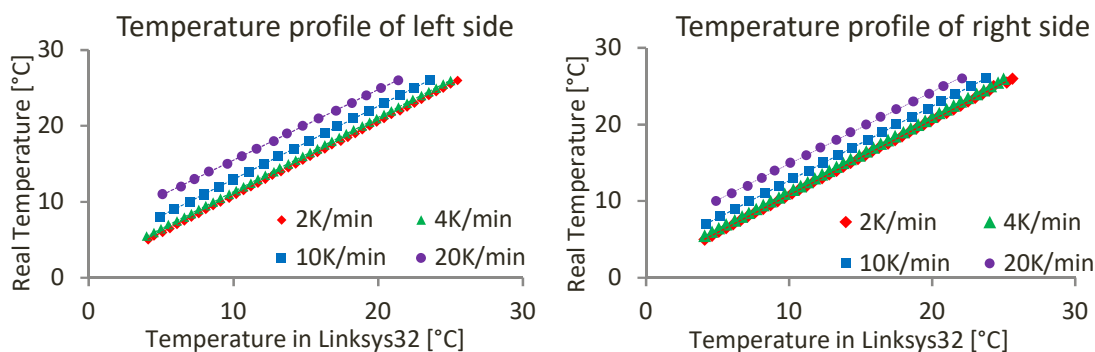


FIGURE 5-20: CALIBRATION OF THE LEFT AND RIGHT SIDES OF THE GRADIENT STAGE WITH AN ALMEMO TEMPERATURE DATA LOGGING MODULE (2890-9) AND A FLAT FOIL SENSOR (ZA 9030-FS1 NORM E4); RESOLUTION  $\pm 0.1^{\circ}\text{C}$

##### 5.3.1.2. High linoleic sunflower oil based PUFA

Induction times of crystallization in sunflower oil PUFA mixture resulting from experiments as a function of supercooling at constant cooling rates were plotted in Figure 5-22. The enthalpy vs. temperature and time graph for this mixture determined by the DSC was added here as Figure 5-21. The samples were cooled from  $50^{\circ}\text{C}$  so as to ensure entirely molten state to the crystallization temperature at a given cooling rate. The induction time measurements were done in isothermal conditions as the time zero in the calculations is the time when the sample reaches desired crystallization temperature. Therefore, the results which depict in accordance to theory that the induction time decreases with increasing amount of supercooling could be associated to specific crystallization temperatures. Of course, there are effects of dynamic supercooling that occurs once the system is cooled beyond its SLE

temperature. The period during which the system remains in this region of dynamic supercooling between the SLE point and the desired crystallization temperature varies with cooling rate as well. As soon as the system is supercooled irrespective of kinetics, it tries to reach an equilibrium composition by trying to cutback the supersaturation. This results in nucleation. In dynamic supercooling, the system is continually trying to reduce the supersaturation. These factors naturally affect and complicate induction time measurements crucially. If nucleation happened before the desired crystallization temperature was reached, the results were not taken into account. On the other hand, for the rest of the cases where there was a positive induction time post desired crystallization temperature, each induction time is always associated to a particular cooling rate and crystallization temperature so as to include the effects mentioned.<sup>24</sup>

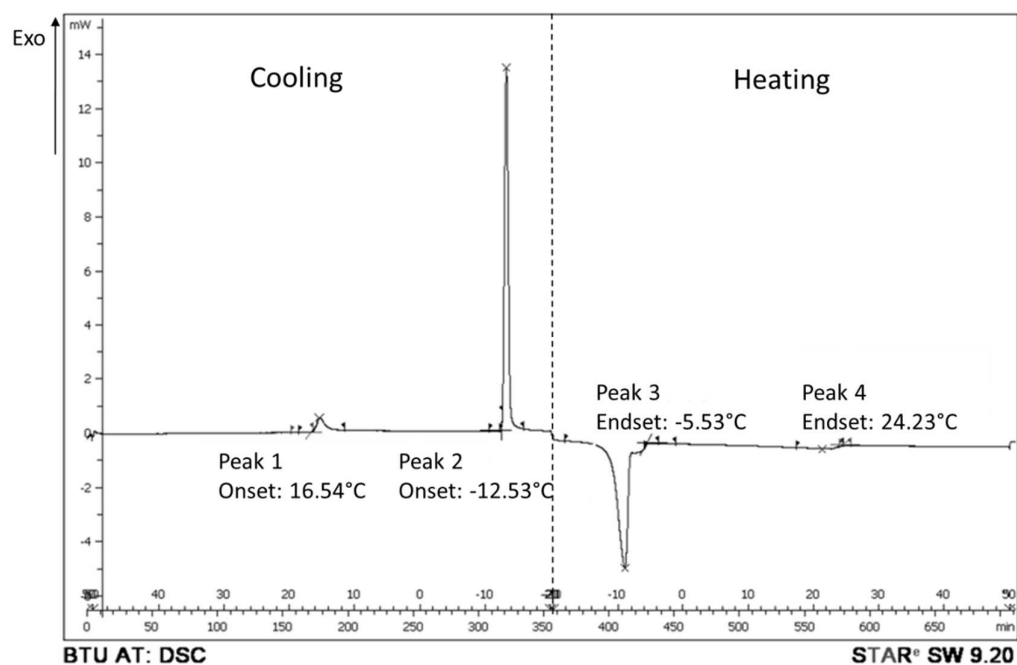


FIGURE 5-21: ENTHALPY VS. TEMPERATURE OF HIGH LINOLEIC SUNFLOWER OIL BASED PUFA MIXTURE IN DSC (50 °C TO -20 °C TO 50 °C AT 0.2KMIN<sup>-1</sup>,<sup>24</sup>

As the supercooling increases the supersaturation increases, thereby reducing induction time. The reactor geometry also enables effective heat transfer owing to its higher surface area and hence making the supercooling established in the sample in a short time. Illustrations of a micro-section of the PUFA mixture upon melt crystallization at a cooling rate of 30Kmin<sup>-1</sup> and varying supercooling has been provided in Section 3.1.3 in the Appendix. The dependence on

various cooling rates have also been shown subsequently in the previously mentioned Section 3.1.3.

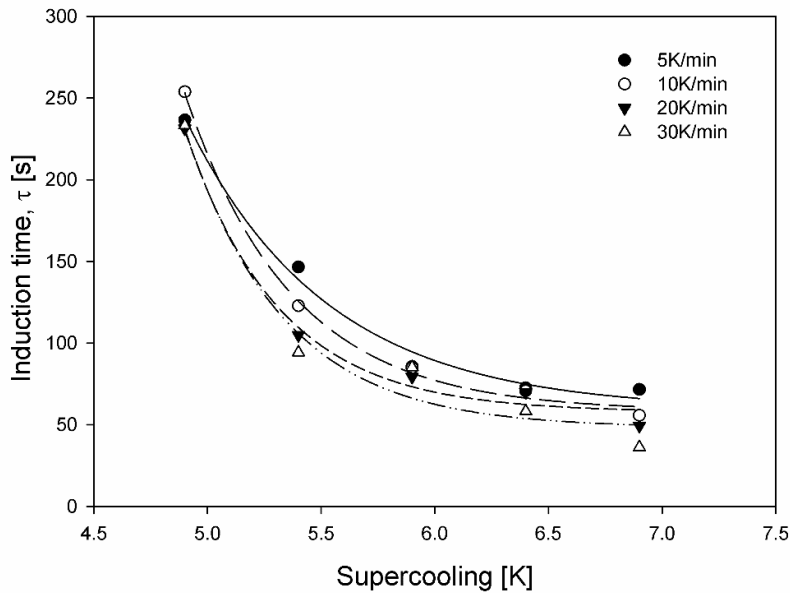
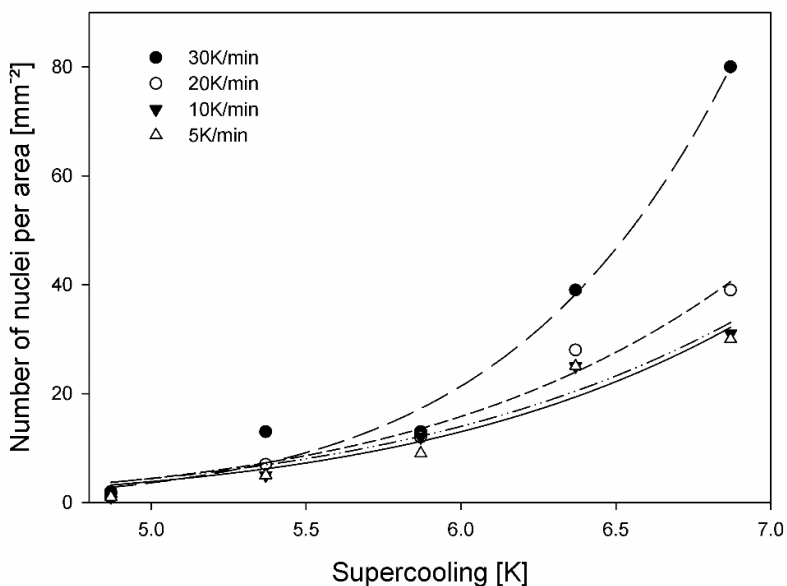


FIGURE 5-22: INDUCTION TIME,  $T_{IND}$  [S] VS. SUPERCOOLING [K] OF HIGH LINOLEIC SUNFLOWER OIL BASED PUFA MIXTURE; REGRESSION EQUATION IN TABLE 5-10 (EQUILIBRIUM TEMPERATURE 24.23 °C; ERROR  $\pm 19.05$  s)<sup>24</sup>

In spite of the isothermal end conditions, once the sample crosses the equilibrium temperature which is 24.23°C in this case (Figure 5-21), there is a certain amount of supersaturation that is affecting the crystallization process. Hence the cooling rate plays a decisive role in giving time for the monomers to find one another even before the pre-determined final crystallization temperature is reached. Naturally with higher cooling rates, the monomers have lesser time to orient themselves than in the case with slower ones. The experiments as mentioned in Section 4.4.1 were thus repeated for different cooling rates. A clear dependence on the cooling rate on the induction time in these samples was very difficult to diagnose. This was quite expected as such small un-agitated sample volume has a higher effect of heterogeneous behavior where such ideal correlations are harder to decipher. The surface to bulk volume in the case of these planar reactor geometry is very high and on the other hand diffusion of a monomer through the sample is very difficult due to lack of mixing. The effect of cooling rates on induction times was further investigated to arrive at agreeable results on larger volumes of samples in continuously stirred reactors in Section 5.3.5.2. On the other hand, when the sample is crystallized at a very high cooling rate of 30Kmin<sup>-1</sup> and subjected to a high supercooling of 6.9K, the tempered plates just below the object slides

inside the chamber cooled more leading to nucleation on the glass surface. This resulted in the least of all the induction times, owing to the heterogeneous factors involved. The dependencies are very different in larger sample volumes which were further investigated in two reactor setups with the help of a FBRM™ sensor.<sup>24</sup>



**FIGURE 5-23: NUMBER OF NUCLEI PER AREA [MM<sup>-2</sup>] VS. SUPERCOOLING [K] OF HIGH LINOLEIC SUNFLOWER OIL BASED PUFA MIXTURE WITH DIFFERENT COOLING RATES; REGRESSION EQUATION IN TABLE 5-10 (ERROR  $\pm 4.15$ )<sup>24</sup>**

The number of nuclei per unit area was also counted manually at the end of each experiment. The duration of each experiment was 60 minutes because no further increase of crystal count was seen thereafter. This has been represented again as a function of supercooling at different cooling rates in Figure 5-23.

One must factor into the limitations of the procedure before analysis. On one hand, this process enables a real time characterization of the nucleation process but on the other a crystal is visible through normal light microscopy only once the size of the crystal reaches the minimum range of the visible spectrum. It has also been assumed that a stable nucleus is one which has crossed the critical size of those conditions of final crystallization temperature, reactor geometry, pressure, etc. grows into a crystal.<sup>14</sup> Therefore, the total number of nuclei remains unchanged whenever one sees it. This assumption is important as although the reactor geometry is quite planar, there might be some crystals which are first seen once they have grown into the focal area and plane of the microscope. The basic thumb rule followed to count the number of nuclei was to note whether the center of the crystal was within the

framework of the area investigated. The number of nuclei ( $N\text{mm}^{-2}$ ) increases with lower crystallization temperatures and increasing cooling rates.

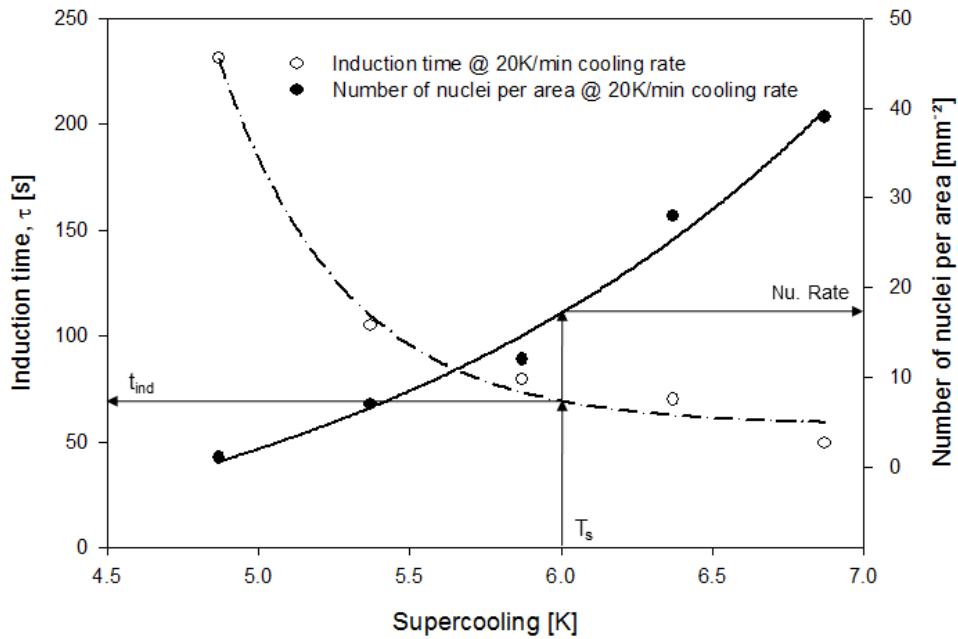


FIGURE 5-24: PREDICTION OF INDUCTION TEMPERATURE,  $T_{\text{IND}}$  [S] AND NUCLEATION PER UNIT AREA,  $N$  [ $\text{MM}^{-2}$ ] AS A FUNCTION OF SUPERCOOLING [K] OF SUNFLOWER OIL PUFA AT A SPECIFIC COOLING RATE OF  $20\text{KMIN}^{-1}$ ,<sup>24</sup>

It is clear from Figure 5-22 and Figure 5-23 that an optimal supercooling and cooling rate needs to be identified so as to obtain both ideal induction times and a comparatively lesser number of crystals in total. Lesser crystal count is favorable to ensure easier and more effective separation post melt crystallization since it would entail better crystal growth. A simple prediction model principle was developed on the basis of these experimental data which is illustrated in Figure 5-24. This model is specific to a cooling rate of  $20\text{Kmin}^{-1}$ . This cooling rate was chosen for the model as the number of nuclei is still manageable here and for application on micro-reactor systems, a faster cooling rate is definitely more economical.

It is very important to note that Figure 5-24 is an example of how these data could be put into use for melt crystallization in micro-reactor systems. Similar predictions for the other cooling rates can also be made from Figure 5-22 and Figure 5-23. A slower cooling rate might be also of more interest if cooling mediums provide different temperatures at different stages in a micro-reactor concept. A relatively simple exponential equation was found to fit the data analyzed for induction time. An intercept  $y_0$  was used to factor in the effects of diffusion as a result of varying cooling rates. In accordance to theory, the fact that the rate of nucleation is

inversely proportional to the induction time was justified by the regression fits, Equation 5-3 and Equation 5-4, used for induction time and nucleation rate respectively. The variables,  $a$  and  $b$  are the coefficients of the exponential term. Coefficient of determination values of mostly 0.99 and all > 0.95 ensure that the models fit the data very well. Each point in the plot is a result of the average of at least 3 experimental results and hence represents a larger set of data.

$$\text{Induction time, } y = y_0 + a \cdot e^{(-bx)}$$

EQUATION 5-3

$$\text{Number of nuclei per unit area, } y = y_0 + a \cdot e^{(bx)}$$

EQUATION 5-4

wherein,  $x$  is the supercooling applied.

Regression equation	Cooling rate [Kmin <sup>-1</sup> ]	Coefficients				R <sup>2</sup>
		y <sub>0</sub>	a	b		
Induction time vs. Supercooling (Figure 5-22) $y = y_0 + a \cdot e^{(-bx)}$	5	59,00	4,863 · 10 <sup>5</sup>	1,614	0,991	
	10	58,22	6,393 · 10 <sup>6</sup>	2,122	0,997	
	20	57,72	2,324 · 10 <sup>7</sup>	2,410	0,990	
	30	40,11	1,115 · 10 <sup>6</sup>	1,776	0,984	
Number of nuclei per area vs. Supercooling (Figure 5-23) $y = y_0 + a \cdot e^{(bx)}$	5	-22,56	2,695	0,436	0,950	
	10	-37,20	8,173	0,311	0,980	
	20	-17,12	1,036	0,583	0,990	
	30	0,23	0,002	1,540	0,990	

TABLE 5-10: REGRESSION COEFFICIENTS AND EQUATIONS WITH RESPECT TO OPERATING PARAMETERS FOR FIGURE 5-22 AND FIGURE 5-23

### 5.3.1.3. High oleic sunflower oil based PUFA

Similar experiments were carried out on the high oleic sunflower oil based PUFA mixture as well (Figure 5-25 and Figure 5-26). It was noted that this particular PUFA mixture on being subjected to crystallization produced relatively quite small and comparatively a larger number of crystals. Owing to this characteristic feature, one can arrive at the conclusion that the separation of the mother liquor of this particular fatty acid mixture post crystallization and centrifugation will pose difficulty. Regression fits for the oil have been provided in the Appendix.

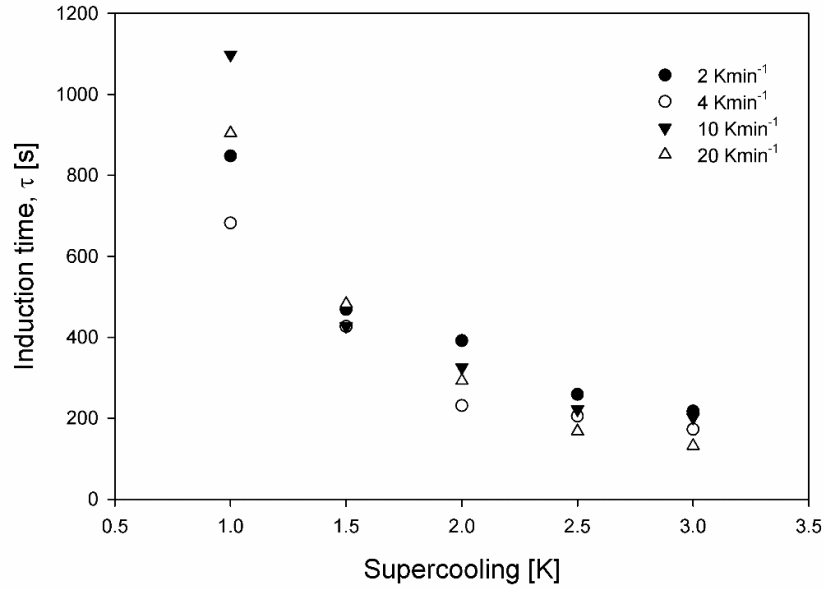


FIGURE 5-25: INDUCTION TIME, T [s] VS. SUPERCOOLING [K] OF HIGH OLEIC SUNFLOWER OIL BASED PUFA MIXTURE (ERROR ± 52,36s)

A lot of the crystal fraction would be still contained in the mother liquor and vice versa. The intersecting curves could be due to the high chances of errors in calculating such fine crystals manually and also that minute differences in temperature affect the results significantly.

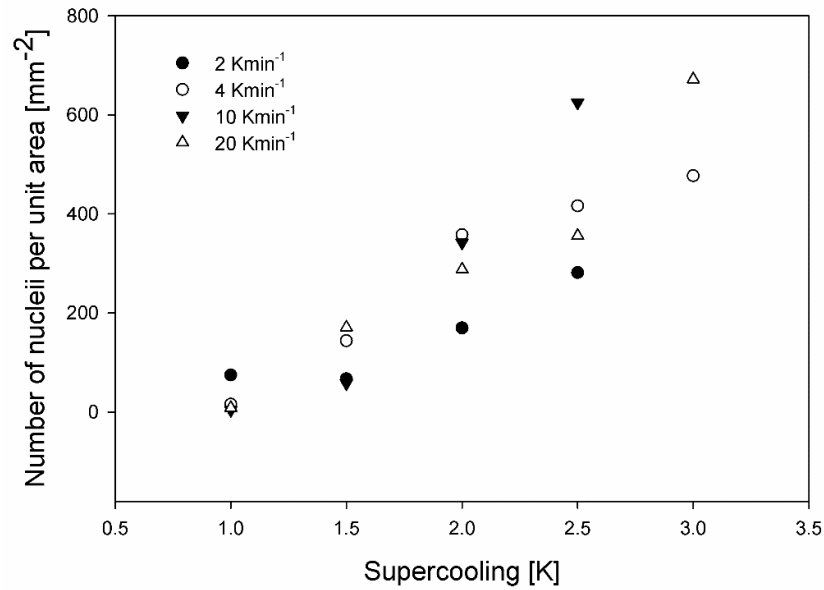
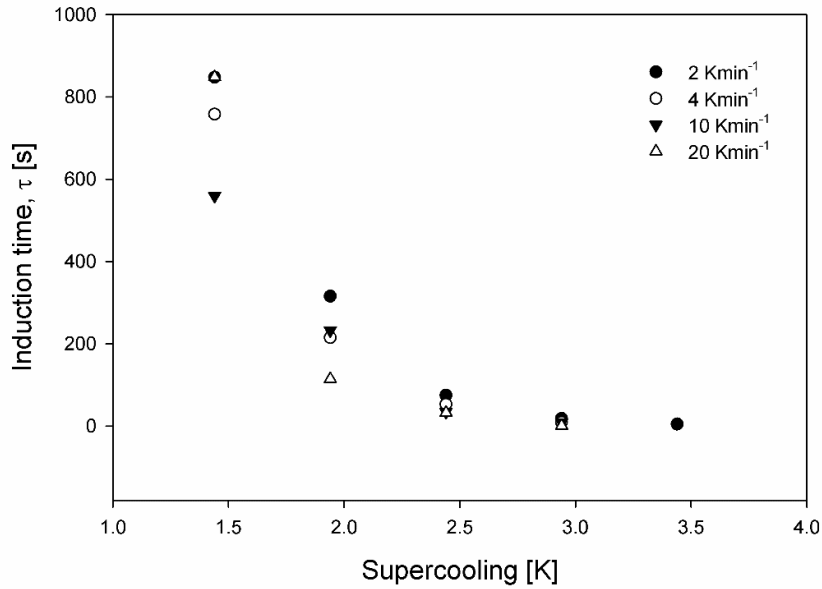


FIGURE 5-26: NUMBER OF NUCLEI PER AREA [MM<sup>-2</sup>] VS. SUPERCOOLING [K] OF HIGH OLEIC SUNFLOWER BASED PUFA MIXTURE WITH DIFFERENT COOLING RATES (ERROR ± 63,95)

**5.3.1.4. Soya oil PUFA mixture**

Every oil has a different nucleation behavior with respect to the supercooling subjected upon them. The supercooling required for crystallizing from soya oil PUFA mixture is similar to that of the high oleic sunflower oil based PUFA. Regression fits for the oil have been provided in the Appendix.



**FIGURE 5-27: INDUCTION TIME, T [s] VS. SUPERCOOLING [K] OF HIGH LINOLEIC SOYA OIL BASED PUFA MIXTURE (ERROR ±37,36s)**

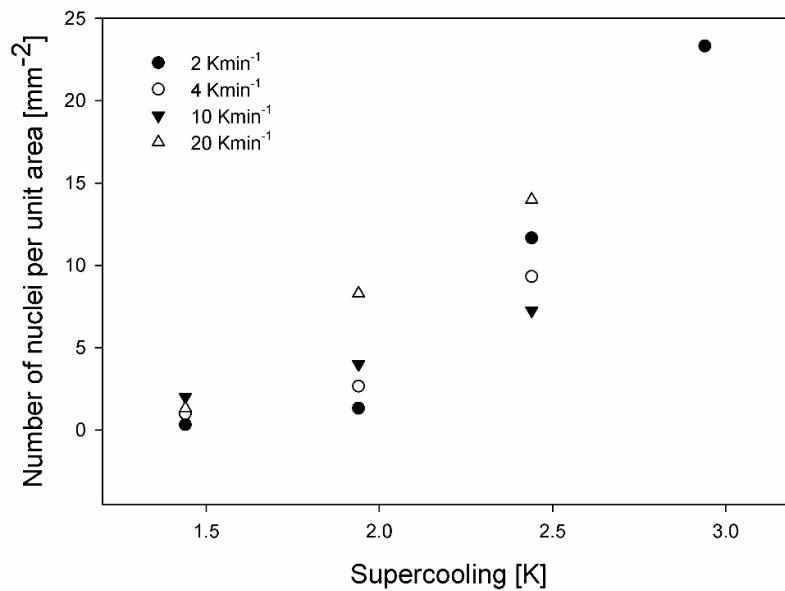


**FIGURE 5-28: NUMBER OF NUCLEI PER AREA [MM<sup>-2</sup>] VS. SUPERCOOLING [K] OF SOYA OIL PUFA MIXTURE WITH DIFFERENT COOLING RATES (ERROR ± 2,34)**



But in terms of shape and crystal count, it is more similar to the high linoleic sunflower oil based PUFA. The results of induction time and the number of nuclei per unit area has been shown in Figure 5-27 and Figure 5-28 respectively. Figure 5-29 depicts the differences in size



FIGURE 5-29: COMPARISON OF CRYSTAL SIZE OF HIGH OLEIC AND HIGH LINOLEIC MIXTURES

of the crystals depending on the composition of the PUFA mixture used. The same supercooling could be chosen for the mixtures to compare as they operated in different temperature ranges but the cooling rate of  $20\text{Kmin}^{-1}$  is constant in Figure 5-29. The crystal sizes ranged between  $200\ \mu\text{m}$  –  $450\ \mu\text{m}$  for the high oleic PUFA mixtures whereas for high oleic sunflower oil based PUFA mixture, the sizes were between  $10\ \mu\text{m}$  and  $75\ \mu\text{m}$ . Crystal sizes also increased with reducing supercooling and increasing cooling rate. Detailed pictorial representation for each PUFA mixture investigated is available in the Appendix.

**Comparison of the nucleation data of the PUFA mixtures ( $\mu\text{scale}$ )**

The crystals formed from the samples as visualized under the microscope seems star or lancet shaped depending on the type and time given for crystallization. The natural tendency of the crystals was although to form creamy white star shaped 3D spherulites. Two dimensional growth of a saturated crystal from the PUFA mixture to form a lancet shape, instead of the 3D star shaped crystal could be influenced by gentle supercooling, cooling rate and micro-reactor geometry. The effects of cooling rates and supercooling can be noted in the pictorial examples of the different PUFA mixtures as shown in Figures 3-2 – 3-5 in the Appendix. It is to be noted that the crystal count and crystal behavior of the two high linoleic soya and sunflower are very similar. On the other hand, the high oleic acid mixture resulted in a much higher number of crystals and also tended towards a more dendrite and finer structure. Pictures to support the claim have been provided in the Appendix. The exact values of the induction times have been shown in Table 5-11. Every experiment was repeated at least 3

times if not more. A detailed tabulation of the data has been done in the Appendix in Section 3.1.3 – 3.1.5. Figure 5-30 explicitly depicts that the induction times all follow a function of exponential decay (with an intercept) with respect to supercooling irrespective of the PUFA mixture. The cooling rate also has an inverse effect on the induction time, which as explained is due to the overwhelming effect of the surface to bulk ratio in this reactor geometry and lack of mixing. This although not ideal is an effect which is to be accounted for in micro-reactor systems wherein diffusion of monomers towards the formation of crystals might be hindered due to lack of mixing.

High linoleic sunflower oil PUFA mixture	Crystallization temperature	Supercooling	Induction time, $\tau$			
	T in °C	$\Delta T$ in K	5 Kmin <sup>-1</sup>	10 Kmin <sup>-1</sup>	20 Kmin <sup>-1</sup>	30 Kmin <sup>-1</sup>
	19.5	4.87	236.56	253.78	231.39	233.26
	19	5.37	146.56	122.78	104.89	94.26
	18.5	5.87	85.56	65.78	79.39	85.26
	18	6.37	72.56	70.78	69.89	58.26
	17.5	6.87	71.56	55.78	49.39	36.26
High oleic sunflower oil PUFA mixture	Crystallization temperature	Supercooling	Induction time, $\tau$			
	T in °C	$\Delta T$ in K	2 Kmin <sup>-1</sup>	4 Kmin <sup>-1</sup>	10 Kmin <sup>-1</sup>	20 Kmin <sup>-1</sup>
	14.5	3	217.67	172.67	201.67	132
	15	2.5	259	205.33	222	167.67
	15.5	2	391.67	231.33	325.75	292.67
	16	1.5	469	426.67	427.33	482.67
	16.5	1	848	682.33	1098	904.33
High linoleic soya oil PUFA mixture	Crystallization temperature	Supercooling	Induction time, $\tau$			
	T in °C	$\Delta T$ in K	2 Kmin <sup>-1</sup>	4 Kmin <sup>-1</sup>	10 Kmin <sup>-1</sup>	20 Kmin <sup>-1</sup>
	22.5	3.44	5			
	23	2.94	18.33	9.67	9	1
	23.5	2.44	75	53.33	34.75	32.6
	24	1.94	315.67	215.33	232.67	114.43
	24.5	1.44	848	758.33	559.5	848

**TABLE 5-11: INDUCTION TIME,  $T_{IND}$  OR  $T$ , OF THE MELT CRYSTALLIZATION OF THE PUFA MIXTURES AS A FUNCTION OF SUPERCOOLING AND COOLING RATES**

As per theory, the nucleation trend follows an inverse function of the induction time, that is of exponential growth. In the case of nucleation per area, the direct effect of cooling rate is noticed, although fluctuations are higher. The higher the cooling rate, the more is the number of crystals. This is also due to the factor of wall nucleation. Although, when dealt with the high oleic acid PUFA mixture, it is difficult to follow the influence of cooling rate as the crystals are

fine and small and very many to deal with. The effect of supercooling on the number of nuclei formed is consistent as shown in Figure 5-26. An illustrative representation of the comparison of the induction times and nucleation data has been done in Figure 5-30 and Figure 5-31.

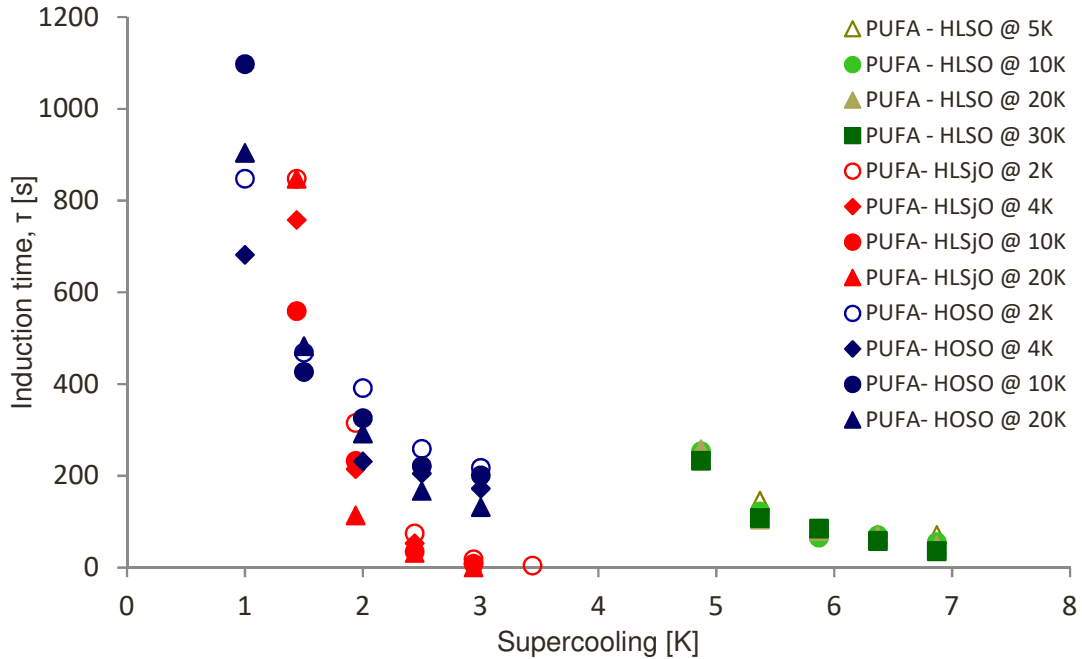


FIGURE 5-30: INDUCTION TIME,  $T$  [s] VS. SUPERCOOLING [K] OF HIGH LINOLEIC AND HIGH OLEIC SUNFLOWER AND HIGH LINOLEIC SOYA OIL BASED PUFA MIXTURES (*HLSO* – *HIGH LINOLEIC AND HIGH OLEIC SUNFLOWER OIL* AND *HLSjO* – *HIGH LINOLEIC SOYA OIL*)

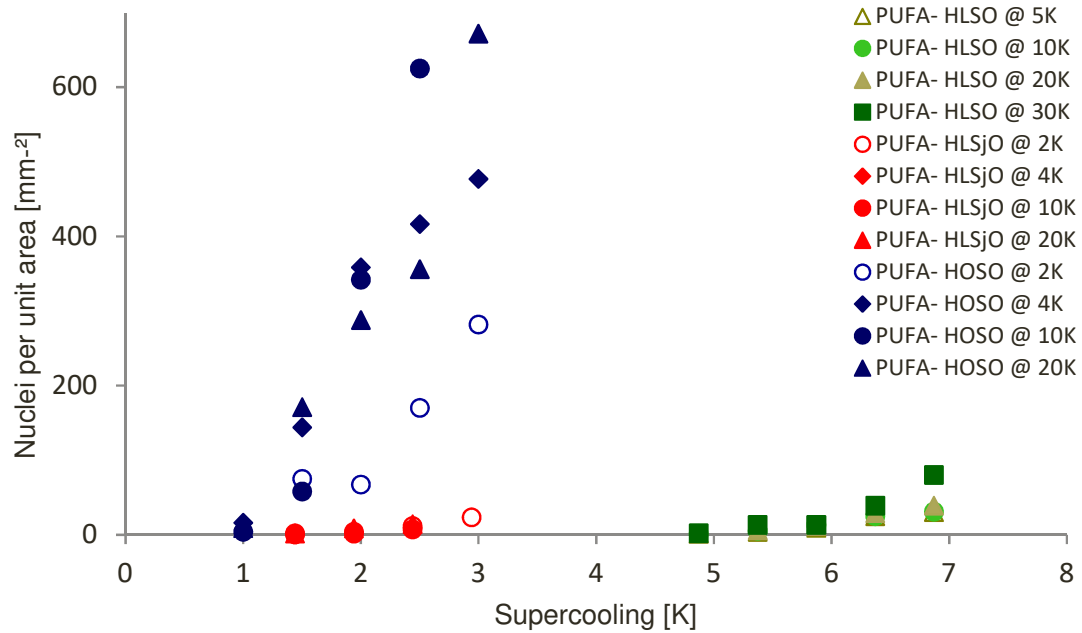


FIGURE 5-31: NUMBER OF NUCLEI PER AREA [ $\text{MM}^{-2}$ ] VS. SUPERCOOLING [K] OF VARIOUS PUFA MIXTURES WITH DIFFERENT COOLING RATES (*HLSO* AND *HOSO* – *HIGH LINOLEIC AND HIGH OLEIC SUNFLOWER OIL* AND *HLSjO* – *HIGH LINOLEIC SOYA OIL*)

### **Verification of fit with theory**

The 2D regression equation of exponential decay, fitted and applied to the induction time results obtained needs to comply with the theoretical phenomena of nucleation fundamentally. When the supercooling,  $\Delta T$ , increases, the induction time,  $\tau$ , also decreases till when

$$\Delta T: x \rightarrow \infty,$$

in regression Equation 5-5 for induction time,

$$\tau: y = y_0 + a \cdot e^{(-bx)}$$

**EQUATION 5-5**

the exponential term becomes infinitely small and hence insignificant, thereby making the induction term also almost independent of supercooling,  $\Delta T: x$ . Effectively, the induction time then remains only a function of cooling rate,  $y_0$ , which is plausible as then the nucleation is only a function of how fast and no longer how much the supercooling is put into effect.

On the other hand, when

$$\Delta T: x = 0,$$

Then,  $e^0 = 1$ , thereby making the second term invariably large as the variable 'a' will increase exponentially and become infinitely large as well. Then, the induction time  $\tau : y$  will also become infinitely large irrespective of the cooling rate. The term  $y_0$ , will then in turn become insignificant to the second term, making supercooling the limiting factor.

### **Errors in measurement and outlook**

The errors in measurement could rise due to limitation in terms of visibility and on a higher level, due to human handling. Every person looks through the microscope differently and might end up calculating different induction times. The crystal is noticed through the microscope for the first time up on supercooling the system, only when it reaches a certain size within the visibility range. There could be wrong representation due to non-homogeneity of sample. To this regard, it must be noted that there is no continuous mixing of the probe and hence wall nucleation has a larger effect. The microscope used is also limited to focusing on a particular focus layer. Practically, it is a matter of luck to see the first crystal. Different parts of the probe are in contact with different surfaces, as for example, some part of the PUFA mixture might be in direct contact with the glass slide and some with only the bulk of

the solution and some even with air (on the sides). Hence induction time can greatly vary on where the microscope is focused.

**One needs to although keep in mind that such effects are not merely errors but also natural effects that are seen in a micro reactor system. Hence these experimental results are in fact adequate in such reactor circumstances. Naturally to compare with more ideal (bulk) conditions, a larger sample volume and setup was chosen for the next set of experiments.**

### 5.3.2. Crystal growth kinetics ( $\mu\text{l}$ scale)

A comparison of the linear crystal growth rates of the pure saturated and unsaturated fatty acid standards in the aforementioned capillaries depending on the supercooling are depicted in Figure 5-32. All 2D regression and modeling was performed by SigmaPlot Version 11.0. The linear equation as shown in Table 5-12, is made with the assumption of the fit passing through  $x,y: 0,0$ . This need not be the case as there might be a lag phase at the beginning of the growth. To summarize, the growth rates of the unsaturated fatty acids are much lower than that of the saturated fatty acids and also decrease in the order of their unsaturations. The ratio of the linear crystal growth rates at a constant supercooling is presented in Table 5-13.<sup>24</sup>

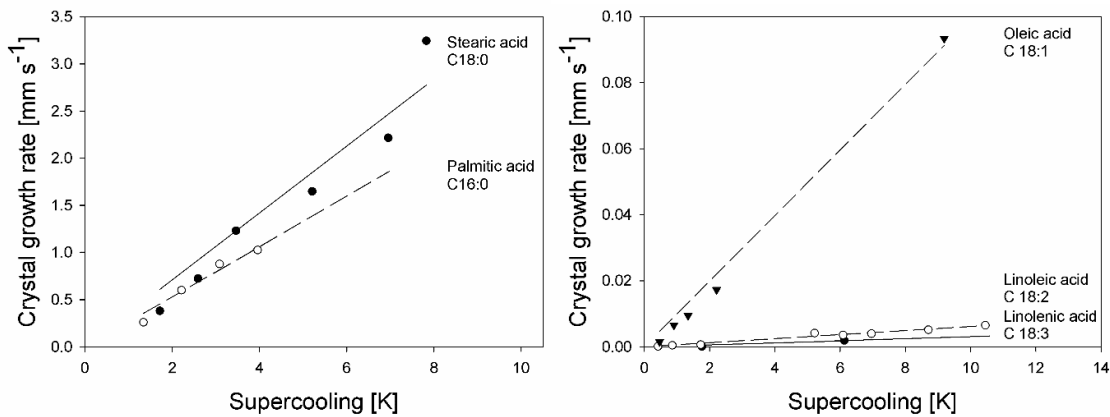


**FIGURE 5-32: COMPARISON OF THE AVERAGE CRYSTAL GROWTH RATES OF STANDARD SATURATED (LEFT) AND UNSATURATED (RIGHT) FATTY ACID SAMPLES DEPENDING ON THE DEGREE OF SUPERCOOLING IN CAPILLARIES (INNER DIAMETER,  $D_i=0.68$  MM; ERROR  $\pm 2.4$  %) <sup>24</sup>**

	Regression equation	Cooling rate [Kmin <sup>-1</sup> ]	Coefficients a
Linear crystal growth rate (Figure 5-32)	$y = a \cdot x$	Stearic acid	0.36
		Palmitic acid	0.27
		Oleic acid	0.009
		Linoleic acid	0.0006
		Linolenic acid	0.0003

**TABLE 5-12: REGRESSION COEFFICIENTS AND EQUATIONS WITH RESPECT TO OPERATING PARAMETERS FOR FIGURE 5-32**

Stearic Acid C18:0	Palmitic Acid C16:0	Oleic Acid C18:1	Linoleic Acid C18:2	Linolenic Acid C18:3
1200:	900:	30:	2:	1

**TABLE 5-13: RATIO OF THE CRYSTAL GROWTH RATES (MAINTAINING THE GROWTH RATE OF C 18:3 AS BASE) OF THE PURE COMPONENTS OF PUFA AT A CONSTANT SUPERCOOLING**

The crystal growth rate of PUFA was also measured for a specific supercooling of 9.15 K in the same capillaries. The crystal growth rate of PUFA at the beginning as shown in the data in Figure 5-33 was calculated to be  $0.0004 \text{ mms}^{-1}$  by using the first derivative of the first segment of the trend. As expected the crystal growth is fast at the beginning, after which it slows down and eventually almost approaches zero. This crystal growth rate depends on various inhibiting factors such as diffusion, heat transfer to the bulk of solution, depletion of the saturated content in mother liquor. Thus, the more the crystal grows, the slower the process is. Consequently, it is noted that the growth rate reduces significantly, that is, to  $0.00016 \text{ mm/sec}$  by 3000 seconds.<sup>24</sup>

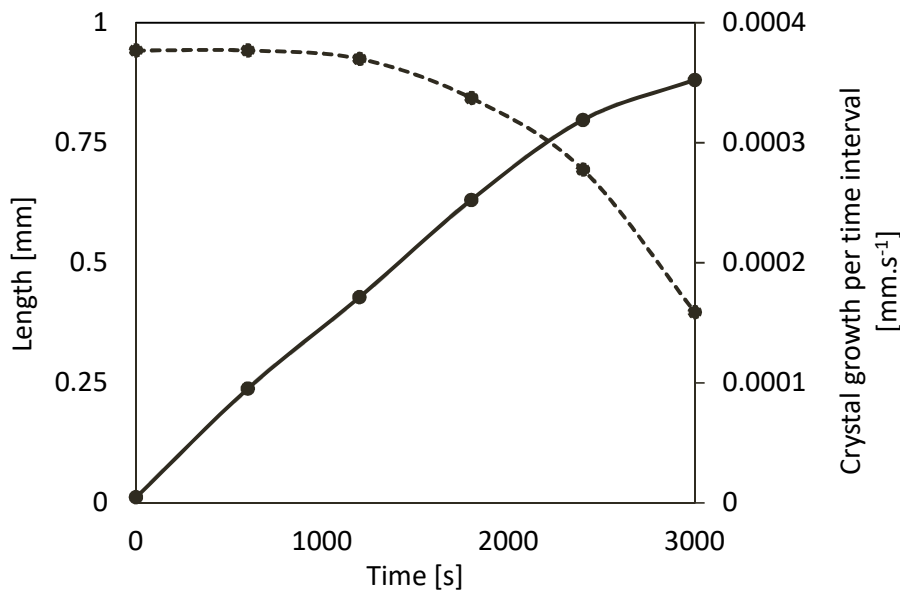


FIGURE 5-33:CRYSTAL GROWTH RATE OF SUNFLOWER OIL BASED PUFA AT A SPECIFIC SUPERCOOLING OF 9.15 K IN CAPILLARIES (INNER DIAMETER, DI=0.68 MM)<sup>24</sup>

The crystal growth rates of the high linoleic sunflower oil based PUFA was also investigated and compared in 25  $\mu\text{m}$  and 68  $\mu\text{m}$  diameter capillaries. As can be seen in Figure 5-34a, wherein the capillary diameter is 68  $\mu\text{m}$ , the crystal started growing in all directions such that an arm or needle of the star shaped crystal could be taken into consideration for the measurements. In comparison, the crystal in the 25  $\mu\text{m}$  capillary grew in a more twisted or helical fashion (Figure 5-34b), where the projected x-axis length was taken into consideration. The crystal growths in the 25  $\mu\text{m}$  capillaries were further analyzed to check their dependencies on cooling rates and degree of supercooling.

<sup>24</sup> Crystal growth rate of PUFA mixture was rounded off to  $0.0004 \text{ mm}^{-1}$ . Actual value is  $0.000377 \text{ mms}^{-1}$ .

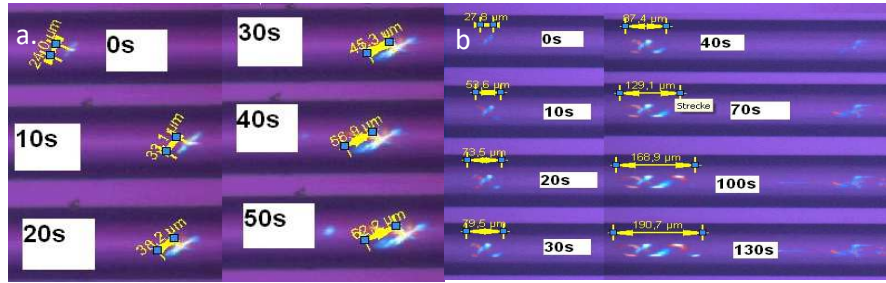


FIGURE 5-34: CRYSTALLIZATION OF SUNFLOWER OIL FATTY ACID MIXTURE IN A.) 68  $\mu\text{m}$  AND B.) 25  $\mu\text{m}$  CAPILLARIES UNDER THE MICROSCOPE

The correlation between the mean total lengths (the projected length on the horizontal axis in one dimension) of a sunflower oil PUFA crystals upon melt crystallization in the capillaries (68  $\mu\text{m}$  and 25 $\mu\text{m}$ ) and their corresponding supercooling and cooling rate showed that at lesser cooling rates (1  $\text{Kmin}^{-1}$ ), the crystals tend to be considerably longer. It was also noted that crystal lengths were considerably larger when the capillary diameter was reduced from 68  $\mu\text{m}$  to 25  $\mu\text{m}$ . This is naturally because the smaller capillary could influence a stronger unidimensional crystal growth leading to an increase in length from 147-365  $\mu\text{m}$  to 639-947  $\mu\text{m}$ . A capillary shaped reactor for further crystal growth studies could be pursued. At higher cooling rates no dependency between the cooling rate and the total length of the crystal was noticed. These results have been shown in Figure 5-35 and Figure 5-36.

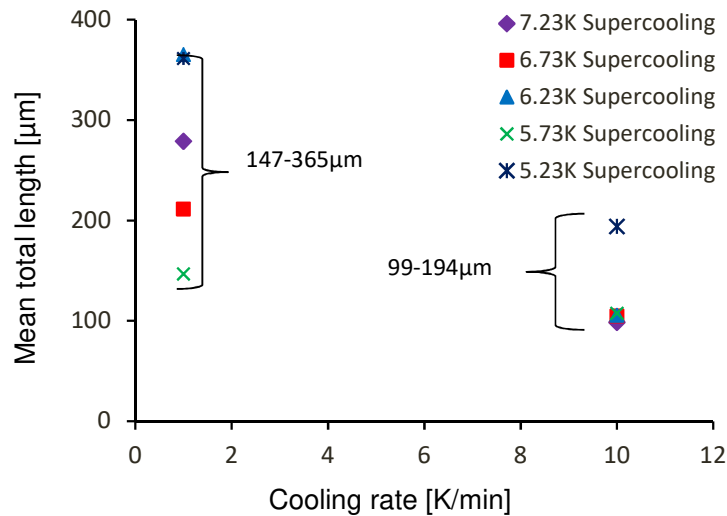


FIGURE 5-35: MEAN TOTAL LENGTH [ $\mu\text{m}$ ] OF HIGH LINOLEIC SUNFLOWER OIL PUFA MIXTURE (EQUILIBRIUM TEMPERATURE 24.23  $^{\circ}\text{C}$ ) CRYSTALS AS A FUNCTION OF COOLING RATE [ $\text{KMIN}^{-1}$ ] AND SUPERCOOLING [K] IN CAPILLARIES [68  $\mu\text{m}$ ]



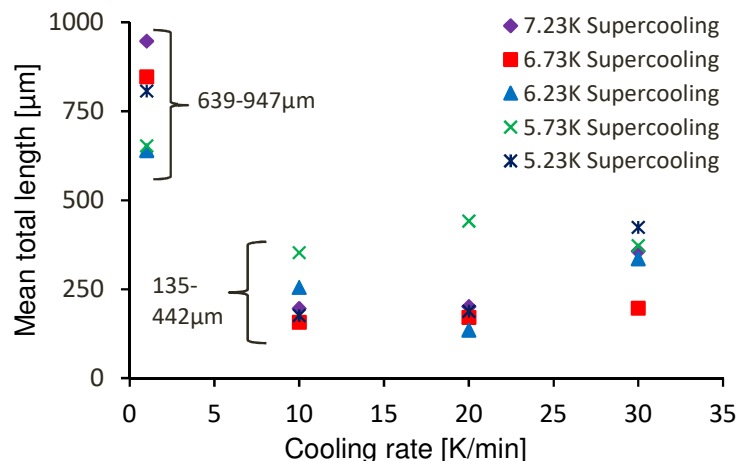


FIGURE 5-36: MEAN TOTAL LENGTH [ $\mu\text{m}$ ] OF HIGH LINOLEIC SUNFLOWER OIL PUFA MIXTURE (EQUILIBRIUM TEMPERATURE  $24.23\text{ }^{\circ}\text{C}$ ) CRYSTALS AS A FUNCTION OF COOLING RATE [ $\text{KMIN}^{-1}$ ] AND SUPERCOOLING [K] IN CAPILLARIES [ $25\text{ }\mu\text{M}$ ]

It was also difficult to see any correlation or function between the total crystal length and the degrees of supercooling. But the crystal size is definitely dependent on the capillary size. As previously mentioned, larger crystal length is preferred to smaller ones as it leads to a more effective and easier separation. It could also be deciphered from the helical form of the crystal growth in the narrower capillary,  $25\text{ }\mu\text{m}$  that the pattern tended to towards a 2D growth from a 3D free spherulites growth in the larger capillaries. The smaller diameter capillary, limited to its  $25\text{ }\mu\text{m}$  diameter, therefore gives very little freedom to the crystal arm to grow. As soon as the crystal reaches the inner surface of the glass capillary, it is forced to move back to the bulk of the liquid. The PUFAs tend to move away from the glass owing to its lower wettability index with respect to fatty acids. It also has to be added that the crystallizing saturated fat, having only non-polar carbon hydrogen bonds, is more hydrophobic than unsaturated ones.

### ***Errors in measurement and outlook***

The measurement of crystal growth rate in these capillaries is a difficult task. Firstly, it is almost impossible to know where the first crystal would appear. Similar to the experiments to characterize the nucleation kinetics, the microscope is needed to be focused on the right layer such that, if and when a crystal grew, it was noticed as soon as it entered the visible spectrum. Generally, the crystals were caught in the visuals at  $10\text{ -}20\text{ }\mu\text{m}$ . Hence, the crystal growth rate right at the beginning of nucleation was impossible to determine through this method. The more the crystal grew, the lesser was the concentration of the saturated crystal fraction in the melt reducing diffusion of monomers towards the crystal. Lack of mixing therefore, played a

larger negative effect on the growth. In other words, crystal growth rate was curbed due to the increasing non-homogeneity of the sample, more precisely, due to the lack of saturated content in the vicinity of the crystal. These factors affected the growth rate so much that an influence of supercooling or cooling rate was no longer detectable. It was pertinent at this point to get an idea of the composition of the crystal and mother liquor fractions qualitatively before moving on to the experiments in the larger volume scale. That leads to the investigations in the next section.

### 5.3.3. Confocal Raman Spectroscopy ( $\mu\text{l}$ scale)

A 7X7 mapping of a single crystal with surrounding melt with the measuring distance of 5  $\mu\text{m}$  was done. Two positions one from the crystal and one from the mother liquor were taken and analyzed under the confocal Raman microscope. Each of the peaks in the spectra obtained as in Figure 5-37 represent a certain functional group such as C=C or CH<sub>2</sub> or C-C. The functional group C=C stands for an unsaturated acid owing to its double bond. Naturally similar to chromatography, a standard reference is passed so as to find out which wavelength would represent which functional group. Figure 5-37 shows a comparison of the spectral images of the melt (picture left, green spectra) and the crystal fraction (picture right; red down).

One can see a typical star shaped crystal was chosen for the analysis. Similar analysis was also done on a lancet shaped crystal. The results of the lancet shaped crystal are shown in Figure 5-38.

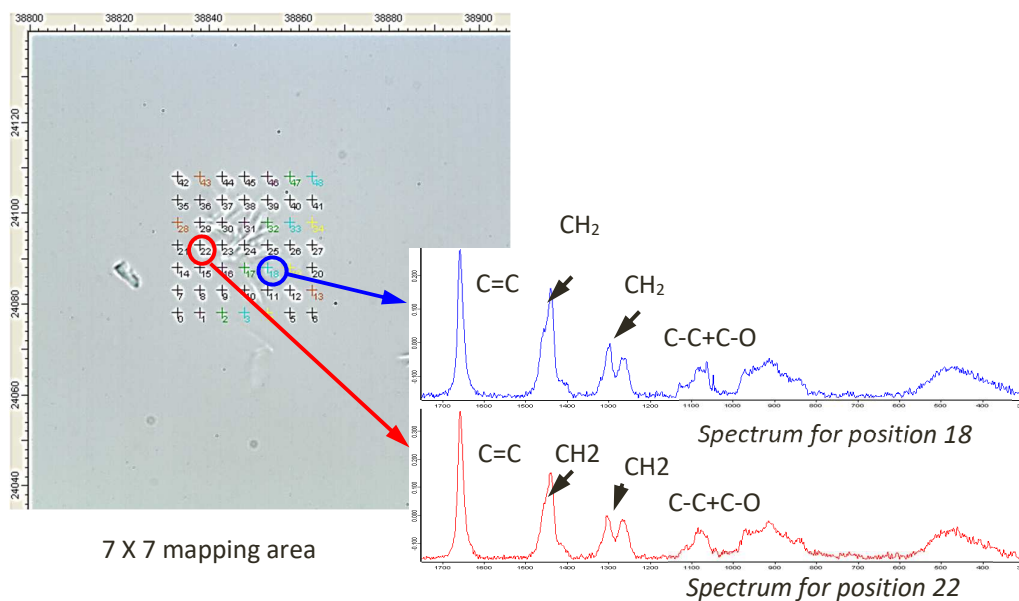


**FIGURE 5-37: SPECTRUM OBTAINED FROM CRYSTAL FRACTION (POSITION 18) AND FROM MOTHER LIQUOR (POSITION 22) BY MEANS OF CONFOCAL RAMAN SPECTROSCOPE FOR A DENDRITE SHAPED CRYSTAL, SENTERRA®\*\*\*\*\***

\*\*\*\*\* Data and illustrations taken and edited from the report submitted by Mr. Eric Klein and Mr. Matthias Boese from Bruker Optik GmbH for the test measurements for the compositional analysis of high oleic PUFA. Acknowledgements also to the organization of Bruker Optik GmbH in Ettlingen, Germany to make the confocal Raman microscope available for measurements.

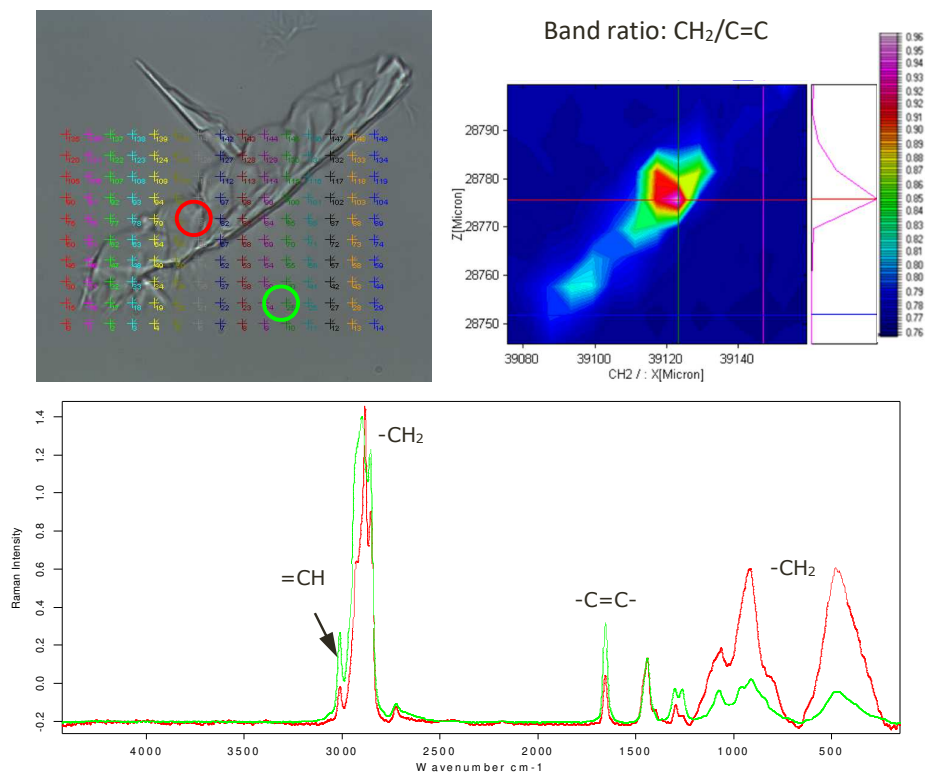


**FIGURE 5-38: COMPARISON OF SPECTRA OBTAINED FROM A LANCET SHAPED CRYSTAL (RED) AND MOTHER LIQUOR (GREEN) BY MEANS OF CONFOCAL RAMAN SPECTROSCOPE, SENTERRA<sup>®</sup>§§§§§§**

The ratio of saturated to unsaturated content was made by taking the respective bandwidths - Bandwidth intensity ratio of CH<sub>2</sub>/C=C: Bandwidth intensity at 1440 cm<sup>-1</sup>/1656 cm<sup>-1</sup>. The basis lines of the spectra are corrected and normalized to the band of 1440 cm<sup>-1</sup>. Both showed a high intensity of saturated content in the crystal fraction whereas a low intensity of the same in the mother liquor. The higher intensity is represented with the red color in the top right picture of Figure 5-38 and the blue color represents a low bandwidth intensity ratio. The saturated content is at its highest in the center of the crystal and reduces as the crystal radius increases. It is the least in the mother liquor and hence blue in color. This spectral graph also suggests that more and more unsaturated content gets trapped as the saturated crystallizes. This is more in the case of the dendrite crystal rather than the lancet shaped crystal owing to the fact that more mother liquor gets entrapped in the dendrite arms rather than a more solid

§§§§§§ Data and illustrations taken and edited from the report submitted by Mr. Eric Klein and Mr. Matthias Boese from Bruker Optik GmbH for the test measurements for the compositional analysis of high oleic PUFA. Acknowledgements also to the organization of Bruker Optik GmbH in Ettlingen, Germany to make the confocal Raman microscope available for measurements.

and planar structure such as the lancet. One could see the possibility of the shift in the saturated content in the mother liquor to the crystal but a final quantitative measurement was not possible.

***Outlook***

This and the validation from the analyses obtained from the GC-FID and the DSC proves without any doubt that the saturated content crystallizes out of the mother liquor thereby enriching the unsaturated content. Both the lancet shaped and the star form crystals showed similar results also validating that the shapes are to be modified more to ensure easier separation rather than different composition of crystal fraction. Another important point to note is the easier and bigger the geometry of the crystals, the easier it would be separate the same from its mother liquor.

The star shaped crystals would entrap a lot of the mother liquor in between its dendrite formed arms although the lancet formed crystals need to be also stable and thick enough for easy separation.

### 5.3.4. Contact angle measurement as a function of surface type and composition of PUFA

Three different PUFAs – high oleic, linoleic and linolenic were chosen so as to compare the effects of the wettability of glass as a function of the degree of unsaturation of sample. Three drops of the sample were measured for the same final temperatures for the purpose of reproducibility. The contact angle,  $\vartheta$ , was measured as shown in Figure 4-6. The average of the contact angles on either side of 3 drops were taken and compared at each temperature and for each sample type. Multiple surfaces resulting in diverse contact angles with PUFA have been investigated ranging from very low angles such as for polymers over glass to higher ones as in the case of steel. The results obtained as shown in Figure 5-39, portray that normal steel has the most favorable outcome with minimal wettability and maximum contact angle.

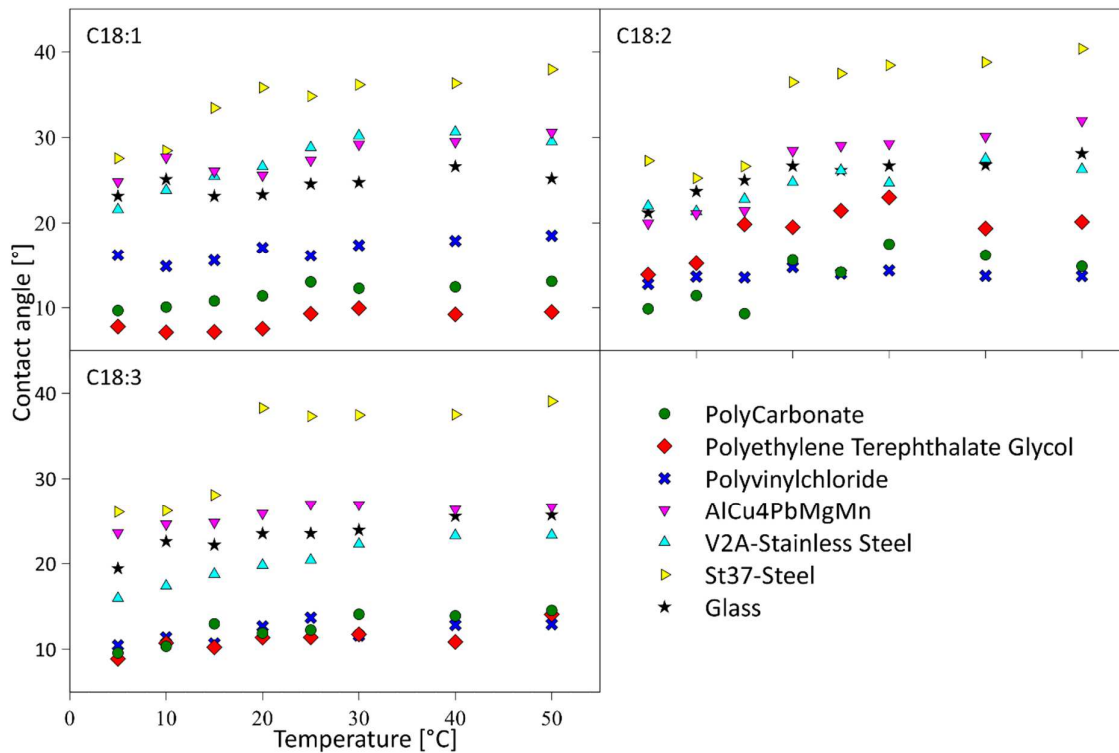
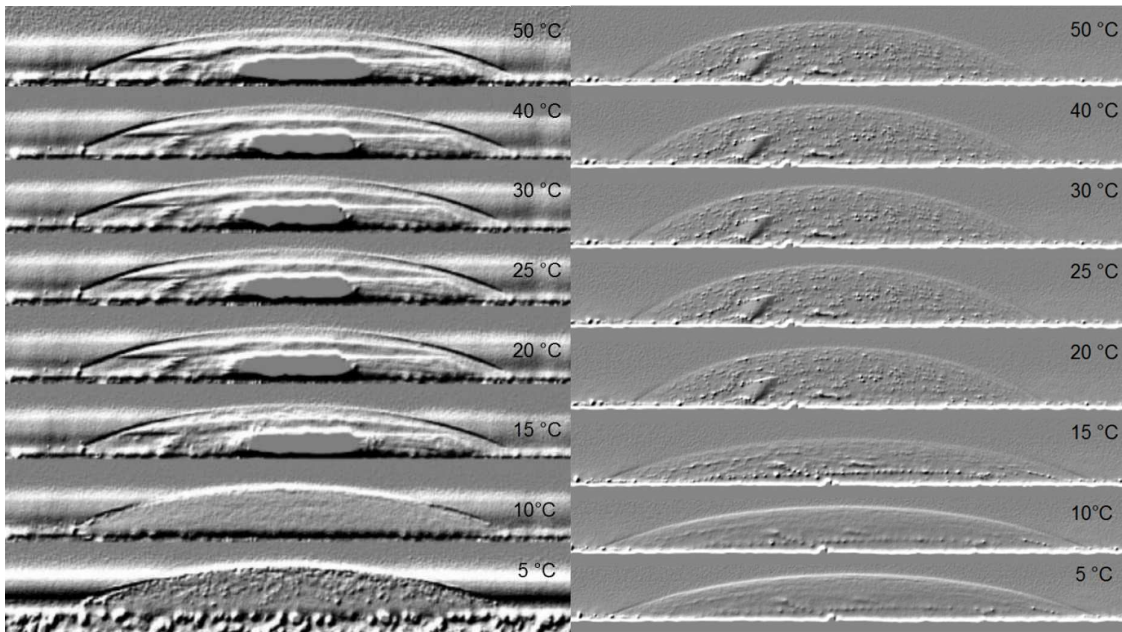


FIGURE 5-39: CONTACT ANGLE OF A HIGH OLEIC, HIGH LINOLEIC AND A HIGH LINOLENIC FATTY ACID BASED PUFA ON DIVERSE MATERIAL SUBSTRATES \*\*\*\*\*

Glass which was used for the investigations carried out here fare somewhere in the top average when compared to all the tested materials. Naturally, plastics like Polyvinylchloride (PVC), Polyethylene Terephthalate Glycol (PETG) and Polycarbonate (PC) fared poorly having

\*\*\*\*\* Acknowledgements to Mr. Benjamin Selge for help with the experiments.

high wettability and lower contact angles. It is to be noted that contact angles on stainless steel are in similar range as in the case of glass. Hence, investigations made on glass due to ease of visualization offers representative results as expected on stainless steel with respect to contact angles while ignoring heat transfer properties. In addition, this property of glass can be noticed in the crystal growth experiments and results as shown in Section 5.3.2 wherein irrespective of however small the inner diameter of the capillaries were, the saturated crystals on reaching the inner walls tended to move away and back to the bulk of the melt. This lead to a helical structure of the crystal growth in the smaller capillaries. Figure 5-40 illustrates high linoleic PUFA drops measured at different temperatures on glass and steel. It clearly shows that the PUFA drop is flatter on glass than on steel.



**FIGURE 5-40: HIGH LINOLEIC PUFA DROPS MEASURED ON GLASS SURFACE (LEFT) AND STEEL - ST 37 (RIGHT) BY KEYENCE VHX 2000D MICROSCOPE**

The contact angle of all the PUFA mixtures irrespective of the unsaturation have similar contact angles on diverse surfaces. This confirms as well that glass does not play a large role on influencing the nucleation kinetics of the PUFA samples.

### 5.3.5. Effects of supercooling and cooling rate on induction time (ml scale)

To get a better perspective on the effects of cooling rate and also a validation of the effects of supercooling, investigations on the nucleation kinetics of the two main types of PUFA mixtures, namely the high linoleic and high oleic sunflower oil based PUFAs were repeated in the V-form reactor and the EasyMax™ – FBRM™ setup.

#### 5.3.5.1. V-form Reactor – FBRM™ setup

Enhanced heat transfer was made possible in the V-form reactor so as to quickly remove the heat generated during melt crystallization through minimal volume of sample, optimized mixing and the special V shape of the reactor. Important parameters like induction time, mixing speed, etc. have been determined and compared as functions of degree of supercooling (Figure 5-41 and Figure 5-42).

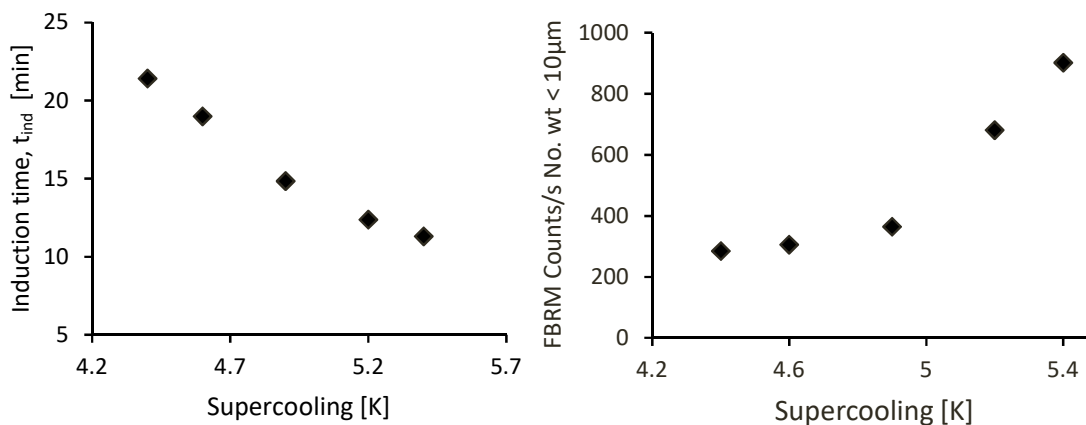


FIGURE 5-41: COMPARISON OF INDUCTION TIME,  $T_{IND}$ [S] (LEFT, AVERAGE ERROR  $\pm 0.8$ ) AND FBRM™ COUNTS PER SECOND <10 $\mu$ m (RIGHT, ERROR  $\pm 14.4$ ) VS. SUPERCOOLING [K] OF HIGH LINOLEIC SUNFLOWER OIL PUFA MIXTURE (SOLID LIQUID EQUILIBRIUM TEMPERATURE: 24.23 °C) MEASURED BY FBRM™ IN V-FORM REACTOR @ 15 RPM<sup>135</sup>

Induction times in the mixture decreased with increasing supercooling and mixer speed. Higher speed led to better mixing and heat transfer, thereby enabling the sample to reach and maintain the crystallization temperature faster and better. The negative effects such as high mixing speed lead to more crystal collisions and thereby breakage. The ideal supercooling zones obtained for this high linoleic mixture, wherein the sample does not nucleate before the crystallization temperature is reached on one hand and the induction time is within an acceptable range on the other. Naturally, the induction time is a bit higher



here than in the case of microscope owing to larger sample volume and lesser heat conductivity to the bulk of the sample. Every experiment was carried out at least thrice.

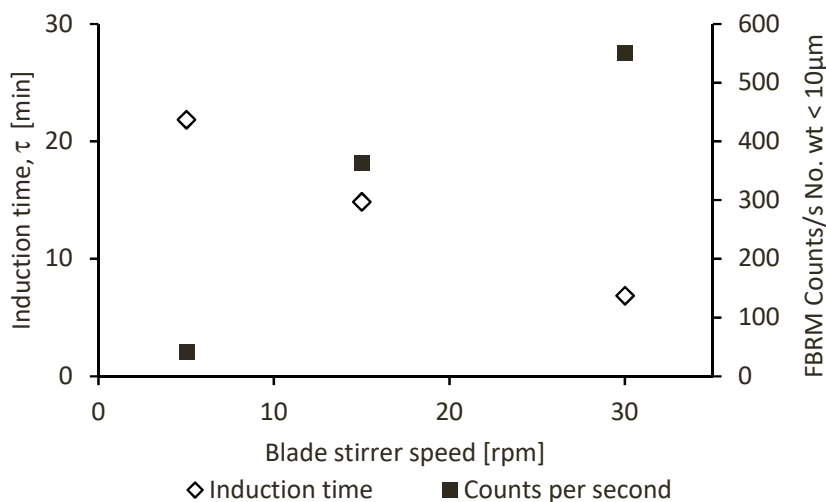


FIGURE 5-42: : INDUCTION TIME,  $T_{\text{IND}}$  [s] AND COUNTS PER SECOND (<10 $\mu\text{m}$ ) VS. BLADE STIRRER SPEED (RPM) AND OF HIGH LINOLEIC SUNFLOWER OIL PUFA MIXTURE (EQUILIBRIUM TEMPERATURE 24.23 °C) MEASURED BY FBRM™ IN V-FORM REACTOR AT A SUPERCOOLING OF 4.9K<sup>135</sup>

### Outlook

Investigation by means of the V - form reactor and the FBRM™ validates that although time consuming, it is an almost accurate (depending on the cryostat and temperature control system used) and inexpensive alternative to automated reactors. Research was furthered in this work with the help of an automated reactor called the EasyMax™ from Mettler Toledo GmbH.

#### 5.3.5.2. EasyMax™ Reactor – FBRM™ setup

Multiple charges of the same sample were required for these experiments as the sample volume required per experiment was much larger. An average of the characteristics thermal transition points from the DSC thermograms were taken as basis for the calculations of the induction times. The thermograms of one of the charges of each the PUFA mixtures are shown in the following Figure 5-43.

Investigations showed that a high oleic content in the PUFA mixtures lead to higher induction times,  $\tau$ . Unlike previous investigations, a clear relation between  $\tau_i$  and cooling rates was established.  $\tau$  increases with increasing cooling rates and decreasing supercooling. Activation energies of nucleation,  $\Delta G_c'$  were determined by means of the Fisher Turnbull equation

wherein  $\Delta G'_c$  decreases exponentially with increasing supercooling. Investigations and further evaluations conclude that while the plot establishes the effect of supercooling on  $\Delta G'_c$ , it does not incorporate the effects of molecular diffusion or the cooling rate. Hence, 3D modeling was performed to visualize the combined effects of cooling rate and supercooling on induction time.<sup>10</sup>

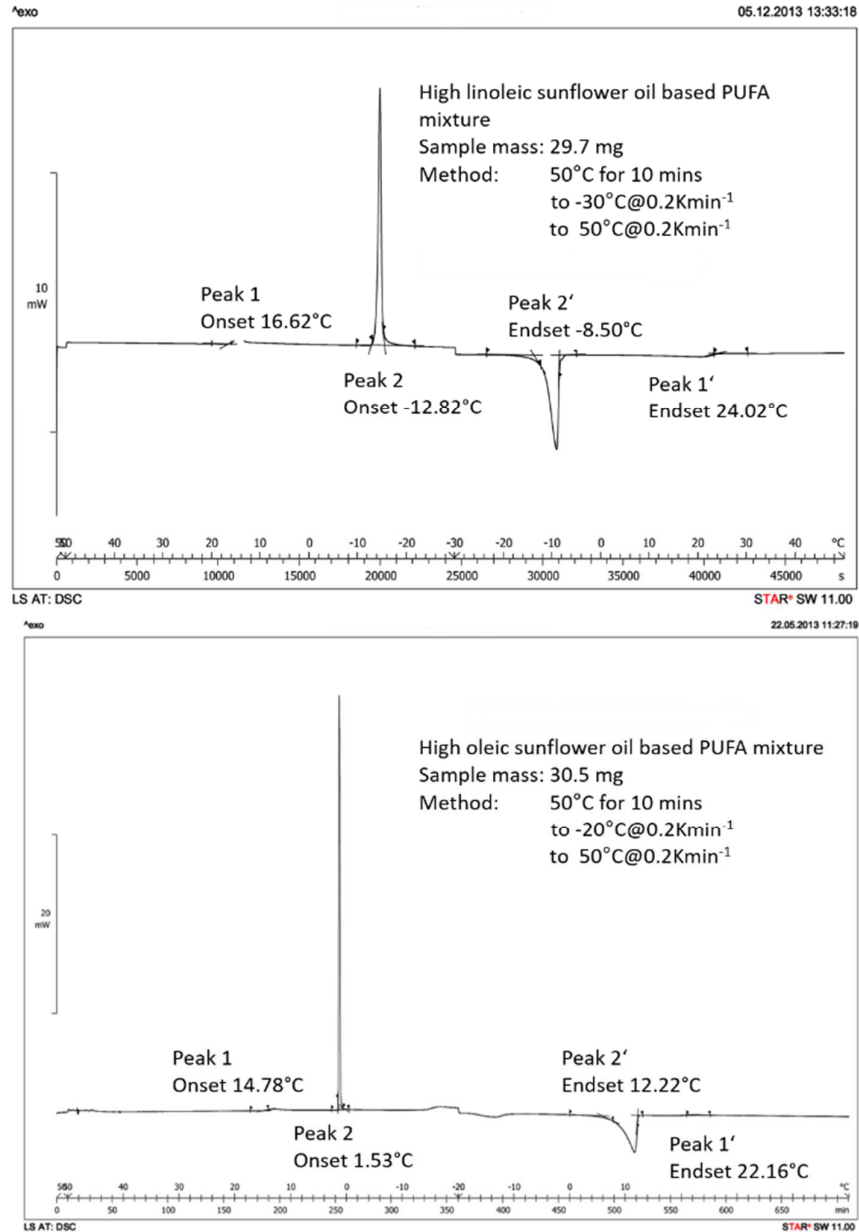


**FIGURE 5-43:EXAMPLE OF A HIGH LINOLEIC (PUFA 1 - TOP) AND HIGH OLEIC (PUFA 2 - BOTTOM) SUNFLOWER OIL BASED PUFA MIXTURE THERMOGRAM BY THE DSC<sup>10</sup>**

Induction time measurements with FBRM™ show higher values for the high oleic fatty acid mixture named PUFA 2 for ease of identification in this section. The high linoleic acid based

sunflower oil mixture has been termed as PUFA 1 to enable an easier read. PUFA 1 and 2 differ in their compositions owing to the type of sunflower oil, high linoleic and high oleic they are sought from. Saturated fatty acids are primarily responsible for nucleation in these mixtures. Hence, lower content of palmitic and stearic acid in PUFA 2 reduces the probability of nucleation leading to higher induction times. <sup>10</sup>

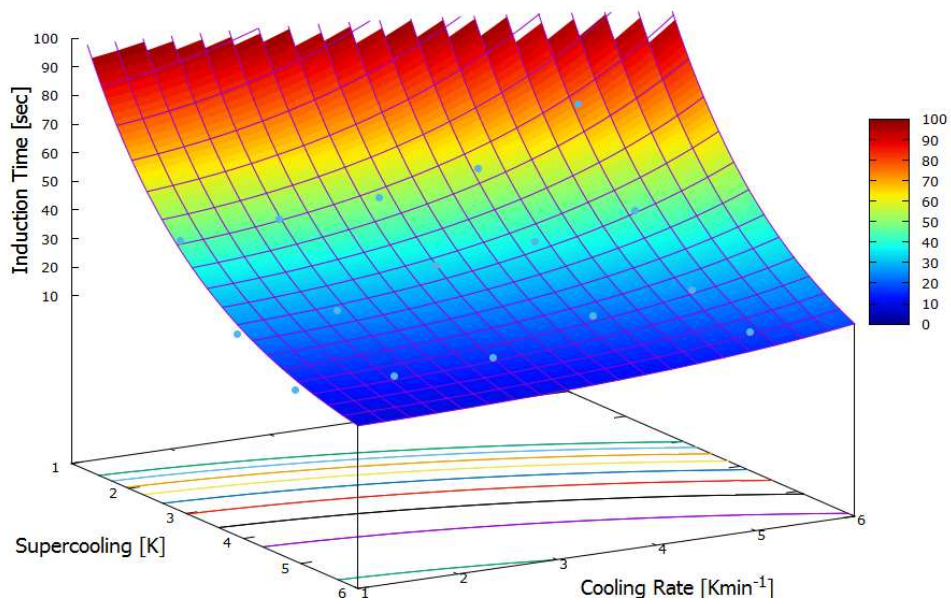
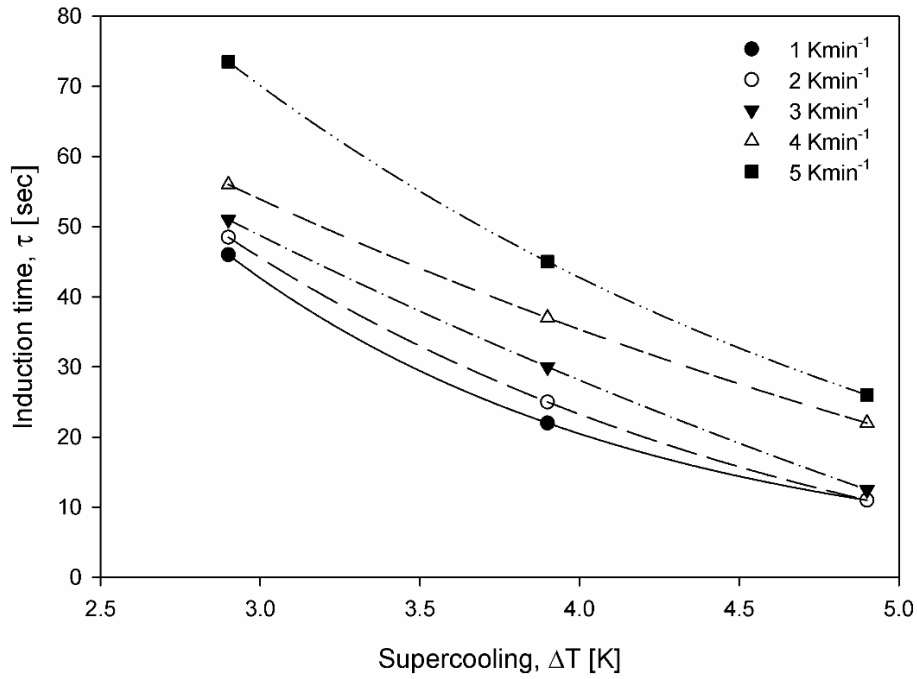


FIGURE 5-44: **TOP:** INDUCTION TIME VS. SUPERCOOLING FOR PUFA 1 AT DIFFERENT COOLING RATES; **BOTTOM:** 3D MODELING OF INDUCTION TIME OVER COOLING RATE AND SUPERCOOLING FOR PUFA 1<sup>10</sup>

Further, higher viscosity  $\eta$ , of PUFA 2 owing to the presence of a high percentage of oleic acid ( $\eta_{18:1} > \eta_{18:2}$ ), causes greater diffusion resistance to the process of nucleation.<sup>158</sup> These results are also in accordance to the results in the micro-scale experiments on the same samples. The metastable range of crystallization is significantly increased by the increase in sample bulk volume. The measurements also show a clear dependency of induction time on crystallization temperature. A higher level of supercooling leads to a faster nucleation. Apart from this, the cooling rate is also an influencing factor on the induction time as shown in Figure 5-44 and Figure 5-45. The 2D regression and modeling was performed by SigmaPlot Version 11.0.

	Regression equation	Cooling rate [K/min]	Coefficient			R <sup>2</sup>
			y <sub>0</sub>	a	b	
Induction time vs. Supercooling (Figure 5-44 and Figure 5-45)	PUFA 1 $y = y_0 + a \cdot e^{-bx}$	1	1.69	425.7	0.78	1
		2	-9.63	261	0.53	0.99
		3	-7.5	214	0.55	0.92
		4	-3.43	179	0.24	0.99
		5	-1.2	277	0.41	1
	PUFA 2 $y = y_0 + a \cdot e^{-bx}$	1	100	13110	0.90	1
		2	118	11410	0.85	1
		3	136	19900	0.98	1
		4	108	8734	0.74	1
		5	202	30410	1.08	1
3D modeling of Induction time over supercooling and cooling rate (Figure 5-44 and Figure 5-45)	PUFA 1 $f(x, y) = a \cdot e^{bx+cy^2}$	a	199.67	0.53	0.23	
		b				
	PUFA 2 $f(x, y) = a \cdot e^{b/x+cy}$	a	22.72	-0.52	0.01	
			c			

TABLE 5-14: REGRESSION COEFFICIENTS AND EQUATIONS WITH RESPECT TO OPERATING PARAMETERS FOR 4-14 AND 4-15<sup>10</sup>

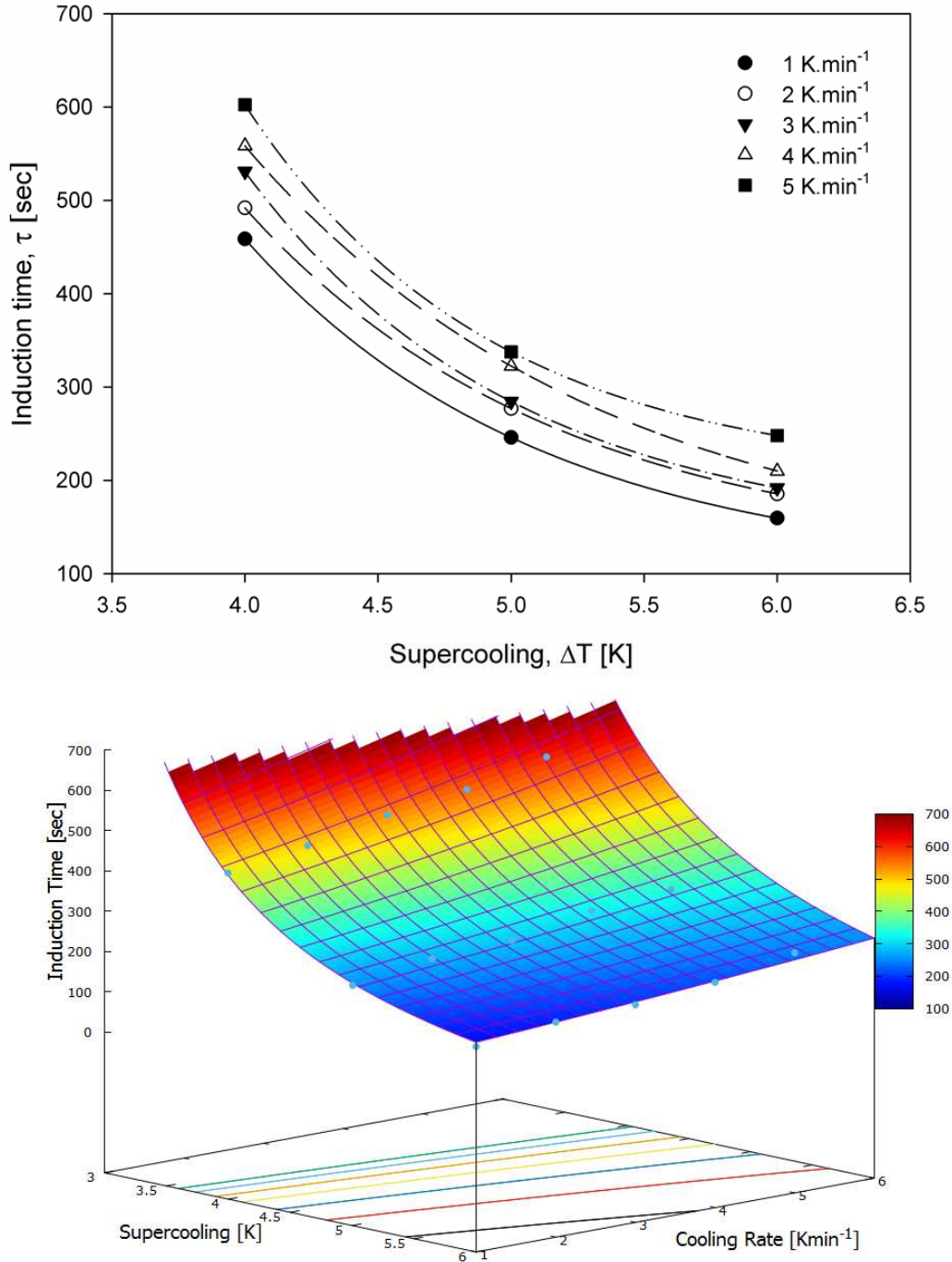


FIGURE 5-45: TOP: INDUCTION TIME VS. SUPERCOOLING FOR PUFA 2 AT DIFFERENT COOLING RATES; BOTTOM. 3D MODELING OF INDUCTION TIME OVER COOLING RATE AND SUPERCOOLING FOR PUFA 2<sup>10</sup>

The viscosity in the pertinent temperature range is the key influencing factor as higher cooling rate enables faster reaching of lower temperatures which in turn leads to higher viscosities. Therefore, it reduces the probability of nucleation due to molecular diffusion resistance. The opposing effects of supercooling and cooling rate decides the magnitude of induction time.<sup>25</sup>

3D modeling of the combined influence of cooling rate and supercooling on induction time has been performed with the help of a data fitting library of pyeq2, a collection of python equations and a plotting program called gnuplot Version 5.0 (Figure 5-44B and Figure 5-45B). The empirical formula behind these 3D functions fitting the aforementioned tested range of supercooling and cooling rates are given in Table 5-14.<sup>10</sup>

This modeling enables one to visualize the combined opposing effect of supercooling and cooling rates shows that the induction time continues to slowly reduce with increasing supercooling in spite of increasing cooling rate. The 3D hulls for both PUFA 1 and 2 have been illustrated in an angle such that it is possible to visualize the exponential decay on one hand (between supercooling and induction time) and the linear increase on the other (between cooling rate and induction time).<sup>10</sup>

The experiments were left to run long enough in order to check the maximum deviation in temperatures that could occur in various significant positions in the reactor. Multiple thermal sensors were placed in order to check temperature discrepancies in the reactor filled with sample over a period of time.

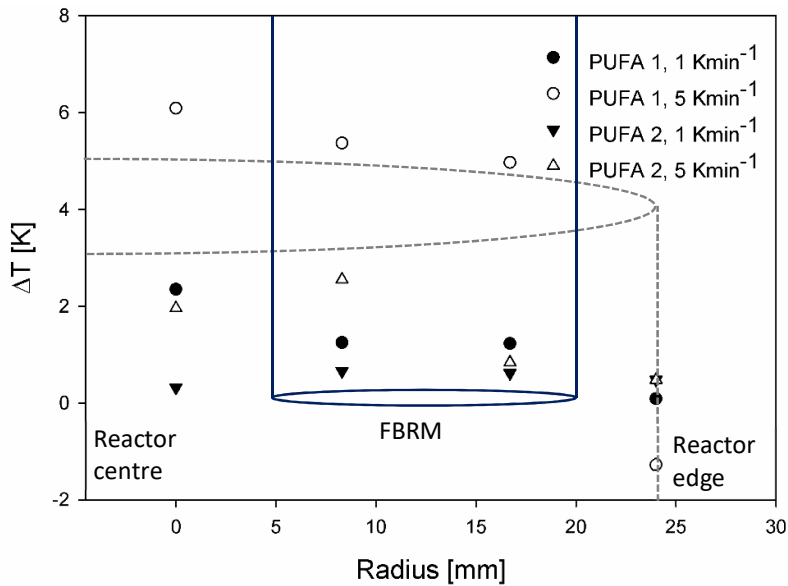


FIGURE 5-46: TEMPERATURE DISCREPANCY PLOT FOR PUFA 1 AND 2 AS A FUNCTION OF THE RADIUS OF THE EASYMAX™ REACTOR<sup>10</sup>

Two cooling rates 1 Kmin<sup>-1</sup> and 5 Kmin<sup>-1</sup> were chosen for the comparison. Both the samples PUFA 1 and 2 were used so as to check the effects of viscosities as well. The temperature set,

was 20°C for PUFA 1 and 17°C for PUFA 2. The evaluated temperature profile in Figure 5-46 illustrates high internal temperature gradients as expected which increased dramatically with increasing cooling rate. It depicts how the level of super-saturation increases as one goes away from the bulk and towards the cooling jacket. The unavoidable local higher levels of supersaturation near the wall as a result of higher cooling rates should lead to decreasing induction times because the probability of nucleation increases. In spite of this, experimental results as shown in Figure 5-44 and Figure 5-45 arrive at a conclusion in accordance to theory because the significant influence of the viscosity or the diffusion resistance masks the effect of discrepancies in super-saturation. In other words, higher cooling rate leads to longer times in higher viscosity range leading to a higher induction time irrespective of super-saturation inconsistencies.<sup>10</sup>

It can be noted in the 3D plot illustrating the influence of supercooling and cooling rate as for example in Figure 5-45, that for the investigated range, super-saturation is the dominating factor of influence. In the range of cooling rate investigated, which is between 1 – 5 Kmin<sup>-1</sup>, the effect of cooling rate on induction time appears to follow a linear trend. The models shown can be used to predict induction times in the nearby ranges and for the values in between as well. Due to equipment limitations higher cooling rate could not be applied without avoiding a relatively large temperature difference between the jacket and inner wall temperatures of the reactors in the Easymax™. On the other hand, precise cooling rates higher than 5 kmin<sup>-1</sup> is difficult to realize in bulk phenomena reactors in the industry as well. As for using the data for micro-reactor development, higher cooling rates were applied and results were also investigated.<sup>10</sup>

The range of supercoolings investigated started at a temperature below the liquidus point in the reactor and went down to a temperature post which spontaneous and dynamic nucleation occurred wherein the induction time was negative. Such results could not be taken into consideration as the induction times could not be associated with a particular supercooling. As it is noted here and in literature<sup>73</sup>, less supercooling and higher cooling rate amounts to less number of nuclei but that does not necessarily mean that the crystal growth rate would be the same or higher for less number of nuclei than for higher number of crystals. There is only one literature<sup>14</sup> wherein the detection of nucleation of fatty acids as a function of crystallization temperature has been depicted. The results of this dissertation have not

been compared with this literature<sup>14</sup>, as according to the latter crystal count reduces to zero with time at constant crystallization temperature which is incomprehensible in real systems. The results generated in literature<sup>14</sup> was performed by PsyA, also a Laser beam reflectance method.



### 5.3.6. Minimum size class detected under the FBRM- Easymax setup

Two examples of the some of the online nucleation detection data collected from the Easymax™ and FBRM™ setup have been plotted in Figure 5-47 and Figure 5-48. These figures plot the increase in the number of nuclei per second as detected by the FBRM™ for the lowest count classes available, which are namely, less than 10 μm and 10-50 μm against time. The sample has been cooled from 50°C to 21°C at a cooling rate of 2Kmin<sup>-1</sup> in Figure 5-47 whereas the desired crystallization temperature in Figure 5-48 is 19°C also cooled at a rate of 2Kmin<sup>-1</sup>.

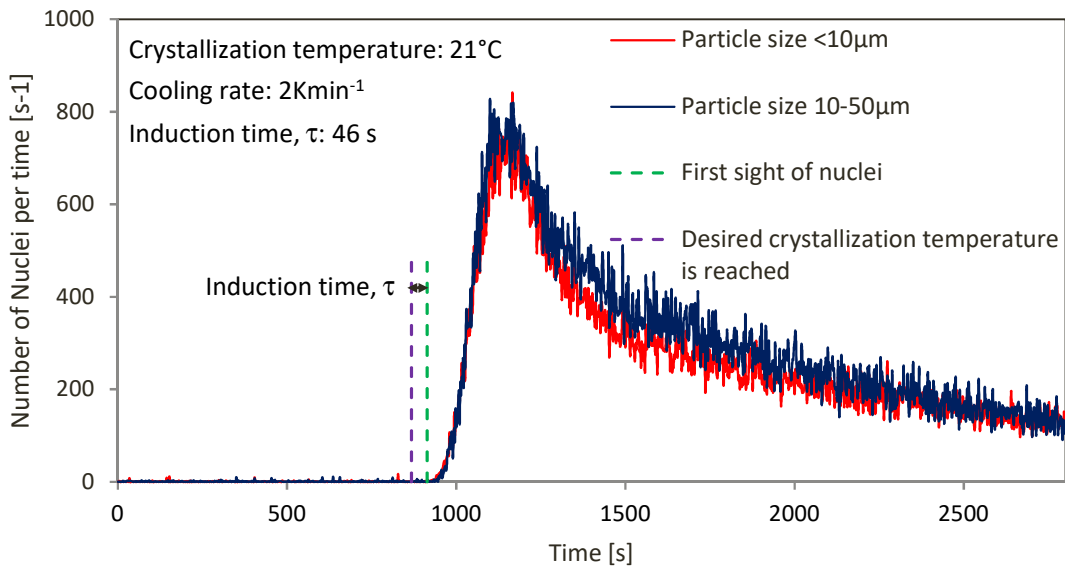


FIGURE 5-47: NUMBER OF NUCLEI PER SECOND COUNTED BY THE FBRM™ INSERTED INTO A HIGH LINOLEIC PUFA MIXTURE CRYSTALLIZED IN THE EASYMAX™ AT 21°C

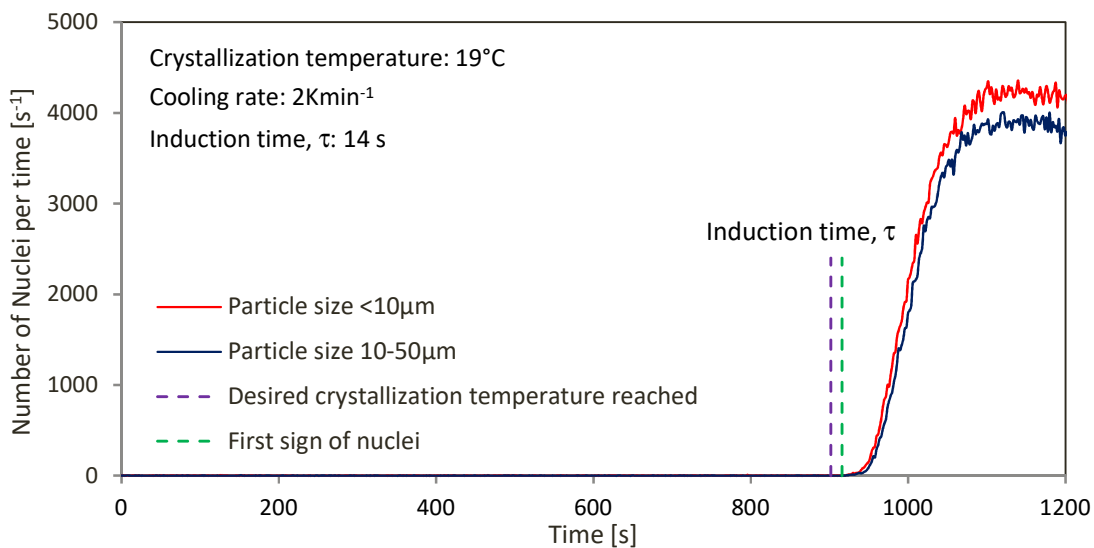


FIGURE 5-48: NUMBER OF NUCLEI PER SECOND COUNTED BY THE FBRM™ INSERTED INTO A HIGH LINOLEIC PUFA MIXTURE CRYSTALLIZED IN THE EASYMAX™ AT 19°C

As illustrated, the induction time determined in this work under this setup, which for example in Figure 5-47 is 46 seconds, represents the time required to detect the crystals of a size class less than 10 $\mu\text{m}$ . This means that the crystals of this class are less than 10 $\mu\text{m}$  at least in one dimension. As multiple crystals below 10 $\mu\text{m}$  and between 10 and 50  $\mu\text{m}$  are being detected in a matter of a few seconds, statistically there is a good chance that some of the first few detected crystals might be less than 10  $\mu\text{m}$ . The FBRM™ detected crystals in the melt before it caught the naked eye of the investigator as well. The accuracy of the crystal sizes detected in denser and larger reactors have been discussed in Section 5.3.8.

### 5.3.7. Gibbs free energy for nucleation using the Fisher Turnbull and Gibbs Thompson model (ml scale)

Additionally, the induction time measurements were used to calculate the activation barrier for nucleation with the Fisher Turnbull Plot (Figure 5-49 for PUFA 2) as described earlier in Equation 3-1 to Equation 3-24. The slopes and corresponding activation barriers are summarized in Table 5-15 and Table 5-16.

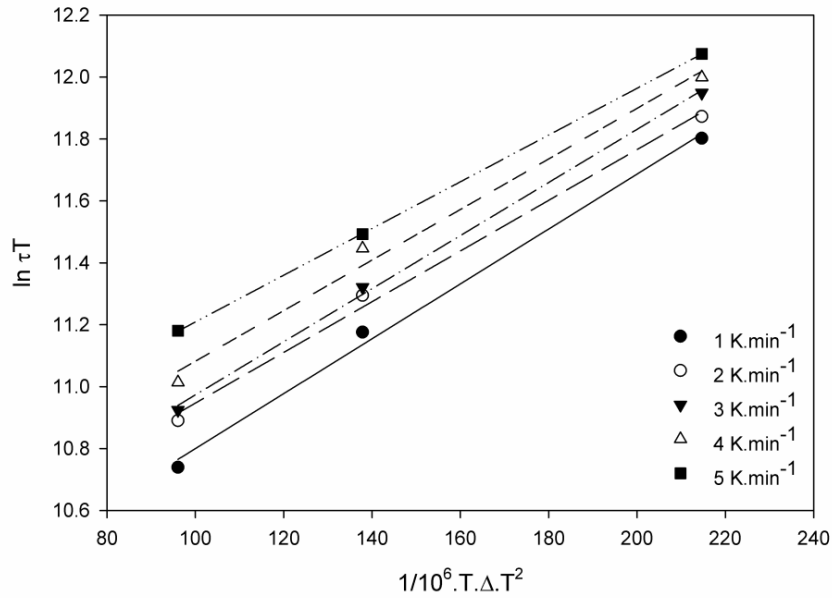


FIGURE 5-49: FISHER TURNBULL MODEL FITTED FOR NUCLEATION DATA FOR PUFA 2<sup>10</sup>

Supercooling [K]	Cooling rate [K.min <sup>-1</sup> ]				
	1	2	3	4	5
1	45728	43234	38246	24943	22449
1,5	20324	19215	16998	11086	9977
2	11432	10809	9561	6236	5612
2,5	7317	6917	6119	3991	3592
3	5081	4804	4250	2771	2494
3,5	3733	3529	3122	2036	1833
4	2858	2702	2390	1559	1403
4,5	2258	2135	1889	1232	1109
5	1829	1729	1530	998	898

TABLE 5-15: :  $\Delta G_c$  VALUES [J/MOL] FOR PUFA 1 FROM FISHER TURNBULL PLOT<sup>10</sup>

The high oleic PUFA 2 has higher activation barriers, which leads to the higher values of induction time than those of PUFA 1. Furthermore, the activation free energy of nucleation decreases exponentially with increasing supercooling and therefore is in good agreement

with theory. It is observed to be more sensitive for PUFA 1 owing to the bigger range of the slope for the given cooling rates. Upon evaluation with the Fisher Turnbull plot, it is observed that the  $\Delta G_c'$  decreases with increasing cooling rates (Figure 5-50 and Figure 5-51).<sup>10</sup>

Supercooling [K]	Cooling rate [K.min <sup>-1</sup> ]				
	1	2	3	4	5
1	73997	68177	71503	68177	62357
1,5	32888	30301	31779	30301	27714
2	18499	17044	17876	17044	15589
2,5	11840	10908	11440	10908	9977
3	8222	7575	7945	7575	6929
3,5	6041	5565	5837	5565	5090
4	4625	4261	4469	4261	3897
4,5	3654	3367	3531	3367	3079
5	2960	2727	2860	2727	2494

TABLE 5-16:  $\Delta G_c'$  VALUES [J/MOL] FOR PUFA 2 FROM FISHER TURNBULL PLOT<sup>10</sup>

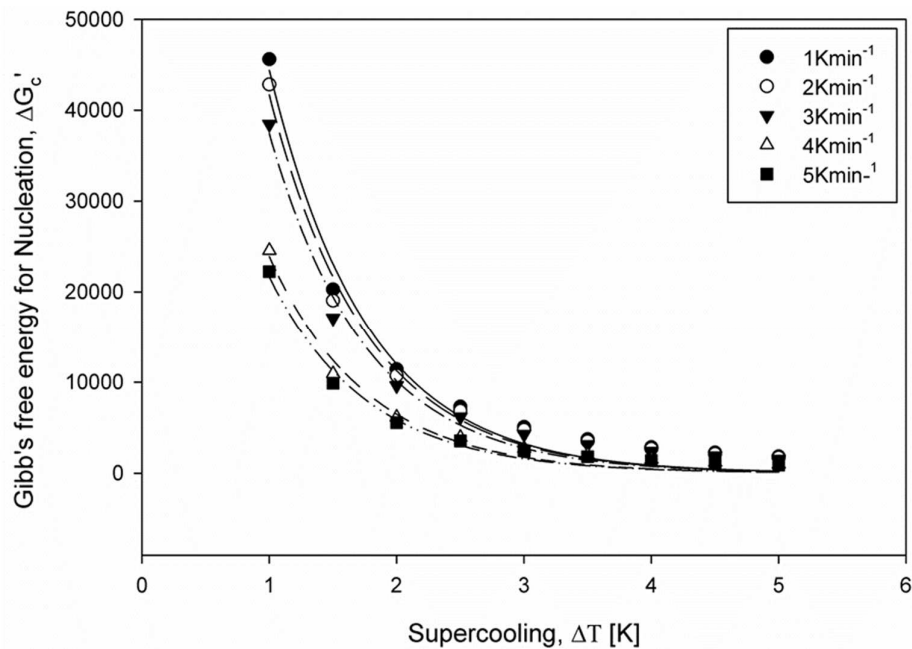


FIGURE 5-50: GIBB'S FREE ENERGY FOR NUCLEATION FOR PUFA 1<sup>10</sup>

This is, although it seems, not in contradiction to the induction time results determined in this work. Similar results for  $\Delta G_c'$  although for other systems were presented by Toro-Vazquez et al.<sup>25</sup> by means of scanning diffusive light scattering method. It is to be noted that these are the values of only the Gibb's free energy of nucleation or formation.

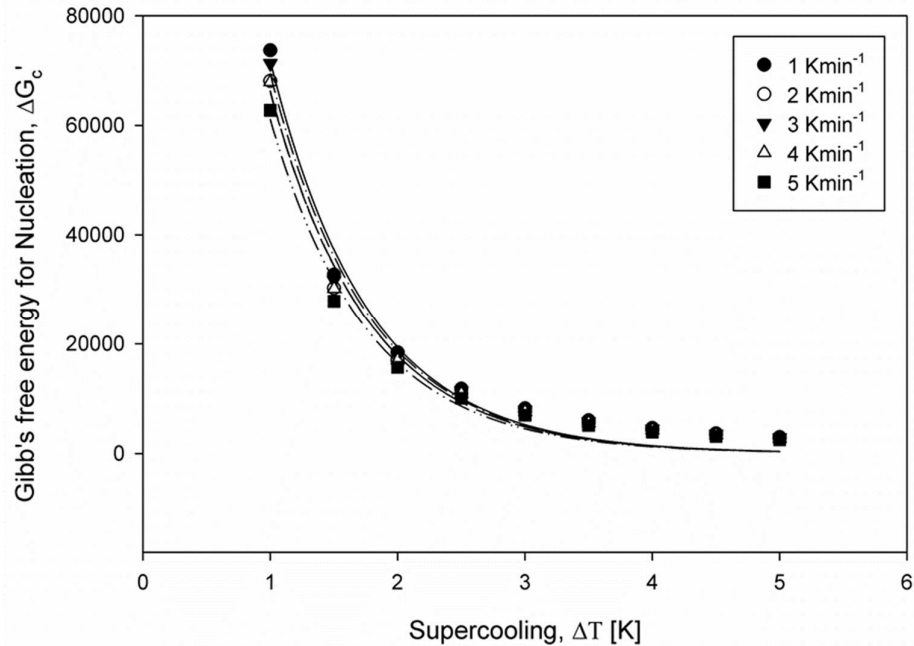


FIGURE 5-51: GIBB'S FREE ENERGY FOR NUCLEATION FOR PUFA 2<sup>10</sup>

This phenomenon can be explained by the fact that the enthalpy of diffusion is not taken as a variant in the slope that is evaluated. As already explained, this diffusion enthalpy as a result of changing viscosities is a key influencing factor for induction times. Hence, while with the help of the Fisher Turnbull plot, the Gibbs's free energy of formation is evaluated, the combined effects of supercooling and viscosity determines the final induction time of nucleation. The Fisher Turnbull equation comprises of two exponential parts, one for the Gibbs free enthalpy for formation,  $\Delta G'_c$ , and other for diffusion,  $\Delta G'_d$ .  $\Delta G'_d$  by definition is based on the fraction of molecules that are in the right confirmation to add on to the embryo to form a nucleus and the reduction in the randomness of saturated molecules upon crystallization. It can be concluded that while the plot accurately justifies the effect of supercooling on  $\Delta G'_c$ , it does not incorporate the entire (although almost) effects of molecular diffusion or viscosity and hence the entire effect of the cooling rate within the metastable range of crystallization.  $\Delta G'_d$  is a very small value in this case when compared to the  $\Delta G'_c$  value. Therefore, it is correct to note that cooling rate has very little influence on the Gibbs free enthalpy of formation from an embryo state to a nucleus. The combined effect of these opposing factors of supercooling and diffusion were successfully interpreted upon visualization of the hull obtained by 3D modeling of the parameters.

### 5.3.8. Outlook: FBRM™ on crystal growth kinetics in a Vibromix reactor (L scale)

Melt crystallization of a fraction of a linseed oil based PUFA was also performed in a Vibromix™ reactor.<sup>28</sup> The Vibromix is a cylindrical glass vessel with a capacity of 3L and a radius of 55 mm. It comes with a cooling jacket. Thermal sensors to track the temperature of

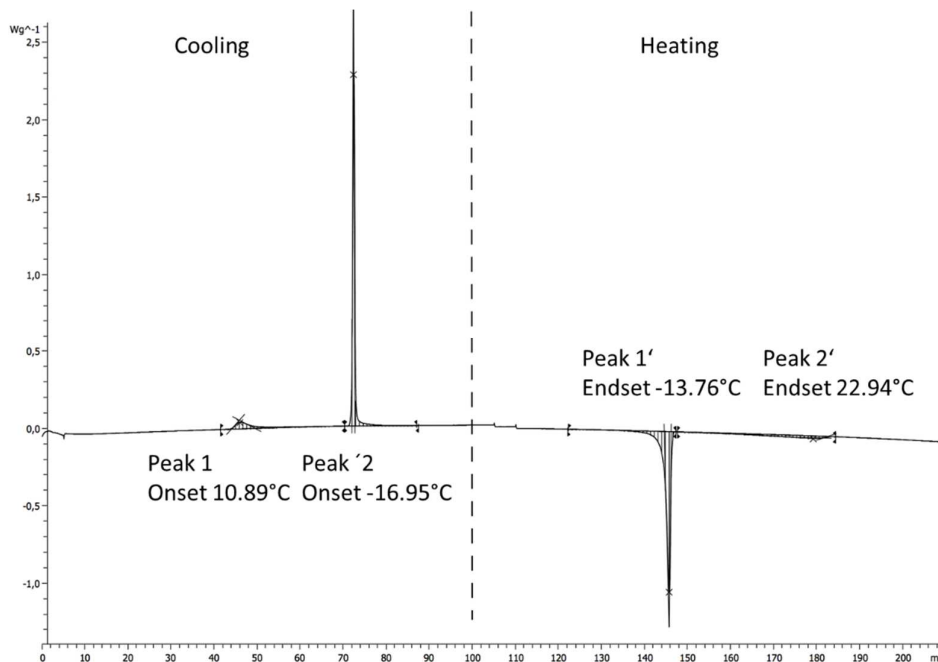
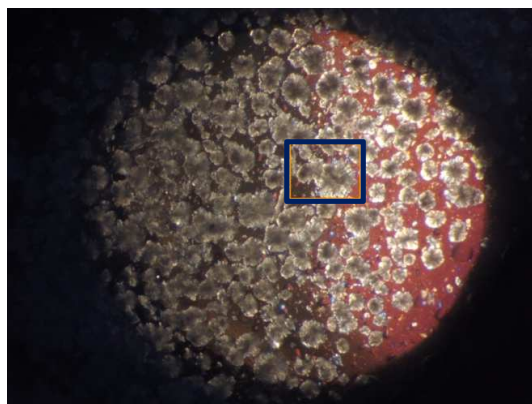


FIGURE 5-52: DSC THERMOGRAM OF A LINSEED OIL BASED PUFA FRACTION (50°C TO -50°C TO 50°C AT 1 KMIN<sup>-1</sup>)<sup>28</sup>

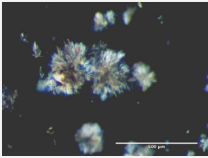
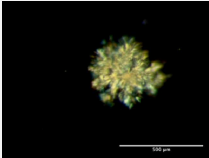
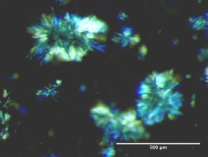
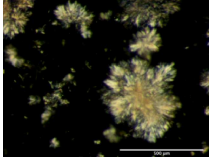
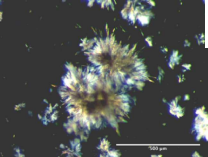
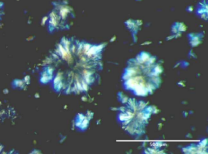
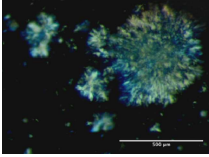
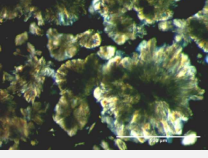
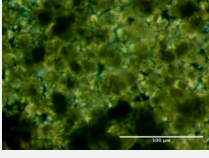
the sample inside the reactor were installed at evenly distributed heights (37; 74; 111; 148 mm from reactor bottom) and radii (29; 34; 39; 44 mm to axis) enabling a 3 dimensional temperature sensing system. Agitation was applied by a vertically moving perforated disk at different speeds (10; 15; 25; 35 mms<sup>-1</sup>) manufactured specially to fit the FBRM™ and the thermocouples. Sample volume of 2L was heated up to 40°C at the beginning of each experiment to remove any crystallization history.<sup>28</sup> The thermogram pertaining to the fraction involved is given in Figure 5-52. It can be noted from the thermogram that spontaneous nucleation starts at 10.89°C whereas the liquidus point lies at 22.94°C, defining the metastable range for this fraction.<sup>28</sup> Naturally due to the presence of a large stirrer in this reactor, the point of spontaneous nucleation is significantly raised as a result of secondary heterogeneous nucleation. Experimental results suggested that for crystallization temperatures below 17°C, the system started to nucleate even before the end temperatures were attained. An exothermic reaction was noted by the temperature control system wherein

the temperature of the system was suddenly raised in spite of the subjected cooling. As noted in the previous section, the reactor volume to surface ratio is larger than before. Although in this case, the cooling medium was unable to take out the enthalpy of crystallization as well as in the automated EasyMax™ reactor. Results also showed that a higher rate of agitation amounted to a higher number and lower size of crystals produced which is in accordance to theory. The samples were further cooled at a very slow cooling rate of  $0.01 \text{ Kmin}^{-1}$  in order to favor crystal growth over nucleation. This was done based on the success of results achieved for the original linseed oil based PUFA mixture as shown in Figure 5-1 and Figure 5-2.<sup>11,18</sup> Higher cooling rates such as  $0.1 \text{ Kmin}^{-1}$  and  $0.5 \text{ Kmin}^{-1}$  resulted in negative results giving way to nucleation over crystal growth. A linear cooling rate could not be enabled inside the reactor owing to real conditions and therefore the temperature of the cooling medium served as the reference. Hence it was difficult to refer to a real time zero so as to calculate the induction times. Better heat transfer is to be applied for ideal temperature control as for example by introducing the cooling medium also inside the stirring device. Owing to the gentle mixing of the reactor contents, the crystal content was clearly distinguishable from the mother liquor as can be seen in Table 5-17.<sup>28</sup> Samples from the experiment with  $17^\circ\text{C}$  as the first crystallization temperature were taken at regular intervals and checked under the microscope. This was done to validate and understand the success of FBRM™ as a sensor for crystal growth kinetics during the melt crystallization of PUFA mixtures.<sup>28</sup>



**FIGURE 5-53:: ENTIRE PICTURE AREA, VIBROMIX AT T=21:00 MINUTES; MARKED SECTION REPRESENTS THE MAGNIFICATION IN TABLE 5-17<sup>28</sup>**

A comparison between identical experimental conditions applied to the Vibromix™ reactor and a reactor with a blade stirrer is made in Table 5-17.<sup>28</sup> Figure 5-53 represents the entire picture of which a magnification has been used for comparison in Table 5-17. The temperature profile used has been shown in the table itself. It showed that the Vibromix can create crystals of adequate size for easy separation by means of pressure filtration. Information gathered from the fundamental nucleation studies along with metastable zone width determination eased the process of deciding the optimal temperature profiles.<sup>28</sup>

Time[h:min]	Vibromix reactor ( $v_d=10\text{mms}^{-1}$ )	Reactor with blade impeller ( $v_b=5\text{rpm}$ )
CR 1		
		
CR 2		Start of second cooling sequence
		
		

**TABLE 5-17: IMAGES OF FATTY ACID CRYSTALS, TAKEN AFTER FIRST CRYSTALS WERE DETECTED (T≈1:00). APPLYING THE VIBROMIX REACTOR (LEFT) AND THE BLADE IMPELLER REACTOR (RIGHT). TC=17°C; COOLING RATE 1=2KMIN<sup>-1</sup>; COOLING RATE 2=0.01KMIN<sup>-1</sup>,<sup>28</sup>**



The next investigations should concentrate based on the information gathered from this work, on crystal growth kinetics both in micro reactor and larger bulk reactor scale and apply them for effective separation technologies. It was also noticed as the critical analysis of FBRM™ was made in detail in Section 4.5.3 that although the crystal size was well around a diameter of 500µm approximately, the FBRM™ mostly detected only chord lengths of 30-40 µm. This again highlights the point that FBRM™ is more suited for investigations on nucleation than crystal growth studies.<sup>28</sup>

## 6. Summary

This work primarily aims to provide a detailed and fundamental understanding of the crystallization especially nucleation kinetics of vegetable oil based fatty acid mixtures. It also describes the SLE phase diagrams of these PUFA mixtures including their metastable zone widths of nucleation and solidification. Firstly, an extensive review on the global production and application of vegetable oils and their derivatives has been made in Section 2. A clear mathematical and physical road map for the application of the Fisher Turnbull model to calculate the enthalpy values starting from the basic supersaturation equation has been established and extensively explained in Section 3. The importance and the reasons behind the methods and equipment chosen for these investigations along with a critical analysis of the main nucleation detector, FBRM™ chosen has been made in Section 4. Nucleation studies have been carried out on various reactor setups in micro-, milli- and liter-scale.

Interpretation and construction of SLE phase diagrams of natural plant based fatty acids mixtures by means of a DSC and GC-FID setup was performed firstly in order to identify their characteristic melt crystallization behaviors. To check and validate the performance of the DSC in order to construct the SLE diagrams, a visualization of the process was enabled in-situ during DSC measurements. The visuals from the microscope not only validated the performance but also showed that the DSC measures the phase transition much before the microscope catches any change. Flash DSC performances were also checked for effects on the metastable ranges. To understand and control the execution of the two underlying mechanisms of crystallization, namely, nucleation and growth, metastable zone width were determined both for the liquidus as well as the solidus curves for each of the systems. A definite dependency of the liquidus as well as the solidus lines of the SLE diagrams of all PUFA mixtures on the oleic acid content of the PUFA mixture was established.

Further investigations were made to justify the effectiveness of melt crystallization on purification of the unsaturated content from the natural PUFA mixtures. Compositions of up to less than 1% C18:0 and less than 2% C16:0 were easily achievable in a single stage crystallization of the melt. The deciding factor is the temperature profile and the engineering issue to enable optimal application on the PUFA mixture. On one hand, the metastable range of crystallization of the PUFA mixtures while on the other the techniques applied to

investigate the kinetics are directly dependent on the reactor geometry and sample volume. The other factor is also whether an in-situ or offline measurement is taken into account. Coming to nucleation kinetics, the ratio of bulk to surface kinetics radically reduces with lesser sample volume and for example, micro-reactor geometry. In spite of using appropriate measurement techniques for at-line real time investigations, the changing effects of heterogeneous nucleation owing to variations in contact with foreign surfaces caused by stirrer, FBRM™, reactor, temperature sensor etc. cannot be undermined. Therefore, every result is very specific to its setup. However, such influences in real systems are inevitable. Thus both micro and milliliter scale investigations were carried out so as to obtain a trend and understanding and also generate fundamental data for the kinetics of crystal formation including induction time and Gibb's free enthalpy of crystallization. It can be inferred and concluded from the results that although the effects of cooling rates differ in micro and macro scale experiments, the consistent effect of supercooling is the dominating factor. Induction time reduces exponentially with increasing supercooling irrespective of the range of cooling rates, investigated. In the milliliter tests, induction time increases with decreasing cooling rates which is adhering to the bulk phenomena and is in accordance to theory. On the other hand, for micro-volume flat reactors, nucleation is faster with higher cooling rates, owing to surface kinetics or even maybe wall nucleation depending on cooling setups. Finally, it successfully models the induction times of nucleation as a function of supercooling at different cooling rates both in micro and macro scale. 3D modeling of this parameter to see the combined effects of temperature and viscosity have also been successfully implemented on the milliliter scale results, as more of the bulk nucleation phenomenon was observed in the latter. It can be summarized for the bulk phenomena that the investigated two parameters of supercooling and cooling rate influencing the nucleation followed by the melt crystal growth process, affect the viscosity of the liquid in different manners. Supercooling affects also the final viscosity of the sample but in spite of that if nucleation has not yet taken place till this supercooling has been fully implemented, then the induction time will be shorter than in the case of lesser super-saturation. The liquid although relatively more viscous at a higher supercooling and hence amounting to a higher diffusion resistance, will still work in the favor of a shorter induction time to nucleation due to the higher supersaturation created by the thermal effect, making the latter the dominating effect. On the other hand, there are the cases where the parameter supercooling is kept constant at a temperature below the

liquidus point and the cooling rate is varied to reach this constant supercooling. In the latter, the cooling rate would decide how long the sample would require to nucleate. In this case, the higher the cooling rate, the lesser the time that the sample has, to settle into equilibrium with the dynamic super-saturations over the temperature profile once it crosses the liquidus point. The higher the cooling rate, the longer it would take for the sample to nucleate owing to a higher diffusion resistance. Although supercooling results in supersaturating the liquid and cooling rate amounts to mainly varied diffusion resistance periods, one cannot separate one effect from another. This is plainly because both affect the viscosity and thereafter the diffusive property of the sample. But in spite of that, it is true, that their effects are opposite as shown in Section 5.3.5.2.

Supplementary crystal growth investigations carried out capillaries suggested that a thinner capillary can influence the crystal to grow unidimensionally. These results can be applied in conceptualizing reactor designs in future. Contact angle measurements were also performed on a variety of material substrates so as to check the behavior of each type of PUFA droplet on each of them. The conclusions inferred from experiments on glass were similar to those obtained on stainless steel, which ensures that the results obtained on glass can be directly applied over on stainless steel reactor provided every other conditions and parameters are met with. Structural steel, although proved to be having the highest contact angle amongst all the substrates. All the PUFA mixtures, irrespective of their unsaturations behaved similarly with respect to contact angle measurements.

## References

- (1) Biermann, U.; Bornscheuer, U.; Meier, M. A. R.; Metzger, J. O.; Schafer, H. J. Oils and fats as renewable raw materials in chemistry. *Angewandte Chemie (International ed. in English)* **2011**, *50*, 3854–3871.
- (2) D. M. Ohlmann. Neue katalytische Reaktionen zur Funktionalisierung ungesättigter Fettsäuren und ihrer Derivate: Effiziente Doppelbindungsisomerisierung als Schlüsselschritt, University of Kaiserslautern, 2012.
- (3) Bayerische Landesanstalt für Landwirtschaft. Agrarmärkte 2014.
- (4) Dasgupta, S.; Ay, P.; Schulz, S. Determination and Comparison of Equilibrium Data of Various Plant-Based Fatty Acid Mixtures. *Chem. Eng. Technol.* **2014**, *37*, 1002–1008.
- (5) Ma, F.; Hanna, M. A. Biodiesel production: A review. *Journal Series #12109, Agricultural Research Division, Institute of Agriculture and Natural Resources, University of Nebraska–Lincoln*.1. *Bioresource Technology* **1999**, *70*, 1–15.
- (6) MEHER, L.; VIDYASAGAR, D.; NAIK, S. Technical aspects of biodiesel production by transesterification—a review. *Renewable and Sustainable Energy Reviews* **2006**, *10*, 248–268.
- (7) Peterson, C. L.; Auld, D. L.; Korus, R. A. Winter rape oil fuel for diesel engines: Recovery and utilization. *J Am Oil Chem Soc* **1983**, *60*, 1579–1587.
- (8) Stemmelen, M.; Pessel, F.; Lapinte, V.; Caillol, S.; Habas, J.-P.; Robin, J.-J. A fully biobased epoxy resin from vegetable oils: From the synthesis of the precursors by thiol-ene reaction to the study of the final material. *J. Polym. Sci. A Polym. Chem.* **2011**, *49*, 2434–2444.
- (9) López Téllez, G.; Viguera-Santiago, E.; Hernández-López, S.; Bilyeu, B. Synthesis and Thermal Cross-Linking Study of Partially-Aminated Epoxidized Linseed Oil. *des monomers polym* **2008**, *11*, 435–445.
- (10) Dasgupta, S.; Rettig, F.; Ay, P. Nucleation Kinetics during Melt Crystallization of Plant Based High Oleic and Linoleic Polyunsaturated Fatty Acid Mixtures. *Crystal Growth & Design* **2016**, *16*, 861–866.
- (11) Dasgupta S., Dreijack N., Ay P. Melt crystallization kinetics for enrichment of highly unsaturated fatty acid fractions based on Linseed oil. *J. Environ. Res. Develop* **2016**, *11*, 1–6.
- (12) W. Stein. Fettchemische und petrochemische Rohstoffe - Gegensatz oder Ergänzung? *Fette, Seifen, Anstrichm* **1982**, *84*, 45–54.
- (13) Lide, D. R. *CRC handbook of chemistry and physics: A ready-reference book of chemical and physical data*, 85th ed.; CRC Press: Boca Raton, Fla., 2004.
- (14) Lüdecke, U. *Fractionation of multi-component fatty acid mixtures by melt crystallization*; Berichte aus der Verfahrenstechnik; Shaker: Aachen, 2004.
- (15) Wanasundara, U. N.; Peterson, R. *Process for separating saturated and unsaturated fatty acids*; Google Patents, 2011. <http://www.google.de/patents/US8003813>.
- (16) Arkenbout, G. F. *Melt crystallization technology*; Technomic: Lancaster, Pa., 1995.

- (17) Mersmann, A. *Crystallization technology handbook*; Marcel Dekker: New York, 1995.
- (18) Dasgupta S., Dreijack N., Ay P. Enrichment of unsaturated fractions in a Linseed oil based fatty acid mixture by melt crystallisation. In *5th Workshop on Fats and Oils as Renewable Feedstocks for the Chemical Industry*; Metzger, J. O., Meier, M. A. R., Eds., 2012.
- (19) McCabe, W. L.; Smith, J. C.; Harriott, P. *Unit operations of chemical engineering*, 7th ed. / Warren L. McCabe, Julian C. Smith, Peter Harriott; McGraw-Hill chemical engineering series; McGraw-Hill: Boston, 2005.
- (20) Barrett, P.; Smith, B.; Worlitschek, J.; Bracken, V.; O'Sullivan, B.; Des O'Grady. A Review of the Use of Process Analytical Technology for the Understanding and Optimization of Production Batch Crystallization Processes. *Org. Process Res. Dev.* **2005**, *9*, 348–355.
- (21) Kulkarni, S. A.; Kadam, S. S.; Meekes, H.; Stankiewicz, A. I.; ter Horst, J. H. Crystal Nucleation Kinetics from Induction Times and Metastable Zone Widths. *Crystal Growth & Design* **2013**, *13*, 2435–2440.
- (22) Ulrich, J.; Strege, C. Some aspects of the importance of metastable zone width and nucleation in industrial crystallizers. *Journal of Crystal Growth* **2002**, *237-239*, 2130–2135.
- (23) A Mersmann. *Fundamentals of Crystallization: Crystallization Technology Handbook*; Marcel Dekker Inc.: New York, 1995.
- (24) Dasgupta, S.; Ay, P.; Kommolk, R.; Xu, S. Kinetics of Melt Crystallization of a Sunflower Oil-Based Polyunsaturated Fatty Acid Mixture. *Chem. Eng. Technol.* **2013**, *36*, 1225–1230.
- (25) Toro-Vazquez, J.; Herrera-Coronado, V.; Dibildox-Alvarado, E.; Charo-Alonso, M.; Gomez-Aldapa, C. Induction Time of Crystallization in Vegetable Oils, Comparative Measurements by Differential Scanning Calorimetry and Diffusive Light Scattering. *J Food Science* **2002**, *67*, 1057–1064.
- (26) Toro-Vazquez, J. F.; Briceño-Montelongo, M.; Dibildox-Alvarado, E.; Charó-Alonso, M.; Reyes-Hernández, J. Crystallization kinetics of palm stearin in blends with sesame seed oil. *J Amer Oil Chem Soc* **2000**, *77*, 297–310.
- (27) gnuplot. gnuplot documentation.
- (28) Poessnecker J., Eckert K., Dasgupta S., Ay P. Solvent-free crystallization of a vegetable oil based fatty acid fraction in a Vibromix reactor. *J. Environ. Res. Develop* **2017**, *11*.
- (29) Baumann, H.; Bühler, M.; Fochem, H.; Hirsinger, F.; Zobelein, H.; Falbe, J. Natural Fats and Oils—Renewable Raw Materials for the Chemical Industry. *Angew. Chem. Int. Ed. Engl.* **1988**, *27*, 41–62.
- (30) Satyarthi, J. K.; Srinivas, D.; Ratnasamy, P. Hydrolysis of vegetable oils and fats to fatty acids over solid acid catalysts. *Applied Catalysis A: General* **2011**, *391*, 427–435.
- (31) Brown, J. B. Low-temperature Crystallization of the Fatty Acids and Glycerides. *Chem. Rev.* **1941**, *29*, 333–354.
- (32) Pubchem. palmitic acid | C16H32O2 - PubChem. <https://pubchem.ncbi.nlm.nih.gov/compound/985> (accessed October 20, 2016).

- (33) Pubchem. stearic acid | CH<sub>3</sub>(CH<sub>2</sub>)<sub>16</sub>COOH - PubChem. <https://pubchem.ncbi.nlm.nih.gov/compound/5281> (accessed October 20, 2016).
- (34) Pubchem. oleic acid | C<sub>18</sub>H<sub>34</sub>O<sub>2</sub> - PubChem. [https://pubchem.ncbi.nlm.nih.gov/compound/oleic\\_acid](https://pubchem.ncbi.nlm.nih.gov/compound/oleic_acid) (accessed October 19, 2016).
- (35) Pubchem. linoleic acid | C<sub>18</sub>H<sub>32</sub>O<sub>2</sub> - PubChem. <https://pubchem.ncbi.nlm.nih.gov/compound/5280450> (accessed October 20, 2016).
- (36) Pubchem. linolenic acid | C<sub>18</sub>H<sub>30</sub>O<sub>2</sub> - PubChem. <https://pubchem.ncbi.nlm.nih.gov/compound/5280934> (accessed October 20, 2016).
- (37) Meiri, N.; Berman, P.; Colnago, L. A.; Moraes, T. B.; Linder, C.; Wiesman, Z. Liquid-phase characterization of molecular interactions in polyunsaturated and n-fatty acid methyl esters by (1)H low-field nuclear magnetic resonance. *Biotechnology for biofuels* **2015**, *8*, 96.
- (38) Nelson, D. L.; Cox, M. M.; on, B. *Lehninger principles of biochemistry*, Sixth edition, international edition.
- (39) Anneken, D. J.; Both, S.; Christoph, R.; Fieg, G.; Steinberner, U.; Westfechtel, A. Fatty Acids. In *Ullmann's encyclopedia of industrial chemistry*, 6th, completely rev. ed.; Bohnet, M., Ed.; Wiley-VCH: Weinheim, Germany, 2003.
- (40) Noweck, K.; Grafahrend, W. Fatty Alcohols. In *Ullmann's encyclopedia of industrial chemistry*, 6th, completely rev. ed.; Bohnet, M., Ed.; Wiley-VCH: Weinheim, Germany, 2003.
- (41) Ma, F.; Hanna, M. A. Biodiesel production: A review1Journal Series #12109, Agricultural Research Division, Institute of Agriculture and Natural Resources, University of Nebraska–Lincoln.1. *Bioresource Technology* **1999**, *70*, 1–15.
- (42) Pagliaro, M.; Ciriminna, R.; Kimura, H.; Rossi, M.; Della Pina, C. From glycerol to value-added products. *Angewandte Chemie (International ed. in English)* **2007**, *46*, 4434–4440.
- (43) Zhou, C.-H. C.; Beltramini, J. N.; Fan, Y.-X.; Lu, G. Q. M. Chemoselective catalytic conversion of glycerol as a biorenewable source to valuable commodity chemicals. *Chemical Society reviews* **2008**, *37*, 527–549.
- (44) Behr, A.; Eilting, J.; Irawadi, K.; Leschinski, J.; Lindner, F. Improved utilisation of renewable resources: New important derivatives of glycerol. *Green Chem* **2008**, *10*, 13–30.
- (45) Office of Global Analysis, Foreign Agricultural Service. World Agricultural Production.
- (46) Statista GmbH. Marktforschung & Beratung: Business Service, Consulting.
- (47) YUAN, W.; HANSEN, A.; ZHANG, Q. Vapor pressure and normal boiling point predictions for pure methyl esters and biodiesel fuels. *Fuel* **2005**, *84*, 943–950.
- (48) Allen, C.; Watts, K. C.; Ackman, R. G.; Pegg, M. J. Predicting the viscosity of biodiesel fuels from their fatty acid ester composition. *Fuel* **1999**, *78*, 1319–1326.
- (49) Goering, C. E.; Schwab, A. W.; Daugherty, M. J.; Pryde, E. H.; Heakin, A. J. Fuel Properties of Eleven Vegetable Oils. *Transactions of the ASAE* **1982**, *25*, 1472–1477.

(50) International Olive Council. <http://www.internationaloliveoil.org/estaticos/view/131-world-olive-oil-figures>.

(51) Robertson, J. A.; Chapman, G. W.; Wilson, R. L. Relation of days after flowering to chemical composition and physiological maturity of sunflower seed. *J Am Oil Chem Soc* **1978**, *55*, 266–269.

(52) Anderson, W. K. Maturation of sunflower. *Aust. J. Exp. Agric.* **1975**, *15*, 833.

(53) Robertson, J. A.; THOMAS, J. K.; BURDICK, D. CHEMICAL COMPOSITION OF THE SEED OF SUNFLOWER HYBRIDS AND OPEN POLLINATED VARIETIES. *J Food Science* **1971**, *36*, 873–876.

(54) Canvin, D. T. THE EFFECT OF TEMPERATURE ON THE OIL CONTENT AND FATTY ACID COMPOSITION OF THE OILS FROM SEVERAL OIL SEED CROPS. *Can. J. Bot.* **1965**, *43*, 63–69.

(55) Kinman, M. L.; Earle, F. R. Agronomic Performance and Chemical Composition of the Seed of Sunflower Hybrids and Introduced Varieties<sup>1</sup>. *Crop Science* **1964**, *4*, 417.

(56) Harris, P.; James, A. T. Effect of low temperature on fatty acid biosynthesis in seeds. *Biochimica et Biophysica Acta (BBA) - Lipids and Lipid Metabolism* **1969**, *187*, 13–18.

(57) BALDINI M., GIOVANARDI R., TAHMASEBI-ENFERADI S., VANNOZZI G.P. Effects of water regime on fatty acid accumulation and final fatty acid composition in the oil of standard and high oleic sunflower hybrids. *Ital. J. Agron* **2002**, *6*, 119–126.

(58) Garcés, R.; Mancha, M. In vitro oleate desaturase in developing sunflower seeds. *Phytochemistry* **1991**, *30*, 2127–2130.

(59) Norhaizan, M. E.; Hosseini, S.; Gangadaran, S.; Lee, S. T.; Kapourchali, F. R.; Moghadasian, M. H. Palm oil: Features and applications. *Lipid Technology* **2013**, *25*, 39–42.

(60) Infografik: Palmöl und seine Alternativen. <https://de.statista.com/infografik/5639/palmoel-und-seine-alternativen/> (accessed October 11, 2016).

(61) Ma J, Folsom AR, Lewis L, Eckfeldt JH. Relation of plasma phospholipid and cholesterol ester fatty acid composition to carotid artery intima-media thickness: the Atherosclerosis Risk in ... - PubMed - NCBI. <https://www.ncbi.nlm.nih.gov/pubmed/9022543> (accessed September 29, 2016).

(62) Lajara, J. R.; Diaz, U.; Quidiello, R. D. Definite influence of location and climatic conditions on the fatty acid composition of sunflower seed oil. *J Am Oil Chem Soc* **1990**, *67*, 618–623.

(63) Broaddus, H. Types Of Sunlower Oil: High Oleic vs. Mid Oleic vs. Linoleic. <http://www.centrafoods.com/blog/types-of-sunlower-oil-high-oleic-vs.-mid-oleic-vs.-linoleic> (accessed October 7, 2016).

(64) Grundy, S. M. Comparison of monounsaturated fatty acids and carbohydrates for lowering plasma cholesterol. *The New England journal of medicine* **1986**, *314*, 745–748.

(65) Kinter, M.; Spitz, D. R.; Robert, R. J. Oleic Acid Incorporation Protects Cultured Hamster Fibroblasts from Oxygen-Induced Cytotoxicity. *J. Nutr.* **1996**, *126*, 2952–2959.

(66) Berry, E. M. Dietary fatty acids in the management of diabetes mellitus. *The American journal of clinical nutrition* **1997**, *66*, 991.



(67) Produktion der führenden Erzeugerländer von Olivenöl weltweit 2016/17 | Statistik. <https://de.statista.com/statistik/daten/studie/443282/umfrage/produktion-der-fuehrenden-erzeugerlaender-von-olivenoel-weltweit/> (accessed October 20, 2016).

(68) USDA Foreign Agricultural Service. Produktion der führenden Erzeugerländer von Olivenöl weltweit 2016/17 | Statistik. <https://de.statista.com/statistik/daten/studie/443282/umfrage/produktion-der-fuehrenden-erzeugerlaender-von-olivenoel-weltweit/> (accessed October 20, 2016).

(69) USDA Foreign Agricultural Service. Konsum von Olivenöl in den wichtigsten Absatzmärkten weltweit 2016/17 | Statistik. <https://de.statista.com/statistik/daten/studie/443473/umfrage/konsum-von-olivenoel-in-den-wichtigsten-absatzmaerkten-weltweit/> (accessed October 20, 2016).

(70) International Olive Council. World Olive Oil Figures. <http://www.internationaloliveoil.org/estaticos/view/131-world-olive-oil-figures> (accessed October 20, 2016).

(71) USDA Foreign Agricultural Service. Umsatz mit Speiseöl im LEH in Deutschland nach Produktgruppen 2013/14 | Statistik. <https://de.statista.com/statistik/daten/studie/360241/umfrage/umsatz-mit-speiseoel-im-leh-in-deutschland-nach-produktgruppen/> (accessed October 20, 2016).

(72) Canapi, E. C.; Agustin, Y. T.; Moro, E. A.; Pedrosa, E.Jr., Bendano, M.L.J. Coconut oil. In *Bailey's industrial oil and fat products*, 6th ed. / edited by Fereidoon Shahidi; Shahidi, F., Bailey, A. E., Eds.; Wiley-Interscience: New York, Chichester, 2005; pp 123–147.

(73) Chaleepa, K.; Szepes, A.; Ulrich, J. Dry fractionation of coconut oil by melt crystallization. *Chemical Engineering Research and Design* **2010**, *88*, 1217–1222.

(74) Toda, T.; Oku, H. Effect of medium-chain fatty acids on cholesterolemia and atherosclerosis in Japanese quails. *Nutrition Research* **1995**, *15*, 99–113.

(75) Pryde, E. H. Vegetable oils as fuel alternatives — Symposium overview. *J Am Oil Chem Soc* **1984**, *61*, 1609–1610.

(76) Sajjadi, B.; Raman, A. A. A.; Arandiyani, H. A comprehensive review on properties of edible and non-edible vegetable oil-based biodiesel: Composition, specifications and prediction models. *Renewable and Sustainable Energy Reviews* **2016**, *63*, 62–92.

(77) Dasgupta S., Dreijack N., Ay P. Melt crystallization kinetics for enrichment of highly unsaturated fatty acid fractions based on Linseed oil. *J. Environ. Res. Develop* **2016**, *11*, 1–6.

(78) Entwicklung der weltweiten Produktionskapazität von Biopolymeren bis 2019 | Statistik. <https://de.statista.com/statistik/daten/studie/258991/umfrage/entwicklung-der-weltweiten-produktionskapazitaet-von-biopolymeren/> (accessed October 11, 2016).

(79) Institute for Bioplastics and Biocomposites (FH Hannover). Entwicklung der weltweiten Produktionskapazität von Biokunststoffen (Biopolymere) in den Jahren von 2010 bis 2019 (in 1.000 Tonnen). <https://de.statista.com/statistik/daten/studie/258991/umfrage/entwicklung-der-weltweiten-produktionskapazitaet-von-biopolymeren/> (accessed on 2012.20Januar%202017).

(80) European Bioplastics. What are bioplastics? Fact Sheet. <http://www.european-bioplastics.org/bioplastics/standards/> (accessed January 12, 2017).

(81) Rettig, M. Flammfeste, elektronenstrahlhärtbare Reaktivharze auf Basis nachwachsender Rohstoffe. PhD. Thesis, Brandenburg University of Technology, Cottbus-Senftenberg, Cottbus, Germany, 2010.

(82) Mallécol, J.; Lemaire, J.; Gardette, J.-L. Drier influence on the curing of linseed oil. *Progress in Organic Coatings* **2000**, *39*, 107–113.

(83) Haslbeck, F.; Grosch, W.; Firl, J. Formation of hydroperoxides with unconjugated diene systems during autoxidation and enzymic oxygenation of linoleic acid. *Biochimica et Biophysica Acta (BBA) - Lipids and Lipid Metabolism* **1983**, *750*, 185–193.

(84) Muizebelt, W. J.; Donkerbroek, J. J.; Nielen, M. W. F.; Hussem, J. B.; Biemond, M. E. F.; Klaasen, R. P.; Zabel, K. H. Oxidative crosslinking of alkyd resins studied with mass spectrometry and NMR using model compounds. *J. Coatings Tech.* **1998**, *70*, 83–93.

(85) Mallécol, J.; Gardette, J.-L.; Lemaire, J. Long-term behavior of oil-based varnishes and paints. Photo- and thermooxidation of cured linseed oil. *J Amer Oil Chem Soc* **2000**, *77*, 257–263.

(86) Frankel, E. N. Lipid oxidation: Mechanisms, products and biological significance. *J Am Oil Chem Soc* **1984**, *61*, 1908–1917.

(87) Vetter, T.; Iggländ, M.; Ochsenbein, D. R.; Hänsele, F. S.; Mazzotti, M. Modeling Nucleation, Growth, and Ostwald Ripening in Crystallization Processes: A Comparison between Population Balance and Kinetic Rate Equation. *Crystal Growth & Design* **2013**, *13*, 4890–4905.

(88) Uhlmann, D. R.; Chalmers, B. THE ENERGETICS OF NUCLEATION. *Ind. Eng. Chem.* **1965**, *57*, 19–31.

(89) Liotta, V.; Sabesan, V. Monitoring and Feedback Control of Supersaturation Using ATR-FTIR to Produce an Active Pharmaceutical Ingredient of a Desired Crystal Size. *Org. Process Res. Dev.* **2004**, *8*, 488–494.

(90) Ostwald, W. Über die vermeintliche Isomerie des roten und gelben Quecksilberoxyds und die Oberflächenspannung fester Körper. *Z. phys. Chem* **1900**, *34*, 495–503.

(91) Ostwald, W. Z. Blocking of Ostwald ripening allowing long-term stabilization. *Phys. Chem* **1901**, *37*, 385.

(92) Voorhees, P. W. The theory of Ostwald ripening. *J Stat Phys* **1985**, *38*, 231–252.

(93) Noorduyn, W. L.; Vlieg, E.; Kellogg, R. M.; Kaptein, B. From Ostwald ripening to single chirality. *Angewandte Chemie (International ed. in English)* **2009**, *48*, 9600–9606.

(94) Gibbs, J. W. *Thermodynamics, vol I*; Yale University Press, New Haven, 1948.

(95) Randolph, A. D.; Larson, M. A. *Theory of particulate processes: Analysis and techniques of continuous crystallization / Alan D. Randolph, Maurice A. Larson*; Academic Press: New York, London (24 Oval Rd, N.W.1), 1971.

(96) Ramkrishna, D. *Population balances: Theory and applications to particulate systems in engineering / Doraiswami Ramkrishna*; Academic: San Diego, Calif., London, 2000.

(97) Leblanc, S. E.; Fogler, H. S. Population balance modeling of the dissolution of polydisperse solids: Rate limiting regimes. *AIChE J.* **1987**, *33*, 54–63.

(98) Kashchiev, D. *Nucleation: Basic theory with applications / Dimo Kashchiev*; Butterworth Heinemann: Oxford, 2000.

(99) Kloek, W.; Walstra, P.; van Vliet, T. Crystallization kinetics of fully hydrogenated palm oil in sunflower oil mixtures. *J Amer Oil Chem Soc* **2000**, *77*, 389–398.

(100) Dubrovskii, V. G. *Nucleation theory and growth of nanostructures*; Nanoscience and technology; Springer: Berlin, Heidelberg, 2014.

(101) Lacmann, R.; Herden, A.; Mayer, C. Kinetics of Nucleation and Crystal Growth. *Chem. Eng. Technol.* **1999**, *22*, 279–289.

(102) Zimmermann, N. E. R.; Vorselaars, B.; Quigley, D.; Peters, B. Nucleation of NaCl from Aqueous Solution: Critical Sizes, Ion-Attachment Kinetics, and Rates. *Journal of the American Chemical Society* **2015**, *137*, 13352–13361.

(103) Agarwal, V.; Peters, B. Solute Precipitate Nucleation: A Review of Theory and Simulation Advances. In *Advances in chemical physics*; Rice, S. A., Dinner, A. R., Eds.; Advances in Chemical Physics v. 155; Wiley: Hoboken, New Jersey, 2014; pp 97–160.

(104) Davey, R. J.; Schroeder, S. L. M.; ter Horst, J. H. Nucleation of organic crystals--a molecular perspective. *Angewandte Chemie (International ed. in English)* **2013**, *52*, 2166–2179.

(105) Maibaum, L. Phase transformation near the classical limit of stability. *Physical review letters* **2008**, *101*, 256102.

(106) Dye David. *MSE 104: Microstructure and Properties of Materials: Phase Metallurgy - 7.1 Diffusion, Nucleation and Growth.*; Imperial College, London SW7 2AZ, UK, 2012.

(107) Turnbull, D.; Fisher, J. C. Rate of Nucleation in Condensed Systems. *J. Chem. Phys.* **1949**, *17*, 71.

(108) Boistelle, R. Fundamentals of nucleation and crystal growth. In *Crystallization and polymorphism of fats and fatty acids*; Garti, N., Satō, K., Eds.; Marcel Dekker Inc.: New York, 1988; pp 189–226.

(109) Toro-Vazquez, J.; Dibildox-Alvarado, E.; Herrera-Coronado, V.; Charo-Alonso, M. Triacylglyceride Crystallization in Vegetable oils: Application of Models, Measurements, and Limitations. In *Crystallization and Solidification Properties of Lipids*; Neil Widlak, Richard W. Hartel, Suresh Narine, Ed.; AOCS Press: Champaign, Ill., 2001; pp 53–78.

(110) Garti, N.; Sato, K. Crystallization of Fats and Fatty Acids. In *Crystallization and polymorphism of fats and fatty acids*; Garti, N., Satō, K., Eds.; Marcel Dekker Inc.: New York, 1988.

(111) Šipušić, J.; Kurajica, S.; Bezjak, A. Method for induction time determination using data obtained from isothermal crystallization experiment monitored by DSC. *J. Appl. Polym. Sci.* **2004**, *93*, 2454–2458.

(112) Walton, A. G. Nucleation in liquids and solutions. In *Nucleation*; Zettlemoyer, A. C., Ed.; Marcel Dekker Inc.: New York, 1969; pp 225–308.

(113) Widlak, N.; Hartel, R. W.; Narine, S. *Crystallization and solidification properties of lipids*; AOCS Press: Champaign, Ill., 2001.

- (114) Chaleepa, K. A New Concept in Layer - Based Fractional Crystallization Processes for Fats. PhD, Martin-Luther-University Halle-Wittenberg, Halle (Saale), 2010.
- (115) Ng, W. L. Nucleation behaviour of tripalmitin from a triolein solution. *J Am Oil Chem Soc* **1989**, *66*, 1103–1106.
- (116) Parsons, A. R.; Black, S. N.; Colling, R. Automated Measurement of Metastable Zones for Pharmaceutical Compounds. *Chemical Engineering Research and Design* **2003**, *81*, 700–704.
- (117) Fujiwara, M.; Chow, P. S.; Ma, D. L.; Braatz, R. D. Paracetamol Crystallization Using Laser Backscattering and ATR-FTIR Spectroscopy: Metastability, Agglomeration, and Control. *Crystal Growth & Design* **2002**, *2*, 363–370.
- (118) Collins, A. N. *Developments in the commercial manufacture and applications of optically active compounds*, Repr. in paperback; Chirality in industry / ed. by A. N. Collins ... ; 2; Wiley: Chichester, 1997.
- (119) Hussain, K.; Thorsen, G.; Malthe-Sørensen, D. Nucleation and metastability in crystallization of vanillin and ethyl vanillin. *Chemical Engineering Science* **2001**, *56*, 2295–2304.
- (120) Herden, A.; Mayer, C.; Kuch, S.; Lacmann, R. About the Metastable Zone Width of Primary and Secondary Nucleation. *Chem. Eng. Technol.* **2001**, *24*, 1248–1254.
- (121) Höhne, G. W. H.; Hemminger, W. F.; Flammersheim, H.-J. *Differential Scanning Calorimetry*, 2nd rev. and enlarged edition; Springer Berlin Heidelberg: Berlin, Heidelberg, 2003.
- (122) Jablonski, P. Kalorimetrische Untersuchungen des Systems Polyethylenglykol/Wasser. Ph.D. thesis, University of Duisburg-Essen, Essen, 2002.
- (123) Cammenga, H. K.; Epple, M. Basic Principles of Thermoanalytical Techniques and Their Applications in Preparative Chemistry. *Angew. Chem. Int. Ed. Engl.* **1995**, *34*, 1171–1187.
- (124) Schubnell, M. *DSC Microscopy, Chemiluminescence and Photocalorimetry Version 3.0*; Mettler Toledo, 2010.
- (125) Mettler-Toledo AG, A. Flash Differential Scanning Calorimetry. [http://www.mt.com/de/en/home/library/product-brochures/lab-analytical-instruments/Flash\\_DSC\\_1/jcr:content/download/file/file.res/51725315\\_Flash\\_DSC1\\_Brochure\\_e.pdf](http://www.mt.com/de/en/home/library/product-brochures/lab-analytical-instruments/Flash_DSC_1/jcr:content/download/file/file.res/51725315_Flash_DSC1_Brochure_e.pdf) (accessed November 21, 2016).
- (126) Deutsche Gesellschaft für Fettforschung. *Analysis of fatty acids and fatty acid composition by gas chromatography*, 2016 (C-VI 10a (16)). <http://www.dgfett.de/methods/inhaltsverzeichnis.pdf>.
- (127) Deutsche Gesellschaft für Fettforschung. *Fatty acid methyl ester and fatty acid propyl ester – Esterification or transesterification*, 2016 (C-VI 11b (81)). <http://www.dgfett.de/methods/inhaltsverzeichnis.pdf>.
- (128) Gas Chromatography. [http://chem.libretexts.org/Core/Analytical\\_Chemistry/Instrumental\\_Analysis/Chromatography/Gas\\_Chromatography](http://chem.libretexts.org/Core/Analytical_Chemistry/Instrumental_Analysis/Chromatography/Gas_Chromatography) (accessed November 24, 2016).
- (129) Hughes, D. E. P. Flame-ionization detector for gas chromatography. *J. Chem. Educ.* **1965**, *42*, 450.
- (130) Poole, C. F. *Gas chromatography*; Elsevier: Oxford, 2012.

- (131) Herrera, M. L. Crystallization behavior of hydrogenated sunflowerseed oil: Kinetics and polymorphism. *J Am Oil Chem Soc* **1994**, *71*, 1255–1260.
- (132) Ng, W. L. A study of the kinetics of nucleation in a palm oil melt. *J Am Oil Chem Soc* **1990**, *67*, 879–882.
- (133) Eckert, K.-A.; Dasgupta, S.; Ay, P. Novel techniques to optically characterize melt crystallization kinetics of high oleic sunflower oil based fatty acid mixture **2014**.
- (134) Particle System Characterization Group, Mettler-Toledo GmbH, Autochem. FBRM Method of Measurement - Introduction. <https://www.youtube.com/watch?v=W35BHuDgqc&feature=youtu.be> (accessed December 19, 2016).
- (135) Dasgupta, S.; Ay, P. In-situ monitoring and induction time measurements during melt crystallization of plant based fatty acid mixtures in V-form reactor. In *6th Workshop on Fats and Oils as Renewable Feedstocks for the Chemical Industry*; Metzger, J. O., Meier, M. A. R., Eds., 2013.
- (136) Dasgupta, S.; Dreijack, N.; Ay, P. Enrichment of unsaturated fractions in a Linseed oil based fatty acid mixture by melt crystallisation. In *5th Workshop on Fats and Oils as Renewable Feedstock for the Chemical Industry, abiosus e.V. Conferences*; Metzger, J., Meier, M., Eds.; Karlsruhe, 2012.
- (137) Rettig, F. Bestimmung und Charakterisierung der Induktionszeit der Schmelzkristallisation von Fettsäuremischungen natürlichen Ursprungs. Bachelor, Brandenburg University of Technology, Cottbus-Senftenberg, Cottbus, Germany, 2014.
- (138) IOI Oleo GmbH. Production site - Wittenberge. <http://www.ioioleo.de/en/ioi/ioi-oleo-gmbh.php> (accessed January 13, 2017).
- (139) Chen, S.; Zhang, P.; Chen, L. Fe/Zn double metal cyanide (DMC) catalyzed ring-opening polymerization of propylene oxide. *Progress in Organic Coatings* **2004**, *50*, 269–272.
- (140) Kellens, M.; Gibon, V.; Hendrix, M.; Greyt, W. de. Palm oil fractionation. *Eur. J. Lipid Sci. Technol.* **2007**, *109*, 336–349.
- (141) Morin, O.; Pagès-Xatart-Parès, X. Huiles et corps gras végétaux: Ressources fonctionnelles et intérêt nutritionnel. *OCL* **2012**, *19*, 63–75.
- (142) Lehninger, A. L.; Nelson, D. L.; Cox, M. M. *Lehninger principles of biochemistry*, 4th ed.; W.H. Freeman: New York, N.Y., Basingstoke, 2005.
- (143) Yu, Z. Q.; Chow, P. S.; Tan, R. B. H. Interpretation of Focused Beam Reflectance Measurement (FBRM) Data via Simulated Crystallization. *Org. Process Res. Dev.* **2008**, *12*, 646–654.
- (144) Ruf, A.; Worlitschek, J.; Mazzotti, M. Modeling and Experimental Analysis of PSD Measurements through FBRM. *Part. Part. Syst. Charact.* **2000**, *17*, 167–179.
- (145) Scott, C.; Black, S. In-Line Analysis of Impurity Effects on Crystallisation. *Org. Process Res. Dev.* **2005**, *9*, 890–893.
- (146) Hu, X.; Cunningham, J. C.; Winstead, D. Study growth kinetics in fluidized bed granulation with at-line FBRM. *International journal of pharmaceuticals* **2008**, *347*, 54–61.

- (147) Lyko, H. Optische Verfahren zur Partikelanalyse. *Filtrieren und Separieren (F & S)* **2001**, 5, 296–299.
- (148) Peda, S.; Bröckel, U.; Ay, P.; Stollberg, C. Anwendbarkeit der Lasermessverfahren FBRM und 3D ORM SMF in Batch-Kristallisationen. *Chemie Ingenieur Technik* **2011**, 83, 558–562.
- (149) Etzler, F. M.; Sanderson, M. S. Particle Size Analysis: A comparative study of various methods. *Part. Part. Syst. Charact.* **1995**, 12, 217–224.
- (150) Dasgupta, S.; Dreiack, N.; Ay, P. Enrichment of unsaturated fractions in a Linseed oil based fatty acid mixture by melt crystallisation. In ; Metzger, J. O., Meier, M. A. R., Eds.; Karlsruhe, 2012.
- (151) Perry, R. H.; Green, D. W.; Maloney, J. O. *Perry's chemical engineers' handbook*, 7th ed. / prepared by a staff of specialists under the editorial direction of late editor, Robert H. Perry / editor, Don W. Green / associate editor, James O. Maloney; McGraw-Hill: New York, London, 1997.
- (152) *Distillation - Advances from Modeling to Applications*; Zereshki, S., Ed.; InTech, 2012.
- (153) Budde, W.M., Jr. General physical and chemical properties of fatty acids. In *Fatty Acids and Their Industrial Applications*; Pattison, S. E., Ed.; Soap & Detergent Assn, 1968; pp 47–76.
- (154) Kobayashi, M.; Kaneko, F.; Sato, K.; Suzuki, M. Vibrational spectroscopic study on polymorphism and order-disorder phase transition in oleic acid. *J. Phys. Chem.* **1986**, 90, 6371–6378.
- (155) Eckert, K.-A.; Dasgupta, S.; Selge, B.; Ay, P. Novel model for the prediction of SSLE temperatures and crystallization paths of any mixture containing palmitic, stearic, oleic, linoleic and linolenic acid. *Thermochimica Acta* **2017**, 652, 126–140.
- (156) Suzuki, M.; Ogaki, T.; Sato, K. Crystallization and transformation mechanisms of  $\alpha$ ,  $\beta$ - and  $\gamma$ -polymorphs of ultra-pure oleic acid. *J Am Oil Chem Soc* **1985**, 62, 1600–1604.
- (157) Dasgupta, S.; Glaser, C.; Ay, P. SLE diagram for a high oleic palm oil based fatty acid mixture at low saturated content. In *9th Workshop on Fats and Oils as Renewable Feedstocks for the Chemical Industry*; Metzger, J. O., Meier, M. A. R., Eds., 2017.
- (158) Rabelo, J.; Batista, E.; Cavaleri, F. v. W.; Meirelles, A. J. A. Viscosity prediction for fatty systems. *J Amer Oil Chem Soc* **2000**, 77, 1255–1262.
- (159) Mettler-Toledo AG, A. Differential Scanning Calorimetry for Routine Analysis. [http://www.mt.com/dam/Analytical/ThermalAnalysis/TA-PDF/DSC3\\_Brochure\\_en\\_30247073A\\_V05.15\\_Original\\_38549.pdf](http://www.mt.com/dam/Analytical/ThermalAnalysis/TA-PDF/DSC3_Brochure_en_30247073A_V05.15_Original_38549.pdf).

---

## List of Figures

<i>Figure 2-1: Molecular structures of the main fatty acids: a.-Palmitic acid, b.-Stearic acid, c.-Oleic acid, d.-Linoleic acid and e.-Linolenic acid.....</i>	<i>8</i>
<i>Figure 2-2: Global annual plant oil production<sup>45,46</sup> .....</i>	<i>10</i>
<i>Figure 2-3: Annual production of vegetable oils in different countries in the year 2015/2016<sup>45,46,50</sup> .</i>	<i>12</i>
<i>Figure 2-4: Effect of maturity (days after flowering) of seed on fatty acid distribution in the sunflower oil seed – data collected from and replotted from Robertson et. al. <sup>51</sup> .....</i>	<i>13</i>
<i>Figure 2-5: Global consumption of vegetable oils in the year 2015/2016<sup>45,46</sup> .....</i>	<i>15</i>
<i>Figure 2-6: Edible vegetable oils as biodiesel feedstock<sup>76</sup> .....</i>	<i>18</i>
<i>Figure 2-7: Production of biodegradable and non-biodegradable polymers over the years<sup>79</sup> .....</i>	<i>19</i>
<i>Figure 3-1: Free enthalpy <math>\Delta G</math> as a function of radius of the nucleus .....</i>	<i>26</i>
<i>Figure 3-2: Types of nucleation in the metastable range of an SLE phase diagram.....</i>	<i>31</i>
<i>Figure 4-1: Example standard DSC temperature profile (50 °C ► -20 °C ► 50 °C at 0.2 K/min) .....</i>	<i>37</i>
<i>Figure 4-2: DSC - Microscopy system .....</i>	<i>38</i>
<i>Figure 4-3: Gas Chromatography Flame Ionization Detector - GCFID Setup .....</i>	<i>41</i>
<i>Figure 4-4: Confocal Raman microscopy Principle in Senterra® .....</i>	<i>43</i>
<i>Figure 4-5: Contact Angle measurement setup with a Keyence VHX 2000D® Microscope fitted at 90° to the Sample .....</i>	<i>44</i>
<i>Figure 4-6: Determination of Contact Angle on different Substrates .....</i>	<i>45</i>
<i>Figure 4-7: Thermal and chemical sample characterization from multi-step melt crystallization .....</i>	<i>46</i>
<i>Figure 4-8: EasyMax™ - Automated reactor setup with Two independent reactor systems.....</i>	<i>47</i>
<i>Figure 4-9: Mathematical definitions of Induction time, <math>\tau</math> and Supercooling, <math>\Delta T</math> used in this work... </i>	<i>49</i>
<i>Figure 4-10: Polarized light microscope, Leica DM-RME with high definition Leica DFC 500/320 camera<sup>133</sup> .....</i>	<i>51</i>
<i>Figure 4-11: Pictorial and schematic representation of sample preparation on the object slide in the gradient chamber (LTS 120, Linkam Scientific Instruments Ltd.) under the microscope (Leica DM-RME, Leica Microsystems).....</i>	<i>52</i>



Figure 4-12: Pictorial and schematic representation of Temperature calibration with the high oleic sunflower oil based PUFA mixture in the gradient chamber (LTS 120, Linkam Scientific Instruments Ltd.) with a Almemo RTD foil Sensor..... 52

Figure 4-13: Introduction of the fatty acid mixture samples into capillaries for crystal growth tests.. 53

Figure 4-14: Schematic illustration of In-situ particle sensor based on Focused beam reflectance technology, Mettler Toledo AC, Mettler Toledo GmbH ..... 54

Figure 4-15: Evolution of V Reactor for online detection by FBRM™ in a stirred reactor DETECTION BY FBRM IN A STIRRED REACTOR<sup>135</sup>, ..... 55

Figure 4-16: Schematic representation of Jacketed V reactor ..... 56

Figure 4-17: EasyMax™ - FBRM™ setup,<sup>137</sup> ..... 58

Figure 4-18: Fatty acids present in the high oleic sunflower oil based PUFA mixture (see Table 5-3 for precise composition) ..... 61

Figure 4-19: Comparison of absolute particle size analysis of MCC granules by FBRM™ and Coulter LS Diffractionmeter..... 64

Figure 5-1: Temperature profile for the melt crystallization of linseed oil based fatty acid mixture at end temperature of -2°C<sup>10,17</sup> ..... 69

Figure 5-2: Depletion of Palmitic acid (C 16:0) and Stearic acid (C 18:0) at different crystallization temperatures (25°C; 16°C; 8°C; 3°C and -2°C) analyzed by GC, isothermal at 190°C, 0.2 µL injection volume and 150 KPa<sup>10,17</sup> ..... 69

Figure 5-3: a) Enthalpy vs. Temperature of a linseed oil based PUFA fraction in the DSC [50 °C to -40 °C to 50 °C at 0.2 Kmin-1] b) Placement of DSC onsets and endsets of significant peaks in a small section of a generalized liquid solid equilibrium diagram<sup>19</sup> ..... 73

Figure 5-4: Enthalpy vs. Temperature of PUFA in the DSC [50°C to -20°C to 50°C at 0.2 K/min] with interpretation of what happens in a crucible..... 74

Figure 5-5: Thermograms of pure a. Stearic and b. Linoleic acid analyzed by the DSC and Star<sup>E</sup> Software ..... 75

Figure 5-6: Enthalpy vs. Temperature of a crystal fraction of an high oleic sunflower oil based PUFA mixture in the DSC [50 °C to -60 °C to 50 °C at 10 K/min] with pictorial representation of characteristic stages in the cooling curve<sup>19</sup> ..... 77

Figure 5-7: Phase behavior of enriched crystal fraction of high oleic sunflower oil @ 10Kmin-1 cooling rate from 50°C to - 60°C; 1. Onset of spontaneous nucleation - 1 in Figure 5-6, Onset of solidification - 2 in Figure 5-6, Onset of third exothermic peak - 3 in Figure 5-6 (white light in top left corner of each picture is the reflection of the incident light from microscope) ..... 78



Figure 5-8: DSC thermogram of a crystal fraction of a high oleic sunflower oil based PUFA mixture (fractionation temperature 15°C) ..... 80

Figure 5-9: Cooling of an enriched crystal fraction of a large and Small specimen of high oleic sunflower oil based PUFA mixture in the Flash DSC (fractionation temperature 15°C) ..... 81

Figure 5-10: Validation of reproducibility during Cooling of an enriched crystal fraction of high oleic sunflower oil based PUFA mixture in the Flash DSC (fractionation temperature 15°C)..... 82

Figure 5-11: Heating of an enriched crystal fraction of high oleic sunflower oil based PUFA mixture in the Flash DSC (fractionation temperature 15°C)..... 83

Figure 5-12: Gas chromatogram of the linseed oil based fatty acid mixture measured with GC parameter conditions of 190°C (isothermal), 0.2 µL injection volume and 150 KPa ..... 84

Figure 5-13: Liquid solid equilibrium data of stearic acid in high linoleic sunflower oil based PUFA mixture<sup>19</sup> ..... 86

Figure 5-14: Liquid solid equilibrium data of stearic acid in high linoleic soya oil based PUFA mixture<sup>19</sup> ..... 87

Figure 5-15: Enthalpy vs. Temperature of high oleic sunflower oil PUFA mixture in the DSC [50 °C to -40 °C to 50 °C at 0.2 K/min]<sup>19</sup> ..... 88

Figure 5-16: Liquid solid equilibrium data of stearic acid in high oleic sunflower oil based PUFA mixture<sup>19</sup> ..... 88

Figure 5-17: Liquid solid equilibrium data of stearic acid in high linolenic linseed oil based PUFA mixture<sup>19</sup> ..... 89

Figure 5-18: Dependency of parameters  $Y_0$  and  $a$  of liquidus curve fit on the C18:1 fraction present in vegetable oil based PUFA mixtures along with the contour map..... 92

Figure 5-19: Dependency of Parameter  $y_0$  of solidus line fit on the C18:1 fraction present in Vegetable oil based PUFA mixtures..... 93

Figure 5-20: Calibration of the left and right sides of the gradient stage with an Almemo temperature data logging module (2890-9) and a flat foil sensor (ZA 9030-FS1 Norm E4); Resolution  $\pm 0.1^\circ\text{C}$ ..... 94

Figure 5-21: Enthalpy vs. Temperature of high linoleic sunflower oil based PUFA mixture in DSC (50 °C to -20 °C to 50 °C at  $0.2\text{Kmin}^{-1}$ ,<sup>24</sup> ..... 95

Figure 5-22: Induction time,  $t_{ind}$  [s] vs. supercooling [K] of high linoleic sunflower oil based PUFA mixture; regression equation in Table 5-10 (Equilibrium temperature 24.23 °C; Error  $\pm 19.05 \text{ s}$ )<sup>24</sup> ..... 96

Figure 5-23: Number of nuclei per area [ $\text{mm}^{-2}$ ] vs. supercooling [K] of high linoleic sunflower oil based PUFA mixture with different cooling rates; regression equation in Table 5-10 (Error  $\pm 4.15$ )<sup>24</sup> ..... 97

Figure 5-24: Prediction of induction temperature,  $t_{ind}$  [s] and nucleation per unit area,  $n$  [ $\text{mm}^{-2}$ ] as a function of supercooling [K] of sunflower oil PUFA at a specific cooling rate of  $20\text{Kmin}^{-1}$ ,<sup>24</sup> ..... 98

Figure 5-25: Induction time,  $\tau$  [s] vs. supercooling [K] of high oleic sunflower oil based PUFA mixture (Error  $\pm 52,36s$ )..... 100

Figure 5-26: Number of nuclei per area [ $mm^{-2}$ ] vs. supercooling [K] of high oleic sunflower based PUFA mixture with different cooling rates (Error  $\pm 63,95$ ) ..... 100

Figure 5-27: Induction time,  $\tau$  [s] vs. Supercooling [K] of high linoleic soya oil based PUFA mixture (Error  $\pm 37,36s$ )..... 101

Figure 5-28: Number of nuclei per area [ $mm^{-2}$ ] vs. supercooling [K] of soya oil PUFA mixture with different cooling rates (Error  $\pm 2,34$ )..... 101

Figure 5-29: Comparison of crystal size of high oleic and high linoleic mixtures..... 102

Figure 5-30: Induction time,  $\tau$  [s] vs. supercooling [K] of high linoleic and high oleic sunflower and high linoleic soya oil based PUFA mixtures (HLSO and HOSO – High Linoleic and High Oleic Sunflower Oil and HLSjO – High Linoleic Soya Oil)..... 104

Figure 5-31: Number of nuclei per area [ $mm^{-2}$ ] vs. supercooling [K] of various PUFA mixtures with different cooling rates (HLSO and HOSO – High Linoleic and High Oleic Sunflower Oil and HLSjO – High Linoleic Soya Oil) ..... 104

Figure 5-32: Comparison of the average crystal growth rates of standard saturated (left) and unsaturated (right) fatty acid samples depending on the degree of supercooling in capillaries (inner diameter,  $d_i=0.68$  mm; Error  $\pm 2.4\%$ )<sup>24</sup> ..... 107

Figure 5-33: Crystal growth rate of sunflower oil based PUFA at a specific supercooling of 9.15 K in capillaries (inner diameter,  $d_i=0.68$  mm)<sup>24</sup> ..... 108

Figure 5-34: Crystallization of sunflower oil fatty acid mixture in a.) 68  $\mu m$  and b.) 25  $\mu m$  capillaries under the microscope..... 109

Figure 5-35: Mean total length [ $\mu m$ ] of high linoleic sunflower oil PUFA mixture (Equilibrium Temperature 24.23  $^{\circ}C$ ) crystals as a function of cooling rate [ $Kmin^{-1}$ ] and supercooling [K] in capillaries [68  $\mu m$ ]..... 109

Figure 5-36: Mean total length [ $\mu m$ ] of high linoleic sunflower oil PUFA mixture (Equilibrium Temperature 24.23  $^{\circ}C$ ) crystals as a function of cooling rate [ $Kmin^{-1}$ ] and supercooling [K] in capillaries [25  $\mu m$ ]..... 110

Figure 5-37: Spectrum obtained from Crystal fraction (position 18) and from mother liquor (Position 22) by means of Confocal Raman Spectroscope for a dendrite shaped crystal, Senterra<sup>®</sup> ..... 112

Figure 5-38: Comparison of Spectra obtained from a lancet shaped crystal (red) and mother liquor (Green) by means of Confocal Raman Spectroscope, Senterra<sup>®</sup> ..... 113

Figure 5-39: Contact angle of a High Oleic, High Linoleic and a High Linolenic Fatty Acid based PUFA on Diverse Material Substrates..... 115

Figure 5-40: High Linoleic PUFA Drops measured on glass surface (left) and steel - St 37 (right) by Keyence VHX 2000D microscope..... 116

Figure 5-41: Comparison of induction time,  $\tau_{ind}[s]$  (left, Average Error  $\pm 0.8$ ) and FBRM™ Counts per second  $<10\mu m$  (right, Error  $\pm 14.4$ ) Vs. supercooling [K] of high linoleic sunflower oil PUFA mixture (solid liquid equilibrium temperature: 24.23 °C) measured by FBRM™ in V-form Reactor @ 15 rpm 117

Figure 5-42: : Induction time,  $\tau_{ind} [s]$  and Counts per second( $<10\mu m$ ) vs. blade stirrer speed (rpm) and of high linoleic sunflower oil PUFA mixture (Equilibrium Temperature 24.23 °C) measured by FBRM™ in V-form Reactor at a supercooling of 4.9K..... 118

Figure 5-43: Example of a high linoleic (PUFA 1 - Top) and high oleic (PUFA 2 - Bottom) sunflower oil based PUFA mixture thermogram by the DSC<sup>9</sup> ..... 119

Figure 5-44: Top: Induction time vs. supercooling for PUFA 1 at different cooling rates; Bottom: 3D modeling of Induction time over cooling rate and supercooling for PUFA 1<sup>9</sup> ..... 120

Figure 5-45: Top: Induction time vs. supercooling for PUFA 2 at different cooling rates; Bottom. 3D modeling of Induction time over cooling rate and supercooling for PUFA 2<sup>9</sup> ..... 122

Figure 5-46: Temperature discrepancy plot for PUFA 1 and 2 as a function of the radius of the EasyMax™ reactor<sup>9</sup> ..... 123

Figure 5-47: Number of nuclei per second counted by the FBRM™ inserted into a High linoleic PUFA mixture crystallized in the Easymax™ at 21°C ..... 126

Figure 5-48: Number of nuclei per second counted by the FBRM™ inserted into a High linoleic PUFA mixture crystallized in the Easymax™ at 19°C ..... 126

Figure 5-49: Fisher Turnbull model fitted for nucleation data for PUFA 2<sup>9</sup>..... 128

Figure 5-50: Gibb's free energy for Nucleation for PUFA 1<sup>9</sup>..... 129

Figure 5-51: Gibb's free energy for Nucleation for PUFA 2<sup>9</sup>..... 130

Figure 5-52: DSC thermogram of a linseed oil based PUFA fraction (50°C to -50°C to 50°C at 1 Kmin<sup>-1</sup>)<sup>28</sup> ..... 131

Figure 5-53: Entire picture area, Vibromix at t=21:00 minutes; Marked section represents the magnification in Table 5-17 ..... 132

## List of Tables

<i>Table 2-1: Brief Summary of reactions of oils and fatty acids</i> <sup>30</sup> .....	7
<i>Table 2-2: Fatty acid distribution of different vegetable oils from literature</i> <sup>47-49</sup> and GC-FID analyses .....	11
<i>Table 2-3: Classification of bio-based and fossil based plastics</i> <sup>80</sup> .....	20
<i>Table 2-4: Number of double bonds per Triacylglyceride in various vegetable oils</i> <sup>81</sup> .....	21
<i>Table 3-1: Classification of nucleation</i> .....	24
<i>Table 4-1: List of Chemicals used</i> .....	33
<i>Table 4-2: List of Instruments used</i> .....	34
<i>Table 4-3: List of Software used</i> .....	35
<i>Table 5-1: Composition and retention times of the fatty acids in the mother liquor fraction after melt crystallization and separation with the centrifuge analyzed by gas chromatography (isothermal at 190°C, 0.2 µL injection volume and 150 kPa)</i> <sup>10,17</sup> .....	70
<i>Table 5-2: Regression coefficients and equations with respect to operating parameters for Figure 4-2</i> <sup>10</sup> .....	71
<i>Table 5-3: Boiling and Liquidus points of the five main fatty acids in vegetable oils</i> .....	76
<i>Table 5-4: Comparison of black oxidized copper and silver aluminum crucibles (white light on top left corner of each picture is the reflection of the incident light from microscope)</i> .....	78
<i>Table 5-5: Chemical names and abbreviations of the five main components of the PUFA mixtures investigated</i> .....	84
<i>Table 5-6: Gas chromatographic analysis and the SLE points</i> <sup>24</sup> of individual fatty acids of the used linseed oil based fatty acid mixture in Figure 5-10 .....	85
<i>Table 5-7: Compositions of the different PUFA mixtures obtained from naturally occurring plant oils</i> <sup>19</sup> .....	85
<i>Table 5-8: Liquidus and solidus curves at low saturated concentrations for PUFA mixtures</i> .....	90
<i>Table 5-9: Coefficients for the linear surface fit used in equation for the dependency of the liquidus line fit on fraction of mono-unsaturated acid</i> .....	93
<i>Table 5-10: Regression coefficients and equations with respect to operating parameters for Figure 5-22 and Figure 5-23</i> .....	99
<i>Table 5-11: Induction time, <math>t_{ind}</math> or <math>\tau</math>, of the melt crystallization of the PUFA mixtures as a function of supercooling and cooling rates</i> .....	103
<i>Table 5-12: Regression coefficients and equations with respect to operating parameters for</i> .....	107

Table 5-13: Ratio of the crystal growth rates (maintaining the growth rate of C 18:3 as base) of the pure components of PUFA at a constant supercooling..... 107

Table 5-14: Regression coefficients and equations with respect to operating parameters for 4-14 and 4-15<sup>9</sup> ..... 121

Table 5-15: :  $\Delta G_c$  values [J/mol] for PUFA 1 from Fisher Turnbull plot<sup>9</sup> ..... 128

Table 5-16:  $\Delta G_c'$  values [J/mol] for PUFA 2 from Fisher Turnbull plot<sup>9</sup> ..... 129

Table 5-17: Images of fatty acid crystals, taken after first crystals were detected ( $t \approx 1:00$ ). Applying the Vibromix reactor (left) and the blade impeller reactor (right).  $T_c = 17^\circ\text{C}$ ; Cooling rate 1 =  $2\text{Kmin}^{-1}$ ; Cooling rate 2 =  $0.01\text{Kmin}^{-1}$ ,<sup>28</sup> ..... 133



# Appendix

# 1. Sample Characterization

## 1.1. Differential Scanning Calorimeter – Thermal Analysis

The following figures depict the thermograms of the five main pure fatty acids when subjected to a temperature profile according to their melting and points at a cooling or heating rate of 0.2Kmin<sup>-1</sup>.

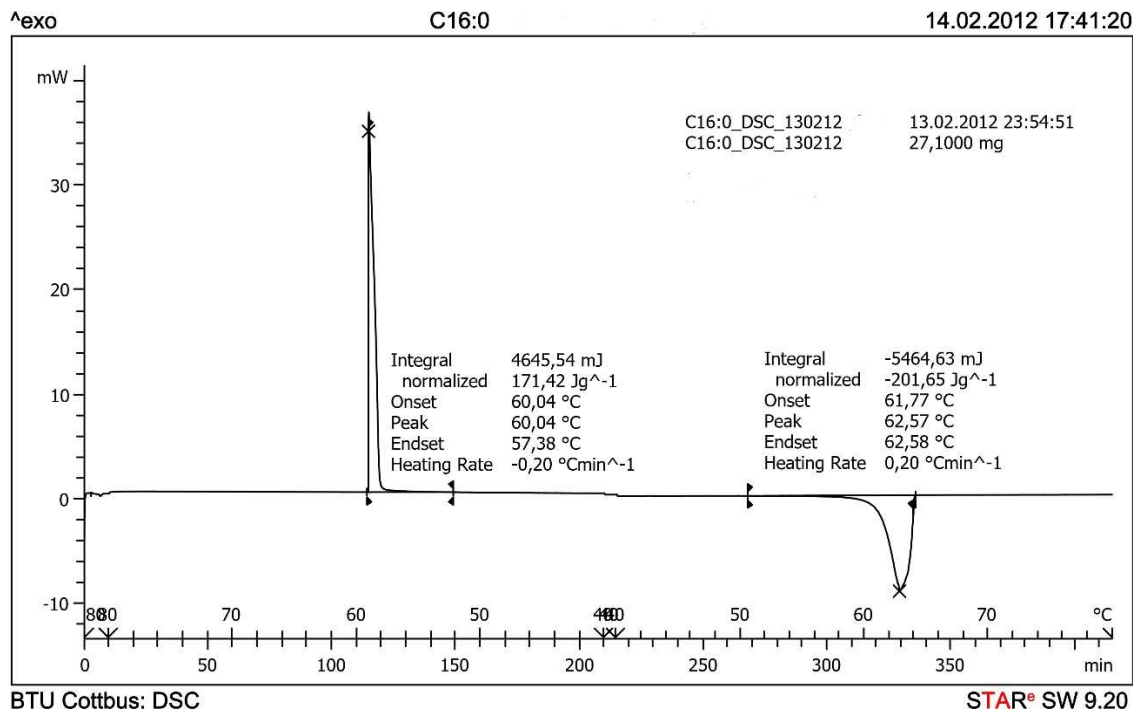


FIGURE 1-1: THERMOGRAMS OF PALMITIC ACID, C16:0, ANALYZED BY THE DSC AND STAR<sup>E</sup> SOFTWARE



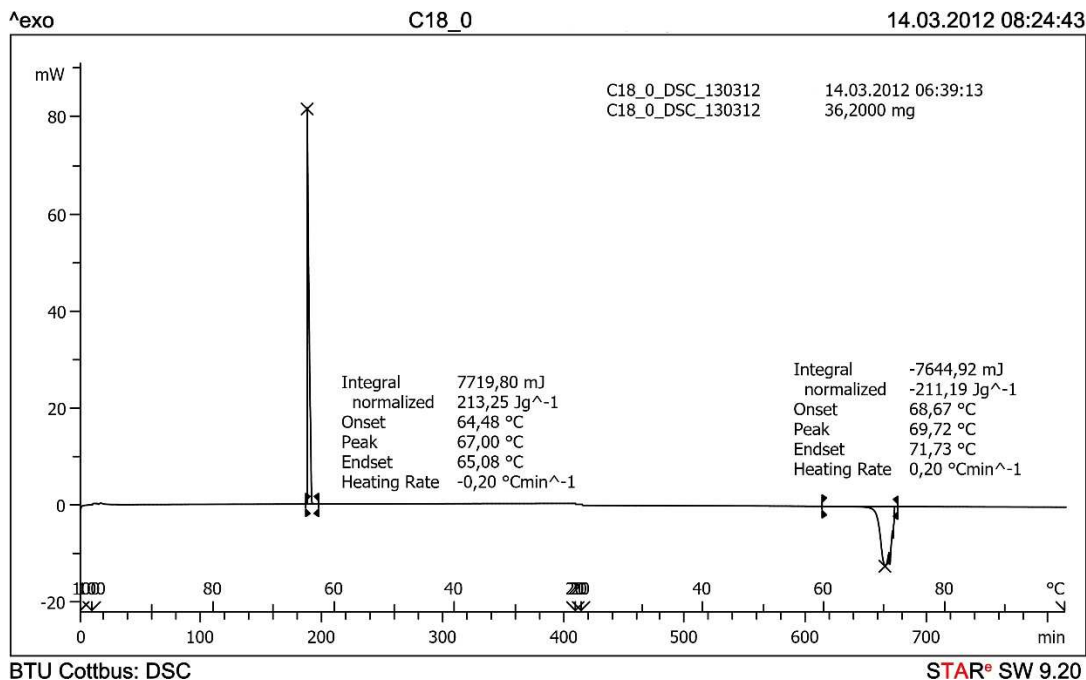


FIGURE 1-2: THERMOGRAMS OF STEARIC ACID, C18:0, ANALYZED BY THE DSC AND STAR<sup>E</sup> SOFTWARE

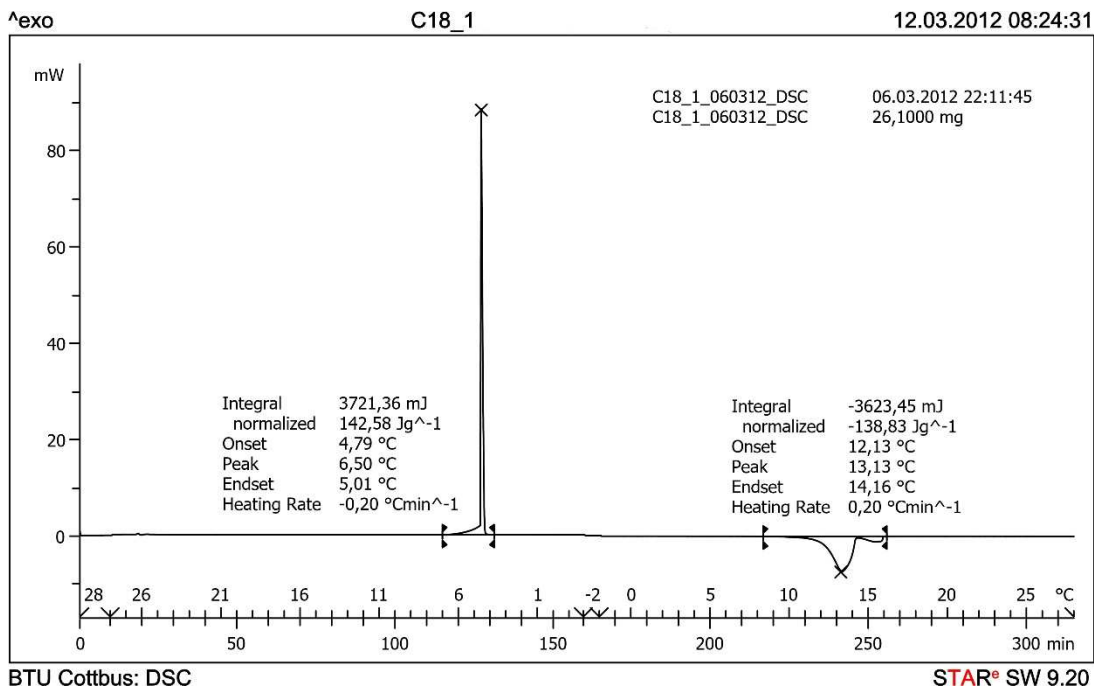


FIGURE 1-3: THERMOGRAMS OF OLEIC ACID, C18:1, ANALYZED BY THE DSC AND STAR<sup>E</sup> SOFTWARE

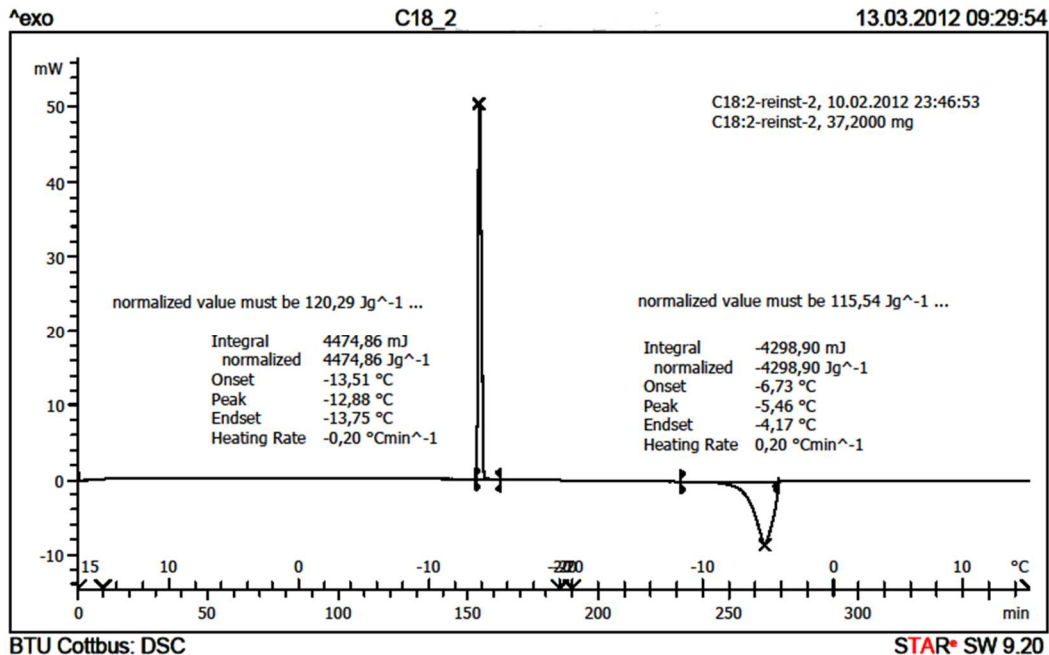


FIGURE 1-4: THERMOGRAMS OF LINOLEIC ACID, C18:2, ANALYZED BY THE DSC AND STAR<sup>E</sup> SOFTWARE

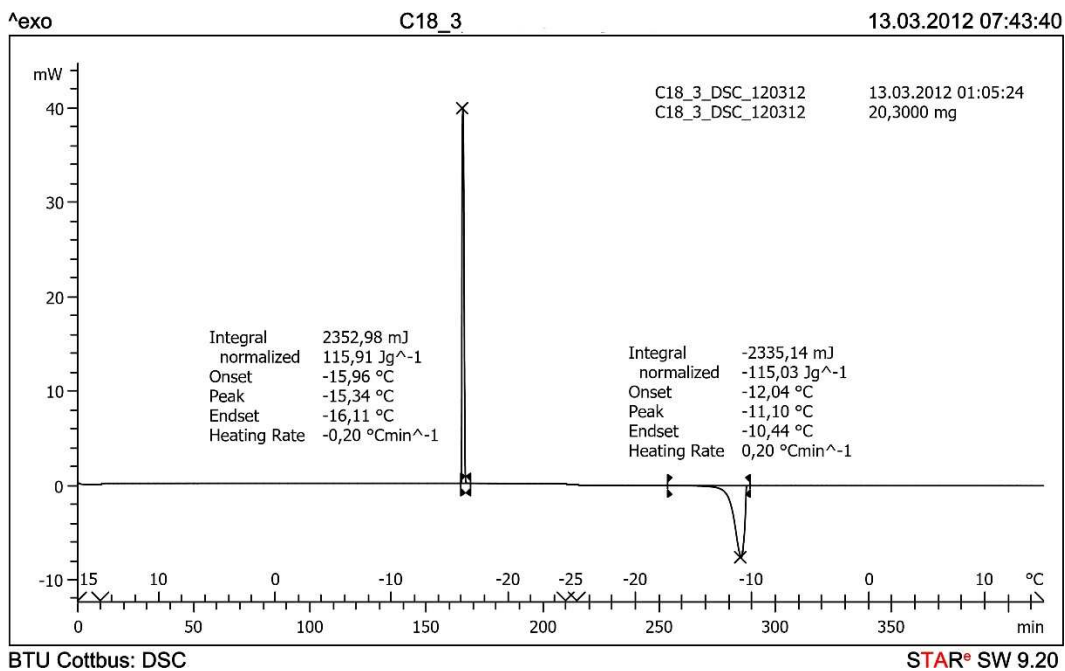


FIGURE 1-5: THERMOGRAMS OF LINOLEIC ACID, C18:3, ANALYZED BY THE DSC AND STAR<sup>E</sup> SOFTWARE

## 1.2. Differential Scanning Calorimeter – Thermal - Visual analysis (Microscopy)

The following Figure 1-6, Figure 1-7 and Figure 1-8 depict the differences in the thermograms and pictures taken between the sample crystallized in an aluminum and oxidized copper crucible.

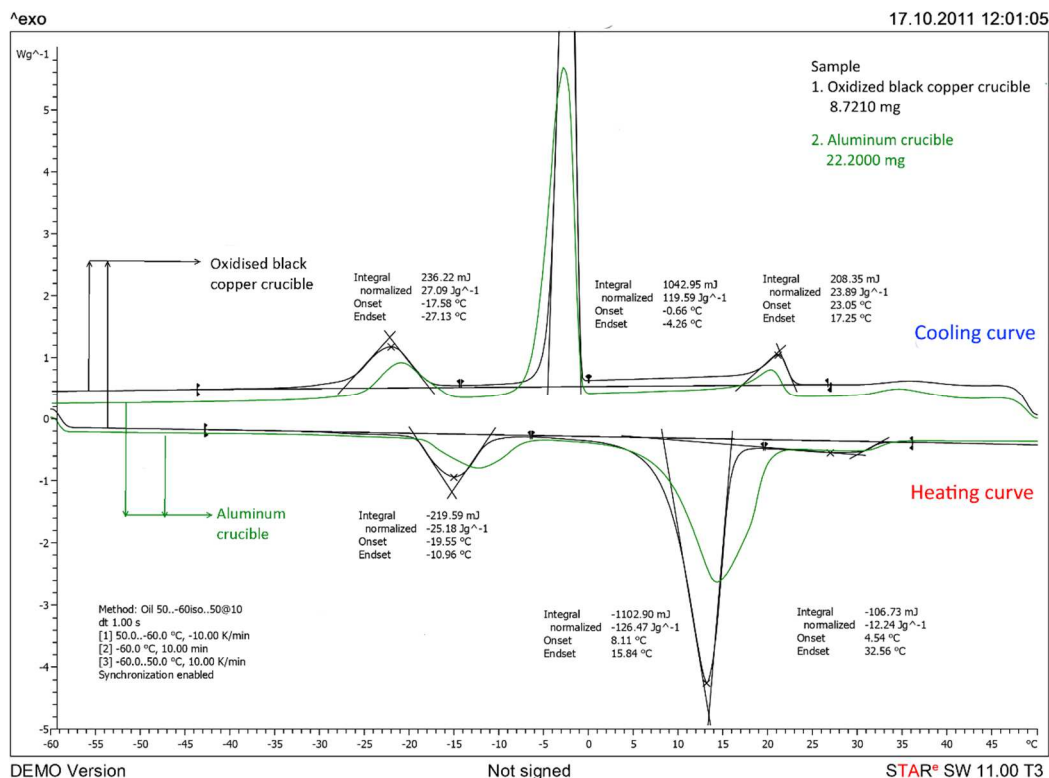


FIGURE 1-6: COMPARISON OF DSC THERMOGRAMS OF SAME SAMPLE IN AN ALUMINUM (SAMPLE MASS 22.2 MG) AND OXIDIZED COPPER CRUCIBLE (SAMPLE MASS 8.72 MG).<sup>26</sup>

<sup>26</sup> Acknowledgements to Dr. Rudolf Riesen for supporting us in carrying out some experiments and providing us with the data at the Materials Characterization Market Support Lab of Mettler Toledo Analytical in Schwerzenbach, Switzerland.

A more detailed photo series of the crystallization of the enriched crystal fraction of high oleic sunflower oil PUFA mixture with pictures taken every 6 seconds has been illustrated in Figure 1-7 and Figure 1-8. The method has been discussed in Section 4.2.1-4.2.2 in the main manuscript.



**FIGURE 1-7: PHASE BEHAVIOR OF ENRICHED CRYSTAL FRACTION OF HIGH OLEIC SUNFLOWER OIL @ 10<sup>KMIN-1</sup>, 50°C TO - 60°C IN AN OXIDIZED BLACK COPPER CRUCIBLE<sup>27</sup>**

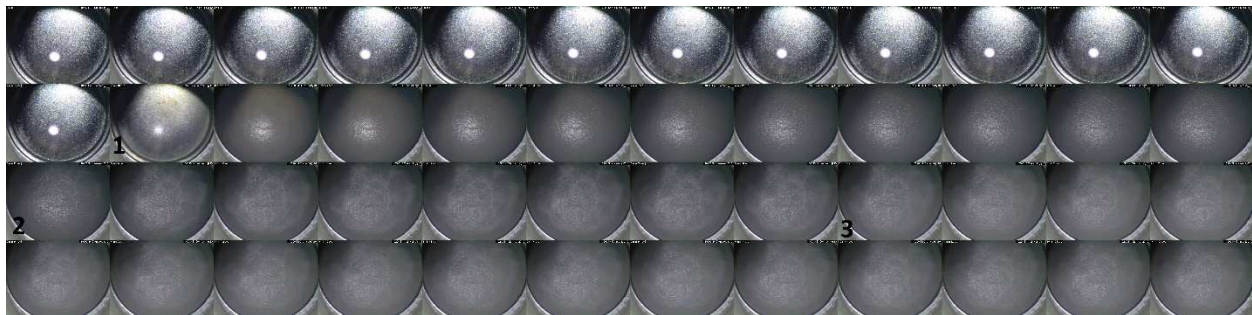


**FIGURE 1-8: : PHASE BEHAVIOR OF ENRICHED CRYSTAL FRACTION OF HIGH OLEIC SUNFLOWER OIL @ 10<sup>KMIN-1</sup>, 50°C TO - 60°C IN AN ALUMINUM CRUCIBLE**

As can be clearly seen in the pictures, the oxidized black copper crucible delivers much better results than the visuals of the sample crystallization in the aluminum crucibles.

---

<sup>27</sup> Acknowledgements to Dr. Rudolf Riesen for supporting us in carrying out some experiments and providing us with the data at the Materials Characterization Market Support Lab of Mettler Toledo Analytical in Schwerzenbach, Switzerland.

### 1.3. Flash Differential Scanning Calorimeter

The technical specifications of the Flash DSC are given in Table 1-1. All data has directly taken from the product brochure by Mettler-Toledo AG, Analytical.

<b>Temperature Data</b>	
Cooling rate range	-0.1 K/s to -4000 K/s
Heating rate range	0.5 K/s to 40,000 K/s
Temperature range (Intracooler 2 stage)	-95°C to 450°C
<b>Sensor data</b>	
Material	Ceramic
Thermocouples	16
Sample size	10ng to 1µg
<b>DSC sensor</b>	
Sensor type	Ultra-fast-sensor 1st generation
P <sub>max</sub> heat flow signal	20 mW
<b>Signal resolution</b>	
Resolution	0.005 K (0 °C ... 250 °C) 0.01 K (-100 °C ... 400 °C)

**TABLE 1-1: TECHNICAL SPECIFICATIONS OF FLASH DSC<sup>12528</sup>**

<sup>28</sup> Mettler-Toledo AG, Analytical. Flash Differential Scanning Calorimetry. [http://www.mt.com/de/en/home/library/product-brochures/lab-analytical-instruments/Flash\\_DSC\\_1/jcr:content/download/file/file.res/51725315\\_Flash\\_DSC1\\_Brochure\\_e.pdf](http://www.mt.com/de/en/home/library/product-brochures/lab-analytical-instruments/Flash_DSC_1/jcr:content/download/file/file.res/51725315_Flash_DSC1_Brochure_e.pdf) (accessed November 21, 2016).

A magnified illustration of the sensors of standard DSC and a Flash DSC has been given in Figure 1-9 so as to understand the differences in magnitude of the samples so as to enable fast heat transfer as well signal detection.

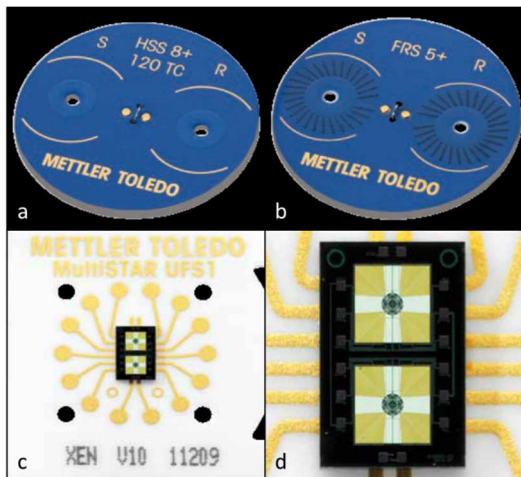


**FIGURE 1-9: DSC SENSORS A. HSS8 SENSOR WITH 120 THERMOCOUPLES IN A STANDARD DSC; B. FRS5 WITH 56 THERMOCOUPLES IN A STANDARD DSC; C. MULTISTAR SENSOR IN A FLASH DSC WITH 16 THERMOCOUPLES; D. MAGNIFIED VERSION OF FIGURE 2C SHOWING THE MEMS TECHNOLOGY<sup>125,15929, 30</sup>**

<sup>29</sup> Mettler-Toledo AG, Analytical. Differential Scanning Calorimetry for Routine Analysis. [http://www.mt.com/dam/Analytical/ThermalAnalysis/TA-PDF/DSC3\\_Brochure\\_en\\_30247073A\\_V05.15\\_Original\\_38549.pdf](http://www.mt.com/dam/Analytical/ThermalAnalysis/TA-PDF/DSC3_Brochure_en_30247073A_V05.15_Original_38549.pdf).

<sup>30</sup> Schubnell, M. *DSC Microscopy, Chemiluminescence and Photocalorimetry Version 3.0*; Mettler Toledo, 2010.

### 1.4. Gas chromatography – Flame Ionization Detector

The following figures illustrate chromatograms for each type of PUFA mixture investigated in this work. They differ a little bit from the one used in the main manuscript. This was shown deliberately to depict that different charges of supply of the same mixtures had naturally slightly different compositions which is due to the efficiency and quality of fractionation accomplished in the supplier industry.

Poly-unsaturated Fatty Acid Mixture (PUFA)	Palmitic acid	Stearic acid	Oleic acid	Linoleic acid	Linolenic acid
	C16:0 [%]	C18:0 [%]	C18:1 [%]	C18:2 [%]	C18:3 [%]
High linoleic Sunflower oil based PUFA	6.1	3.3	25.32	63.9	0.3
High linoleic Soya oil based PUFA	11.2	4.1	25.23	51.1	7.1
High oleic Sunflower oil based PUFA	3.5	3.2	84.7	7.0	0.1
High oleic Palm oil based PUFA	3.2	8.5	76.8	9.7	0.6
High linoleic Linseed Oil based PUFA	5.6	3.4	19.26	16.8	54.7

**TABLE 1-2: COMPOSITIONS OF DIFFERENT PUFA MIXTURES OBTAINED FROM NATURALLY OCCURRING PLANT OILS**



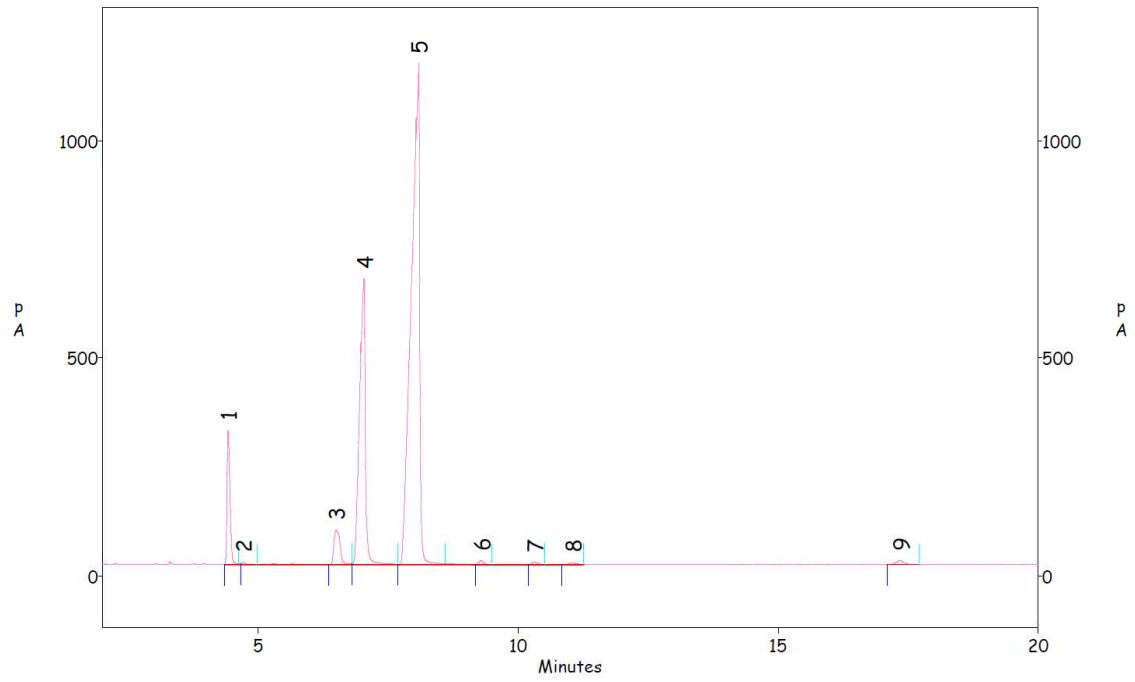


**FIGURE 1-10: CHROMATOGRAM OF A HIGH LINOLEIC SUNFLOWER OIL BASED PUFA MIXTURE ANALYZED BY GC-FID**

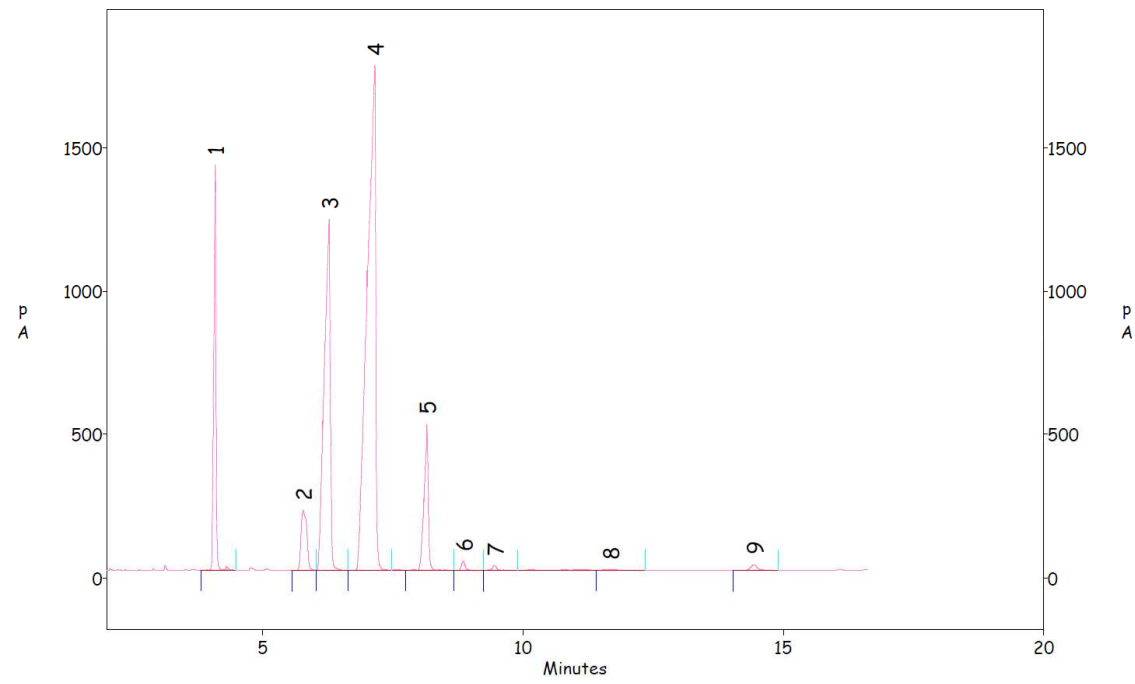


**FIGURE 1-11: CHROMATOGRAM OF A HIGH LINOLEIC SOYA OIL BASED PUFA MIXTURE ANALYZED BY GC-FID**



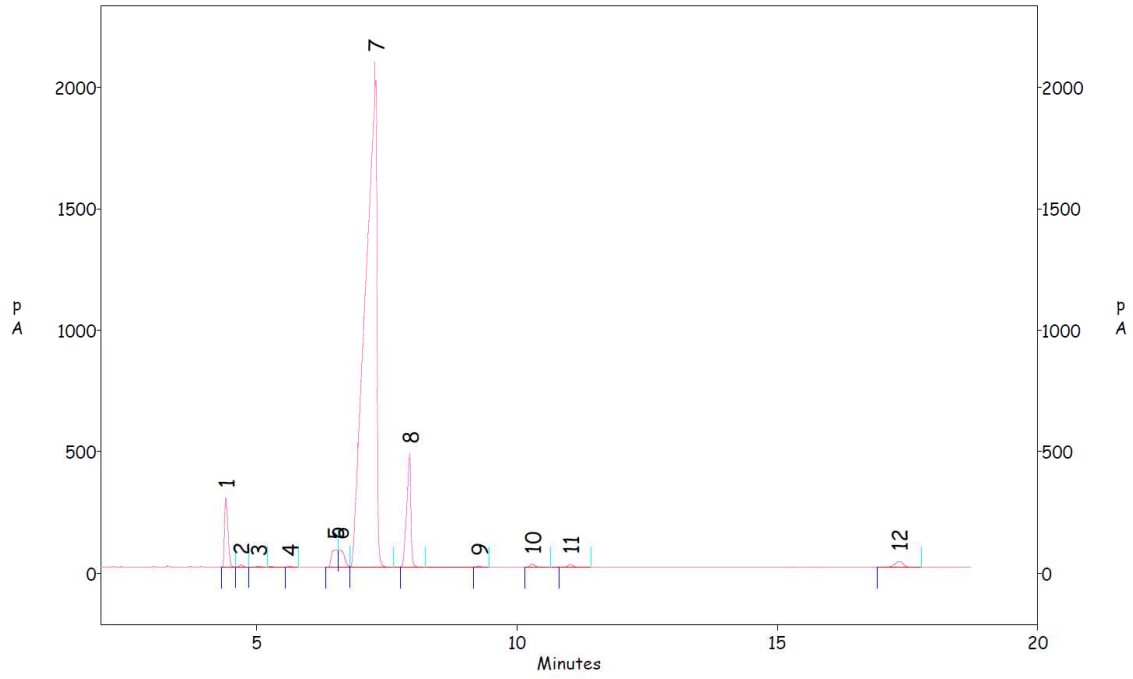


**FIGURE 1-12: CHROMATOGRAM OF A HIGH OLEIC SUNFLOWER OIL BASED PUFA MIXTURE ANALYZED BY GC-FID**

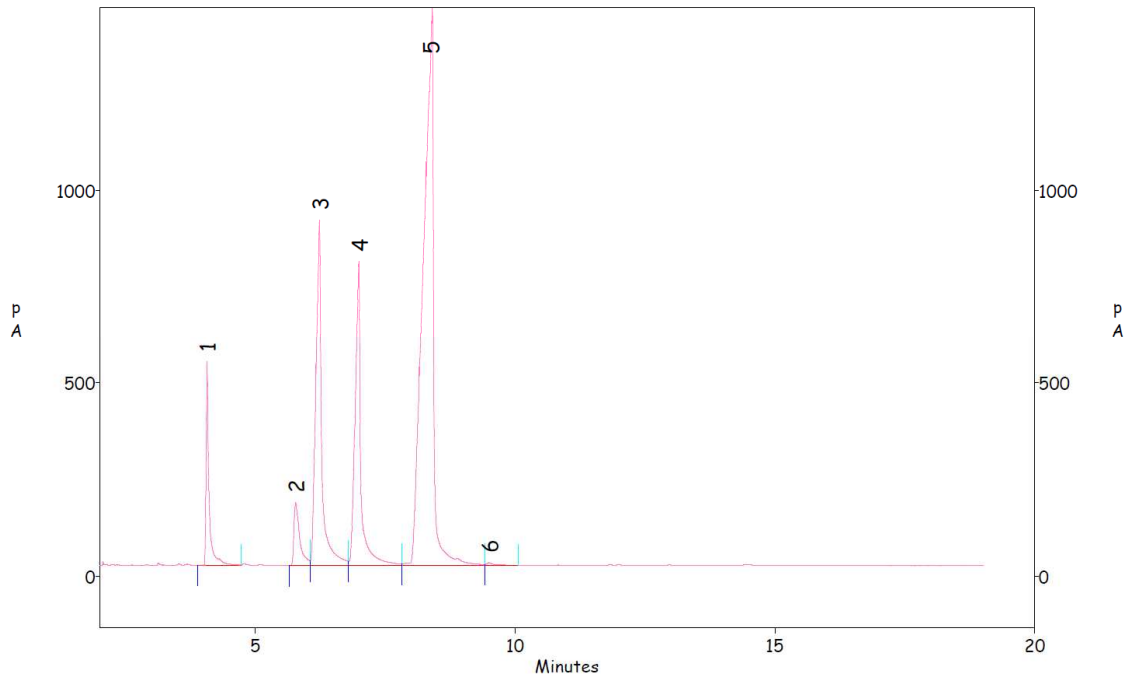


**FIGURE 1-13: CHROMATOGRAM OF A HIGH LINOLENIC LINSEED OIL BASED PUFA MIXTURE ANALYZED BY GC-FID**

## 2. Solid liquid phase diagrams

### 2.1. Phase diagram of high oleic palm oil PUFA mixture at low saturated content including metastable ranges

The high oleic palm oil PUFA mixture was taken from the storage and passed on to a tempered CSTR at 50°C with a retention time of 1 hour. The melt was further processed in a series of 3 scrapped layer jacketed crystallizers. The temperature in the jacket was maintained such that  $\Delta T < 5K$  from the liquidus point obtained from the Differential Scanning Calorimeter (DSC) thermal analyses. Each crystallizer was also maintained at a temperature 5K below the previous one. This way a slow and successive cooling of the PUFA was achieved such probes from every fraction could be obtained. Probes were taken from every stage and crystallizers and analyzed both in the DSC and Gas Chromatography – Flame Ionization Detector (GC-FID). Phase transitions were recorded in the DSC with the following temperature regime: 50°C to -20°C to 50°C @ 0.2 Kmin<sup>-1</sup>. Enthalpy differences between high oleic palm oil mixture and air were measured. Fatty acids were esterified before analyses. The thermogram results were plotted as a function of the concentration of stearic acid (use generally as standard representative for saturated content in vegetable oils). It can be noted that the liquidus and the solidus curves do not intersect till about 1.5 mol % of stearic acid.<sup>155</sup>

Onset 1[°C]	Onset 2[°C]	Endset 2'[°C]	Endset 1' [°C]
Spontaneous nucleation	Solidification point	Melting of solidified phase	Liquidus point
23.38	5.6875	10.51	36.8075

TABLE 2-1: SIGNIFICANT TEMPERATURES OBTAINED FROM THERMOGRAMS IN THE DSC (50°C TO -20°C TO 50°C @0.2KMIN-1)<sup>155</sup>

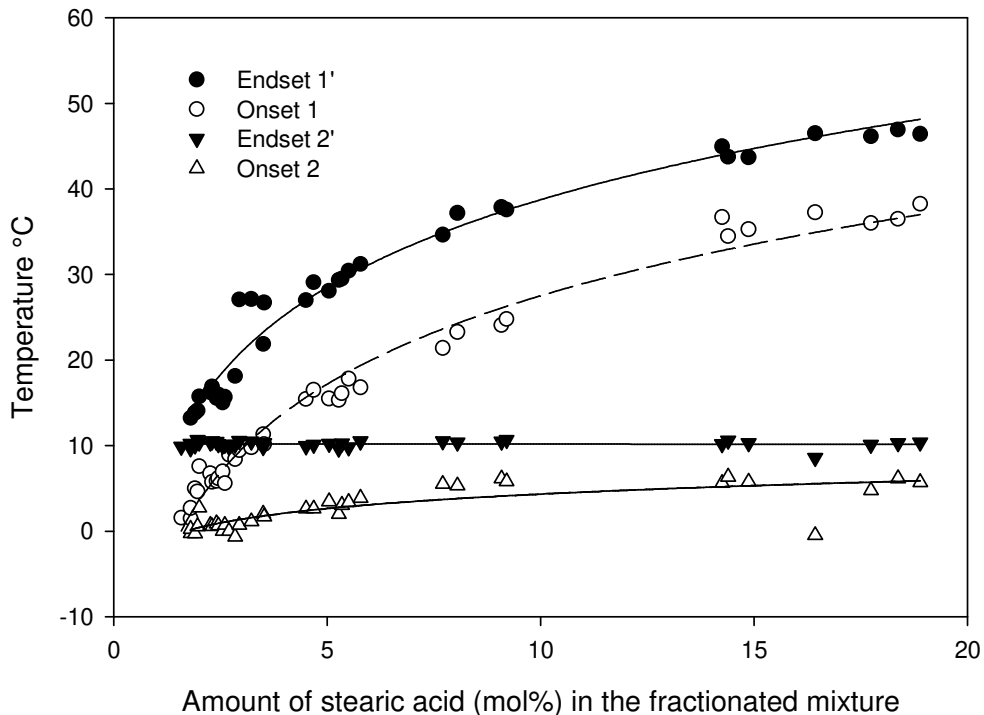
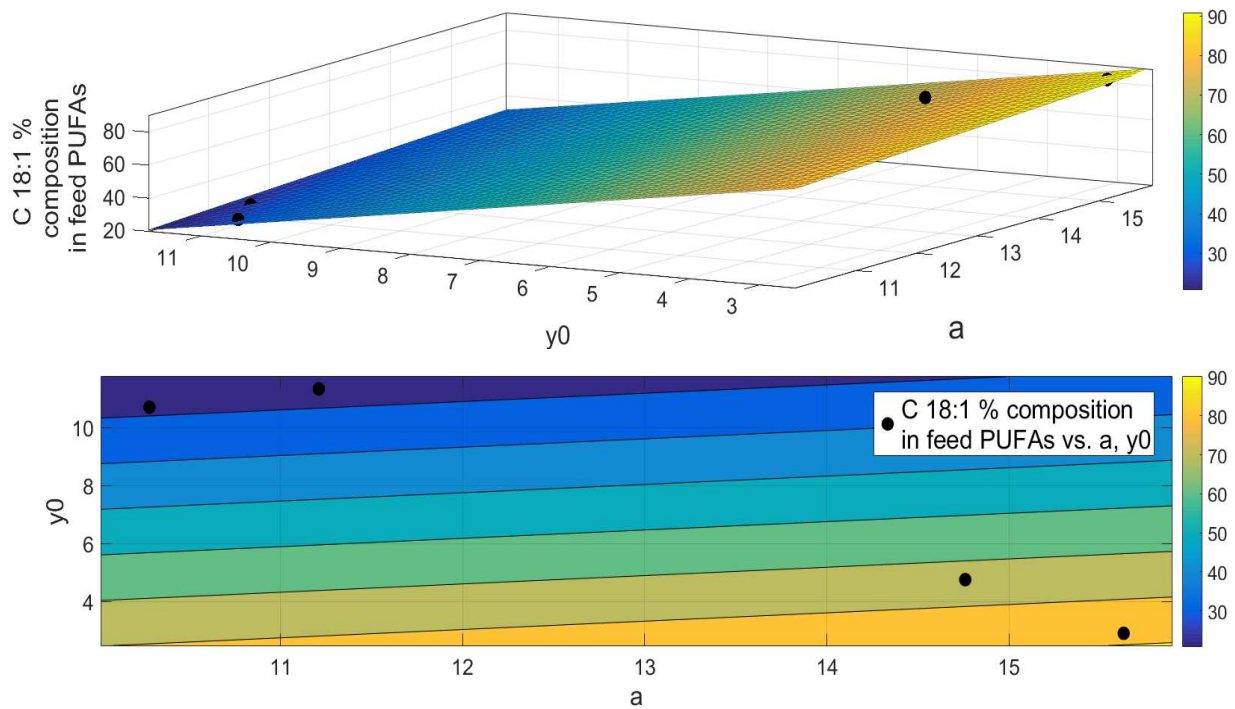


FIGURE 2-1: LIQUID SOLID EQUILIBRIUM DATA OF STEARIC ACID IN HIGH LINOLEIC SUNFLOWER OIL BASED PUFA MIXTURE<sup>155</sup>

## 2.2. Dependency of liquidus and solidus curves on mono-unsaturated acid fraction in mixture

As discussed in Section 5.2.8 there is a clear dependency on the composition of the PUFAs when it comes to the temperatures range in which the crystallization occurs. This has been illustrated in Figure 5-16 and 5-17 in the main manuscript. Figure 2-2 is a 3D plot depicting the effects of the C18:1 fraction in the original composition of the oil PUFA mixtures on parameters 'a' and 'y<sub>0</sub>' of the liquidus line fit. The difference between Figure 2-2 and Figure 5-16 is that the former does not include the results of the linseed oil PUFA mixture. There is an effect although not the dominant one of the presence of a high amount of linolenic acid in the mixture on the results as mentioned before. If we remove this mixture and compare the effects of oleic acid on the liquidus lines on the other four acids (high oleic and high linoleic) then the dependency is even more prominent. Naturally the coefficient of variation is better in this case which amounts to 0.996.



**FIGURE 2-2: DEPENDENCY OF PARAMETERS  $y_0$  AND  $a$  OF LIQUIDUS CURVE FIT ON THE C18:1 FRACTION PRESENT IN VEGETABLE OIL BASED PUFA MIXTURES ALONG WITH THE CONTOUR WITHOUT LINSEED OIL BASED PUFA MIXTURE**

A simple linear surface fit was used to fit the data.

$$f(x, y) = p_{00} + p_{10} * x + p_{01} * y$$

Coefficients	Value	95% confidence bounds	$R^2$
$p_{00}$	77.42	(-732.8, 887.7)	0.996
$p_{10}$	1.829	(-44.44, 48.1)	
$p_{01}$	-6.37	(-35.1, 22.36)	

**TABLE 2-2: COEFFICIENTS FOR THE LINEAR SURFACE FIT USED IN EQUATION FOR THE DEPENDENCY OF THE LIQUIDUS LINE FIT ON FRACTION OF MONO-UNSATURATED ACID**

### 3. Nucleation kinetics

#### 3.1. Polarized light microscopy coupled with high definition camera

##### 3.1.1. Calibration

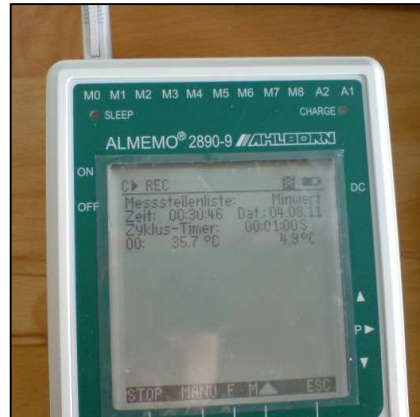
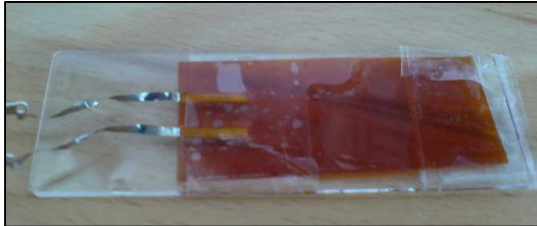


**FIGURE 3-1: ALMEMO PT 100 4-WIRE FLEXIBLE TEMPERATURE SENSOR(ZA 9030-FS1 NORM E4) AND DATA LOGGER(2890-9) FOR TEMPERATURE CALIBRATION IN THE GRADIENT CHAMBER LTS 120**

The stabilization time is defined as the time required by the gradient stage to stabilize at the temperature given by the sensor. The calibrated temperatures were then used for the correction of the supercooling values as a result of changing crystallization temperatures. This led to although correct but little unconventional values of supercooling.

Left side of the gradient stage							
Sensor Linksys 2 Kmin <sup>-1</sup>		Sensor Linksys 4 Kmin <sup>-1</sup>		Sensor Linksys 10 Kmin <sup>-1</sup>		Sensor Linksys 20Kmin <sup>-1</sup>	
Stabilization time							
0 s		12 s		27 s		38 s	
26	25.5	26	25	26	23.6	26	21.4
25.5	25	25.5	24.5	25.5		25	20.2
25	24.5	25	24	25	22.5	24	19.2
24.5	24	24.5	23.5	24.5		23	18.2
24	23.5	24	23	24	21.5	22	17.1
23.5	23	23.5	22.4	23.5		21	15.9
23	22.5	23	22	23	20.4	20	14.8
22.5	22	22.5	21.4	22.5		19	13.7
22	21.5	22	20.9	22	19.4	18	12.8
21.5	20.9	21.5	20.4	21.5		17	11.6
21	20.4	21	19.9	21	18.3	16	10.6
20.5	19.9	20.5	19.4	20.5		15	9.6
20	19.4	20	18.9	20	17.2	14	8.3
19.5	18.9	19.5	18.3	19.5		13	7.3
19	18.4	19	17.8	19	16.3	12	6.4
18.5	17.9	18.5	17.3	18.5		11	5.1
18	17.4	18	16.8	18	15.2	10	
17.5	16.8	17.5	16.3	17.5		9	
17	16.3	17	15.8	17	14.2	8	
16.5	15.8	16.5	15.3	16.5		7	
16	15.3	16	14.8	16	13.1	6	
15.5	14.8	15.5	14.3	15.5		5	
15	14.3	15	13.8	15	12.1		
14.5	13.8	14.5	13.2	14.5			
14	13.3	14	12.8	14	11.1		
13.5	12.7	13.5	12.2	13.5			
13	12.2	13	11.7	13	10		
12.5	11.7	12.5	11.2	12.5			
12	11.2	12	10.7	12	9		
11.5	10.7	11.5	10.2	11.5			
11	10.2	11	9.7	11	8		
10.5	9.7	10.5	9.1	10.5			
10	9.1	10	8.6	10	7		
9.5	8.6	9.5	8.1	9.5			
9	8.1	9	7.6	9	5.9		
8.5	7.6	8.5	7.1	8.5			
8	7.1	8	6.6	8	4.9		
7.5	6.6	7.5	6.1	7.5			
7	6.1	7	5.5	7			
6.5	5.6	6.5	5	6.5			
6	5.1	6	4.5	6			
5.5	4.5	5.5	4	5.5			

**TABLE 3-1: CALIBRATION OF THE LEFT SIDE OF THE GRADIENT STAGE (TEMPERATURE CONTROLLER SOFTWARE LINKSYS) WITH AN ALMEMO TEMPERATURE DATA LOGGING MODULE (2890-9) AND A FLAT FOIL SENSOR (ZA 9030-FS1 NORM E4); RESOLUTION  $\pm 0.1^{\circ}\text{C}$**

Right side of the gradient stage							
Sensor Linksys 2 Kmin <sup>-1</sup>		Sensor Linksys 4 Kmin <sup>-1</sup>		Sensor Linksys 10 Kmin <sup>-1</sup>		Sensor Linksys 20Kmin <sup>-1</sup>	
Stabilization time							
0 s		12 s		27 s		38 s	
26	25.6	26	25	26	23.8	26	22.1
25.5	25.2	25.5	24.6	25.5		25	20.8
25	24.3	25	24.1	25	22.7	24	19.8
24.5	24	24.5	23.6	24.5		23	18.7
24	23.5	24	23.1	24	21.6	22	17.5
23.5	23	23.5	22.5	23.5		21	16.4
23	22.5	23	22	23	20.6	20	15.4
22.5	22	22.5	21.5	22.5		19	14.3
22	21.5	22	21	22	19.7	18	13.3
21.5	21	21.5	20.5	21.5		17	12.2
21	20.4	21	20	21	18.6	16	11.2
20.5	19.9	20.5	19.5	20.5		15	10.1
20	19.4	20	19	20	17.5	14	9
19.5	18.9	19.5	18.5	19.5		13	8.1
19	18.4	19	18	19	16.5	12	7.1
18.5	17.9	18.5	17.4	18.5		11	6
18	17.4	18	16.9	18	15.5	10	4.9
17.5	16.9	17.5	16.4	17.5		9	
17	16.3	17	15.9	17	14.4	8	
16.5	15.8	16.5	15.4	16.5		7	
16	15.3	16	14.9	16	13.4	6	
15.5	14.8	15.5	14.3	15.5		5	
15	14.3	15	13.8	15	12.4		
14.5	13.8	14.5	13.3	14.5			
14	13.3	14	12.8	14	11.4		
13.5	12.8	13.5	12.3	13.5			
13	12.3	13	11.8	13	10.3		
12.5	11.7	12.5	11.3	12.5			
12	11.2	12	10.8	12	9.3		
11.5	10.7	11.5	10.3	11.5			
11	10.2	11	9.7	11	8.3		
10.5	9.7	10.5	9.3	10.5			
10	9.2	10	8.7	10	7.2		
9.5	8.7	9.5	8.2	9.5			
9	8.2	9	7.7	9	6.2		
8.5	7.6	8.5	7.2	8.5			
8	7.1	8	6.7	8	5.2		
7.5	6.6	7.5	6.2	7.5			
7	6.1	7	5.6	7	4.2		
6.5	5.6	6.5	5.1	6.5			
6	5.1	6	4.6	6			
5.5	4.6	5.5	4.1	5.5			
5	4.1	5		5			

**TABLE 3-2: CALIBRATION OF THE RIGHT SIDE OF THE GRADIENT STAGE (TEMPERATURE CONTROLLER SOFTWARE LINKSYS) WITH AN ALMEMO TEMPERATURE DATA LOGGING MODULE (2890-9) AND A FLAT FOIL SENSOR (ZA 9030-FS1 NORM E4); RESOLUTION ±0.1°C**

### 3.1.2. Nucleation kinetics modeling

The shape factor, 'a', in Equation 2-8 is generally assumed for spherical crystals. Adjustments into other shapes of crystals are possible by means of correction factors as shown in Table 3-3.

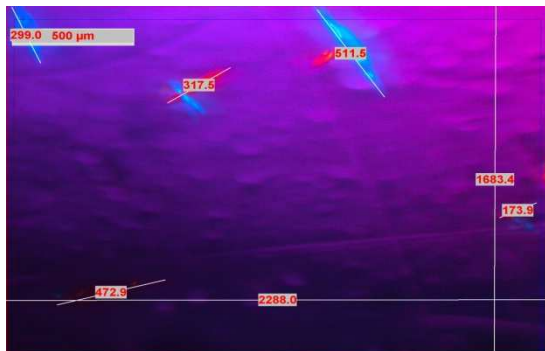
Shape of crystal	Correction factor
Spherical	$4.84u_0^{2/3}$
Tetrahedral	$7.21u_0^{2/3}$
Cube	$6u_0^{2/3}$
Octahedral	$5.72u_0^{2/3}$

TABLE 3-3: VALUES OF A AS A FUNCTION OF THE SHAPE OF THE CRYSTAL



### 3.1.3. High linoleic sunflower oil based PUFA mixture

The following Figure 3-2 and Figure 3-3 are the pictorial evidences with regard to Section 5.3.1.2 and particularly Figure 5-20 and 5-21. Figure 3-2 shows the various sizes and count of the crystals at different crystallization temperatures, thereby showing how a crystal growth is affected with larger crystal count.



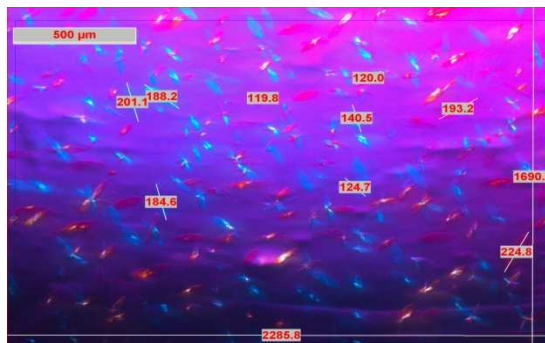
30 Kmin<sup>-1</sup> ΔT=4,87 K



30 Kmin<sup>-1</sup> ΔT=5,37 K



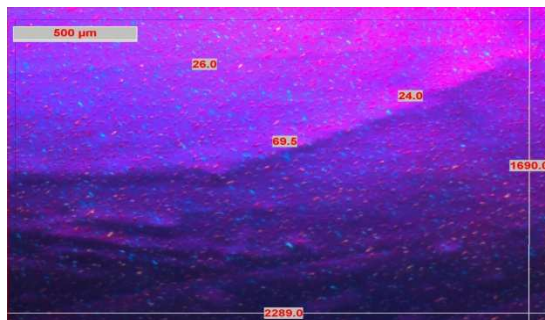
30 Kmin<sup>-1</sup> ΔT=5,87 K



30 Kmin<sup>-1</sup> ΔT=6,37 K



30 Kmin<sup>-1</sup> ΔT=6,87 K



30 Kmin<sup>-1</sup> ΔT=7,37 K

**FIGURE 3-2: PICTOGRAPHIC REPRESENTATION OF THE MELT CRYSTALLIZATION OF HIGH LINOLEIC SUNFLOWER OIL BASED PUFA AT 30 KMIN<sup>-1</sup> AT DIFFERENT SUPERCOOLING**

Figure 3-3 illustrating the crystallization at a specific supercooling of 5.9K and varying cooling rates on the other hand further show that the results are not so drastically different from one another like in Figure 3-2. Crystal pictures are very similar for 20 Kmin<sup>-1</sup> and 30kmin<sup>-1</sup>. Explanations have been provided in detail in Section 4.3.1 in the main manuscript.

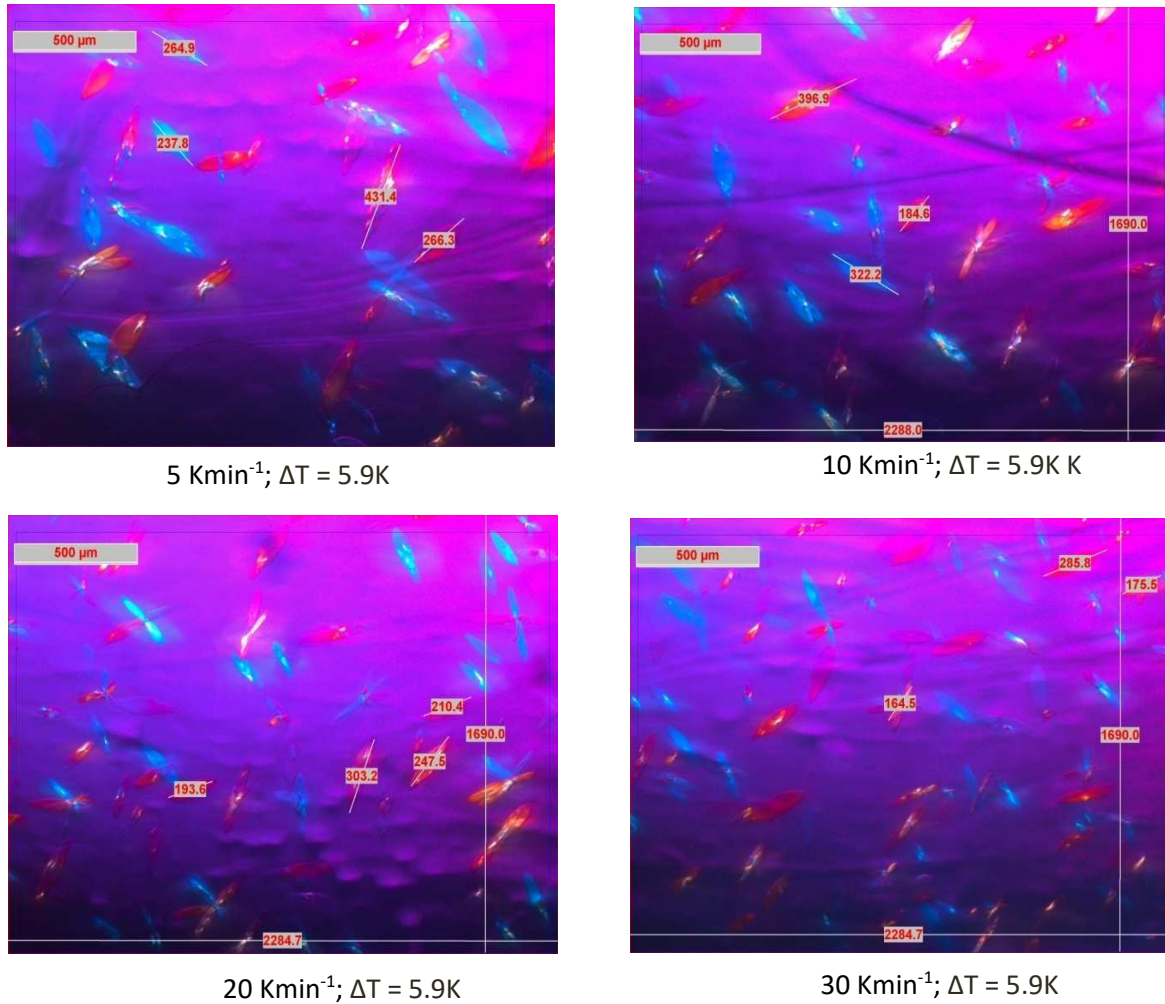


**FIGURE 3-3: PICTOGRAPHIC REPRESENTATION OF THE MELT CRYSTALLIZATION OF HIGH LINOLEIC SUNFLOWER OIL BASED PUFA AT A SUPERCOOLING OF 5.9 K WITH VARYING COOLING RATES**

Cooling rate	Crystallizing temperature [°C]	Supercooling [K]	Induction time [s]	Nuclei per area [mm <sup>-2</sup> ]
5 Kmin <sup>-1</sup>	19.5	4.87	189.56	1
	19.5	4.87	329.56	1
	19.5	4.87	189.56	1
	19	5.37	198.56	1
	19	5.37	98.56	5
	19	5.37	142.56	7
	18.5	5.87	78.56	8
	18.5	5.87	68.56	12
	18.5	5.87	108.56	7
	18	6.37	77.56	27
	18	6.37	70.56	22
	18	6.37	70.56	26
	17.5	6.87	63.56	40
	17.5	6.87	87.56	24
	17.5	6.87	64.56	27

**TABLE 3-4::INDUCTION TIME AND NUMBER OF NUCLEI PER UNIT AREA DURING MELT CRYSTALLIZATION OF A HIGH LINOLEIC SUNFLOWER OIL PUFA MIXTURE AS A FUNCTION OF SUPERCOOLING AT 5KMIN<sup>-1</sup>**

Cooling rate	Crystallizing temperature [°C]	Supercooling [K]	Induction time [s]	Nuclei per area [mm <sup>-2</sup> ]
10 Kmin <sup>-1</sup>	19.5	4.87	244.78	1
	19.5	4.87	284.78	1
	19.5	4.87	232.78	2
	19	5.37	121.78	5
	19	5.37	136.78	7
	19	5.37	110.78	3
	18.5	5.87	56.78	13
	18.5	5.87	71.78	13
	18.5	5.87	68.78	12
	18	6.37	79.78	21
	18	6.37	70.78	19
	18	6.37	60.78	36
	17.5	6.87	54.78	28
	17.5	6.87	57.78	32
	17.5	6.87	55.78	32

**TABLE 3-5: INDUCTION TIME AND NUMBER OF NUCLEI PER UNIT AREA DURING MELT CRYSTALLIZATION OF A HIGH LINOLEIC SUNFLOWER OIL PUFA MIXTURE AS A FUNCTION OF SUPERCOOLING AT 10KMIN<sup>-1</sup>**

Cooling rate	Crystallizing temperature [°C]	Supercooling [K]	Induction time [s]	Nuclei per area [mm <sup>-2</sup> ]
20 Kmin <sup>-1</sup>	19.5	4.87	259.39	1
	19.5	4.87	293.39	1
	19.5	4.87	223.39	2
	19	5.37	116.89	6
	19	5.37	96.89	4
	19	5.37	99.89	9
	18.5	5.87	75.39	3
	18.5	5.87	78.39	19
	18.5	5.87	83.39	14
	18	6.37	68.89	30
	18	6.37	75.89	22
	18	6.37	63.89	34
	17.5	6.87	48.39	31
	17.5	6.87	45.39	35
	17.5	6.87	55.39	50

**TABLE 3-6: INDUCTION TIME AND NUMBER OF NUCLEI PER UNIT AREA DURING MELT CRYSTALLIZATION OF A HIGH LINOLEIC SUNFLOWER OIL PUFA MIXTURE AS A FUNCTION OF SUPERCOOLING AT 20KMIN<sup>-1</sup>**

Cooling rate	Crystallizing temperature [°C]	Supercooling [K]	Induction time [s]	Nuclei per area [mm <sup>-2</sup> ]
30 Kmin <sup>-1</sup>	19.5	4.87	303.26	2
	19.5	4.87	173.26	3
	19.5	4.87	223.26	1
	19	5.37	80.26	25
	19	5.37	96.26	6
	19	5.37	148.26	7
	18.5	5.87	87.26	14
	18.5	5.87	85.26	14
	18.5	5.87	82.26	11
	18	6.37	65.26	46
	18	6.37	54.26	42
	18	6.37	54.26	29
	17.5	6.87	37.26	79
	17.5	6.87	35.26	87
	17.5	6.87	36.26	74

**TABLE 3-7: INDUCTION TIME AND NUMBER OF NUCLEI PER UNIT AREA DURING MELT CRYSTALLIZATION OF A HIGH LINOLEIC SUNFLOWER OIL PUFA MIXTURE AS A FUNCTION OF SUPERCOOLING AT 30KMIN<sup>-1</sup>**

### 3.1.4. High oleic sunflower oil based PUFA mixture

Every experiment run under the microscope to determine the induction time and the number of nuclei per unit area was repeated at least thrice and an average was taken for the final value. All data pertaining to these experiments have been given in the following tables.

Cooling rate	Crystallizing temperature [°C]	Supercooling [K]	Induction time [s]	Nuclei per area [mm <sup>-2</sup> ]
2 Kmin <sup>-1</sup>	14.5	3	225	118
	14.5	3	235	114
	14.5	3	193	186
	15	2.5	226	150
	15	2.5	263	384
	15	2.5	288	312
	15.5	2	313	82
	15.5	2	473	182
	15.5	2	389	246
	16	1.5	415	124
	16	1.5	447	32
	16	1.5	545	46
	16.5	1	586	125
	16.5	1	590	50
	16.5	1	960	50

**TABLE 3-8: INDUCTION TIME AND NUMBER OF NUCLEI PER UNIT AREA DURING MELT CRYSTALLIZATION OF A HIGH OLEIC SUNFLOWER OIL PUFA MIXTURE AS A FUNCTION OF SUPERCOOLING AT 2KMIN<sup>-1</sup>**

Cooling rate	Crystallizing temperature [°C]	Supercooling [K]	Induction time [s]	Nuclei per area [mm <sup>-2</sup> ]
4 Kmin <sup>-1</sup>	14.5	3	158	452
	14.5	3	217	475
	14.5	3	143	505
	15	2.5	171	525
	15	2.5	228	300
	15	2.5	217	425
	15.5	2	196	500
	15.5	2	230	300
	15.5	2	268	275
	16	1.5	374	148
	16	1.5	560	78
	16	1.5	346	206
	16.5	1	658	8
	16.5	1	619	10
	16.5	1	770	30

**TABLE 3-9: INDUCTION TIME AND NUMBER OF NUCLEI PER UNIT AREA DURING MELT CRYSTALLIZATION OF A HIGH OLEIC SUNFLOWER OIL PUFA MIXTURE AS A FUNCTION OF SUPERCOOLING AT 4KMIN<sup>-1</sup>**

Cooling rate	Crystallizing temperature [°C]	Supercooling [K]	Induction time[s]	Nuclei per area [mm <sup>-2</sup> ]
10 Kmin <sup>-1</sup>	14.5	3	205	all crystallized
	14.5	3	167	all crystallized
	14.5	3	233	all crystallized
	15	2.5	212	700
	15	2.5	251	550
	15	2.5	203	all crystallized
	15.5	2	305	616
	15.5	2	262	552
	15.5	2	349	96
	15.5	2	387	104
	16	1.5	379	14
	16	1.5	586	16
	16	1.5	467	144
	16.5	1	1260	2
	16.5	1	-	0
16.5	1	936	10	

**TABLE 3-10: INDUCTION TIME AND NUMBER OF NUCLEI PER UNIT AREA DURING MELT CRYSTALLIZATION OF A HIGH OLEIC SUNFLOWER OIL PUFA MIXTURE AS A FUNCTION OF SUPERCOOLING AT 10KMIN<sup>-1</sup>**



Cooling rate	Crystallizing temperature [°C]	Supercooling [K]	Induction Time [s]	Nuclei per area [mm <sup>-2</sup> ]
20 Kmin <sup>-1</sup>	14.5	3	129	all crystallized
	14.5	3	139	616
	14.5	3	128	728
	15	2.5	178	all crystallized
	15	2.5	173	176
	15	2.5	152	536
	15.5	2	289	all crystallized
	15.5	2	265	all crystallized
	15.5	2	324	288
	16	1.5	555	225
	16	1.5	461	184
	16	1.5	432	104
	16.5	1	970	12
	16.5	1	997	8
	16.5	1	746	6

**TABLE 3-11: INDUCTION TIME AND NUMBER OF NUCLEI PER UNIT AREA DURING MELT CRYSTALLIZATION OF A HIGH OLEIC SUNFLOWER OIL PUFA MIXTURE AS A FUNCTION OF SUPERCOOLING AT 20KMIN<sup>-1</sup>**

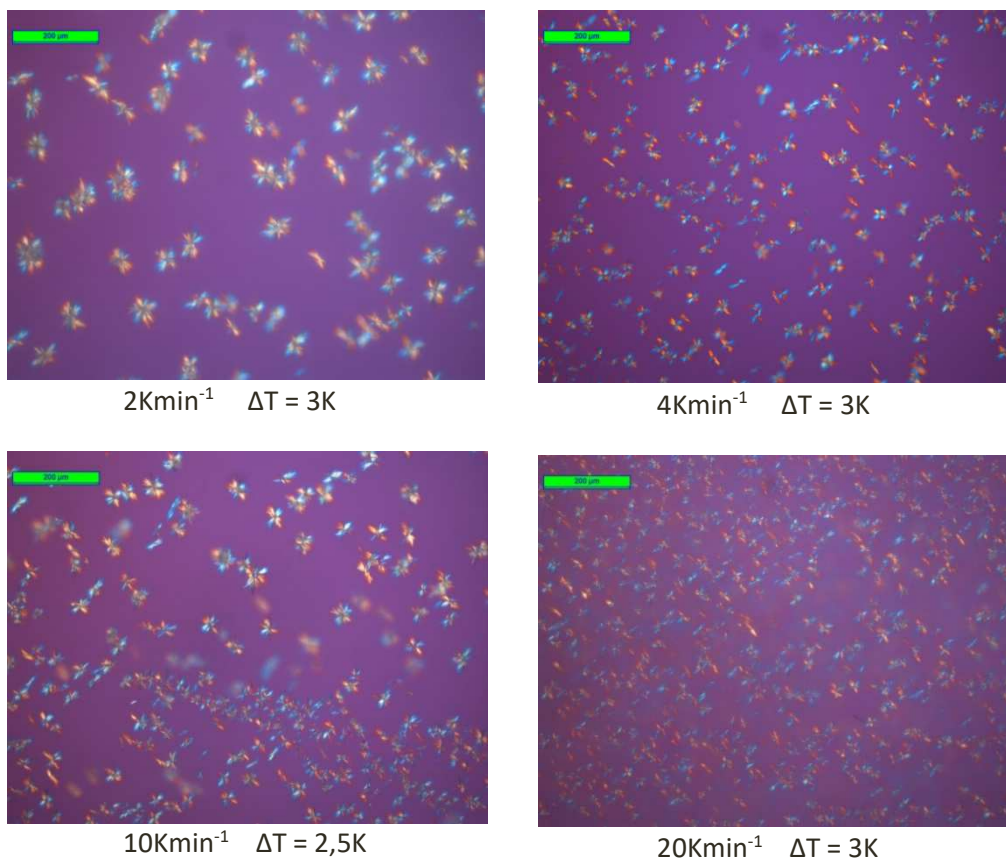


**FIGURE 3-4: PICTOGRAPHIC REPRESENTATION OF THE MELT CRYSTALLIZATION OF HIGH OLEIC SUNFLOWER OIL BASED PUFA AT A SUPERCOOLING OF 3K WITH VARYING COOLING RATES**

Regression equation	Cooling rate [K/min]	Coefficients			
		$y_0$	a	b	$R^2$
Induction time vs. Supercooling (Fig.5-23 – main manuscript)	2	196.6	$2.82 \cdot 10^3$	1.48	0.98
	4	135.2	$2.35 \cdot 10^3$	1.45	0.99
	10	215.8	$1.248 \cdot 10^4$	2.65	0.99
	20	77.93	$3.35 \cdot 10^3$	1.4	1
Number of nuclei per area vs. Supercooling (Fig.5-24- main manuscript)	2	34.48	6.41	1.47	0.97
	4	0	59.98	0.74	0.81
	10	-216.5	75.54	0.97	0.98
	20	-196.7	126.6	0.63	0.96

**TABLE 3-12: REGRESSION COEFFICIENTS AND EQUATIONS WITH RESPECT TO OPERATING PARAMETERS FOR FIGURE 4-20 AND 4-21 FOR THE HIGH OLEIC SUNFLOWER OIL PUFA MIXTURE**



### 3.1.5. High linoleic soya oil based PUFA mixture

Cooling rate	Crystallizing temperature [°C]	Supercooling [K]	Induction time[s]	Nuclei per area [mm <sup>-2</sup> ]
2 Kmin <sup>-1</sup>	22.5	3.44	-23	all crystallized
	22.5	3.44	35	all crystallized
	22.5	3.44	3	all crystallized
	23	2.94	18	28
	23	2.94	20	25
	23	2.94	17	17
	23.5	2.44	100	11
	23.5	2.44	68	11
	23.5	2.44	57	13
	24	1.94	463	1
	24	1.94	320	1
	24	1.94	164	2
	24.5	1.44	-	0
	24.5	1.44	848	1
	24.5	1.44	-	0

**TABLE 3-13: INDUCTION TIME AND NUMBER OF NUCLEI PER UNIT AREA DURING MELT CRYSTALLIZATION OF A HIGH LINOLEIC SOYA OIL PUFA MIXTURE AS A FUNCTION OF SUPERCOOLING AT 2KMIN<sup>-1</sup>**

Cooling rate	Crystallizing temperature [°C]	Supercooling [K]	Induction time[s]	Nuclei per area [mm <sup>-2</sup> ]
4 Kmin <sup>-1</sup>	22.5	3.44	-5	all crystallized
	22.5	3.44	-1	all crystallized
	22.5	3.44	-2	all crystallized
	23	2.94	17	all crystallized
	23	2.94	10	all crystallized
	23	2.94	2	all crystallized
	23.5	2.44	51	8
	23.5	2.44	44	15
	23.5	2.44	65	5
	24	1.94	190	3
	24	1.94	216	3
	24	1.94	240	2
	24.5	1.44	770	1
	24.5	1.44	894	1
	24.5	1.44	611	1

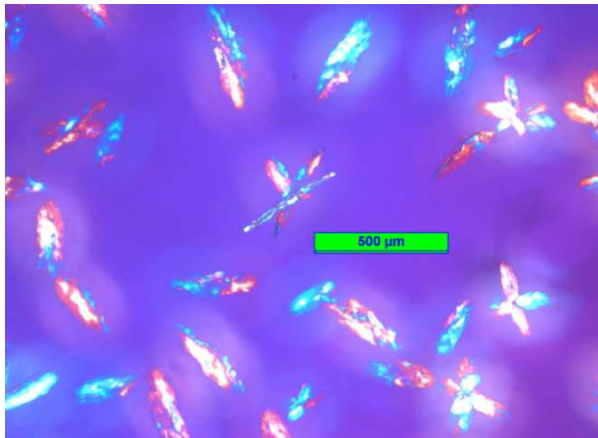
**TABLE 3-14: INDUCTION TIME AND NUMBER OF NUCLEI PER UNIT AREA DURING MELT CRYSTALLIZATION OF A HIGH LINOLEIC SOYA OIL PUFA MIXTURE AS A FUNCTION OF SUPERCOOLING AT 4KMIN<sup>-1</sup>**

Cooling rate	Crystallizing temperature [°C]	Supercooling [K]	Induction time[s]	Nuclei per area [mm <sup>-2</sup> ]
10 Kmin <sup>-1</sup>		3.44	11	all crystallized
	22.5	3.44	-7	all crystallized
	22.5	3.44	-5	all crystallized
	23	2.94	15	all crystallized
	23	2.94	3	all crystallized
	23	2.94	9	all crystallized
	23.5	2.44	32	10
	23.5	2.44	23	7
	23.5	2.44	65	4
	23.5	2.44	19	8
	24	1.94	242	2
	24	1.94	270	5
	24	1.94	186	5
	24.5	1.44	421	5
	24.5	1.44	-	0
	24.5	1.44	698	1

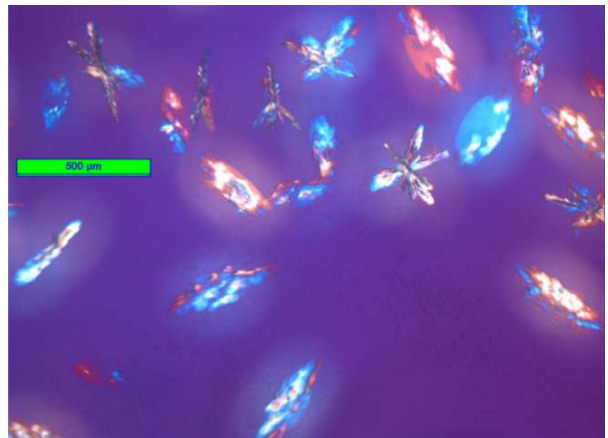
**TABLE 3-15: INDUCTION TIME AND NUMBER OF NUCLEI PER UNIT AREA DURING MELT CRYSTALLIZATION OF A HIGH LINOLEIC SOYA OIL PUFA MIXTURE AS A FUNCTION OF SUPERCOOLING AT 10KMIN<sup>-1</sup>**

Cooling rate	Crystallizing temperature [°C]	Supercooling [K]	Induction time[s]	Nuclei per area [mm <sup>-2</sup> ]
20 Kmin <sup>-1</sup>	22.5	3.44	-9	all crystallized
	22.5	3.44	-11	all crystallized
	22.5	3.44	2	all crystallized
	23	2.94	-2	all crystallized
	23	2.94	0	all crystallized
	23	2.94	2	all crystallized
	23.5	2.44	48	5
	23.5	2.44	24	6
	23.5	2.44	18	10
	23.5	2.44	37	23
	23.5	2.44	36	26
	24	1.94	103	11
	24	1.94	106	7
	24	1.94	163	7
	24	1.94	116	7
	24	1.94	102	6
	24	1.94	91	11
	24	1.94	120	9
24.5	1.44	861	1	
24.5	1.44	622	2	
24.5	1.44	1061	1	

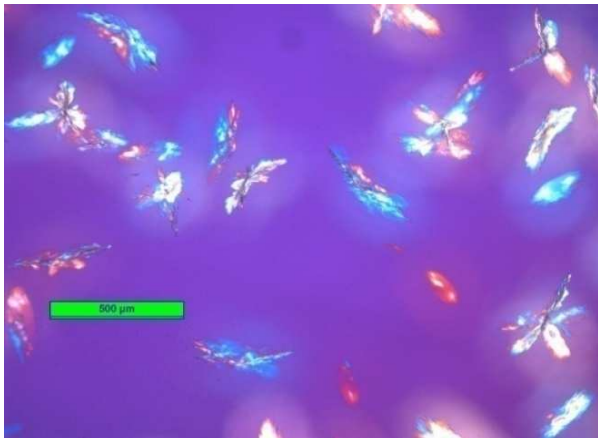
**TABLE 3-16: INDUCTION TIME AND NUMBER OF NUCLEI PER UNIT AREA DURING MELT CRYSTALLIZATION OF A HIGH LINOLEIC SOYA OIL PUFA MIXTURE AS A FUNCTION OF SUPERCOOLING AT 20KMIN<sup>-1</sup>**



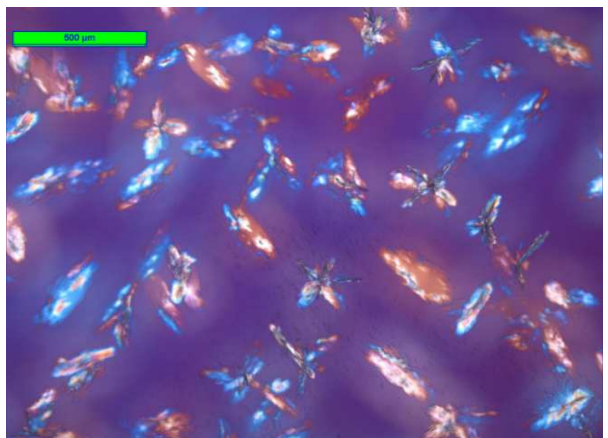
2 Kmin<sup>-1</sup> ΔT = 1.94K



4 Kmin<sup>-1</sup> ΔT = 1.94K



10 Kmin<sup>-1</sup> ΔT = 1.94K



20 Kmin<sup>-1</sup> ΔT = 1.94K

**FIGURE 3-5: PICTOGRAPHIC REPRESENTATION OF THE MELT CRYSTALLIZATION OF HIGH LINOLEIC SOYA OIL BASED PUFA AT A SUPERCOOLING OF 1.94K WITH VARYING COOLING RATES**

	Regression equation	Cooling rate [K/min]	Coefficients				R <sup>2</sup>	
			y <sub>0</sub>	a	b			
Induction time vs. Supercooling (Fig.5-25 – main manuscript)	$y = y_0 + a \cdot e^{(-bx)}$	2	-23.9	1.52E+04	1.98		1	
		4	-	2.64E+04	2.46		1	
		10	6.07E+01	6.42E+03	1.62		0.99	
		20	7.69E+00	3.00E+05	4.08		1	
Number of nuclei per area vs. Supercooling (Fig. 5-26- main manuscript)	$y = y_0 + a \cdot e^{(bx)}$	2	-	7.71E-01	1.23		0.98	
		4	.44	1.04E-02	2.77		1	
		10	-1.20	7.91E-01	.97		1	
		$y = y_0 + a \cdot e^{(bx)} + c \cdot e^{(dx)}$	20	-5.83·10 <sup>9</sup>	5.38·10 <sup>-35</sup>	19.7 9	5.83 ·10 <sup>9</sup>	2.17·10 <sup>-9</sup>

**TABLE 3-17: REGRESSION COEFFICIENTS AND EQUATIONS WITH RESPECT TO OPERATING PARAMETERS FOR FIGURE 4-22 AND 4-23 FOR THE HIGH LINOLEIC SOYA OIL PUFA MIXTURE**

## 3.2. Crystal growth kinetics

### 3.2.1. Calibration

The gradient stage, Linkam GS 120 was recalibrated for the experiments in the capillaries. The temperature displayed by the Linksys software of the temperature controllers were calibrated to the Pt 100 thermal sensor provided by Almemo.

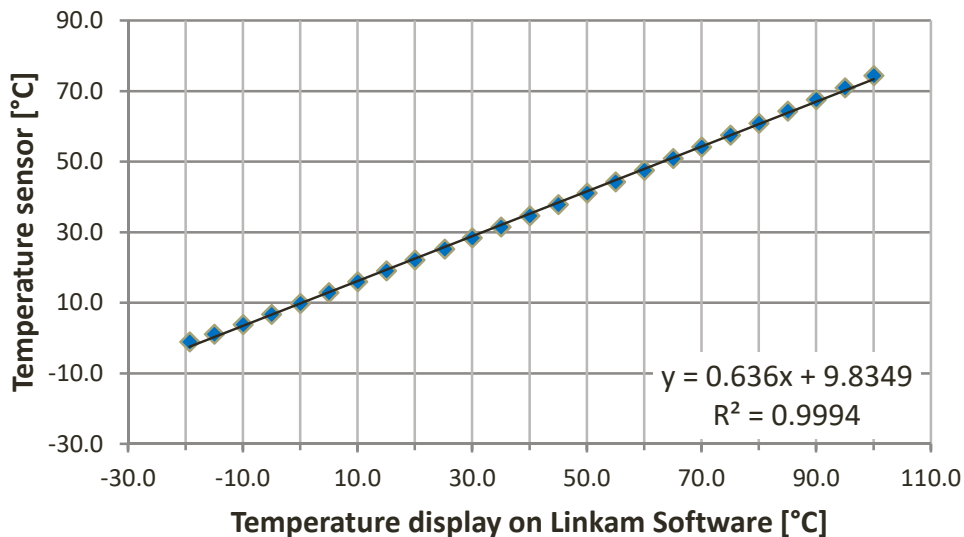


FIGURE 3-6: CALIBRATION OF THE LEFT SIDE OF THE CLOSED TEMPERED STAGE, LINKAM GS 120 ON OBJECT SLIDES WITH SAMPLE

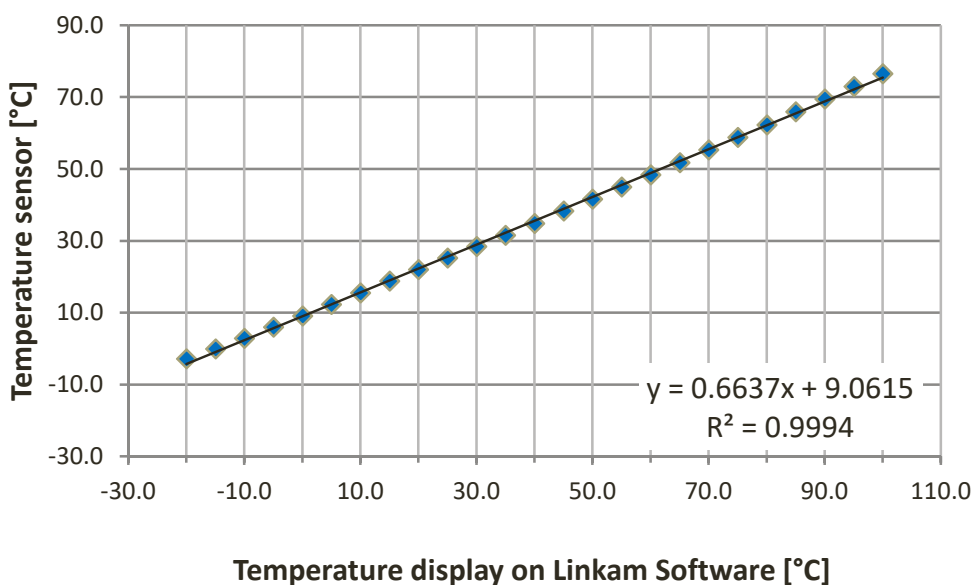


FIGURE 3-7: CALIBRATION OF THE RIGHT SIDE OF THE CLOSED TEMPERED STAGE, LINKAM GS 120 ON OBJECT SLIDES WITH SAMPLE

Temperature / left				Temperature / right			
Sensor [°C]	Linksys [°C]	Sensor [°C]	Linksys [°C]	Sensor [°C]	Linksys [°C]	Sensor [°C]	Linksys [°C]
10.0	0.3	16.5	10.5	10.0	1.4	16.8	11.7
10.2	0.5	16.7	10.8	10.2	1.7	17.0	11.9
10.3	0.8	16.8	11.0	10.3	1.9	17.1	12.2
10.5	1.0	17.0	11.3	10.5	2.2	17.3	12.4
10.6	1.3	17.1	11.5	10.7	2.4	17.5	12.7
10.8	1.5	17.3	11.8	10.8	2.7	17.6	12.9
10.9	1.8	17.5	12.0	11.0	2.9	17.8	13.2
11.1	2.0	17.6	12.3	11.2	3.2	18.0	13.4
11.3	2.3	17.8	12.5	11.3	3.4	18.1	13.7
11.4	2.5	18.0	12.8	11.5	3.7	18.3	13.9
11.6	2.8	18.1	13.0	11.6	3.9	18.5	14.2
11.7	3.0	18.3	13.3	11.8	4.2	18.6	14.4
11.9	3.3	18.5	13.6	12.0	4.4	18.8	14.7
12.1	3.5	18.6	13.8	12.1	4.7	19.0	14.9
12.2	3.8	18.7	14.0	12.3	4.9	19.1	15.2
12.4	4.0	19.0	14.4	12.5	5.2	19.3	15.4
12.5	4.3	19.2	14.8	12.6	5.4	19.4	15.7
12.7	4.5	19.4	15.0	12.8	5.7	19.6	15.9
12.9	4.8	19.5	15.3	13.0	5.9	19.8	16.2
13.0	5.0	19.7	15.5	13.1	6.2	19.9	16.4
13.2	5.3	19.9	15.8	13.3	6.4	20.1	16.7
13.3	5.5	20.0	16.0	13.5	6.7	20.3	16.9
13.5	5.8	20.2	16.3	13.6	6.9	20.4	17.2
13.7	6.0	20.3	16.5	13.8	7.2	20.6	17.4
13.8	6.3	20.5	16.8	14.0	7.4	20.8	17.7
14.0	6.5	20.6	17.0	14.1	7.7	20.9	17.9
14.1	6.8	20.8	17.3	14.3	7.9	21.1	18.2
14.3	7.0	21.0	17.5	14.5	8.2	21.3	18.4
14.4	7.3	21.1	17.8	14.6	8.4	21.4	18.7
14.6	7.5	21.3	18.0	14.8	8.7	21.6	18.9
14.8	7.8	21.4	18.3	15.0	8.9	21.8	19.2
14.9	8.0	21.6	18.5	15.1	9.2	21.9	19.4
15.1	8.3	21.8	18.8	15.3	9.4	22.1	19.7
15.2	8.5	21.9	19.0	15.5	9.7	22.3	19.9
15.4	8.8	22.1	19.3	15.6	9.9	22.4	20.2
15.6	9.0	22.2	19.5	15.8	10.2	22.6	20.4
15.7	9.3	22.4	19.8	16.0	10.4	22.8	20.7
15.9	9.5	22.6	20.0	16.1	10.7	22.9	20.9
16.0	9.8	22.7	20.3	16.3	10.9	23.1	21.2
16.2	10.0	22.9	20.5	16.5	11.2	23.3	21.4
16.4	10.3	23.5	21.5	16.6	11.4	23.4	21.7

**TABLE 3-18: CALIBRATION OF THE TEMPERED STAGE, LINKAM GS 120 ON OBJECT SLIDES CONTAINING SAMPLE WITH A ALMEMO TEMPERATURE DATA LOGGING MODULE (2890-0) AT 30KMIN<sup>-1</sup> AND 3 MINUTES HOLD TIME**

Similar experiments were carried out directly on the stage without any probe or object slides. It showed that the temperature control of the stage is much higher than it is when conductivity is hindered by the glass slides and probe.

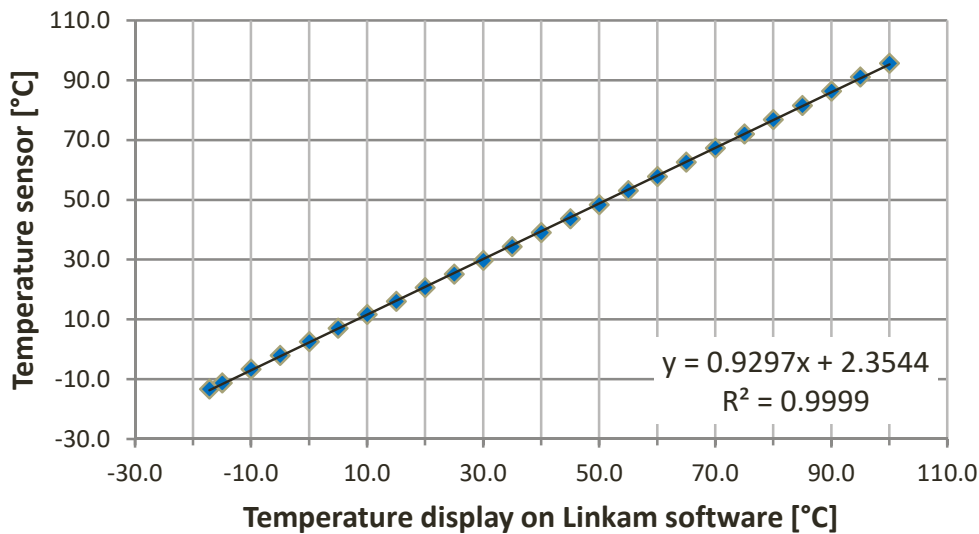


FIGURE 3-8: CALIBRATION OF THE LEFT SIDE OF THE CLOSED TEMPERED STAGE, LINKAM GS 120 WITH A TEMPERATURE RANGE DIRECTLY ON THE STAGE WITHOUT ANY GLASS SLIDE OR PROBE

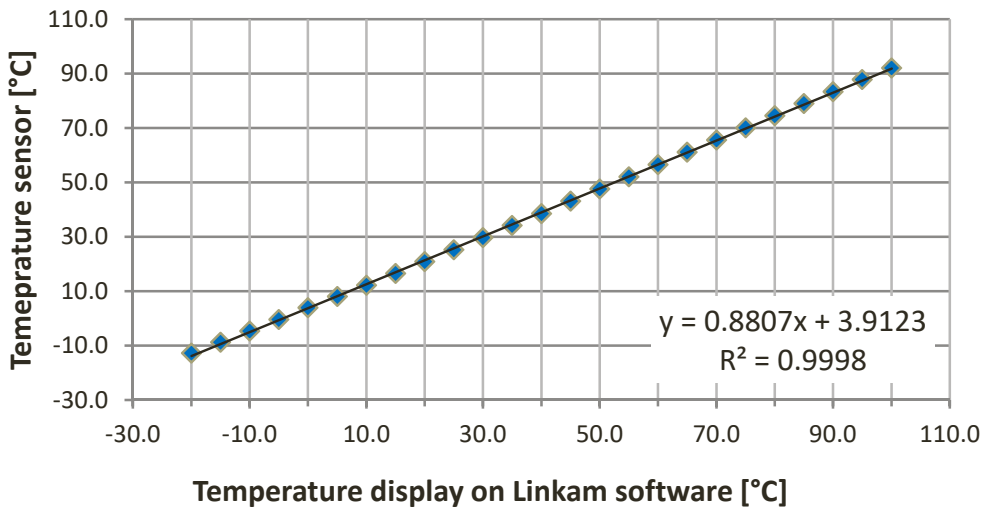


FIGURE 3-9: CALIBRATION OF THE RIGHT SIDE OF THE CLOSED TEMPERED STAGE, LINKAM GS 120 WITH A TEMPERATURE RANGE DIRECTLY ON THE STAGE WITHOUT ANY GLASS SLIDE OR PROBE

### **3.2.2. Crystal growth kinetics**

Crystal growth kinetics of the high linoleic sunflower oil based PUFA in capillaries have been shown in Section 5.3.2. Experimental data is tabulated in the following tables. Each table represent a particular cooling rate and capillary size and includes a range of supercoolings.



Capillaries with 25µm inner diameter - Cooling rate 1K/min														End of growth					
Abbreviation	K [µm] - Absolute crystal growth in µm						K' [µm] - Linear crystal growth in µm												
Supercooling	7,2K	7,2K	7,2K	7,2K	7,2K	7,2K	6,7K	6,7K	6,7K	6,7K	6,7K	6,7K	6,2K	6,2K	6,2K	6,2K	6,2K	6,2K	
Experiment	1	1	2	2	3	3	1	1	2	2	3	3	1	1	2	2	3	3	
Time [s]	K 1	K 1'	K 2	K 2'	K 3	K 3'	K 1	K 1'	K 2	K 2'	K 3	K 3'	K 1	K 1'	K 2	K 2'	K 3	K 3'	
0	35.4	35.4	28.3	28.3	26.3	26.3	22.9	22.9	26.3	26.3	54.9	54.9	42.2	42.2	33.3	33.3	44.1	44.1	
7																			
10	49.7	49.7	35.4	35.4	40.7	40.7	33.1	33.1	42	42	71.8	71.8	75.5	75.5	43.8	43.8	51.8	51.8	
15																			
30	89		60.2		51.4		78.7		75.3		104.5		126		47.3		96.6		
45															73.5				
60	134.5		120.4		65.5		144.9				148.8		174.3		140		144.9		
90	182.1		136.4		115.1		194.6		187.3		212.5		191.1		183.8		228		
120	256.6		263.9		145.2		302.3		288.8		278		214.2		294		289.8		
150	329.1		348.9		221.4		372.7		385		375.4		273		367.5		338.1		
180	393.3				318.8		459.7		518		492.3		348.6		504		352.8		
210	443		596.9		446.3		509.3		645.8		550.7		375.9		603.8		350.7		
240	451.2				510.1		631.5		747.3		568.4		401.1		656.3				
270	451.2		839.5		536.6		728.8		803.3		589.7		419.9		736.8				
285																			
300			967		540.2		801.3		845.3		611		478.7		778.8				
330			1130		542		817.8		878.5		628.7		537.5		855.8				
360							869.6		882		634		577.4		920.5				
380																			
390			1848.5				906.8						611		941.5				
420							950.3						621.5						
450							1000				650.3		625.7						
480							1006.8												
510																			
540																			
570																			
600																			
630																			
660																			
Linear Cryst. growth rate [µm/s]		1.43		0.71		1.44		1.02		1.57		1.69		3.33		1.05		0.77	

**TABLE 3-19: CRYSTAL GROWTH KINETICS OF THE HIGH LINOLEIC SUNFLOWER OIL BASED PUFA MIXTURE IN A 25 µm CAPILLARY AT 1KMIN<sup>-1</sup> COOLING RATE (SUPERCOOLING 7.2K – 6.2K)**

Capillaries with 25µm inner diameter - Cooling rate 1K/min												End of growth	
Abbreviation	K [µm] - Absolute crystal growth in µm						K' [µm] - Linear crystal growth in µm						
Supercooling	5,7K	5,7K	5,7K	5,7K	5,7K	5,7K	5,2K	5,2K	5,2K	5,2K	5,2K	5,2K	
Experiment	1	1	2	2	3	3	1	1	2	2	3	3	
Time [s]	K 1	K 1'	K 2	K 2'	K 3	K 3'	K 1	K 1'	K 2	K 2'	K 3	K 3'	
0	12.5	12.5	30.5	30.5	37.2	37.2	31.9	31.9	21.3	21.3	4.1	4.1	
7					65.3	65.3							
10	37.2	37.2	57.8	57.8			54.9	54.9	59.5	59.5	45.5	45.5	
15			68.1								51.8		
30	57.4		98.6		99.3		101		77.9		153.2		
45													
60	96.8		134.5		153.1		182.4		182.4		310.6		
90	141.6		224.1		215.1		248		246.2		405.8		
120	175.7		267.1		235.8		304.6		320.6		447.2		
150	209.7		301.2		289.6		359.5		382.6		490.7		
180	276.1		320.9		308.2		435.7		449.9		509.3		
210			346		328.9		481.7		483.5		519.7		
240	371.1				362				492.4		528		
270					384.8		573.8		559.7		536.2		
285											544.5		
300	453.5				426.1								
330					461.3		683.6		664.2				
360	564.7				477.9				727.9				
380													
390					511		777.5		736.8				
420	634.6				544.1								
450					581.3		887.3		756.3				
480	690.2				593.7				765.1				
510					612.3		949.3		818.2				
540	731.4				618.5				827.1				
570							1021.9		836				
600	751.1												
630					855.5		1039.6						
660	756.5												
Linear Cryst. growth rate [µm/s]		2.47		2.73		4.01		2.3		3.82		4.14	

**TABLE 3-20: CRYSTAL GROWTH KINETICS OF THE HIGH LINOLEIC SUNFLOWER OIL BASED PUFA MIXTURE IN A 25 µM CAPILLARY AT 1KMIN<sup>-1</sup> COOLING RATE (SUPERCOOLING 5.7K – 5.2K)**

Appendix

Capillaries with 25µm inner diameter - Cooling rate 1K/min																End of growth					
Abbreviation	K [µm] - Absolute crystal growth in µm								K' [µm] - Linear crystal growth in µm												
Supercooling	7,2K	7,2K	7,2K	7,2K	7,2K	7,2K	7,2K	7,2K	6,7K	6,7K	6,7K	6,7K	6,7K	6,7K	6,2K	6,2K	6,2K	6,2K	6,2K	6,2K	
Experiment	1	1	2	2	3	3	4	4	1	1	2	2	3	3	1	1	2	2	3	3	
Time [s]	K 1	K 1'	K 2	K 2'	K 3	K 3'	K 4	K 4'	K 1	K 1'	K 2	K 2'	K 3	K 3'	K 1	K 1'	K 2	K 2'	K 3	K 3'	
0	22.3	22.3	16.7	16.7	22.5	22.5	20.4	20.4	5.4	5.4	32.2	32.2	8.2	8.2	21.9	21.9	18.6	18.6	12.2	12.2	
5																					
10	37.2	37.2	33.5	33.5	42.9	42.9	30.6	30.6	36.3	36.3	46.3	46.3	30.6	30.6	41.8	41.8	37.3	37.3	24.5	24.5	
15																					
20	80		91.1		79.6		42.9		63.5		70.5		47		58.1		58		38.8		
30	115.3		111.6		100		59.2		108.9		86.6		67.4		63.5		72.5		65.3		
40	145.1		120.9		114.3		73.5		123.2		116.8		85.7		98		95.2		69.4		
50	182.3		124.6		136.8		95.9		126.8		132.9		108.2		123.4		105.6		112.3		
60	204.6		135.8		142.9		132.7		124.9		136.9		126.6		134.7		111.8		120.5		
70	228.9		132.1		153.1		161.3				145		142.9		161.5		124.2		136.8		
80	245.6		133.9		153.1		177.6				163.1				177.8		138.7		149		
90	273.5				159.2		189.8				177.2				197.8		144.9		167.4		
100	275.3				157.2		210.3				187.3				205		142.9		175.6		
110	277.2				157.2		214.3				189.3				215.9		147		189.9		
120	284.6				157.2		212.3								232.3		149.1		191.9		
130	279														248.6						
140											189.3				254						
150																	155.3		234.8		
160																					
170											193.3										
180																	159.4		330.7		
190																					
200											201.4										
210																			351.7		
220																					
470																					
480																					
840																					
850																					
860																					
Linear Cryst. Growth rate [µm/s]		1.49		1.68		2.04		1.02		3.09		1.41		2.24		1.99		1.87		1.23	

TABLE 3-21: CRYSTAL GROWTH KINETICS OF THE HIGH LINOLEIC SUNFLOWER OIL BASED PUFA MIXTURE IN A 25 µM CAPILLARY AT 10 KMIN<sup>-1</sup> COOLING RATE (SUPERCOOLING 7.2K – 6.2K)

Capillaries with 25µm inner diameter - Cooling rate 1K/min												End of growth	
Abbreviation	K [µm] - Absolute crystal growth in µm						K' [µm] - Linear crystal growth in µm						
Supercooling	5,7K	5,7K	5,7K	5,7K	5,7K	5,7K	5,2K	5,2K	5,2K	5,2K	5,2K	5,2K	
Experiment	1	1	2	2	3	3	1	1	2	2	3	3	
Time [s]	K 1	K 1'	K 2	K 2'	K 3	K 3'	K 1	K 1'	K 2	K 2'	K 3	K 3'	
0	9.3	9.3	8.3	8.3	6.1	6.1	27.8	27.8	20.4	20.4	23.5	23.5	
5			20.7						36.7				
10	22.4	22.4	41.4	41.4	30.6	30.6	53.6	53.6	38.8	38.8	45.1	45.1	
15			51.8						44.9				
20	44.7		58		47		73.5		61.2		72.5		
30	61.4		70.4		73.5		79.5		71.5		88.2		
40	91.2		93.2		87.8		87.4				117.6		
50	119.1		103.5		104.1						125.4		
60	132.1		107.7		126.6						152.9		
70	141.4		115.9		134.7		129.1		87.8		162.7		
80	147		118		145				100		162.7		
90	161.9		136.6		157.2				114.3		164.5		
100			149.1		171.5		168.9						
110			155.3		206.2								
120	228.8		179.7		222.5				137.1				
130					236.8		190.7						
140					251.1								
150	280.9		196.7		267.5				143				
160					275.6		196.7						
170					281.7								
180	316.3		209.1		310.3				139.1				
190					318.5								
200													
210	357.2		209.1										
220													
470					402.7		223.4						
480													
840													
850	446.4												
860													
Linear Cryst. Growth rate [µm/s]		1.31		3.31		2.45		2.58		1.84		2.16	

TABLE 3-22: CRYSTAL GROWTH KINETICS OF THE HIGH LINOLEIC SUNFLOWER OIL BASED PUFA MIXTURE IN A 25 µm CAPILLARY AT 10 KMIN<sup>-1</sup> COOLING RATE (SUPERCOOLING 5.7K – 6.2K)

Appendix

Capillaries with 25µm inner diameter - Cooling rate 1K/min													End of growth					
Abbreviation	K [µm] - Absolute crystal growth in µm						K' [µm] - Linear crystal growth in µm											
Supercooling	7,2K	7,2K	7,2K	7,2K	7,2K	7,2K	6,7K	6,7K	6,7K	6,7K	6,7K	6,7K	6,2K	6,2K	6,2K	6,2K	6,2K	6,2K
Experiment	1	1	2	2	3	3	1	1	2	2	3	3	1	1	2	2	3	3
Time [s]	K 1	K 1'	K 2	K 2'	K 3	K 3'	K 1	K 1'	K 2	K 2'	K 3	K 3'	K 1	K 1'	K 2	K 2'	K 3	K 3'
0	15.9	15.9	16.1	16.1	28.2	28.2	6	6	13.9	13.9	15.9	15.9	15.7	15.7	28.6	28.6	10.2	10.2
5			44.3		42.3				23.8		27.8				34.7			
10	31.8	31.8	64.4	64.4	76.5	76.5	17.9	17.9	37.7	37.7	37.7	37.7	29.4	29.4	44.9	44.9	26.5	26.5
15			66.5		100.7				47.7		47.7				49			
20	47.7		92.6		110.8		37.7		69.5		57.6				55.1		57.2	
25											69.5				64.2			
30	61.6		110.8		153		47.7		105.3		89.4		37.2		75.5		102.1	
40	83.4		126.9		191.3		59.6		119.2		119.2		54.9		73.5		108.2	
50	117.2		143		193.3		73.5		133.1		137.1		63.6		85.7		112.3	
60	135.1		149		197.3		89.4		139.1		149		78.4		77.6		116.4	
70	149		161.1		187.3		93.4		149		154.9		98		75.5			
80			173.2		199.4		109.3		156.9				111.7		85.7			
90			175.2		195.3		123.2		162.9				115.6		83.7			
100	198.6						133.1				154.9				85.7			
110							133.1											
120							135.1		218.5				137.2					
130	216.5																	
140																		
150													156.8					
160	218.5								220.5									
170																		
180													180.3					
190									222.5									
200																		
210													192.1					
220																		

continued

Appendix

Capillaries with 25µm inner diameter - Cooling rate 1K/min														End of growth					
Abbreviation	K [µm] - Absolute crystal growth in µm						K' [µm] - Linear crystal growth in µm												
Supercooling	7,2K	7,2K	7,2K	7,2K	7,2K	7,2K	6,7K	6,7K	6,7K	6,7K	6,7K	6,7K	6,2K	6,2K	6,2K	6,2K	6,2K	6,2K	
Experiment	1	1	2	2	3	3	1	1	2	2	3	3	1	1	2	2	3	3	
Time [s]	K 1	K 1'	K 2	K 2'	K 3	K 3'	K 1	K 1'	K 2	K 2'	K 3	K 3'	K 1	K 1'	K 2	K 2'	K 3	K 3'	
230																			
240																			
250																			
260																			
270																			
280																			
290																			
300																			
310							135.2												
320																			
330																			
230																			
350	234																		
360																			
370																			
440													202.4						
450																			
510																			
520																			
1030																			
1040																			
1530																			
1540																			
Linear Crystal growth rate [µm/s]		1.59		4.83		4.83		1.19		2.38		2.18		1.37		1.63		1.63	

**TABLE 3-23: CRYSTAL GROWTH KINETICS OF THE HIGH LINOLEIC SUNFLOWER OIL BASED PUFA MIXTURE IN A 25 µM CAPILLARY AT 20 KMIN<sup>-1</sup> COOLING RATE (SUPERCOOLING 7.2K – 6.2K)**

Appendix

Capillaries with 25µm inner diameter - Cooling rate 1K/min							End of growth					
Abbreviation	K [µm] - Absolute crystal growth in µm						K' [µm] - Linear crystal growth in µm					
Supercooling	5,7K	5,7K	5,7K	5,7K	5,7K	5,7K	5,2K	5,2K	5,2K	5,2K	5,2K	5,2K
Experiment	1	1	2	2	3	3	1	1	2	2	3	3
Time [s]	K 1	K 1'	K 2	K 2'	K 3	K 3'	K 1	K 1'	K 2	K 2'	K 3	K 3'
0	20.1	20.1	21.8	21.8	6	6	7.3	7.3	8.1	8.1	18.1	18.1
5			27.8									
10	40.3	40.3	33.8	33.8	51.6	51.6	25.4	25.4	12.1	12.1	22.2	22.2
15			59.6									
20	72.5		69.5		109.3		38.1		18.1		28.2	
25			81.4									
30	76.5		85.4		156.9		47.2		22.2		32.2	
40	80.5		103.3		168.9		56.2		24.2		38.3	
50	112.7		117.2		172.8		56.2		28.2		40.3	
60	122.8		158.9		198.6		61.7		30.2		46.3	
70	142.9		180.8		256.3		67.1		38.3		48.3	
80	153		220.5		272.1		72.6		38.3		62.4	
90	181.2		248.3		282.1		79.8		40.3			
100	199.3		260.2		329.8							
110	215.4		266.2		335.7							
120	217.4		272.1		345.6		90.7		100.7		74.4	
130			274.1		349.6							
140			272.1									
150	247.6						98		130.9		80.5	
160												
170												
180	275.8						103.4		183.2		88.6	
190												
200												
210	310						114.3		241.6		98.7	
220												
230												
240	330.1				517.5		116.1		269.8		104.7	
250												
260												
270	346.2						121.6		259.8		108.7	
280												
290												
300	360.3						123.4		267.8		110.8	
310												
320												

continued

Capillaries with 25µm inner diameter - Cooling rate 1K/min										End of growth			
Abbreviation	K [µm] - Absolute crystal growth in µm						K' [µm] - Linear crystal growth in µm						
Supercooling	5,7K	5,7K	5,7K	5,7K	5,7K	5,7K	5,2K	5,2K	5,2K	5,2K	5,2K	5,2K	5,2K
Experiment	1	1	2	2	3	3	1	1	2	2	3	3	3
Time [s]	K 1	K 1'	K 2	K 2'	K 3	K 3'	K 1	K 1'	K 2	K 2'	K 3	K 3'	K 3'
330	378.4						125.2		269.8		114.8		
340													
350													
360							130.6		271.8		118.8		
370													
440													
450													
510													
520									285.9		126.9		
1030							150.6						
1040													
1530	535.8												
1540													
Linear Crystal growth rate [µm/s]	2.02		1.20		4.56		1.81		0.40		0.41		

**TABLE 3-24: CRYSTAL GROWTH KINETICS OF THE HIGH LINOLEIC SUNFLOWER OIL BASED PUFA MIXTURE IN A 25 µM CAPILLARY AT 20 KMIN<sup>-1</sup> COOLING RATE (SUPERCOOLING 5.7K – 5.2K)**



Appendix

		Capillaries with 25μm inner diameter - Cooling rate 1K/min																		End of growth	
Abbreviation	K [μm] - Absolute crystal growth in μm									K' [μm] - Linear crystal growth in μm											
Supercooling	7,2K	7,2K	7,2K	7,2K	7,2K	7,2K	6,7K	6,7K	6,7K	6,7K	6,7K	6,7K	6,2K	6,2K	6,2K	6,2K	6,2K	6,2K	6,2K	6,2K	
Experiment	1	1	2	2	3	3	1	1	2	2	3	3	1	1	2	2	3	3	4	4	
Time [s]	K 1	K 1'	K 2	K 2'	K 3	K 3'	K 1	K 1'	K 2	K 2'	K 3	K 3'	K 1	K 1'	K 2	K 2'	K 3	K 3'	K 4	K 4'	
0	17.9	17.9	15.3	15.3	14.7	14.7	12.2	12.2	23.8	23.8	11.9	11.9	18.6	18.6	13.9	13.9	14.3	14.3	20.1	20.1	
5									36.7						31.8		30.6				
10	55.6	55.6	53.5	53.5	44.1	44.1	63.3	63.3	45.7	45.7	41.7	41.7	47.6	47.6	41.7	41.7	47	47	46.3	46.3	
15									75.5						57.6		57.2				
20	81.4					79.8			87.8				69.5		72.5		67.5		75.5		58.4
27			76.4									119.2									
30	103.3					144.9			130.7				81.4		97.3		77.5		91.9		70.5
40	133.1					151.2			155.2				93.4		124.2		95.4		112.3		86.6
50	180.8					172.2			169.5			135.1		125.1		144.9		105.3		128.6	114.8
58				177.5																	
60	210.6					186.9			171.5				131.1		161.5		139.1		151.1		120.8
67			206.2																		
70	222.5					231							154.9		209.1		151		165.4		145
80	250.3					245.7			169.5				176.8		234		151		181.7		147
90	250.3			271.1		268.8							190.7		260.9		153		189.9		155.1
97			286.4																		
100						300.3							194.7		269.2		153		210.3		157.1
110						323.4			173.5				204.6		298.1				232.7		
120						344.4							210.6						238.9		
130						357													247		161.8
140						373.8									323						
150			383.7			399															
160						405.3													263.4		161.1
170															366.5						
176			404.7																		
180																					
190																					
200															397.5						277.7
210																					
214				420																	
220																					308.3
230															443.1						
240													279.9								
250																					318.5
260				416.2											465.8						
270																					

continued

Appendix

Capillaries with 25µm inner diameter - Cooling rate 1K/min													End of growth								
Abbreviation	K [µm] - Absolute crystal growth in µm												K' [µm] - Linear crystal growth in µm								
Supercooling	7,2K	7,2K	7,2K	7,2K	7,2K	7,2K	6,7K	6,7K	6,7K	6,7K	6,7K	6,7K	6,2K	6,2K	6,2K	6,2K	6,2K	6,2K	6,2K	6,2K	6,2K
Experiment	1	1	2	2	3	3	1	1	2	2	3	3	1	1	2	2	3	3	4	4	4
Time [s]	K 1	K 1'	K 2	K 2'	K 3	K 3'	K 1	K 1'	K 2	K 2'	K 3	K 3'	K 1	K 1'	K 2	K 2'	K 3	K 3'	K 4	K 4'	
280																	328.7				
290													509.3								
300																					
310																	336.9				
320													534.2								
330																					
340																					
350													536.2								
360																					
370																					
380													552.8								
390																					
400																					
410													565.2								
420																					
430																					
440																					
450																					
460																					
670																					
680																					
1040																					
1050																					
1200														688							
Linear Cryst. growth rate [µm/s]		3.77		3.82		2.94		5.11		2.19		2.98		2.90		2.78		3.27		2.62	

TABLE 3-25: CRYSTAL GROWTH KINETICS OF THE HIGH LINOLEIC SUNFLOWER OIL BASED PUFA MIXTURE IN A 25 µM CAPILLARY AT 30 KMIN<sup>-1</sup> COOLING RATE (SUPERCOOLING 7.2K – 6.2K)

Appendix

Capillaries with 25µm inner diameter - Cooling rate 1K/min											End of growth				
Abbreviation	K [µm] - Absolute crystal growth in µm														
Supercooling Experiment	5,7K 1	5,7K 1	5,7K 2	5,7K 2	5,7K 3	5,7K 3	5,2K 1	5,2K 1	5,2K 2	5,2K 2	5,2K 3	5,2K 3	5,2K 4	5,2K 4	
Time [s]	K 1	K 1'	K 2	K 2'	K 3	K 3'	K 1	K 1'	K 2	K 2'	K 3	K 3'	K 4	K 4'	
0	58.4	58.4	25.2	25.2	18.1	18.1	8.1	8.1	27.1	27.1	23.2	23.2	11.9	11.9	
5			42		26.2										
10	68.5	68.5	46.2	46.2	42.3	42.3	26.2	26.2	32.9	32.9	34.8	34.8	35.8	35.8	
15			60.9		44.3										
20	72.5		65.1		54.4		48.3		32.9		44.5		49.7		
27															
30	100.7		75.6		82.6		86.6		42.6		54.2		77.5		
40	110.8				124.8		101.3		38.7		54.2		87.4		
50	124.8				151		124		56.1		60		93.4		
58															
60	124.8				165.1		141.7		75.4		92.8		101.3		
67															
70	145		132.3		195.3		159.4		83.2		154.7		121.2		
80	149				201.4		218.4		89		185.7		135.1		
90	167.1				209.4		222.4		94.8		203.1		147		
97															
100			214.2		225.5		232.2		96.7		218.6				
110					239.6				102.5		247.6				
120	191.3				243.7				100.6		255.3		162.9		
130			237.3		249.7		272.5								
140															
150	215.5								119.9		290.1		166.9		
160			268.8				310.9								
170															
176															
180	227.5								125.7		323		200.6		
190			325.5				381.8								
200															
210	243.7								135.4		340.4		212.5		
214															
220			340.2				436.9								
230															
240	253.7								152.8		334.6		238.4		
250			359.1				490								
260															
270									145.1		340.4		248.3		

continued

Capillaries with 25µm inner diameter - Cooling rate 1K/min													End of growth		
Abbreviation	K [µm] - Absolute crystal growth in µm						K' [µm] - Linear crystal growth in µm								
Supercooling Experiment	5,7K 1	5,7K 1	5,7K 2	5,7K 2	5,7K 3	5,7K 3	5,2K 1	5,2K 1	5,2K 2	5,2K 2	5,2K 3	5,2K 3	5,2K 4	5,2K 4	5,2K 4
Time [s]	K 1	K 1'	K 2	K 2'	K 3	K 3'	K 1	K 1'	K 2	K 2'	K 3	K 3'	K 4	K 4'	
280							505.7								
290															
300														276.1	
310															
320															
330														298	
340															
350															
360														313.8	
370															
380															
390														335.7	
400															
410			498.2												
420														341.5	
430															
440									276.4		431.2				
450														357.7	
460															
670	367.5														
680															
1040														480.2	
1050															
1200															
Linear Cryst. growth rate [µm/s]		1.01		2.10		2.42		1.81		0.58		1.16		2.39	

TABLE 3-26: CRYSTAL GROWTH KINETICS OF THE HIGH LINOLEIC SUNFLOWER OIL BASED PUFA MIXTURE IN A 25 µM CAPILLARY AT 30 KMIN<sup>-1</sup> COOLING RATE (SUPERCOOLING 5.7K – 5.2K)

### 3.3. Confocal Raman Spectroscopy ( $\mu\text{l}$ scale)

As mentioned in Section 5.3.3, the lancet and the star shaped crystals showed similar results also validating that the shapes are to be modified more only to ensure easier separation rather than changing composition of crystal fraction. The saturated concentration is at the highest at the center of the crystal reducing as the size increases with the least amount present in the melt.

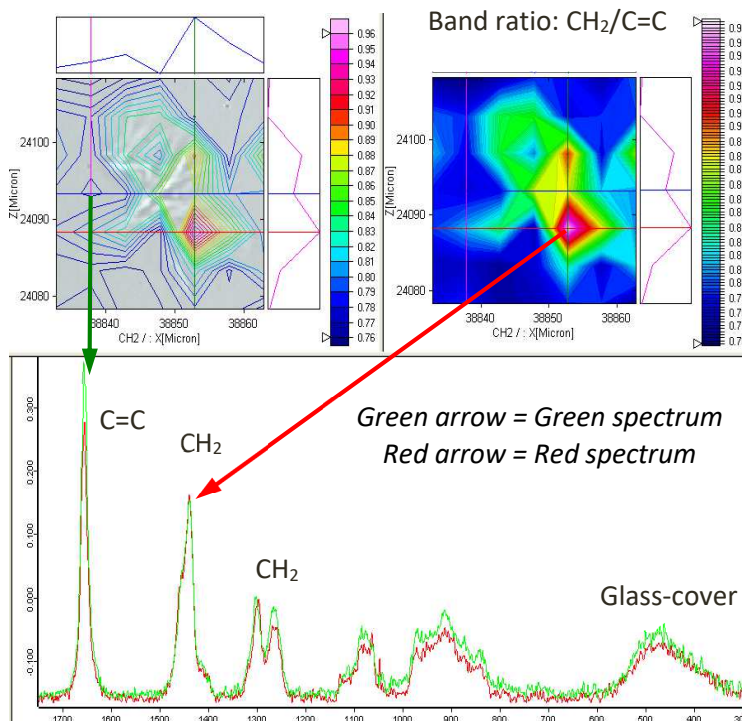


**FIGURE 3-10: COMPARISON OF SPECTRA OBTAINED FROM A STAR SHAPED CRYSTAL (RED) AND FROM MOTHER LIQUOR (GREEN) BY MEANS OF CONFOCAL RAMAN SPECTROSCOPE, SENTERRA<sup>®31</sup>**

The lancet form crystal has been analyzed here with a 15 X 10 mesh for mapping. Every mesh point was separated by 5  $\mu\text{m}$  as before.

<sup>31</sup> Data and illustrations taken and edited from the report submitted by Mr. Eric Klein and Mr. Matthias Boese from Bruker Optik GmbH for the test measurements for the compositional analysis of high oleic PUFA. Acknowledgements also to the organization of Bruker Optik GmbH in Ettlingen, Germany to make the confocal Raman microscope available for measurements.

### 3.4. Contact angle measurement as a function of surface type and composition of PUFA

The contact angles were measured on both sides of the drop on the material substrates under the microscope. The average was taken and used to calculate the contact angle. Every experiment was repeated thrice for each desired temperature. The values obtained for each of them have been tabulated in the following tables. The values for the high oleic PUFA mixture is given in Table 3-27 and Table 3-28.

Temperature [°C]	PVC			PC			PETG		
	Side 1	Side 2	Average	Side 1	Side 2	Average	Side 1	Side 2	Average
50	22.0	14.3	18.2	15.3	11.1	13.2	10.4	9.8	10.1
40	21.0	12.6	16.8	11.3	10.0	10.7	11.9	12.8	12.4
30	20.1	15.0	17.6	13.3	12.9	13.1	14.0	11.6	12.8
25	18.4	12.6	15.5	14.0	12.1	13.1	13.1	12.1	12.6
20	18.6	13.3	16.0	11.4	10.4	10.9	8.6	7.2	7.9
15	16.3	9.8	13.1	11.1	9.0	10.1	10.7	8.4	9.6
10	18.5	10.6	14.6	10.0	9.9	10.0	9.3	7.1	8.2
5	22.2	12.2	17.2	10.6	8.9	9.8	10.2	8.1	9.2
50	23.2	14.5	18.9	14.6	12.9	13.8	11.3	9.4	10.4
40	23.2	18.4	20.8	14.7	12.3	13.5	8.5	7.6	8.1
30	19.5	14.5	17.0	12.5	11.0	11.8	8.4	7.4	7.9
25	20.2	13.8	17.0	14.3	11.2	12.8	10.4	8.9	9.7
20	18.9	14.6	16.8	11.8	10.9	11.4	7.3	6.8	7.1
15	20.9	13.5	17.2	10.8	9.3	10.1	5.8	5.1	5.5
10	19.3	12.0	15.7	10.0	7.7	8.9	6.6	6.7	6.7
5	18.1	12.9	15.5	11.8	7.6	9.7	7.4	5.6	6.5
50	23.0	14.0	18.5	12.5	12.1	12.3	9.2	8.5	8.9
40	19.2	12.9	16.1	13.4	12.9	13.2	7.5	7.0	7.3
30	18.9	16.2	17.6	13.3	10.6	12.0	7.7	6.2	7.0
25	18.5	13.2	15.9	14.1	12.4	13.3	10.8	8.7	9.8
20	21.9	15.1	18.5	12.8	11.0	11.9	9.7	7.9	8.8
15	18.6	14.3	16.5	13.3	11.2	12.3	7.1	5.9	6.5
10	17.1	11.7	14.4	12.4	10.4	11.4	6.5	6.8	6.7
5	18.9	12.8	15.9	10.5	8.6	9.6	6.3	4.8	5.6

**TABLE 3-27: CONTACT ANGLE OF A HIGH OLEIC FATTY ACID PUFA MIXTURE ON PVC, PC AND PETG OBJECT SLIDES UNDER THE MICROSCOPE**

Temperature [°C]	Aluminum			V2A-Steel			Steel (St37)			Glass		
	Side 1	Side 2	Average	Side 1	Side 2	Average	Side 1	Side 2	Average	Side 1	Side 2	Average
50	29.6	29.3	29.5	28.5	29.5	29.0	34.8	37.2	36.0	27.4	24.1	25.7
40	28.1	29.5	28.8	30.4	30.3	30.4	33.7	36.0	34.9	27.8	26.1	27.0
30	27.6	30.3	29.0	29.2	31.0	30.1	34.1	36.0	35.1	25.2	25.6	25.4
25	24.5	28.0	26.3	26.6	31.3	29.0	34.4	35.2	34.8	24.0	25.4	24.7
20	26.8	31.4	29.1	25.9	28.3	27.1	34.1	35.1	34.6	22.2	22.8	22.5
15	28.2	28.6	28.4	23.2	26.6	24.9	31.5	31.2	31.4	22.1	23.8	22.9
10	22.4	24.8	23.6	22.4	23.2	22.8	24.6	26.6	25.6	24.0	27.4	25.7
5	21.2	25.2	23.2	23.6	23.8	23.7	24.9	23.8	24.4	22.0	23.8	22.9
50	29.9	31.6	30.8	32.0	32.6	32.3	38.2	39.4	38.8	24.2	25.7	24.9
40	30.1	30.7	30.4	30.7	31.3	31.0	36.0	37.4	36.7	26.1	29.7	27.9
30	31.7	31.0	31.4	29.9	33.3	31.6	35.8	37.3	36.6	23.8	25.0	24.4
25	28.6	30.1	29.4	29.9	30.3	30.1	34.6	37.2	35.9	23.8	25.3	24.5
20	27.6	27.1	27.4	28.8	28.7	28.8	39.6	42.0	40.8	23.7	23.3	23.5
15	26.6	28.5	27.6	25.4	29.4	27.4	35.1	35.0	35.1	23.7	25.4	24.6
10	29.6	30.1	29.9	27.2	28.8	28.0	28.2	31.0	29.6	25.1	26.9	26.0
5	25.7	27.8	26.8	21.8	20.2	21.0	28.9	31.3	30.1	23.1	21.4	22.2
50	30.2	32.9	31.6	27.9	26.6	27.3	39.0	39.0	39.0	25.4	24.3	24.8
40	28.2	30.3	29.3	30.3	30.7	30.5	37.9	36.9	37.4	25.9	23.8	24.9
30	27.2	27.3	27.3	28.9	28.9	28.9	36.5	37.2	36.9	24.9	23.7	24.3
25	25.6	27.2	26.4	25.9	28.9	27.4	32.3	35.1	33.7	24.6	24.2	24.4
20	20.4	20.2	20.3	22.4	25.4	23.9	32.3	31.8	32.1	24.0	23.9	23.9
15	21.3	23.1	22.2	23.8	24.5	24.2	33.2	34.6	33.9	22.3	21.4	21.8
10	28.6	30.5	29.6	19.5	21.8	20.7	28.9	31.4	30.2	23.8	23.5	23.6
5	23.3	25.7	24.5	19.9	20.1	20.0	28.1	28.3	28.2	24.4	24.1	24.3

**TABLE 3-28: CONTACT ANGLE OF A HIGH OLEIC FATTY ACID PUFA MIXTURE ON ALUMINUM, STAINLESS STEEL, STRUCTURAL STEEL AND GLASS OBJECT SLIDES UNDER THE MICROSCOPE**

The values for the high linoleic PUFA mixture are given in Table 3-29 and Table 3-30.

Temperature [°C]	PVC			PC			PETG		
	Side 1	Side 2	Average	Side 1	Side 2	Average	Side 1	Side 2	Average
50	14.6	12.7	13.7	18.9	14.2	16.6	17.3	17.2	17.3
40	13.9	13.3	13.6	21.5	14.3	17.9	19.4	14.4	16.9
30	16.4	13.4	14.9	17.4	16.7	17.1	17.2	15.6	16.4
25	15.5	13.3	14.4	14.0	13.9	14.0	16.5	14.0	15.3
20	13.6	13.2	13.4	15.5	13.8	14.7	17.4	14.2	15.8
15	13.3	12.4	12.9	9.9	7.0	8.5	17.0	15.3	16.2
10	14.0	14.7	14.4	11.6	10.6	11.1	13.2	10.2	11.7
5	15.0	10.5	12.8	10.1	8.6	9.4	13.5	13.2	13.4
50	13.8	11.7	12.8	14.9	14.0	14.5	22.9	19.1	21.0
40	15.4	11.3	13.4	18.1	13.3	15.7	21.1	18.9	20.0
30	13.7	12.6	13.2	19.2	14.6	16.9	23.8	24.0	23.9
25	12.4	11.6	12.0	16.1	13.1	14.6	23.1	20.9	22.0
20	14.6	13.0	13.8	19.3	16.3	17.8	20.6	17.7	19.2
15	11.7	8.9	10.3	10.1	9.5	9.8	19.6	20.7	20.2
10	11.4	9.7	10.6	15.0	10.6	12.8	16.5	17.5	17.0
5	11.3	9.1	10.2	9.9	9.1	9.5	12.8	13.0	12.9
50	16.4	12.9	14.7	14.0	13.1	13.6	23.1	21.1	22.1
40	13.8	14.6	14.2	16.6	13.3	15.0	21.3	21.0	21.2
30	15.3	14.7	15.0	19.9	17.2	18.6	28.1	29.2	28.7
25	17.0	14.1	15.6	15.4	12.4	13.9	27.0	27.1	27.1
20	18.4	15.7	17.1	16.1	12.5	14.3	22.7	24.4	23.6
15	20.0	14.9	17.5	10.4	8.9	9.7	23.7	22.7	23.2
10	17.3	14.7	16.0	12.4	8.3	10.4	16.3	17.5	16.9
5	15.7	15.0	15.4	11.5	10.0	10.8	15.3	15.4	15.4

**TABLE 3-29: CONTACT ANGLE OF A HIGH LINOLEIC FATTY ACID PUFA MIXTURE ON PVC, PC AND PETG OBJECT SLIDES UNDER THE MICROSCOPE**



Temperature [°C]	Aluminum			V2A-Steel			Steel (St37)			Glass		
	Side 1	Side 2	Average	Side 1	Side 2	Average	Side 1	Side 2	Average	Side 1	Side 2	Average
50	28.5	29.5	29.0	27.3	25.6	26.5	41.6	39.1	40.4	28.5	28.9	28.7
40	30.4	29.2	29.8	27.7	28.2	28.0	41.6	39.5	40.6	27.3	28.3	27.8
30	27.4	27.6	27.5	25.2	24.6	24.9	40.6	39.0	39.8	27.2	28.2	27.7
25	26.6	26.6	26.6	26.6	26.6	26.6	40.2	37.6	38.9	25.7	28.1	26.9
20	26.6	25.8	26.2	24.6	24.6	24.6	35.0	34.5	34.8	27.6	27.3	27.5
15	22.8	23.4	23.1	23.7	24.1	23.9	27.4	26.6	27.0	25.9	27.1	26.5
10	22.1	22.1	22.1	20.4	22.4	21.4	26.6	25.8	26.2	24.1	25.0	24.5
5	20.4	22.0	21.2	21.0	21.5	21.3	28.4	28.6	28.5	21.3	22.3	21.8
50	35.0	36.4	35.7	26.6	26.6	26.6	41.2	38.7	40.0	26.6	28.6	27.6
40	34.2	32.8	33.5	27.4	27.5	27.5	38.4	37.3	37.9	28.1	27.5	27.8
30	31.0	32.3	31.7	25.0	25.9	25.5	36.2	37.3	36.8	27.3	26.6	26.9
25	33.7	33.1	33.4	26.6	27.5	27.1	35.5	36.3	35.9	25.3	27.0	26.1
20	33.0	33.0	33.0	24.1	26.6	25.4	37.9	37.4	37.7	26.9	28.3	27.6
15	21.8	22.8	22.3	24.1	21.4	22.8	26.6	25.9	26.3	24.5	25.0	24.7
10	22.3	23.6	23.0	23.8	23.2	23.5	23.6	24.6	24.1	24.7	22.9	23.8
5	21.4	21.0	21.2	23.2	24.9	24.1	26.6	27.6	27.1	20.1	21.5	20.8
50	31.3	31.0	31.2	24.1	27.4	25.8	40.6	40.9	40.8	28.3	27.7	28.0
40	27.4	26.6	27.0	28.4	25.7	27.1	37.9	37.9	37.9	23.8	25.6	24.7
30	28.9	28.4	28.7	23.2	24.1	23.7	39.5	37.9	38.7	24.9	25.9	25.4
25	26.6	27.5	27.1	24.7	24.9	24.8	36.9	38.2	37.6	24.6	26.2	25.4
20	25.6	26.6	26.1	24.3	24.3	24.3	36.3	37.6	37.0	25.0	24.9	24.9
15	18.9	18.9	18.9	21.5	22.0	21.8	25.8	27.4	26.6	23.1	24.4	23.8
10	18.4	18.0	18.2	19.3	19.0	19.2	25.0	25.8	25.4	22.9	22.5	22.7
5	17.6	17.4	17.5	18.8	22.4	20.6	24.1	28.3	26.2	21.0	20.8	20.9

**TABLE 3-30: CONTACT ANGLE OF A HIGH LINOLEIC FATTY ACID PUFA MIXTURE ON ALUMINUM, STAINLESS STEEL, STRUCTURAL STEEL AND GLASS OBJECT SLIDES UNDER THE MICROSCOPE**

The values for the high linolenic PUFA mixture are given in Table 3-31 and Table 3-32.

Temperature [°C]	PVC			PC			PETG		
	Side 1	Side 2	Average	Side 1	Side 2	Average	Side 1	Side 2	Average
50	13.4	10.7	12.1	16.6	10.8	13.7	17.8	14.4	16.1
40	13.2	10.2	11.7	17.4	15.3	16.4	12.4	11.3	11.9
30	11.4	8.4	9.9	15.8	11.4	13.6	12.8	9.5	11.2
25	16.0	10.2	13.1	14.2	10.3	12.3	11.3	9.1	10.2
20	14.7	12.5	13.6	14.3	11.8	13.1	11.3	9.9	10.6
15	9.5	9.2	9.4	14.4	12.0	13.2	10.4	10.4	10.4
10	12.8	10.1	11.5	12.1	10.6	11.4	14.0	11.0	12.5
5	12.0	8.4	10.2	10.5	8.7	9.6	11.0	8.3	9.7
50	12.9	11.5	12.2	20.9	12.8	16.9	15.8	13.4	14.6
40	13.9	11.4	12.7	15.6	11.6	13.6	12.2	9.6	10.9
30	11.1	11.6	11.4	17.7	13.1	15.4	13.5	10.1	11.8
25	14.0	11.8	12.9	13.3	12.0	12.7	15.7	12.0	13.9
20	10.8	11.2	11.0	12.5	10.8	11.7	14.0	11.3	12.7
15	10.5	9.7	10.1	14.4	12.3	13.4	11.1	10.8	11.0
10	11.9	10.1	11.0	12.7	9.7	11.2	12.3	11.0	11.7
5	11.5	9.5	10.5	12.5	9.7	11.1	12.5	9.7	11.1
50	16.3	12.8	14.6	15.4	10.8	13.1	12.9	10.2	11.6
40	14.5	13.9	14.2	13.2	10.4	11.8	10.5	9.2	9.9
30	14.2	13.0	13.6	14.0	12.6	13.3	13.5	11.1	12.3
25	16.7	13.5	15.1	14.3	9.5	11.9	10.4	9.9	10.2
20	14.0	12.9	13.5	12.1	9.9	11.0	12.4	9.4	10.9
15	13.1	12.1	12.6	14.7	10.1	12.4	10.4	8.4	9.4
10	12.7	10.8	11.8	9.0	8.1	8.6	9.3	6.8	8.1
5	11.3	10.1	10.7	8.9	7.2	8.1	7.1	4.8	6.0

**TABLE 3-31: CONTACT ANGLE OF A HIGH LINOLENIC FATTY ACID PUFA MIXTURE ON PVC, PC AND PETG OBJECT SLIDES UNDER THE MICROSCOPE**

Temperature [°C]	Aluminum			V2A-Steel			Steel (St37)			Glass		
	Side 1	Side 2	Average	Side 1	Side 2	Average	Side 1	Side 2	Average	Side 1	Side 2	Average
50.0	27.1	27.6	27.4	22.9	23.6	23.3	38.8	37.8	38.3	25.9	26.2	26.0
40.0	26.0	27.8	26.9	21.5	23.4	22.5	39.5	37.1	38.3	25.7	26.6	26.1
30.0	28.9	27.0	28.0	24.3	21.6	23.0	37.6	38.1	37.9	23.4	25.8	24.6
25.0	26.6	29.7	28.2	20.4	19.4	19.9	36.4	40.9	38.7	23.0	24.8	23.9
20.0	27.1	26.6	26.9	20.2	20.1	20.2	36.6	37.2	36.9	22.1	23.0	22.6
15.0	25.2	24.0	24.6	16.9	18.0	17.5	28.7	28.2	28.5	21.8	22.1	21.9
10.0	23.6	24.2	23.9	18.0	19.9	19.0	26.6	26.6	26.6	21.8	24.7	23.3
5.0	23.0	23.0	23.0	17.4	18.0	17.7	26.6	25.1	25.9	21.7	21.2	21.4
50.0	28.8	27.6	28.2	22.2	23.7	23.0	38.5	39.2	38.9	23.4	26.6	25.0
40.0	26.8	28.0	27.4	23.5	25.4	24.5	36.9	37.1	37.0	26.2	26.2	26.2
30.0	27.1	27.9	27.5	21.5	21.0	21.3	36.6	36.6	36.6	24.1	24.2	24.1
25.0	28.6	27.8	28.2	20.1	19.7	19.9	38.0	38.5	38.3	23.3	25.4	24.3
20.0	28.2	27.9	28.1	19.5	19.3	19.4	39.6	39.1	39.4	24.3	24.4	24.4
15.0	26.6	27.0	26.8	18.0	17.8	17.9	26.6	27.4	27.0	23.2	22.0	22.6
10.0	26.6	26.8	26.7	15.9	18.9	17.4	26.0	24.9	25.5	23.3	21.8	22.5
5.0	25.1	25.9	25.5	14.3	16.3	15.3	26.9	24.8	25.9	18.3	18.2	18.2
50.0	24.4	24.6	24.5	22.6	25.0	23.8	40.3	39.8	40.1	26.2	26.1	26.1
40.0	24.4	25.3	24.9	22.0	24.0	23.0	37.9	36.6	37.3	22.9	25.9	24.4
30.0	24.3	26.6	25.5	22.5	22.8	22.7	37.3	38.5	37.9	24.3	21.7	23.0
25.0	25.3	24.0	24.7	21.5	21.5	21.5	35.7	34.4	35.1	23.7	21.0	22.4
20.0	22.8	22.7	22.8	20.6	19.3	20.0	40.9	36.3	38.6	22.9	24.3	23.6
15.0	22.2	24.0	23.1	20.0	22.0	21.0	28.9	28.8	28.9	21.9	22.0	22.0
10.0	21.8	24.7	23.3	14.8	16.9	15.9	26.6	26.6	26.6	21.4	22.6	22.0
5.0	22.5	22.2	22.4	14.3	15.5	14.9	27.3	25.7	26.5	18.6	18.7	18.7

**TABLE 3-32: CONTACT ANGLE OF A HIGH LINOLENIC FATTY ACID PUFA MIXTURE ON ALUMINUM, STAINLESS STEEL, STRUCTURAL STEEL AND GLASS OBJECT SLIDES UNDER THE MICROSCOPE**

## 3.5.V-Reactor – FBRM setup (ml scale)

T [°C]	Supercooling [K]	Induction time, $\tau$ [min]	FBRM Counts/sec, <10 $\mu$ m
19	5.4	12.6315789	901
19	5.4	9.63157895	899
19	5.4	11.6315789	905
19.5	4.9	15.8508772	386
19.5	4.9	14.8508772	392
19.5	4.9	13.8508772	315
20	4.4	23.0701754	285
20	4.4	20.0701754	316
20	4.4	21.0701754	251
20.5	3.9	0	0
20.5	3.9	0	0

**TABLE 3-33: COMPARISON OF INDUCTION TIME,  $\tau$ [s] VS. SUPERCOOLING [K] OF HIGH LINOLEIC SUNFLOWER OIL PUFA MIXTURE (SOLID LIQUID EQUILIBRIUM TEMPERATURE: 24.23 °C) MEASURED BY FBRM IN V-FORM REACTOR @ 15 RPM**

T [°C]	Supercooling [K]	Induction time, $\tau$ [min]	FBRM Counts/sec, <10 $\mu$ m	Blade stirrer speed [rpm]
19.5	4.9	21.8508772	42	5
19.5	4.9	14.8508772	364	15
19.5	4.9	6.85087719	552	30

**TABLE 3-34: INDUCTION TIME,  $\tau$  [s] VS. BLADE STIRRER SPEED OF HIGH LINOLEIC SUNFLOWER OIL PUFA MIXTURE (EQUILIBRIUM TEMPERATURE 24.23 °C) MEASURED BY FBRM IN V-FORM REACTOR AT A SUPERCOOLING OF 4.9K**

### 3.6.Easymax - FBRM setup

The two PUFA mixtures used for these set of experiments are namely, the high linoleic and the high oleic sunflower oil based PUFA mixtures. Each charge of sample sent by the supplier was naturally rechecked and re-analyzed. An average value for the liquidus point used for the determination of the induction time was taken into account.

PUFA mixture	Fraction [%]				
	C16:0	C18:0	C18:1	C18:2	C 18:3
High linoleic sunflower PUFA	6.0	4.0	24.9	63.5	0.2
High oleic sunflower PUFA	4.0	2.9	85.6	5.8	0.15

TABLE 3-35: COMPOSITIONS OF PUFA MIXTURES USED FOR EASYMAX™ - FBRM™ EXPERIMENTS

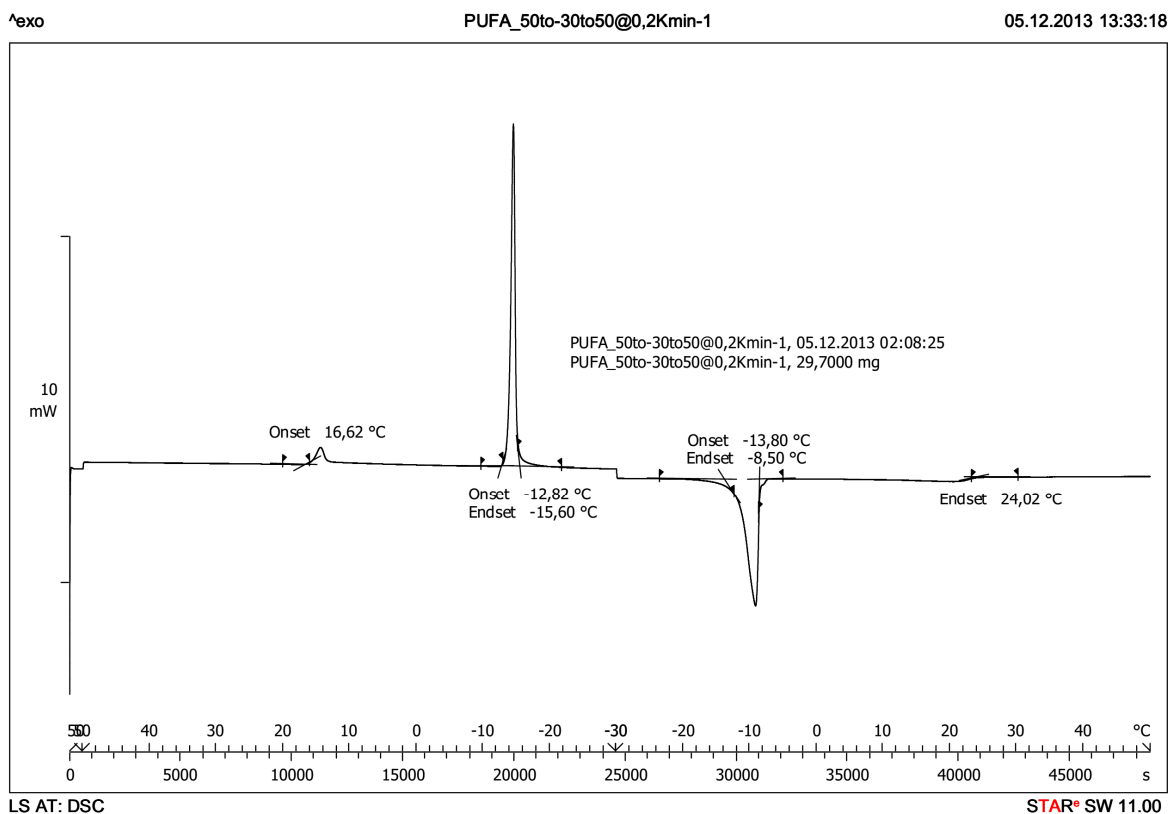


FIGURE 3-11: EXAMPLE OF A HIGH LINOLEIC SUNFLOWER OIL BASED PUFA MIXTURE THERMOGRAM BY THE DSC

High linoleic sunflower PUFA	Peak 1 Onset of spontaneous nucleation[°C]	Peak 2 Solidification peak [°C]		Peak 2' Melting peak [°C]		Peak 1' Liquidus point [°C]
		Onset	Endset	Onset	Endset	
Charge 1	16.74	-12.45	-14.84		-8.02	23.93
Charge 2	16.88	-11.65	-15.93	-14.69	-8.12	23.81
Charge 3	16.62	-12.82	-15.60	-13.80	-8.50	24.02
Average	16.75	-12.31	-15.46	-14.25	-8.21	23.92
High oleic sunflower PUFA	Peak 1 Onset of spontaneous nucleation[°C]	Peak 2 Solidification peak [°C]		Peak 2' Melting peak [°C]		Peak 1' Liquidus point [°C]
		Onset	Endset	Onset	Endset	
Charge 1	14.79	1.83	-0.06	4.95	12.30	21.80
Charge 2	15.38	0.92	-0.30	6.41	12.34	22.10
Charge 3	14.78	1.53	0.37	5.92	12.22	22.16
Average	14.98	1.43	0.00	5.76	12.29	22.02

**TABLE 3-36: THERMAL CHARACTERIZATION OF THE HIGH OLEIC AND LINOLEIC SUNFLOWER OIL PUFA MIXTURES IN THE DSC**

### 3.6.1. High linoleic sunflower oil based PUFA

A detailed overview of the induction time of the nucleation during melt crystallization of the high linoleic PUFA mixture with respect to  $T_{R1}$  and  $T_{R2}$  are shown in Figures 3-12 and 3-13.

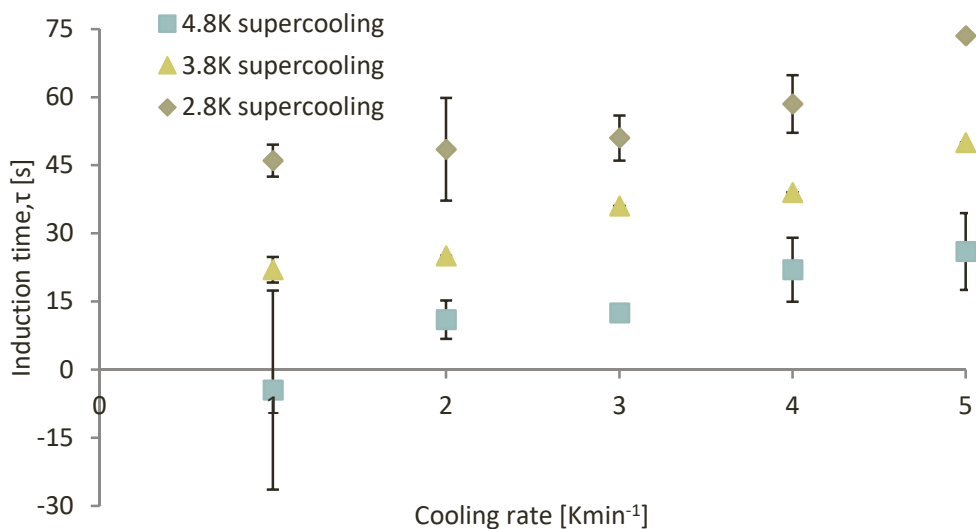


FIGURE 3-12: INDUCTION TIME AS A FUNCTION OF COOLING RATE AT DIFFERENT SUPERCOOLING DURING MELT CRYSTALLIZATION OF HIGH LINOLEIC SUNFLOWER OIL WITH RESPECT TO  $T_{R1}$

### 3.6.2. High oleic sunflower oil based PUFA

A detailed overview of the induction time of the nucleation during melt crystallization of the high oleic PUFA mixture with respect to  $T_{R1}$  and  $T_{R2}$  are shown in Figures 3-14.

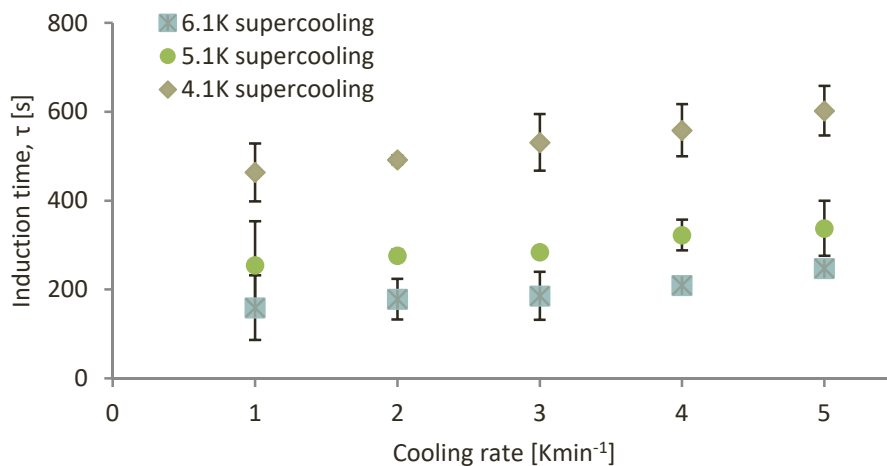


FIGURE 3-13: INDUCTION TIME AS A FUNCTION OF COOLING RATE AT DIFFERENT SUPERCOOLING DURING MELT CRYSTALLIZATION OF HIGH OLEIC SUNFLOWER OIL WITH RESPECT TO  $T_{R1}$

